Aus dem
Universitätsklinikum Düsseldorf
Institut für Diagnostische und Interventionelle Radiologie
Direktor: Univ.-Prof. Dr. med. Gerald Antoch

Chemical Exchange Saturation Transfer: Molekulare Bildgebung mittels Magnetresonanztomographie

Habilitationsschrift

zur Erlangung der venia legendi
für das Fach
Experimentelle Radiologie
des Fachbereichs Medizin

vorgelegt von
Dr. rer. nat. Anja Müller-Lutz

Februar 2021

Inhaltsverzeichnis

Danksagung

Ich möchte mich an dieser Stelle bei allen bedanken, die durch fachliche, persönliche und beratende Unterstützung zum Gelingen dieser Habilitationsschrift beigetragen haben.

Herrn Univ.-Prof. Dr. med. Gerald Antoch danke ich für die Möglichkeit, meine Habilitation an seinem Institut durchführen zu können.

Herrn Prof. Dr. Wittsack danke ich für die herausragende fachliche und beratende Unterstützung.

Meinen Kooperationspartnern Herrn PD Dr. Schleich, Herrn Prof. Dr. Lanzmann und Herrn Dr. Abrar danke ich für die überragende Unterstützung bei der Planung, Durchführung und Auswertung wissenschaftlicher Projekte sowie für die Hilfestellung bei medizinischen Fragen.

Ganz besonders bedanke ich mich bei unserer Arbeitsgruppe für die gute Arbeitsatmosphäre sowie die Offenheit für Kooperationen und der Hilfsbereitschaft beim Lösen auftretender Probleme. Im Besonderen möchte ich hier Julia Stabinska danken für den intensiven wissenschaftlichen Austausch auf dem Gebiet der molekularen Bildgebung.

Ein großer Dank gebührt auch Erika Rädisch für ihre herausragende Unterstützung bei der Datenakquisition.

Meiner Mutter Hildegard Lutz danke ich für ihre fortwährende Unterstützung und Motivation. Sie und meine Schwester Sabrina Lutz haben durch viele Stunden Kinderbetreuung die vorliegende Habilitationsschrift erst ermöglicht.

Meinem Mann Andy Müller danke ich für seine Unterstützung auf dem Weg zu dieser Arbeit sowie für seinen bedingungslosen Rückhalt. Meinem Sohn Frederik Müller danke ich dafür, dass er mit seiner lebensfrohen und offenen Art für einen ausfüllenden und schönen Ausgleich zur wissenschaftlichen Tätigkeit gesorgt hat.

Eidesstattliche Erklärung

Hiermit versichere ich, dass ich die Habilitationsschrift selbstständig verfasst und keine anderen als die angegebenen Hilfsmittel benutzt habe. Alle wörtlich oder inhaltlich übernommenen Stellen habe ich kenntlich gemacht.

Außerdem versichere ich, dass die vorliegende Abhandlung in dieser oder einer ähnlichen Form noch nicht anderweitig als Habilitationsleistung vorgelegt und bewertet wurde.

1 Motivation

Seit Isodor Isaac Rabi im Jahr 1937 die Larmorfrequenz des Kernspins in einem äußeren Magnetfeld gemessen hat [1–3], sind noch vier Jahrzehnte vergangen, bis Peter Mansfield das erste in-vivo Bild eines menschlichen Fingers mit Hilfe des Phänomens der Kernspinresonanz im Jahre 1977 veröffentlichte [4]. In den folgenden Dekaden entwickelte sich die Magnetresonanztomographie (MRT) nicht nur zu einem der wichtigsten Verfahren der anatomischen Bildgebung, sondern es entstand auch das neue Forschungsgebiet der molekularen Bildgebung. Diese Bildgebung ermöglicht eine biochemische Charakterisierung des Gewebes und kann so bedeutende Informationen für die medizinische Diagnostik liefern.

Eine Methode der molekularen Bildgebung, die ohne zusätzliche System-Hardware auskommt und daher an klinischen MR-Systemen eingesetzt werden kann, ist „Chemical Exchange Saturation Transfer“ (CEST) [5]. Sie beruht auf der Beeinflussung des MR-Signals durch den chemischen Austausch von Protonen eines Moleküls mit Protonen des Wassers [5, 6]. Durch die Analyse des chemischen Austausches können wichtige Erkenntnisse über den pH-Wert des Gewebes und die Konzentration der im Gewebe enthaltenen Stoffe gewonnen werden. Ein Nutzen dieser Methode wird in den Feldern der Tumorbildgebung, der Darstellung metabolischer Veränderungen in Folge von Nierenerkrankungen, der Knorpelbildgebung sowie der Beurteilung neurologischer Erkrankungen erwartet [7–12]. Das Potential der CEST-Bildgebung, zukünftig auch in der Klinik eingesetzt zu werden, ist daher evident und macht sie zu einem relevanten Forschungsgegenstand.

Die Weiterentwicklung von CEST zu einem klinisch einsetzbaren Verfahren ist herausfordernd. Die CEST-Technik reagiert sehr sensitiv auf Magnetfeldinhomogenitäten und Bewegung. Zudem werden die Messergebnisse der CEST-Bildgebung oft durch Veränderung der Messparameter selbst, aber auch durch physiologisch bedingte Veränderungen des Gewebes beeinflusst. Daher ist die Erforschung von Methoden notwendig, die eine stabilere quantitative CEST-Bildgebung insbesondere im Bereich klinisch einsetzbarer Magnetfeldstärken ermöglichen.

Folglich sind die Ziele der Studien dieser Habilitationsschrift die Untersuchung der Abhängigkeiten der CEST-Technik von physiologischen Parametern, die Optimierung und Weiterentwicklung der technischen Methoden der molekularen CEST-Bildgebung sowie die Evaluierung der Möglichkeit, quantitative Informationen über den pH-Wert und die Konzentration bestimmter Stoffe mit diesem Verfahren zu gewinnen.

2 Einleitung

In diesem Kapitel wird zunächst die historische Entwicklung der MRT von der Entdeckung des Spins bis hin zur molekularen Bildgebung beschrieben. Es folgt ein Vergleich verschiedener Verfahren zur biochemischen Charakterisierung des Gewebes.

2.1 Entwicklung der MRT: Von der Entdeckung des Spins bis zur molekularen Bildgebung

Die MRT kann mit Hilfe der Spindynamik beschrieben werden. Nach der Einführung der Idee des intrinsischen Spins durch Wolfgang Pauli [13] sowie ersten experimentellen Nachweisen des Spins durch Otto Stern und Walther Gerlach im Jahre 1924 [14] gelang es Isodor Isaac Rabi im Jahre 1937, die Larmorfrequenz des Kernspins in einem äußeren Magnetfeld zu messen [1–3].

1946 wurde von Felix Bloch und Edward Purcell unabhängig voneinander theoretisch und experimentell gezeigt, dass die Kernspin-Resonanz nicht nur in freien Atomen gemessen werden kann, sondern auch in Atomkernen, welche sich in Festkörpern und Flüssigkeiten befinden [3, 15–17], wofür beide im Jahre 1952 den Nobelpreis für Physik erhielten. Erste Untersuchungen von biologischem Gewebe wurden 1955 von Erik Odeblad und Gunnar Lindström durchgeführt [18]. Die Bildgebung mittels der MRT geht auf die Idee von Paul Lauterbur aus dem Jahr 1971 zurück, Magnetfeldgradienten für die räumliche Kodierung des Spinsystems einzusetzen. Bereits zwei Jahre später, im Jahre 1973, konnten erste MR-Bilder akquiriert werden [19]. Die ersten anatomischen in-vivo Bilder im Menschen wurden 1977 durch Peter Mansfield und Andrew A. Maudsley veröffentlicht [4]. Für ihre Entdeckungen im Bereich der Magnetresonanzbildgebung erhielten Mansfield und Lauterbur in Jahr 2003 den Nobelpreis für Medizin.

Wegen der hohen Signalstärke bei der Bildgebung der Wasserstoffkerne (^{1}H-Kerne) werden diese als Signalquelle in der klinischen Routine mittels der MR-Tomographie verwendet. Diverse Studien beschäftigen sich aber auch mit den diagnostischen Möglichkeiten, die anhand anderer Kerne mit einem Kernspin gewonnen werden können. Diese Art der Bildgebung wird auch als X-Kern-Bildgebung bezeichnet. Zu den Kernen, die mittels der X-Kern-Bildgebung untersucht werden, gehören beispielsweise ^{23}Na, ^{17}O und ^{35}Cl. Durch ihre im Vergleich zu Wasserstoffkernen geringere Häufigkeit im menschlichen Körper sowie durch ihr niedrigeres gyromagnetisches Verhältnis hat diese Art der Bildgebung jedoch ein

schlechteres Signal-zu-Rausch Verhältnis (SNR) als die ^{1}H-Bildgebung, welche die anatomische Bildgebung dominiert. Die X-Kern-Bildgebung wird hingegen üblicherweise zur Ermittelung molekularer und metabolischer Informationen eingesetzt [20, 21].

Molekulare Informationen können aber auch mit der ^{1}H-Bildgebung gewonnen werden. Hierzu kann das Verfahren CEST verwendet werden, welches in den Jahren 1989 und 1990 von Steven D. Wolff und Robert S. Balaban eingeführt wurde [22, 23]. CEST basiert auf dem chemischen Austausch von Protonen, welcher das mittels der MRT gemessene Signal der Magnetisierung beeinflusst [22–24]. Inzwischen wurde die CEST-Bildgebung schon in unterschiedlichen Forschungsgebieten eingesetzt. So wurde sie beispielsweise benutzt, um den Tumormetabolismus abzuschätzen [25], um die Knorpelqualität zu beurteilen [26, 27], um molekulare Veränderungen in Folge von Diabetes darzustellen [28], um akutes Nierenversagen zu untersuchen [11] sowie um den Metabolismus des Herzens zu beurteilen [29]. Während die ersten Entwicklungen in der CEST-Bildgebung semi-quantitative Ergebnisse lieferten, entwickelt sich das Verfahren immer weiter hin zur quantitativen Bildgebung [30, 31].

2.2 Gewinnung molekularer Informationen mittels MRS, MRT und PET

Neben der Bildgebung mittels der MRT eignen sich zur Gewinnung molekularer Gewebeinformation auch die Magnetresonanzspektroskopie (MRS) sowie die Positronen-Emmissions-Tomographie (PET).

Die MRS kann an konventionellen MRT-Systemen durchgeführt werden [32] und misst die Signalintensität bei unterschiedlichen Frequenzen in einem vorab definierten Volumen. So entsteht ein Spektrum, welches Rückschlüsse auf die Stoffe im Gewebe ermöglicht.

Ein Nachteil der MRS ist ihre geringe Sensitivität, welche beispielsweise durch die geringe Konzentration und die spektrale Überlagerung einiger Stoffe entsteht.

Bei der PET wird ein Tracer in den Körper des Patienten gebracht. Der Tracer ist dabei ein Molekül, welches einen Positronenstrahler enthält. Die wichtigsten Positronenstrahler, die in der Nuklearmedizin verwendet werden, sind ^{30}P, ^{18}F, ^{15}O, ^{13}N und ^{11}C [33]. Das Ziel ist es, mit Hilfe der PET den Tracer im Körper zu lokalisieren und dadurch Informationen über den Gewebemetabolismus zu erhalten.

Nachteile der PET sind die im Vergleich zur MRT geringere räumliche Auflösung sowie die Belastung des Patienten durch radioaktive Strahlung [32]. Diese entsteht einerseits durch die Verwendung des Tracers, andererseits aber auch durch eine Transmissionsmessung, welche für die Messung der Abschwächung des PET-Signals durch Absorption von Photonen im Körper benutzt wird [32].

Im Gegensatz zu der PET muss bei der MRT keine ionisierende Strahlung verwendet werden. Sie ist eine vielseitig einsetzbare Technik, die neben der Bildgebung der Anatomie auch physiologische und molekulare Eigenschaften darstellen kann [34]. Diese Eigenschaften spielen eine bedeutende Rolle für die moderne medizinische Diagnostik. In der MRT können die in Kapitel 2.1 bereits eingeführte X-Kern-Bildgebung, die Bildgebung mittels Kontrastmitteln sowie die CEST-Bildgebung für die molekulare Bildgebung genutzt werden.

Die X-Kern-Bildgebung erlaubt die Quantifizierung unterschiedlicher molekularer Effekte im Körper. Dazu werden verschiedene Kerne genutzt wie beispielsweise die im Kapitel 2.1 bereits genannten Isotope ^{23}Na, ^{17}O und ^{35}Cl. Die X-Kern-Bildgebung wird in diversen Bereichen wie etwa in der Tumor-Bildgebung, in der Abschätzung der Funktion der Niere und in der Beurteilung der Knorpelqualität eingesetzt [35–39]. Hauptnachteile der X-Kern-Bildgebung sind, wie bereits erwähnt, ein geringeres MR-Signal im Vergleich zur Standard-Bildgebung von Protonen sowie spezielle Anforderungen an die System-Hardware. Daher ist die X-Kern-Bildgebung an vielen klinischen MR-Geräten aktuell noch nicht möglich.

Die molekulare Bildgebung mittels Kontrastmittel wird beispielsweise zur Beurteilung von Knorpelschäden eingesetzt [40]. Die Darstellung von Knorpelschäden erfolgt dabei mit der Methode „dGEMRIC“, welche das negativ geladene Kontrastmittel Gadopentetat-Dimeglumin (Gd-DTPA^{2-}) verwendet, um den Glykosaminoglykangehalt im Knorpel abzuschätzen [40]. Wegen möglicher Begleiterscheinungen beim Einsatz von gadoliumhaltigen Kontrastmitteln wie Gadoliniumablagerungen und die Entwicklung einer nephrogenen systemischen Fibrose wird die Bildgebung ohne Kontrastmittel immer wichtiger [41–44].

Die ^{1}H-basierte Bildgebung des chemischen Austausches mittels CEST ermöglicht es, Informationen über chemische Verbindungen zu gewinnen, welche Protonen besitzen, die an Austauschprozessen mit Wasserprotonen teilnehmen [32]. Die CEST-Bildgebung hat folgende Vorteile:

1. CEST kann sowohl mit als auch ohne Kontrastmittel verwendet werden.
2. CEST ermöglicht die Darstellung quantitativer Information über die biochemische Zusammensetzung.
3. CEST ist eine bildgebende Technik ohne Strahlenbelastung.
4. CEST benötigt keine zusätzliche System-Hardware.
5. CEST kann an klinischen MR-Tomographen benutzt werden.
6. CEST erfordert keine radioaktiven Tracer.

Sie kann in unterschiedlichen Regionen angewendet werden wie beispielsweise im Gehirn, in den Bandscheiben, in der Niere und im Herzen [11, 12, 29, 32]. Sie ermöglicht es auch, quantitative Erkenntnisse über den pH-Wert und die

Konzentrationen bestimmter chemischer Verbindungen zu gewinnen. Die Bestimmung des pH-Werts hat in der medizinischen Diagnostik besondere Relevanz, da dieser sich beispielsweise bei Tumor- und Nierenerkrankungen [10, 45–47] verändert. Auch die Konzentration bestimmter chemischer Verbindungen verändert sich durch pathologische Prozesse. So führen degenerative Knorpelveränderungen zu einer Abnahme des Gehalts der Glykosaminoglykane (GAG) [9] und Nierenerkrankungen haben Auswirkungen auf den corticomedullaren Gradienten der Harnstoff-Konzentration [48].

3 Ziele der Arbeit

Die Hauptziele dieser Arbeit sind die Optimierung des Verfahrens CEST an einem klinischen 3 Tesla Gerät, die Untersuchung der Bestimmung quantitativer Informationen mittels CEST sowie die Herausarbeitung der Abhängigkeiten des CEST-Effekts von physiologischen Parametern.

Die Ziele dieser Arbeit können wie folgt dargestellt werden:

- Bestimmung der Abhängigkeiten des CEST-Effekts vom Alter, vom Geschlecht, vom BMI und von der transversalen Relaxationszeit $T2$
- Erstmalige Messung des CEST-Effekts bei 3T in zervikalen Bandscheiben und im OSG
- Technische Verbesserungen der CEST-Bildgebung in Bandscheiben mittels Bewegungskorrektur
- Entwicklung und Untersuchung verschiedener Methoden zur Korrektur von Magnetfeldinhomogenitäten
- Untersuchung der Abhängigkeit des CEST-Effektes von Messparametern bei der Datenakquisition
- Untersuchung der quantitativen CEST-Bildgebung mit und ohne Kontrastmittel

4 Literaturangaben der zugrunde liegenden Forschungsarbeiten

[I] Müller-Lutz A, Schleich C, Pentang G, Schmitt B, Lanzman RS, Matuschke F, Wittsack HJ, Miese F. Age-dependency of glycosaminoglycan content in lumbar discs: A 3T gagCEST study. *J Magn Reson Imaging*, 2015, 42(6):1517-23

[II] Müller-Lutz A, Schleich C, Schmitt B, Antoch G, Matuschke F, Quentin M, Wittsack HJ, Miese F. Gender, BMI and T2 dependencies of glycosaminoglycan chemical exchange saturation transfer in intervertebral discs. *Magn Reson Imaging*, 2016, 34(3):271-5

[III] Schleich C*, Müller-Lutz A*, Zimmermann L, Boos J, Schmitt B, Wittsack HJ, Antoch G, Miese F. Biochemical imaging of cervical intervertebral discs with glycosaminoglycan chemical exchange saturation transfer magnetic resonance imaging: feasibility and initial results. *Skeletal Radiol*, 2016, 45(1):79-85
*Christoph Schleich and Anja Müller-Lutz have contributed equally.

[IV] Abrar DB, Schleich C, Radke KL, Frenken M, Stabinska J, Ljimani A, Wittsack HJ, Antoch G, Bittersohl B, Hesper T, Nebelung S, Müller-Lutz A. Detection of early cartilage degeneration in the tibiotalar joint using 3T gagCEST imaging: a feasibility study. *Magn Reson Mater Phy*, 2020, doi: 10.1007/s10334-020-00868-y. Online ahead of print

[V] Müller-Lutz A, Schleich C, Schmitt B, Topgöz M, Pentang G, Antoch G, Wittsack HJ, Miese F. Improvement of gagCEST imaging in the human lumbar intervertebral disc by motion correction. *Skeletal Radiol*, 2015, 44(4):505-11

[VI] Müller-Lutz A, Matuschke F, Schleich C, Wickrath F, Boos J, Schmitt B, Wittsack HJ. Improvement of water saturation shift referencing by sequence and analysis optimization to enhance chemical exchange saturation transfer imaging. *Magn Reson Imaging*, 2016, 34(6):771-778

[VII] Müller-Lutz A, Ljimani A, Stabinska J, Zaiss M, Boos J, Wittsack HJ, Schleich C. Comparison of B_0 versus B_0 and B_1 field inhomogeneity correction for glycosaminoglycan chemical exchange saturation transfer imaging. *Magn*

Reson Mater Phy, 2018, 31(5):645-651

[VIII] Müller-Lutz A, Cronenberg T, Schleich C, Wickrath F, Zaiss M, Boos J, Wittsack HJ. Comparison of glycosaminoglycan chemical exchange saturation transfer using Gaussian-shaped and off-resonant spin-lock radiofrequency pulses in intervertebral disks. *Magn Reson Med*, 2017, 78(1):280-284

[IX] Müller-Lutz A, Khalil N, Schmitt B, Jellus V, Pentang G, Oeltzschner G, Antoch G, Lanzman RS, Wittsack HJ. Pilot study of Iopamidol-based quantitative pH imaging on a clinical 3T MR scanner. *Magn Reson Mater Phy*, 2014, 27(6):477-85

[X] Stabinska J, Cronenberg T, Wittsack HJ, Lanzman RS, Müller-Lutz A. Quantitative pulsed CEST-MRI at a clinical 3T MRI system. *Magn Reson Mater Phy*, 2017, 30(5):505-516

[XI] Stabinska J, Neudecker P, Ljimani A, Wittsack HJ, Lanzman RS, Müller-Lutz A. Proton exchange in aqueous urea solutions measured by water-exchange (WEX) NMR spectroscopy and chemical exchange saturation transfer (CEST) imaging in vitro. *Magn Reson Med*, 2019, 82(3):935-947

5 Kurze Zusammenfassung der Inhalte aus den Publikationen

[I] Müller-Lutz A, Schleich C, Pentang G, Schmitt B, Lanzman RS, Matuschke F, Wittsack HJ, Miese F. Age-dependency of glycosaminoglycan content in lumbar discs: A 3T gagCEST study. *J Magn Reson Imaging*, 2015, 42(6):1517-23

In dieser Studie wurde die Abhängigkeit des CEST-Effektes in den Bandscheiben vom Alter untersucht. Hierzu wurde der CEST-Effekt in den lumbalen Bandscheiben von 70 Probanden ohne Rückenschmerzen in einem Alter von 21 bis 69 Jahren analysiert. Die Studie zeigte eine Reduktion des CEST-Effektes in den Bandscheiben mit zunehmendem Alter. Diese Reduktion könnte auf eine Verminderung der Konzentration der Glykosaminoglykane zurückzuführen sein.

[II] Müller-Lutz A, Schleich C, Schmitt B, Antoch G, Matuschke F, Quentin M, Wittsack HJ, Miese F. Gender, BMI and T2 dependencies of glycosaminoglycan chemical exchange saturation transfer in intervertebral discs.*Magn Reson Imaging*, 2016, 34(3):271-5

In dieser Studie wurde die Abhängigkeit des CEST-Effektes von Body Mass Index (BMI) und Geschlecht sowie von der transversalen Relaxationszeit T_2 untersucht. Hierzu wurde der CEST-Effekt der lumbalen Bandscheiben von 17 Männern und 17 Frauen evaluiert. Frauen zeigten in dieser Studie einen höheren CEST-Effekt als Männer. Des Weiteren korrelierte der CEST-Effekt negativ mit dem BMI und positiv mit der transversalen Relaxationszeit T_2.

[III] Schleich C*, Müller-Lutz A*, Zimmermann L, Boos J, Schmitt B, Wittsack HJ, Antoch G, Miese F. Biochemical imaging of cervical intervertebral discs with glycosaminoglycan chemical exchange saturation transfer magnetic resonance imaging: feasibility and initial results. *Skeletal Radiol*, 2016, 45(1):79-85 *Christoph Schleich and Anja Müller-Lutz have contributed equally.

In dieser Studie wurde die Möglichkeit aufgezeigt, mittels biochemischer Bildgebung den CEST-Effekt in den zervikalen Bandscheiben zu bestimmen. Hierzu wurde der CEST-Effekt in 42 zervikalen Bandscheiben von 7 Probanden (Alter:

21, 4±1, 4 Jahre) ohne Rückenschmerzen gemessen. Zusätzlich zur biochemischen Bildgebung wurde eine T2-gewichtete Bildgebung durchgeführt, um anschließend eine Differenzierung zwischen degenerativen und nicht-degenerativen Bandscheiben zu ermöglichen. Die CEST-Bildgebung der zervikalen Bandscheiben war technisch erfolgreich. Bandscheiben mit degenerativen Veränderungen wiesen einen signifikant niedrigeren CEST-Effekt im Vergleich zu Bandscheiben ohne Degeneration auf.

[IV] Abrar DB, Schleich C, Radke KL, Frenken M, Stabinska J, Ljimani A, Wittsack HJ, Antoch G, Bittersohl B, Hesper T, Nebelung S, Müller-Lutz A. Detection of early cartilage degeneration in the tibiotalar joint using 3T gagCEST imaging: a feasibility study. *Magn Reson Mater Phy*, 2020, doi: 10.1007/s10334-020-00868-y. Online ahead of print

In dieser Studie wurden die Messparameter für die CEST-Bildgebung mit Hilfe der Bloch-McConnell Gleichungen für die Darstellung der Glykosaminoglykane im oberen Sprunggelenk (OSG) optimiert. Anschließend wurden die optimierten Parameter für die Messung des CEST-Effektes des OSGs von 17 gesunden Probanden und fünf Patienten mit osteochondralen Läsionen verwendet. Der CEST-Effekt im Knorpel des OSGs war im Patientenkollektiv geringer als im gesunden Vergleichskollektiv.

[V] Müller-Lutz A, Schleich C, Schmitt B, Topgöz M, Pentang G, Antoch G, Wittsack HJ, Miese F. Improvement of gagCEST imaging in the human lumbar intervertebral disc by motion correction. *Skeletal Radiol*, 2015, 44(4):505-11

In dieser Studie wurde untersucht, ob eine Verbesserung der CEST-Bildgebung in den menschlichen Bandscheiben durch Bewegungskorrektur erzielt werden kann. Hierzu wurde der CEST-Effekt der lumbalen Bandscheiben von 12 Probanden mit und ohne Bewegungskorrektur analysiert. Es wurde gezeigt, dass Bewegungskorrektur das Verhältnis zwischen Signal und Rauschen (SNR) verbessert. Dadurch konnte eine signifikante Verbesserung der biochemischen Bildgebung der Bandscheiben erzielt werden.

[VI] Müller-Lutz A, Matuschke F, Schleich C, Wickrath F, Boos J, Schmitt B, Wittsack HJ. Improvement of water saturation shift referencing by sequence and analysis optimization to enhance chemical exchange saturation transfer imaging. *Magn Reson Imaging*, 2016, 34(6):771-778

In dieser Studie wurden die Messparameter zur Korrektur von B_0-Feldinhomogenitäten mit Hilfe von Simulationen optimiert. Anschließend wurden Methoden zur Datenauswertung für die Abschätzung von B_0-Feldinhomogenitäten weiterentwickelt und mit bereits etablierten Verfahren verglichen. Für diesen Vergleich wurden sowohl Simulationen als auch zwei in-vivo Messungen verwendet. Es konnte gezeigt werden, dass durch die in dieser Studie vorgestellten Optimierungen und Weiterentwicklungen die Korrektur von B_0-Feldinhomogenitäten verbessert werden kann.

[VII] Müller-Lutz A, Ljimani A, Stabinska J, Zaiss M, Boos J, Wittsack HJ, Schleich C. Comparison of B_0 versus B_0 and B_1 field inhomogeneity correction for glycosaminoglycan chemical exchange saturation transfer imaging. *Magn Reson Mater Phy*, 2018, 31(5):645-651

In dieser Studie wurde die Auswirkung von zwei unterschiedlichen Methoden zur Feldinhomogenitätskorrektur auf den beobachteten CEST-Effekt der lumbalen Bandscheiben von 20 Probanden untersucht. Die erste Methode (WASSR = Water Saturation Shift Referencing) diente zur Korrektur von B_0- Feldinhomogenitäten, die zweite Methode (WASABI = „mapping of water frequency shift and B_1 amplitude“) hingegen zur Korrektur von sowohl B_0- als auch B_1-Feldinhomogenitäten. Beide Methoden zur Feldinhomogenitätskorrektur führten zu einem signifikant höheren CEST-Effekt im Nucleus Pulposus (Gallertkern der Bandscheibe) im Vergleich zum Annulus Fibrosus (Faserring der Bandscheibe). Die Korrektur beider Arten von Feldinhomogenitäten führte zu einer Steigerung des beobachtbaren CEST-Effekts und des SNRs.

[VIII] Müller-Lutz A, Cronenberg T, Schleich C, Wickrath F, Zaiss M, Boos J, Wittsack HJ. Comparison of glycosaminoglycan chemical exchange saturation transfer using Gaussian-shaped and off-resonant spin-lock radiofrequency pulses in intervertebral disks. *Magn Reson Med*, 2017, 78(1):280-284

In dieser Studie wurde der CEST-Effekt in lumbalen Bandscheiben von 15 Probanden mit einer Präparation der Magnetisierung durch Gauss-förmige und Spin-Lock (SL) Hochfrequenzpulse (HF-Pulse) evaluiert. Die Ergebnisse für den CEST-Effekt waren für beide Techniken der HF-Einstrahlung vergleichbar und ermöglichten eine Differenzierung zwischen dem Nucleus Pulposus und Annulus

Fibrosus. Daher können sowohl SL als auch Gauss-förmige HF-Pulse für die Präparation der Magnetisierung verwendet werden.

[IX] Müller-Lutz A, Khalil N, Schmitt B, Jellus V, Pentang G, Oeltzschner G, Antoch G, Lanzman RS, Wittsack HJ. Pilot study of Iopamidol-based quantitative pH imaging on a clinical 3T MR scanner. *Magn Reson Mater Phy*, 2014, 27(6):477-85

In dieser Pilotstudie wurde die biochemische Bildgebung mittels CEST mit dem Kontrastmittel Iopamidol sowohl in vitro als auch erstmalig in vivo in einer 63 Jahre alten Patientin untersucht. Diese Bildgebung, verknüpft mit einer dedizierten Auswertungsmethode, ermöglichte eine pH-Wert Bestimmung, welche unabhängig von der verwendeten Konzentration des Kontrastmittels Iopamidol war. Der in der Patientin mittels MRT gemessene pH-Wert des Urins stimmte dabei mit dem nach der Messung bestimmten ex-vivo pH-Wert des Urins überein.

[X] Stabinska J, Cronenberg T, Wittsack HJ, Lanzman RS, Müller-Lutz A. Quantitative pulsed CEST-MRI at a clinical 3T MRI system. *Magn Reson Mater Phy*, 2017, 30(5):505-516

In dieser Studie wurde mit Hilfe von Simulationen und MR-Messungen von Phantomen untersucht, ob die Konzentration und chemische Austauschrate von Kreatin an einem klinischen 3 Tesla MR-System bestimmt werden kann. An klinischen MR-Systemen muss aufgrund von Hardware-Limitationen und SAR-Richtlinien eine gepulste Form des Sättigungsmoduls verwendet werden. Die Ergebnisse zeigten, dass eine quantitative Analyse der Kreatin-Konzentration und der Austauschrate von Kreatin mittels der gepulsten CEST-Bildgebung auch bei 3 Tesla möglich ist.

[XI] Stabinska J, Neudecker P, Ljimani A, Wittsack HJ, Lanzman RS, Müller-Lutz A. Proton exchange in aqueous urea solutions measured by water-exchange (WEX) NMR spectroscopy and chemical exchange saturation transfer (CEST) imaging in vitro. *Magn Reson Med*, 2019, 82(3):935-947

In dieser Studie wurde in Phantomen die Austauschrate von Harnstoff bei verschiedenen pH-Werten mittels der CEST-Bildgebung und der WEX-Spektroskopie abgeschätzt. Dabei wurde die CEST-Bildgebung an einem klinischen 3 Tesla MRT und die WEX-Spektroskopie an einem 600 MHz NMR Spektrometer durchgeführt. Die Experimente zeigten, dass die WEX-Spektroskopie die Austauschrate von Harnstoff bestimmen kann und dass mit der CEST-Bildgebung in einem großen Bereich von pH-Werten vergleichbare Ergebnisse der Austauschrate erzielt werden können.

6 Grundlagen der Forschungsarbeiten

Im Folgenden werden zunächst die Grundlagen der Magnetresonanztomographie und die biochemische Bildgebung mit der CEST-Methode präsentiert. Im Anschluss wird dargestellt, wie diese Methode quantitative molekulare Informationen von Gewebe liefern kann. Hierzu gehören - wie im Kapitel 2.2 bereits erwähnt - die Bestimmung des pH-Werts und der Konzentration von Metaboliten im Gewebe. Als nächstes werden technische Limitationen, die bei einer CEST-Messung auftreten können, diskutiert. Neben der CEST-Methode können quantitative Informationen über chemische Austauschprozesse ebenfalls mittels der „Water Exchange“ (WEX)-Spektroskopie erhalten werden, die kurz eingeführt wird. Als Anwendungsgebiete der molekularen Bildgebung dienen die Darstellung der Glykosaminoglykane (GAG) in den Bandscheiben und im oberen Sprunggelenk (OSG). Der Aufbau der Bandscheiben und des OSGs sowie die Möglichkeit, den CEST-Effekt von GAG zu messen, werden daher in den Kapiteln 6.6 und 6.7 erläutert.

6.1 Grundlagen der MRT

Die MRT ist ein Verfahren, welches zur Bildgebung des menschlichen Körpers genutzt werden kann [33, 49]. Sie basiert auf der Dynamik von Spin-Ensembles in einem externen Magnetfeld [49], welche nachfolgend kurz physikalisch beschrieben wird. Dabei entspricht die z-Achse stets der Orientierung des Hauptmagnetfeldes. Des Weiteren ist die Beschreibung der MR-Grundlagen auf die Bildgebung mit Protonen fokussiert.

Die z-Komponente des Drehimpulses ist gegeben durch [49]

$$I_z = \pm 0,5 \cdot \hbar. \tag{6.1}$$

Dabei ist $\hbar$ definiert als $h/(2\pi)$, wobei h das Planck'sche Wirkungsquantum ist. Der Drehimpuls steht in direktem Zusammenhang zum magnetischen Dipolmoment $\boldsymbol{\mu}$: $\boldsymbol{\mu} = \gamma \mathbf{I}$, wobei γ das gyromagnetische Verhältnis beschreibt [49]. Bei Protonen ist das gyromagnetische Verhältnis über die Gleichung $\gamma/2\pi = 42,6\,\mathrm{MHz/T}$ gegeben [49].

Kernspins in einem Magnetfeld $\mathbf{B} = B_0 \cdot \boldsymbol{e_z}$, wobei B_0 die Stärke des Magnet-

feldes und $\boldsymbol{e_z}$ der Einheitsvektor in z-Richtung ist, können zwei Energieniveaus haben [33, 49]:

$$E = -\boldsymbol{\mu}\mathbf{B} = \pm 0,5\gamma\hbar B_0 \tag{6.2}$$

Die Energiedifferenz zwischen den beiden Energieniveaus ist somit gegeben durch [49]

$$\Delta E = \gamma\hbar B_0 = \hbar\omega = 2\pi\hbar f, \tag{6.3}$$

wobei mit $\omega = 2\pi f$ die Kreisfrequenz und mit f die Frequenz bezeichnet wird. Die Frequenz f wird auch Larmorfrequenz genannt und ist durch

$$f_L = \frac{\gamma}{2\pi} B_0 \tag{6.4}$$

gegeben [33, 49].

In den dieser Arbeit zugrunde liegenden Studien wurde eine Magnetfeldstärke B_0 von 3 Tesla benutzt. Bei dieser Magnetfeldstärke liegt die Larmorfrequenz in der Größenordnung von 127,8 MHz.

Für die MR-Bildgebung wird die makroskopische Magnetisierung $\mathbf{M}$ von N Spins in einem Volumen V gemessen [49]. $\mathbf{M}$ ist gegeben als [49]

$$\mathbf{M} = \frac{1}{V} \sum_{i=1}^{N} \boldsymbol{\mu}_i. \tag{6.5}$$

Mit der Magnetresonanztomographie kann die transversale Komponente der Magnetisierung $M_\perp$ gemessen werden [33]. Das Gesamtmagnetfeld ist eine Überlagerung des Hauptmagnetfeldes und des Hochfrequenz-Feldes (HF-Feldes), welches zur Signalanregung nötig ist [49]:

$$\mathbf{B}(t) = B_0 \boldsymbol{e_z} + B_1 \left(\boldsymbol{e_x} \cos\omega t - \boldsymbol{e_y} \sin\omega t\right) \tag{6.6}$$

Hierbei sind $\boldsymbol{e_x}$, $\boldsymbol{e_y}$ und $\boldsymbol{e_z}$ die orthogonalen Einheitsvektoren in die drei Raumrichtungen.

Die zeitliche Entwicklung der Gesamtmagnetisierung wird mit Hilfe der Bloch-Gleichung beschrieben [49]:

$$\frac{d\mathbf{M}(t)}{dt} = \gamma \left(\mathbf{M}(t) \times \mathbf{B}(t)\right) - \frac{1}{T_2} \left(M_x(t)\boldsymbol{e_x} + M_y(t)\boldsymbol{e_y}\right) + \frac{M_0 - M_z(t)}{T_1} \boldsymbol{e_z} \tag{6.7}$$

Dabei ist T_1 die longitudinale Relaxationszeit, T_2 die transversale Relaxationszeit, M_x, M_y und M_z sind die Komponenten der Gesamtmagnetisierung in x-, y- und z-Richtung und die Gleichgewichtsmagnetisierung M_0 ist die Magnetisierung vor der Signalanregung. Die longitudinale Relaxationszeit wird auch als Spin-Gitter-Relaxationszeit bezeichnet, da durch Interaktion der Spins mit der Umgebung Energie abgegeben wird und so eine Relaxation hin zu M_0 erfolgt [33].

Als longitudinale Relaxationsrate wird der Kehrwert der longitudinalen Relaxationszeit bezeichnet [49]. Die transversale Relaxationszeit trägt auch den Namen Spin-Spin-Relaxationszeit und beruht auf der Wechselwirkung der Spins untereinander, die zu ihrer Dephasierung führt [33]. Als transversale Relaxationsrate wird der Kehrwert der transversalen Relaxationszeit bezeichnet [49]. Durch Einfluss weiterer Faktoren wie beispielsweise Feldinhomogenitäten verkürzt sich die transversale Relaxationszeit [49]. Die effektive transversale Relaxationszeit wird als T_2^* bezeichnet [49].

Die Echozeit T_E beschreibt üblicherweise die Zeit zwischen Signalanregung durch das HF-Feld und Signalakquisition [50]. Die Repetitionszeit T_R beschreibt die Zeit zwischen aufeinanderfolgenden Signalanregungen [50]. Bei der Signalaufnahme wird das durch die Quermagnetisierung in der Spule induzierte Signal akquiriert [33].

Im Folgenden wird dargestellt, wie mit Hilfe der MRT unterschiedliche Bildkontraste entstehen können. Hierfür werden die Spinecho-Sequenz (SE-Sequenz) und Gradientenecho-Sequenz (GRE-Sequenz) einführt sowie die Einflüsse unterschiedlicher Echo- und Repetitionszeiten auf den Bildkontrast erörtert.

Bei der SE-Sequenz wird nach der Zeit $T_E/2$ ein 180° HF-Puls eingestrahlt [33]. Dieser sorgt dafür, dass Spins, welche durch die Spin-Spin-Wechselwirkung dephasiert wurden, wieder in Phase gebracht werden [33]. Dadurch entsteht ein Spin-Echo zum Zeitpunkt T_E [33]. Für eine 90°-Signalanregung resultiert bei der SE-Sequenz die transversale Magnetisierung [49]

$$M_\perp(T_E, T_R) = M_\perp(0)\left(1 - \exp\left(-\frac{T_R}{T_1}\right)\right)\exp\left(-\frac{T_E}{T_2}\right). \tag{6.8}$$

Aus Gleichung (6.8) lässt sich Folgendes ableiten: Falls $T_E \ll T_2$ sowie $T_R \gg T_1$ gilt, resultiert ein MR-Signal, welches unabhängig von den Relaxationszeiten T_1 und T_2 ist [33]. Unter der Bedingung, dass $T_E \ll T_2$ sowie $T_R < T_1$ ist, ist das gemessene MR-Signal abhängig von der T_1-Zeit, nicht aber von der T_2-Zeit [33]. Wenn $T_E \approx T_2$ und $T_R \gg T_1$ ist, wird das MR-Signal durch die T_2-Zeit, nicht aber durch die T_1-Zeit beeinflusst [33].

Im Gegensatz zur SE-Sequenz werden bei der GRE-Sequenz Magnetfeldgradienten benutzt, um ein Signalecho, welches auch als Feldecho bezeichnet wird, zu erzeugen [51]. Zunächst wird ein Gradient angewendet, welcher die Spins dephasiert [51]. Nach einer Zeit $T_E/2$ wird ein Gradient mit umgekehrter Polarität angewendet, welcher die Spins rephasiert [51], wodurch ein Signalecho entsteht. Nach dem Signalecho bleibt der umgedrehte Gradient für die Zeit $T_E/2$ eingeschaltet [33]. Erwähnenswert ist, dass die GRE-Sequenz im Gegensatz zur SE-Sequenz lokale Feldinhomogenitäten nicht refokussieren kann, wodurch bei geeigneter Wahl von T_E und T_R ein T_2*-gewichtetes Bild akquiriert werden kann [51]. Ein großer Vorteil der Bildgebung mit der GRE-Sequenz ist die Möglichkeit der schnellen Bildgebung [51].

Um den genauen Ursprungsort der gemessenen Magnetisierung bestimmen zu können, ist es nötig, $M_\perp$ ortsabhängig zu rekonstruieren [33].

Da in dieser Habilitationsschrift die kartesische Bildgebung angewendet wird, möchte ich mich im Folgenden auf die Beschreibung der kartesischen Ortskodierung beschränken. Diese erfolgt unter Verwendung von drei orthogonalen Gradienten [51]. Der Punkt, an dem durch die drei orthogonalen Gradienten kein Magnetfeld erzeugt wird, wird als Isozentrum bezeichnet [51].

Die Auswahl einer Schicht wird Schichtkodierung genannt [51]. Sie erfolgt durch die gleichzeitige Anwendung eines Schichtselektionsgradienten $\mathbf{G}_s$ und eines HF-Pulses [51]. Die Larmorfrequenz wird durch die Anwendung des Gradienten beeinflusst und beträgt

$$f_{L,s}(\mathbf{r}) = \frac{\gamma}{2\pi}(B_0 + \mathbf{G}_s\mathbf{r}), \tag{6.9}$$

wobei $\mathbf{r}$ den Abstand zum Isozentrum der Gradienten beschreibt [51]. Die Schichtdicke der mittels des Schichtselektionsgradienten definierten Schicht ist abhängig von der Bandbreite des HF-Pulses Δf und beträgt [51]:

$$\Delta s = \frac{2\pi\Delta f}{\gamma\,|\mathbf{G}_s|} \tag{6.10}$$

Nach der Schichtselektion ist die Ortskodierung für jedes Pixel innerhalb der selektierten Schicht erforderlich. Dafür kann die Frequenz- und die Phasenkodierung benutzt werden [33].

Die Phasenkodierung wird durch die Anwendung eines Phasenkodiergradienten $\mathbf{G}_p$ zwischen HF-Anregung und Auslesen des Signals realisiert [33]. Dadurch ändert sich die Larmorfrequenz $f_{L,p}$ abhängig vom Ort $\mathbf{r}$ [33]:

$$f_{L,p}(\mathbf{r}) = \frac{\gamma}{2\pi}(B_0 + \mathbf{G}_p\mathbf{r}) \tag{6.11}$$

Nach Abschalten des Gradienten ist die Larmorfrequenz wieder für jeden Spin identisch, die Phase Φ_p unterscheidet sich aber abhängig vom Ort $\mathbf{r}$ [51]:

$$\Phi(\mathbf{r})_p = \gamma\mathbf{r}\int_0^T \mathbf{G}_p(t)dt \tag{6.12}$$

Die Frequenzkodierung erfolgt während des Signalauslesens [33]. Der Frequenzkodiergradient $\mathbf{G}_f$ führt dazu, dass die Spins während der Signalaufnahme mit der Frequenz

$$f_{L,f}(\mathbf{r}) = \frac{\gamma}{2\pi}(B_0 + \mathbf{G}_f\mathbf{r}) \tag{6.13}$$

präzedieren [33, 49], wodurch die Empfangsspule ein Frequenzgemisch aufnimmt [33]. Mittels Fourier Transformation kann folglich Information über den Ort der Spins in Richtung des Frequenzkodiergradienten $\mathbf{G}_f$ gewonnen werden [49].

6.2 CEST-Bildgebung

Die Bildgebung mittels des CEST-Kontrastes liefert Informationen über chemische Verbindungen, welche Protonen besitzen, die an Austauschprozessen mit Wasserprotonen beteiligt sind [32]. Diese Verbindungen können dabei in so geringen Konzentrationen vorliegen, dass sie mittels der Standard-MR-Bildgebung nicht beobachtbar sind [32]. CEST nutzt den chemischen Austauschprozess, um die Verbindungen indirekt über die Magnetisierung des Wassers darzustellen [22, 24]. Dies ist nur möglich, da Protonen einer chemischen Verbindung, welche im Folgenden auch als Lösungsprotonen bezeichnet werden, eine andere Resonanzfrequenz aufweisen als die Wasserprotonen [32]. Wenn Lösungsprotonen mittels eines HF-Pulses so angeregt werden, dass die resultierende Magnetisierung des Spinensembles keine longitudinale Komponente der Magnetisierung mehr aufweist, wird von einer Sättigung des MR-Signals gesprochen. Der Prozess der selektiven Anregung der Protonen der chemischen Verbindung wird als „Labeling“ bezeichnet [52]. Durch den chemischen Austausch wird die Magnetisierung des Wassers reduziert, das heißt, es resultiert eine Verminderung des Wassersignals. Durch den ständigen Austausch von Lösungsprotonen mit Protonen des Wassers während der Hochfrequenzanregung kann eine messbare Veränderung des Wassersignals erzeugt werden [52].

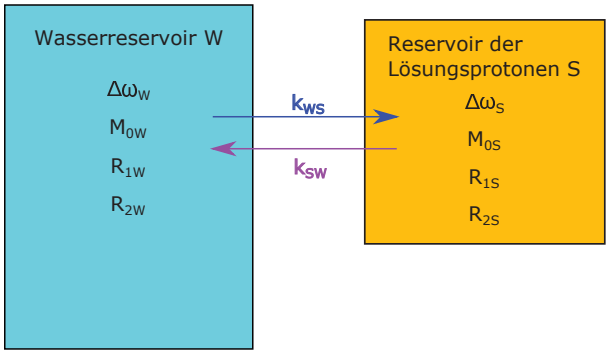

Abbildung 6.1: 2-Pool-Modell. Die Anzahl der Protonen des Reservoirs S ist im Vergleich zu der Anzahl der Protonen im Reservoir W gering. $\Delta\omega_W = \omega_W - \omega_0$ und $\Delta\omega_S = \omega_S - \omega_0$ sind die Differenzen der Resonanzfrequenzen des Reservoirs W bzw. S und der Larmorfrequenz $\omega_0 = \gamma B_0$. M_{0W} bzw. M_{0S} ist die Magnetisierung der Protonen im Reservoir W bzw. S ohne Sättigung. R_{1W} bzw. R_{1S} sowie R_{2W} bzw. R_{2S} sind die longitudinale bzw. transversale Relaxationsrate des Reservoirs S bzw. W. Eigene Abbildung modifiziert nach [53].

Der CEST-Effekt kann physikalisch mittels des 2-Pool-Modells beschrieben werden, bei dem die Gesamtheit der Lösungsprotonen als Reservoir S und die

Wasserprotonen als Reservoir W dargestellt werden (siehe Abbildung 6.1)[53]. Das Reservoir S ist dabei klein im Vergleich zum Reservoir W. In diesem Modell findet ein Austausch zwischen den Lösungsprotonen aus Reservoir S und den Wasserprotonen aus Reservoir W statt.

In dem 2-Pool-Modell werden mit R_{1W}, R_{1S} R_{2W}, R_{2S}, M_W und M_S die longitudinale (R_1) bzw. transversale (R_2) Relaxationsrate und die Gleichgewichtsmagnetisierung (M) des Reservoirs W bzw. des Reservoirs S beschrieben. Mit $\omega_0 = \gamma B_0$, $\omega_1 = \gamma B_1$ und $\Delta\omega = \omega - \omega_0$ können die Bloch-Gleichungen des 2-Pool-Modells unter Berücksichtigung des chemischen Austauschs aufgestellt werden [53]:

$$\begin{aligned}
\frac{dM_{xS}}{dt} &= -\Delta\omega_S M_{yS} - R_{2S} M_{xS} - k_{SW} M_{xS} + k_{WS} M_{xW} \\
\frac{dM_{yS}}{dt} &= \Delta\omega_S M_{xS} + \omega_1 M_{zS} - R_{2S} M_{yS} - k_{SW} M_{yS} + k_{WS} M_{yW} \\
\frac{dM_{zS}}{dt} &= -\omega_1 M_{yS} - R_{1S}(M_{zS} - M_{0S}) - k_{SW} M_{zS} + k_{WS} M_{zW} \\
\frac{dM_{xW}}{dt} &= -\Delta\omega_W M_{yW} - R_{2W} M_{xW} + k_{SW} M_{xS} - k_{WS} M_{xW} \\
\frac{dM_{yW}}{dt} &= \Delta\omega_W M_{xW} + \omega_1 M_{zW} - R_{2W} M_{yW} + k_{SW} M_{yS} - k_{WS} M_{yW} \\
\frac{dM_{zW}}{dt} &= -\omega_1 M_{yW} - R_{1W}(M_{zW} - M_{0W}) + k_{SW} M_{zS} - k_{WS} M_{zW}
\end{aligned} \tag{6.14}$$

Dabei ist B_0 die Hauptmagnetfeldstärke, B_1 die durch HF-Einstrahlung erzeugte Feldstärke, γ das gyromagnetische Verhältnis, k_{SW} die Austauschrate der Protonen von Reservoir S nach Reservoir W und k_{WS} die Austauschrate der Protonen von Reservoir W nach Reservoir S. Die gekoppelten Differentialgleichungen 6.14 werden auch Bloch-McConnell Gleichungen genannt. Es gilt:

$$k_{WS} = f \cdot k_{SW} \tag{6.15}$$

Der Parameter f ist die fraktionelle Konzentration der Lösungsprotonen. Im Gleichgewichtszustand gilt ferner [53]:

$$k_{WS} M_{0W} = k_{SW} M_{0S} \tag{6.16}$$

Für CEST Experimente wird vorausgesetzt, dass die Protonen im Reservoir W eine andere Resonanzfrequenz aufweisen als die Protonen im Reservoir S.

Aus den Gleichungen 6.14 lässt sich schlussfolgern, dass Reduktionen des Wassersignals zu erwarten sind, falls die HF-Anregung (1) mit der Resonanzfrequenz der Wasserprotonen erfolgt oder (2) mit der Resonanzfrequenz der Protonen des Reservoirs S übereinstimmt.

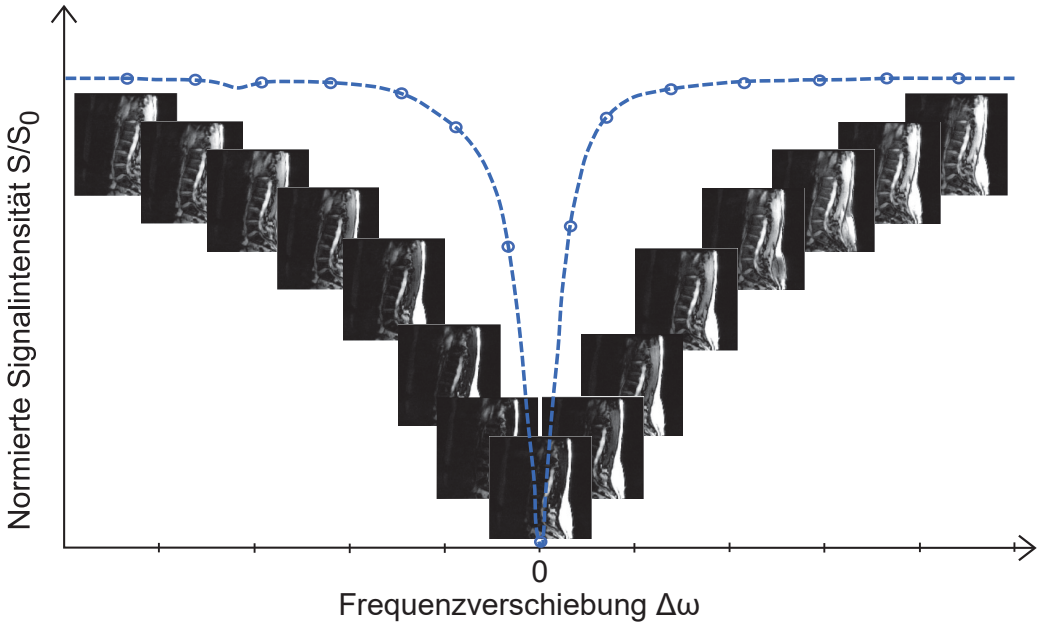

Abbildung 6.2: Schematische Darstellung des Z-Spektrums am Beispiel der Bandscheiben. Die Akquisition von Bildern bei verschiedenen Frequenzverschiebungen $\Delta\omega$ führt zu einer sich verändernden Signalintensität. Eigene Abbildung modifiziert nach [52].

Bei der CEST-Bildgebung wird nach jeder Präparation der Magnetisierung durch die Hochfrequenzeinstrahlung mit einer bestimmten Frequenzverschiebung $\Delta\omega$ ein Bild akquiriert. So entsteht eine Reihe von Bildern, deren Signalintensität abhängig von der gewählten Frequenzverschiebung $\Delta\omega$ ist. Die normierte Signalintensität aufgetragen gegen $\Delta\omega$ wird als Z-Spektrum bezeichnet und ist schematisch in Abbildung 6.2 dargestellt.

Im einfachsten Fall wird für die Präparation der Magnetisierung ein langer HF-Puls verwendet („continuous wave“ (CW) Hochfrequenzeinstrahlung). Diese Methode ist bei klinischen MR-Systemen wegen Hardware-bedingten Einschränkungen sowie einer hohen spezifischen Absorptionsrate oft nicht anwendbar. An Stelle der CW-Hochfrequenzeinstrahlung wird daher oft eine Folge von HF-Pulsen, welche Gauss-Pulse oder Spin-Lock-Pulse (SL-Pulse) sein können, verwendet (siehe Abbildung 6.3).

Um sowohl Magnetisierungstransfereffekte (MT-Effekte) rigider makromolekularer Strukturen als auch Effekte der direkten Wassersättigung zu reduzieren, wird bei der Analyse des CEST-Effekts eine Magnetisierungstranferasymmetrieanalyse durchgeführt [54]. Dazu wird das Magnetisierungstransferasymmetrieverhältnis MTR_{asym} in Abhängigkeit von der Frequenzverschiebung $\Delta\omega$ eingeführt. Es gilt [55]:

$$MTR_{asym}(\Delta\omega) = \frac{S(-\Delta\omega) - S(\Delta\omega)}{S_0} \tag{6.17}$$

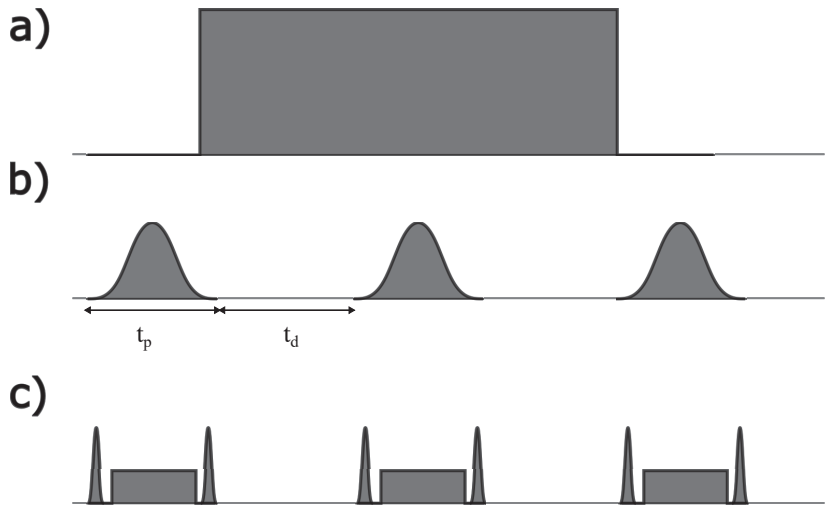

Abbildung 6.3: Techniken für die Präparation der Magnetisierung a) Einstrahlung eines langen Hochfrequenzpulses (CW); b) Verwendung einer Folge von Gauss-Pulsen zur Sättigung. Die Dauer der Gausspulse wird mit t_p bezeichnet, die Pause zwischen den Gauss-Pulsen mit t_d; c) Verwendung einer Folge von SL-Pulsen. Eigene Abbildung modifiziert nach [52].

Hierbei sind $S(-\Delta\omega)$ und $S(\Delta\omega)$ die Signalintensitäten nach einer Hochfrequenzeinstrahlung zur Präparation der Magnetisierung mit einer Frequenzverschiebung $-\Delta\omega$ bzw. $\Delta\omega$ und S_0 ist die Signalintensität, die ohne eine Präparation der Magnetisierung resultiert [55].

6.3 Quantitative CEST-Bildgebung

Eine quantitative Analyse des CEST-Effekts ist sowohl mit Kontrastmitteln, welche austauschbare Protonen besitzen und die Bestimmung des pH-Werts ermöglichen, als auch ohne Kontrastmittel unter Ausnutzen des endogenen CEST-Effekts möglich. Als CEST-sensitives Kontrastmittel wird in der vorliegenden Arbeit Iopamidol verwendet, da dieses bereits als Kontrastmittel für CT-Untersuchungen zugelassen ist und die Bestimmung des pH-Werts ermöglicht [56].

6.3.1 Quantitative CEST-Bildgebung mittels Iopamidol

Das Kontrastmittel Iopamidol zeigt CEST-Effekte bei unterschiedlichen Frequenzverschiebungen [56]. Dadurch ist mit Iopamidol eine CEST-Analyse möglich, welche den pH-Wert unabhängig von der Iopamidol-Konzentration bestimmen kann [56].

Bei der CEST-Analyse unter Verwendung von Iopamidol dient der ratiometrische Sättigungstransfer RST der Bestimmung des pH-Werts. Dazu muss zunächst der Sättigungstransfer ST bestimmt werden [56]:

$$ST(\Delta\omega)[\%] = \frac{S(-\Delta\omega) - S(\Delta\omega)}{S(-\Delta\omega)} \cdot 100 \tag{6.18}$$

RST lässt sich nun definieren über [56]:

$$RST = \frac{(100 - ST(\Delta\omega_1)) \cdot ST(\Delta\omega_2)}{(100 - ST(\Delta\omega_2)) \cdot ST(\Delta\omega_1)}. \tag{6.19}$$

Bei Iopamidol wird $\Delta\omega_1 = 4,2$ ppm und $\Delta\omega_2 = 5,4$ ppm gewählt. Hierbei steht ppm für *parts per million* und 1 ppm entspricht bei einer Hauptmagnetfeldstärke von 3 Tesla einer Frequenzverschiebung von $127,728$ Hz. Die oben gewählten Frequenzverschiebungen stimmen mit den Resonanzen der austauschbaren Amidprotonen von Iopamidol überein [56]. Um nun den pH-Wert mittels Iopamidol bestimmen zu können, ist eine Kalibrierung erforderlich. Hierfür können beispielsweise CEST-Messungen von Phantomen mit bekanntem pH-Werten herangezogen werden. Wenn RST gegen den pH-Wert aufgetragen wird, lässt sich eine Kalibrierungsfunktion fitten, welche den Zusammenhang zwischen RST und pH-Wert beschreibt. Diese Kalibrierungen können für in-vivo Messungen zur pH-Bestimmung verwendet werden.

6.3.2 Endogene quantitative CEST-Bildgebung

Bei der Untersuchung des CEST-Effekts ohne Kontrastmittel wird ausgenutzt, dass viele im Körper vorhandene Metabolite Protonen besitzen, welche im chemischen Austausch mit Wasserprotonen stehen und so einen CEST-Effekt verursachen.

Die Stärke des CEST-Effekts hängt von diversen Faktoren ab. Dazu gehören die Konzentration der Protonen im Reservoir S und die Austauschrate. Andere Parameter, die ebenso den CEST-Effekt beeinflussen, sind die Form und Dauer des HF-Moduls (siehe Abbildung 6.3), die Stärke der benutzten HF-Pulse und die Hauptmagnetfeldstärke des MR-Systems.

Die Bildgebung mittels der CEST-Technik ermöglicht auch die quantitative Analyse von Parametern wie beispielsweise die fraktionelle Konzentration sowie die vom pH-Wert abhängige Austauschrate bestimmter Stoffe [30, 57]. Für diese Analyse wurden einige Methoden eingeführt, welche in Tabelle 6.1 kurz zusammengefasst sind [31, 58–61].

Im Hinblick auf die klinische Relevanz beschränkt sich die folgende Beschreibung auf die Methoden, die in der Literatur für Sättigungsmodule mit gepulster

Methode	Akquisition mit	Modul	Ergebnis
QUEST	mehreren t_{sat}, $B_1 = const.$	CW	k_{SW}
QUESP	mehreren B_1, $t_{sat} = const.$	CW	k_{SW}, f_S
Ω-Plot	mehreren B_1, $t_{sat} = const.$	CW	k_{SW}, f_S
QUESTRA	mehreren t_{sat}, $B_1 = const.$	CW	k_{WS}
AREX	$B_1 = const.$, $t_{sat} = const.$	CW, gepulst	k_{WS}
AREX-basierter Ω-Plot	mehreren B_1, $t_{sat} = const.$	gepulst	k_{SW} und f_S

Tabelle 6.1: Auflistung der bislang eingeführten quantitativen CEST-Methoden. t_{sat} bezeichnet die Sättigunszeit und B_1 die Feldstärke der Hochfrequenzeinstrahlung zur Präparation der Magnetisierung. In der Modul-Spalte ist festgehalten, ob die quantitativen CEST-Methoden mittels gepulster HF-Einstrahlung oder „Continuous wave“ HF-Einstrahlung (CW) erfolgt. In der Ergebnis-Spalte ist notiert, welche Parameter aus der quantitativen Auswertung resultieren.

Vorsättigung vorgestellt wurden. Dazu gehört die quantitative Bestimmung der CEST-Parameter mittels der AREX-Metrik sowie die auf der AREX-Metrik basierende Ω-Plot Methode (vergleiche Tabelle 6.1).

AREX („apparent exchange-dependent relaxation“) beschreibt die vom chemischen Austausch abhängige Relaxation und ist definiert als [61]:

$$AREX = \left(\frac{1}{S(\Delta\omega)} - \frac{1}{S(-\Delta\omega)} \right) R_{1W} = MTR_{REX} R_{1W}, \tag{6.20}$$

wobei R_{1W} die longitudinale Relaxationsrate von Wasser ist.

Im Falle der Einstrahlung mit einem einzigen langen Hochfrequenzpuls (CW-Einstrahlung) gilt [61]:

$$MTR_{REX} = \frac{R_{ex}}{\cos^2(\theta) R_{1W}} \tag{6.21}$$

Dabei ist R_{ex} die vom Austausch abhängige Relaxationsrate im rotierenden Koordinatensystem und $\theta = \tan^{-1}\left(\frac{-\omega_1}{\Delta\omega}\right)$ ist der Winkel zwischen effektivem Magnetfeld und dem Hauptmagnetfeld (siehe Abbildung 6.4). Falls $\Delta\omega \gg \omega_1$ ist, kann $\cos^2(\theta) \approx 1$ angenommen werden und es gilt:

$$AREX \approx R_{ex} \tag{6.22}$$

Mit $R_{ex} = f \cdot k_{SW}$ folgt somit für den CW-Fall:

$$k_{SW} = \frac{AREX}{f} \tag{6.23}$$

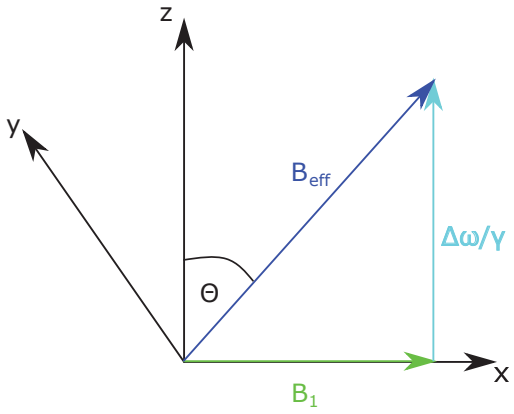

Abbildung 6.4: Lage des effektiven Magnetfeldes in Bezug auf das Hauptmagnetfeld. Eigene Abbildung modifiziert nach [63]

Im Falle gepulster Sättigung modifiziert sich Gleichung 6.21 unter Berücksichtigung des „Duty Cycles“ $DC = t_p/(t_p + t_d)$ zu [31]

$$MTR_{REX} = \frac{R_{ex} \cdot DC}{R_{1W}} \tag{6.24}$$

Daher resultiert für die gepulste CEST-Bildgebung [62]:

$$k_{SW} = \frac{AREX}{DC \cdot f} \tag{6.25}$$

Zusammenfassend lässt sich sagen, dass die AREX-Metrik unabhängig von der T_1-Zeit ist und die Austauschrate bei bekannter fraktioneller Konzentration f bestimmt werden kann.

Die auf der AREX-Metrik basierende Ω-Plot Methode ermöglicht eine simultane Bestimmung der fraktionellen Konzentration und der Austauschrate. Dafür muss AREX bei unterschiedlichen B_1-Feldstärken gemessen werden. Ziwschen AREX^{-1} und ω^{-2} besteht nach [31, 62] eine lineare Abhängigkeit der Form

$$\frac{1}{AREX}\left(\frac{1}{\omega^2}\right) = p_0 + p_1 \cdot \frac{1}{\omega^2}. \tag{6.26}$$

Die fraktionelle Konzentration f und die Austauschrate k_{SW} können unter Benutzung des y-Achsenabschnitts p_0, der Steigung p_1 und der Formfaktoren c_1 und c_2 berechnet werden [62]:

$$f = \frac{1}{c_1 \cdot DC \cdot p_0 \left(-\frac{R_{2S}}{2} + \sqrt{\frac{(R_{2S})^2}{4} + \frac{p_1}{p_0 c_2^2}}\right)} \tag{6.27}$$

$$k_{SW} = -\frac{R_{2S}}{2} + \sqrt{\frac{(R_{2S})^2}{4} + \frac{p_1}{p_0 \cdot c_2^2}}. \tag{6.28}$$

6.4 Technische Limitationen der CEST-Bildgebung

Zu den technischen Limitationen der CEST-Bildgebung gehören die Anfälligkeit auf Bewegung, der große Einfluss von B_0- und B_1-Feldinhomogenitäten auf den CEST-Effekt sowie Veränderungen der Form des Z-Spektrums durch den Magnetisierungstransfereffekt (MT-Effekt), den „Nuclear Overhauser Effect (NOE)“ und den Effekt der direkten Wassersättigung. Dabei beschreibt der MT-Effekt den Austausch der Spinpolarisation von an Makromolekülen gebundenen Wasserprotonen oder Protonen geordneter Strukturen mit Protonen des nicht gebundenen Wassers [64, 65]. Um diesen Effekt zu reduzieren, wurde durch Lee et al. bereits eine Sequenz entwickelt, welche die Trennung des CEST-Effekts vom MT-Effekt ermöglicht [65]. Der NOE wird in der MR-Spektroskopie zur Strukturanalyse eingesetzt und beschreibt die Übertragung der Kernspin-Polarisation mittels dipolarer Kopplung [66]. Dieser Übertrag ist vom Abstand der interagierenden Protonen abhängig. Der NOE kann durch geeignete Fit-Funktionen analysiert werden, so dass der CEST-Effekt getrennt vom NOE evaluiert werden kann [67].

Um den Einfluss von Bewegung zu minimieren, kann eine geeignete Stabilisierung z.B. bei der Datenakquisition in den Extremitäten oder im Kopf erfolgen. Bei bewegten Organen kann auch eine von der Atmung gesteuerte Sequenz verwendet werden [68]. Außerdem kann nach der CEST-Bildgebung eine Bildregistrierung erfolgen [69].

Um den Einfluss von B_0-Feldinhomogenitäten zu reduzieren, müssen diese schon vor der Messung durch Feinjustage des Magnetfeldes mit speziellen Spulen reduziert werden. Dieser Vorgang wird als „Shimming“ bezeichnet. Es ist jedoch nicht möglich, die Feldinhomogenitäten vor der Messung vollständig zu eliminieren. Daher ist in der Nachverarbeitung eine Korrektur des Einflusses der Feldinhomogenitäten auf das Z-Spektrum notwendig. Zur Detektion der nach dem Shimming noch vorhandenen Feldinhomogenitäten kann eine modifizierte CEST-Sequenz genutzt werden. Die Abtastung des Z-Spektrums für die B_0-Feldinhomogenitätskorrektur erfolgt dabei in einem engen Fenster um die Wasserresonanzfrequenz herum. Das so akquirierte Z-Spektrum wird als „Water saturation shift referencing“ (WASSR)-Spektrum bezeichnet [55]. Aus der Position des Minimums des WASSR-Spektrums kann die Verschiebung der Resonanzfrequenz festgestellt werden [70]. Weitere Methoden, das WASSR-Spektrum auszuwerten, sind der von Kim et al. eingeführte „maximum symmetry center frequency“ (MSCF)-Algorithmus [55] sowie ein Fit der WASSR-Daten mit den Bloch-Gleichungen [70]. Die mit diesen Methoden bestimmten Frequenzverschiebungen

werden dazu benutzt, die Position des Z-Spektrum entlang der Frequenzachse zu korrigieren. Eine alternative Methode, welche es ermöglicht, sowohl B_0 als auch B_1-Feldinhomogenitäten zu korrigieren, „WASABI “, wurde von Schuenke et al. eingeführt [71]. WASABI steht dabei für „mapping of water frequency shift and B_1 amplitude“, also für eine Methode, die sowohl eine Kartierung der Verschiebung der Resonanzfrequenz des Wassers als auch eine Kartierung des B_1-Feldes ermöglicht [71].

Die WASABI-Sequenz besteht aus einem kurzen Sättigungsmodul (Dauer ca. 5 ms, B_1-Feldstärke ca. 3,7 μT), einem anschließenden Spoilergradienten sowie einer konventionellen MR-Datenakquisition [71]. Durch die Abtastung mehrerer Frequenzoffsets um die Wasserresonanz herum entsteht das WASABI Z-Spektrum. Während die Verschiebung der Resonanzfrequenz des Wassers über die Verschiebung der Symmetrieachse des WASABI Z-Spektrums bestimmt werden kann, beeinflusst die B_1-Amplitude die Periodizität des Spektrums [71].

Der Einfluss der direkten Wassersättigung auf den CEST-Effekt kann, wie in Abschnitt 6.2 beschrieben, durch die Berechnung des Parameters MTR_{asym} eliminiert werden.

6.5 WEX-Spektroskopie

Water-Exchange (WEX)-Spektroskopie basiert - wie CEST - auf dem chemischen Austausch von Protonen und liefert folglich Informationen über Metabolite und Proteine mit an Austauschprozessen beteiligten Protonen. Anders als CEST handelt es sich hierbei aber nicht um eine bildgebende Methode. Die WEX-Spektroskopie ist eine alternative Methode zur Charakterisierung des chemischen Austauschprozesses.

Im Folgenden wird kurz das Prinzip der WEX-Spektroskopie dargestellt. Zunächst erfolgt eine selektive Präparation (Labeling) des Wassersignals [53]. Anschließend erfolgt während der Mischungszeit t_M eine Übertragung der präparierten Wassermagnetisierung auf Protonen anderer Metabolite oder Proteine. Nach der Zeit t_M erfolgt erneut eine Anregung des Spinsystems, wobei die Wassermagnetisierung unterdrückt wird [53]. Die gemessene WEX-Signalintensität ist folglich abhängig von der Mischungszeit t_M und der chemischen Austauschrate [53].

6.6 Bandscheiben und oberes Sprunggelenk

Da Studien in den Bandscheiben und im Sprunggelenk durchgeführt wurden, wird die Anatomie dieser Regionen im Folgenden kurz beschrieben.

Die Disci Intervebrales (IVDs = „Intervertebral discs“), auch Zwischenwirbelscheiben oder Bandscheiben genannt, verbinden die Wirbelkörper miteinander

[72]. Die IVDs bestehen aus zwei Teilen, dem kollagenfasrigen Annulus Fibrosus (AF) und dem vorwiegend aus Proteoglykanen (PGs) bestehenden Nucleus Pulposus, welcher auch als Gallertkern bezeichnet wird [72]. Eine sehr dünne hyalinknorpelige Schicht, die Symphysis Intervebralis, verbindet die Bandscheiben mit der Grund- und Deckplatte der benachbarten Wirbelkörper [72]. Die Bandscheiben dienen dem Abmildern von Stößen. Der Nucleus Pulposus hat die Funktion, den Druck auf die benachbarten Wirbelkörper zu verteilen. Der AF wandelt einen Teil der Druckkräfte in Zugspannungen um [72].

Das obere Sprunggelenk (OSG), auch Articulatio talocruralis genannt, ermöglicht eine Plantarflexion und Dorsalextension [72]. Es spielt eine wichtige Rolle beim Abrollen des Fußes, zum Beispiel beim Gehen [72]. Das OSG verbindet den Talus mit den Unterschenkelknochen.

6.7 gagCEST

Die Glykosaminoglykane (GAG) sind ein Bestandteil des Knorpels und kommen somit sowohl in den Bandscheiben als auch im OSG vor. Sie sind lineare Polysaccharide, welche aus sich wiederholenden Disaccharideinheiten zusammengesetzt sind [73]. Jede Disaccharideinheit besitzt drei -OH und eine -NH-Gruppe, welche austauschbare Protonen besitzen [9]. GAG bilden die Seitenketten des komplexen Moleküls PG [74]. Durch die austauschbaren Protonen der GAG können diese mittels der endogenen CEST-Bildgebung dargestellt werden. Dies wird auch als gagCEST-Bildgebung bezeichnet.

Als Folge von Degeneration verringert sich der Gehalt von Wasser und PG [75]. Dadurch reduziert sich die GAG-Konzentration. Neben der Degeneration ist auch eine Verminderung der GAG-Konzentration ein bekannter Faktor bei Patienten mit rheumatoider Arthritis [76, 77]. Die molekulare gagCEST-Bildgebung ist daher besonders bei der frühen Erkennung von Veränderungen des Knorpels, welche mit einer anatomischen Darstellung des Gelenks noch nicht diagnostiziert werden können, relevant [78, 79].

7 Umfassende Ausführung der Untersuchungen und Ergebnisse

Die molekulare Bildgebung mittels CEST ermöglicht es, exogene und endogene Stoffe, welche austauschbare Protonen besitzen, darzustellen, wodurch biochemische Informationen mittels der MRT erhalten werden können [6].

Die vorliegende kumulative Habilitationsschrift behandelt physiologische, technische und methodische Aspekte im Bereich der Bildgebung mittels CEST.

Zu den physiologischen Aspekten, die in dieser Arbeit untersucht wurden, gehören Abhängigkeiten des CEST-Effekts im Knorpel von Alter, Geschlecht, BMI und den T_2-Relaxationszeiten (siehe Publikationen I und II)[80, 81]. Letztere sind sensitiv auf Knorpeldegeneration, wodurch eine Abhängigigkeit zwischen der T_2-Relaxationszeit und dem gagCEST Effekt erwartet werden kann. So wurde beispielsweise in dieser Arbeit zugrundeliegenden Studien gezeigt, dass der CEST-Effekt bei degenerativen Veränderungen des Knorpels sowie bei Knorpelläsionen abnimmt (siehe Publikationen I, III und IV)[80, 82, 83]. Ferner besteht auch eine mathematisch beschriebene Abhängigkeit des CEST-Effekts von der T_2-Relaxationszeit, welche auch als T_2-Shine-Through-Effekt bezeichnet wird [81].

Die Abhängigkeit des CEST-Effekts von physiologischen Aspekten lässt sich wie folgt zusammenfassen:

- Der CEST-Effekt im Knorpel nimmt mit fortschreitendem Alter ab. Dabei gibt es einen signifikanten Unterschied des CEST-Effekts zwischen Probanden im Alter von 20-29 Jahren und Probanden im Alter von 50-59 Jahren. Die Abnahme des CEST-Effekts könnte durch eine Reduzierung des GAG-Gehalts während des Alterungsprozesses hervorgerufen werden. (Siehe Publikation I [80])
- Der CEST-Effekt im Nucleus Pulposus der Bandscheiben ist in weiblichen Probanden signifikant höher als in männlichen Probanden. (Siehe Publikation II [81])
- Der BMI und der CEST-Effekt im Nucleus Pulposus weisen eine negative Korrelation auf. (Siehe Publikation II [81])

- Die Korrelation zwischen dem CEST-Effekt und dem T_2-Wert ist hoch signifikant. (Siehe Publikationen II und VIII [81, 84])

- Der Knorpel von Patienten mit osteochondralen Läsionen im Bereich des OSGs hat einen signifikant niedrigeren CEST-Effekt als der Knorpel im OSG von gesunden Probanden. (Siehe Publikation IV [83])

- In lumbaren und zervikalen Bandscheiben ist der CEST-Effekt bei degenerativen Veränderungen niedriger als der CEST-Effekt ohne solche Veränderungen. (Siehe Publikationen I und III [80, 82])

Der CEST-Effekt im Knorpel ist somit stark abhängig von physiologischen Parametern (siehe Publikationen I-IV und VIII [80–84]). Neben diesen Abhängigkeiten wird der CEST-Effekt auch durch Effekte wie beispielsweise B_0- und B_1-Feldinhomogenitäten, Bewegung, aber auch den verwendeten Sequenzparametern beeinflusst (siehe Publikationen IV-VIII) [70, 83–86]. Daher wurden in dieser Arbeit technische Untersuchungen durchgeführt, deren Ergebnisse wie folgt zusammengefasst werden können:

- Die Bloch-McConnell-Gleichungen ermöglichen eine Optimierung der CEST-Sequenz und somit, den gemessenen CEST-Effekt in vivo zu maximieren. (Siehe Publikation IV [83])

- Die Qualität der CEST-Bildgebung kann durch Bewegungskorrektur verbessert werden und äußert sich in einem verbesserten SNR.(Siehe Publikation V [85])

- Eine geeignete Kombination aus Dauer und B_1-Feldstärke des verwendeten Sättigungspulses ist bei der Aufnahme einer WASSR-Sequenz für die B_0-Feldinhomogenitätskorrektur notwendig. Dadurch wird ermöglicht, dass im WASSR-Spektrum nur ein Peak entsteht. Dies erleichtert die Kartierung der B_0-Feldinhomogenitäten. Zusätzlich können erweiterte Nachverarbeitungsalgorithmen wie ein Fit mit den Bloch-Gleichungen und der periodische MSCF-Algorithmus zu einer verbesserten Bestimmung der vorhandenen B_0-Feldinhomogenitäten benutzt werden. (Siehe Publikation VI [70])

- Sowohl eine Folge von Spin-Lock Pulsen als auch eine Folge von Gaussförmigen Pulsen kann zur Sättigung der Magnetisierung bei der CEST-Bildgebung angewendet werden (Siehe Publikation VIII [84])

- Die Korrektur von sowohl B_0- als auch B_1-Feldinhomogenitäten führt zu einem erhöhten Signal-Rausch-Verhältnis und zu einer gesteigerten Korrelation zwischen gagCEST-Effekt und den T_2-Werten. Daher ist eine Korrektur beider Arten von Feldinhomogenitäten empfehlenswert. (Siehe Publikation VII [86])

Aus methodischer Sicht wurde die CEST-Bildgebung dahingehend untersucht, ob eine quantitative Analyse der Material- oder Gewebezusammensetzung möglich ist.

Zunächst wurde eine explorative Studie mit dem Kontrastmittel Iopamidol durchgeführt. Dabei wurde nach einer in vitro Untersuchung des CEST-Effekts mittels Iopamidol auch erstmalig eine CEST-Untersuchung in vivo im Menschen mit diesem Kontrastmittel durchgeführt (siehe Publikation IX [87]). Es wurden folgende Ergebnisse erzielt:

- In einem pH-Bereich von 5,6 bis 7 ist eine Bestimmung des pH-Wertes mit Iopamidol möglich. Dabei ist der bestimmte pH-Wert unabhängig von der verwendeten Iopamidol-Konzentration. (Siehe Publikation IX [87])

- Es konnte erstmalig in vivo der pH-Wert in der menschlichen Blase mittels der CEST-MRT bestimmt werden. (Siehe Publikation IX [87])

Es können aber auch quantitative biochemische Informationen ohne Verwendung eines Kontrastmittels gewonnen werden. Als Beispiel wurde zunächst anhand von Kreatin untersucht, ob die chemische Austauschrate zwischen austauschbaren Kreatin-Protonen und Wasserprotonen bestimmt werden kann und von welchen CEST-Sequenzparametern die Möglichkeit der quantitativen Kreatin-Bildgebung abhängt (siehe Publikation X [62]). Des Weiteren wurde untersucht, ob es möglich ist, die Kreatinkonzentration mittels CEST-MRT zu bestimmen (siehe Publikation X [62]). Bei dieser Studie konnten folgende Erkenntnisse gewonnen werden:

- Quantitative CEST-Bildgebung von Kreatin an einem klinischen 3 Tesla Gerät ist möglich. (Siehe Publikation X [62])

- Die Verwendung eines Sättigungs-Pulszuges aus Spin-Lock-Pulsen ermöglicht es, einen größeren Bereich der Austauschrate korrekt abzutasten als bei Messungen mit einem Pulszug aus Gauss-Pulsen. (Siehe Publikation X [62])

- Sowohl Simulationen als auch Phantomexperimente zeigen, dass kleine Austauschraten sowohl mit der AREX-Methode als auch mit der Ω-Plot Methode tendenziell überschätzt werden, wohingegen bei hohen Austauschraten eine Unterschätzung dieser Raten erfolgt. (Siehe Publikation X [62])

Neben Kreatin wurde in dieser Arbeit Harnstoff mittels der quantitativen CEST-Bildgebung untersucht. Harnstoff zeigt einen CEST-Effekt bei einem Frequenzoffset von $\Delta\omega = 1$ ppm und trägt wesentlich zum CEST-Effekt in der Niere bei [88].

Daher wurde Harnstoff hinsichtlich seiner Eignung für die quantitative CEST-Bildgebung untersucht (siehe Publikation XI [89]). Dafür wurden die CEST-Ergebnisse mit denen der WEX-Spektroskopie verglichen. Außerdem wurde die Spezifizität des Harnstoff-CEST-Effekts analysiert, indem auch andere Substanzen, die einen CEST-Effekt in der Niere erzeugen könnten, mittels einer CEST-Analyse untersucht wurden. Die folgenden Ergebnisse resultieren aus dieser Studie:

- Mittels der quantitativen CEST-Analyse konnte ermittelt werden, dass Harnstoff vier labile Protonen besitzt, die am chemischen Austausch mit Wasserprotonen beteiligt sind. (Siehe Publikation XI [89])

- In einem pH-Bereich von pH = 5.66 bis pH = 6.20 und von pH = 7.37 bis pH = 8.41 konnte in dieser Studie die Austauschrate mittels CEST bestimmt werden. Demnach war es in einem großen Bereich physiologischer pH-Werte nicht möglich, die Austauschrate von Harnstoff zu bestimmen. (Siehe Publikation XI [89])

- Der quantitative CEST-Parameter AREX ist direkt proportional zur Harnstoff-Konzentration. (Siehe Publikation XI [89])

- Mit Hilfe der WEX-Spektroskopie wurde gezeigt, dass der chemische Austausch zwischen Harnstoff- und Wasserprotonen sowohl Säure- als auch Basen-katalysiert ist. Das dadurch resultierende bi-exponentielle Verhalten der Austauschrate spiegelt sich auch in den Ergebnissen der Austauschrate der quantitativen CEST-Bildgebung von Harnstoff wieder. Deshalb ist es mit Hilfe der CEST-Bildgebung aber auch nicht möglich, den pH-Wert eindeutig zu bestimmen. (Siehe Publikation XI [89])

- Für die in der Niere vorkommenden Metabolite Kreatinin, Kreatin, Glutamin, Alanin und Allantoin war es möglich, einen CEST-Effekt bei 3 Tesla zu messen. (Siehe Publikation XI [89])

- Die mittels der quantitativen CEST-Bildgebung bestimmte Austauschrate der gemischten Lösung aus Harnstoff, Kreatinin und Kreatin bei Konzentrationen, welche dem Vorkommen dieser Metaboliten im Urin entsprechen, stimmt mit der Austauschrate der Harnstofflösung überein. (Siehe Publikation XI [89])

- Die aus der CEST-Bildgebung resultierenden Z-Spektren und MTR_{asym}-Spektren von der gemischten Lösung und der Urinprobe liegen nahe beieinander und zeigen einen dominanten CEST-Effekt bei ca. 1 ppm. Der Effekt bei dieser Resonanzfrequenz kann daher den Amidprotonen von Harnstoff zugeordnet werden. (Siehe Publikation XI [89])

Die in dieser Arbeit erzielten Ergebnisse zur quantitativen Bildgebung mittels CEST lassen sich wie folgt kurz zusammenfassen:

Mit dem Kontrastmittel Iopamidol ist eine Bestimmung des pH-Wertes in einem physiologischen pH-Bereich möglich ist (siehe Publikation IX [87]). Mit der endogenen quantitativen CEST-Bildgebung scheint die korrekte Bestimmung des pH-Werts im physiologischen Bereich zunächst schwieriger zu sein (siehe Publikationen X und XI [62, 89]). Weitere Forschungsarbeiten sind daher notwendig, um auch mit der endogenen quantitative CEST-Bildgebung den pH-Wert eindeutig abschätzen zu können und somit diese Methode einen weiteren Schritt näher in Richtung klinischer Anwendbarkeit zu bringen.

8 Diskussion

Die molekulare Bildgebung mittels CEST bietet das Potenzial, die Diagnostik einer Vielzahl von Erkrankungen, wie beispielsweise Knorpeldegenerationen, Fehlfunktionen der Niere, Veränderungen der metabolischen Aktivität des Herzens, Ischämie und Krebs, zu verbessern [29, 90]. Neben den diagnostischen Möglichkeiten wird durch den Einsatz dieser Methode auch ein besseres Verständnis der molekularen Prozesse im Gewebe und der Veränderungen dieser Prozesse bei alters- oder krankheitsbedingten Prozessen erwartet. Eine Ergänzung der Standard-MR-Untersuchung mit der CEST Technik bietet die Möglichkeit, molekulare Informationen darzustellen und diese mit anderen anatomischen Messungen in Bezug zu setzen.

Durch die Studienergebnisse konnte eine Abhängigkeit des CEST-Effekts im Knorpel vom Alter, vom Geschlecht und vom BMI beschrieben werden. Weitere Studien könnten untersuchen, ob sich der CEST-Effekt auch in anderen Geweben bei gesunden Probanden in Abhängigkeit physiologischer Parameter verändert.

Ferner zeigten Studien der vorliegenden Habilitationsschrift eine Korrelation zwischen dem CEST-Effekt im Knorpel und der T_2-Zeit [81, 84]. Eine solche Abhängigkeit wurde auch in einer Studie von Peterson et al. beschrieben [91]. Die Stärke des Einflusses der T_2-Zeit auf den CEST-Effekt wird sowohl durch Messparameter der CEST-Bildgebung als auch durch die verwendete Magnetfeldstärke B_0 des MR-Gerätes beeinflusst [91]. Zukünftig könnten Möglichkeiten zur Reduzierung oder Korrektur des T_2-Bias an klinischen MR-Systemen näher analysiert werden. Neben dem T_2-Bias wird in der Literatur auch der Einfluss der T_1-Zeit auf den CEST-Effekt diskutiert [61, 92]. Daher könnten weitere Studien zur Quantifizierung dieses Einflusses auf den CEST-Effekt im Knorpel sinnvoll sein.

Eine Studie der vorliegenden Arbeit [83] zeigte die Abnahme des CEST-Effekts im Knorpel bei osteochondralen Läsionen und bei degenerativen Prozessen im Vergleich zum CEST-Effekt in gesundem Knorpel. Ein reduzierter CEST-Effekt bei geschädigtem oder degenerativem Knorpel wurde auch in anderen Studien gezeigt [93–95]. In Zukunft könnte das Potential der CEST-Technik für die Differenzierung zwischen rheumatoider Arthritis und Arthrose untersucht werden.

Ein weiterer klinischer Aspekt, der zukünftig neben der biochemischen Beurteilung des Knorpels ausführlich betrachtet werden könnte, ist beispielsweise die Untersuchung des Nierenmetabolismus bei diversen Nierenerkrankungen im Menschen. Schwierigkeiten bereiten dabei die großen Feldinhomogenitäten im Abdomen sowie die Bewegung der Niere durch die Atmung. Nichtsdestotrotz sind

bereits vielversprechende Tierexperimente in der Niere mittels der CEST-Technik erfolgt [10, 28, 96, 97], bei denen aber meistens eine höhere B_0-Feldstärke verwendet oder ein Kontrastmittel eingesetzt wurde.

Die Qualität der CEST-Bildgebung ist stark von technischen Details abhängig. So können Feldinhomogenitäten und Bewegung die Resultate verfälschen. Während B_0-Feldinhomogenitäten zu einer Verschiebung des Z-Spektrums führen, äußern sich B_1-Feldinhomogenitäten in einer lokal variierenden Veränderung der Stärke des CEST-Effekts. Eine Korrektur der Feldinhomogenitäten ist mit unterschiedlichen Methoden möglich, von denen folgende für die CEST-Bildgebung der Bandscheiben in den der Arbeit zugrunde liegenden Forschungsuntersuchungen getestet wurden: Die Verwendung des Minimums des WASSR Z-Spektrums [70], die von Kim et al. eingeführte Bestimmung des Intensitätsminimums des WASSR Z-Spektrums mit Hilfe des MSCF- („maximum symmetry center frequency") Algorithmus [55], die Erweiterung der Technik durch den periodischen MSCF-Algorithmus [70], die Korrektur mit Hilfe eines Fits mit den Bloch-Gleichungen [70] sowie die Korrektur mit Hilfe der WASABI-Technik [71, 86]. Die Korrektur von Feldinhomogenitäten ist auch in stark inhomogenen Regionen wie den Bandscheiben möglich [86]. Zukünftig könnte analysiert werden, ob sich die angewendeten Methoden auch für die Feldinhomogenitätskorrektur bei Organen wie etwa der Niere oder der Leber eignen, bei denen Änderungen der Magnetfeldinhomogenitäten in Folge von peristaltischer Bewegung auftreten könnten. Alternativ könnten in diesen Regionen auch dynamische Ansätze zur Feldinhomogenitätskorrektur zum Einsatz kommen, wie zum Beispiel die Verwendung der Phase des MR-Signals während des Auslesens der dynamischen CEST-Bilder [98].

Bei der CEST-Bildgebung führt Bewegung während Datenakquisition dazu, dass das Z-Spektrum eines Pixels das Signal unterschiedlicher Regionen beinhaltet. In der vorliegenden Arbeit wurde die Bewegung nach der Akquisition der CEST-Daten korrigiert [85]. Alternativ könnte aber auch eine prospektive Korrektur mit Hilfe von Navigatoren erfolgen, welche Bewegungen durch Translation oder Rotation detektieren, indem ein kleiner Teil des k-Raums akquiriert wird [51, 99, 100]. Die Vor- und Nachteile beider Techniken für die CEST-Bildgebung könnten in zukünftigen Forschungsarbeiten evaluiert werden.

Der CEST-Effekt hängt sehr stark von der Anzahl und der B_1-Feldstärke der verwendeten Hochfrequenzpulse zur Sättigung der Magnetisierung ab [83]. Daher ist es sinnvoll, vor Beginn einer CEST-Studie Bloch-McConnell Simulationen zur Optimierung dieser Hochfrequenzeinstrahlung für die gewählte Anwendung durchzuführen.

Ein weiteres Ziel in der CEST-Bildgebung besteht darin, eine quantitative Analyse des chemischen Austausches zu ermöglichen. Als quantitative Messgrößen eignen sich der pH-Wert des Gewebes, die chemische Austauschrate sowie die Konzentration bestimmter Stoffe. Mit Hilfe des Kontrastmittels Iopamidol kann der pH-Wert in vivo bestimmt werden [87]. Als alternatives Kontrastmittel zur pH-Bildgebung eignet sich Iopromide, welches unter anderem zur Abschätzung

des pH-Wertes von Tumoren in einem Bereich von pH = 6.5 bis pH = 7.2 eingesetzt wurde [101]. Neben diesen Iod-haltigen Kontrastmitteln können ebenfalls paramagnetische Kontrastmittel für die Bildgebung des pH-Wertes zum Einsatz kommen [102]. Auch endogene Stoffe mit austauschbaren Protonen eignen sich in Kombination mit einer geeigneten Nachverarbeitungs-Pipeline zur Abschätzung des pH-Wertes, wie am Beispiel von Kreatin von Sun et al. gezeigt worden ist [103].

Die chemische Austauschrate verändert sich in Abhängigkeit vom pH-Wert. Auch sie kann als quantitatives Maß der CEST-Bildgebung herangezogen werden. Studien dieser Arbeit behandeln die quantitative CEST-Bildgebung ausführlich für die Stoffe Kreatin und Harnstoff und zeigen, dass der Bereich, in dem die Austauschrate korrekt bestimmt werden kann, von der verwendeten Hochfrequenzeinstrahlung zur Sättigung der Magnetisierung abhängt [62, 89]. Mittels Simulationen besteht die Möglichkeit, die Form dieser Hochfrequenzeinstrahlung für die gewünschte Anwendung zu optimieren. In weiteren Studien könnte ferner getestet werden, ob die Austauschrate adäquat mit Hilfe der Bloch-McConnell Gleichungen evaluiert werden kann.

Neben der Abschätzung des pH-Wertes und der chemischen Austauschrate wird in dieser Arbeit auch die Möglichkeit untersucht, die Stoffkonzentration mittels der quantitativen CEST-Bildgebung zu bestimmen. So besteht eine Proportionalität zwischen dem quantitativen CEST-Parameter AREX und der Harnstoff-Konzentration [89]. Ob die Konzentrationsbestimmung auch für die GAG im Knorpel in vivo im Menschen mittels quantitativer CEST-Bildgebung möglich ist, ist zum aktuellen Zeitpunkt noch Gegenstand der Forschung.

Aus den Resultaten dieser Arbeit lässt sich folgern, dass der CEST-Effekt von diversen Faktoren beeinflusst werden kann. Zu diesen Faktoren gehören physiologische Parameter, aber auch Artefakte in Folge technischer Limitationen. Daher sind auf die Anwendung hin optimierte CEST-Sequenzen und geeignete Korrekturen in der Datenverarbeitung wie beispielsweise die B_0- und B_1-Feldinhomogenitätskorrektur entscheidend für die Qualität der CEST-Bildgebung. Mittels einer quantitativen Analyse des CEST-Effekts sind Rückschlüsse über den pH-Wert oder die Konzentration von Lösungsprotonen einer chemischen Verbindung möglich. Dies könnte in Zukunft die Diagnostik in vielen Bereichen der Medizin verbessern.

9 Fazit

Der Forschungsschwerpunkt dieser Habilitationsschrift ist die molekulare Bildgebung mittels der Magnetresonanztomographie. Dazu wurde der chemische Austausch mit der Methode CEST eingehend untersucht.

Die durchgeführten Studien liefern relevante neue Erkenntnisse im Bereich der biomedizinischen Bildgebung. Es konnte gezeigt werden, dass CEST sensitiv auf molekulare Gewebeveränderungen ist, welche beispielsweise durch Alterungsprozesse oder durch Pathologien hervorgerufen werden können. Technische Verbesserungen der CEST-Methode führten zu einer Reduktion von Artefakten in der CEST-Bildgebung.

Zudem wurde gezeigt, dass eine quantitative CEST-Bildgebung bei einer Feldstärke von 3 Tesla möglich ist. So konnte beispielsweise der pH-Wert in vivo im Patienten mit dem Kontrastmittel Iopamidol gemessen werden. Die Studienergebnisse lassen aber auch deutlich das Potenzial der CEST-Bildgebung erkennen, an klinisch eingesetzten MRT-Geräten ohne den Einsatz von Kontrastmitteln quantitative Informationen beispielsweise über die chemische Austauschrate und die Stoffkonzentration zu gewinnen.

10 Abkürzungen

AF	Annulus Fibrosus
AREX	apparent exchange-dependent relaxation
B_0	Hauptmagnetfeldstärke des MRT-Systems
B_1	Radiofrequenz-Feldstärke
BMI	Body Mass Index
CEST	Chemical Exchange Saturation Transfer
CW	Continuous Wave
CT	Computertomographie
DC	Duty Cycle
dGEMRIC	delayed Gadolinium-enhanced MRI of the cartilage
GAG	Glykosaminoglykane
gagCEST	CEST-Effekt der Glykosaminoglykane
GRE	Gradientenecho
HF	Hochfrequenz
HF-Puls	Hochfrequenzpuls
IVD	Intervertebral Disc
MSCF	maximum-symmetry center frequency
MR	Magnetresonanz
MRS	Magnetresonanzspektroskopie
MRT	Magnetresonanztomographie
MT	Magnetisierungstranfer
MTR_{asym}	Magnetisierungstransfer-Asymmetrieverhältnis
NOE	Nuclear Overhauser Effect
NP	Nucleus Pulposus
PET	Positronen-Emissions-Tomographie
PG	Proteoglykan
SE	Spinecho
SL	Spin-Lock
ST	Sättigungstransfer
RST	Ratiometrischer Sättigungstransfer
T1	Longitudinale Relaxationszeit
T2	Transversale Relaxationszeit
T_E	Echo Time
T_R	Repetition Time
WASABI	Simultaneous mapping of water shift and B1
WASSR	Water Saturation Shift Referencing
WEX	Water Exchange

11 Literaturverzeichnis

[1] I. I. Rabi, J. R. Zacharias, S. Millman, and P. Kusch. A New Method of Measuring Nuclear Magnetic Moment. *Physical Review*, 53(4):318–318, February 1938. doi: 10.1103/PhysRev.53.318.

[2] I. I. Rabi, S. Millman, P. Kusch, and J. R. Zacharias. The Molecular Beam Resonance Method for Measuring Nuclear Magnetic Moments. The Magnetic Moments of $_{3}\mathrm{Li}^{6}$, $_{3}\mathrm{Li}^{7}$ and $_{9}\mathrm{F}^{19}$. *Physical Review*, 55(6):526–535, March 1939. doi: 10.1103/PhysRev.55.526.

[3] Hermann Haken; Hans Christoph Wolf. *Atom- und Quantenphysik*. Springer, 2004.

[4] P. Mansfield and A. A. Maudsley. Medical imaging by NMR. *The British Journal of Radiology*, 50(591):188–194, March 1977. doi: 10.1259/0007-1285-50-591-188.

[5] Benjamin Schmitt. *Selektive NMR-Bildgebung am Menschen mittels des Protonenaustauschs zwischen Metaboliten und Wasser*. PhD thesis, Ruprecht-Karls-Universität Heidelberg, 2011.

[6] Peter C.M. van Zijl and Nirbhay N. Yadav. Chemical Exchange Saturation Transfer (CEST): what is in a name and what isn't? *Magnetic resonance in medicine : official journal of the Society of Magnetic Resonance in Medicine / Society of Magnetic Resonance in Medicine*, 65(4):927–948, April 2011. doi: 10.1002/mrm.22761.

[7] Jinyuan Zhou, Erik Tryggestad, Zhibo Wen, Bachchu Lal, Tingting Zhou, Rachel Grossman, Silun Wang, Kun Yan, De-Xue Fu, Eric Ford, Betty Tyler, Jaishri Blakeley, John Laterra, and Peter C. M. van Zijl. Differentiation between glioma and radiation necrosis using molecular magnetic resonance imaging of endogenous proteins and peptides. *Nature Medicine*, 17(1):130–134, January 2011. doi: 10.1038/nm.2268. Number: 1 Publisher: Nature Publishing Group.

[8] Runrun Wang, Peidong Chen, Zhiwei Shen, Guisen Lin, Gang Xiao, Zhuozhi Dai, Bingna Zhang, Yuanfeng Chen, Lihua Lai, Xiaodan Zong, Yan Li, Yanyan Tang, and Renhua Wu. Brain Amide Proton Transfer Imaging of

Rat With Alzheimer's Disease Using Saturation With Frequency Alternating RF Irradiation Method. *Frontiers in Aging Neuroscience*, 11, August 2019. doi: 10.3389/fnagi.2019.00217.

[9] Wen Ling, Ravinder R. Regatte, Gil Navon, and Alexej Jerschow. Assessment of glycosaminoglycan concentration in vivo by chemical exchange-dependent saturation transfer (gagCEST). *Proceedings of the National Academy of Sciences of the United States of America*, 105(7):2266–2270, February 2008. doi: 10.1073/pnas.0707666105.

[10] Dario Livio Longo, Alice Busato, Stefania Lanzardo, Federica Antico, and Silvio Aime. Imaging the pH evolution of an acute kidney injury model by means of iopamidol, a MRI-CEST pH-responsive contrast agent. *Magnetic Resonance in Medicine*, 70(3):859–864, September 2013. doi: 10.1002/mrm.24513.

[11] Jing Liu, Zheng Han, Guoli Chen, Yuguo Li, Jia Zhang, Jiadi Xu, Peter C. M. van Zijl, Shuixing Zhang, and Guanshu Liu. CEST MRI of sepsis-induced acute kidney injury. *NMR in biomedicine*, 31(8):e3942, 2018. doi: 10.1002/nbm.3942.

[12] Galit Saar, Boyang Zhang, Wen Ling, Ravinder R. Regatte, Gil Navon, and Alexej Jerschow. Assessment of glycosaminoglycan concentration changes in the intervertebral disc via chemical exchange saturation transfer. *NMR in biomedicine*, 25(2):255–261, February 2012. doi: 10.1002/nbm.1741.

[13] Wolfgang Pauli. Zur Frage der theoretischen Deutung der Satelliten einiger Spektrallinien und ihrer Beeinflussung durch magnetische Felder. In Charles P. Enz and Karl v. Meyenn, editors, *Wolfgang Pauli: Das Gewissen der Physik*, pages 167–171. Vieweg+Teubner Verlag, Wiesbaden, 1988. ISBN 978-3-322-90270-2. doi: 10.1007/978-3-322-90270-2_20.

[14] Walther Gerlach and Otto Stern. Über die Richtungsquantelung im Magnetfeld. *Annalen der Physik*, 379(16):673–699, 1924. doi: 10.1002/andp.19243791602.

[15] E. M. Purcell, H. C. Torrey, and R. V. Pound. Resonance Absorption by Nuclear Magnetic Moments in a Solid. *Physical Review*, 69(1-2):37–38, January 1946. doi: 10.1103/PhysRev.69.37.

[16] E. M. Purcell, R. V. Pound, and N. Bloembergen. Nuclear Magnetic Resonance Absorption in Hydrogen Gas. *Physical Review*, 70(11-12):986–987, December 1946. doi: 10.1103/PhysRev.70.986.

[17] F. Bloch, W. W. Hansen, and M. Packard. The Nuclear Induction Experiment. *Physical Review*, 70(7-8):474–485, October 1946. doi: 10.1103/PhysRev.70.474.

[18] E. Odeblad and G. Lindstrom. Some preliminary observations on the proton magnetic resonance in biologic samples. *Acta Radiologica*, 43(6):469–476, June 1955. doi: 10.3109/00016925509172514.

[19] P. C. Lauterbur. Image formation by induced local interactions. Examples employing nuclear magnetic resonance. 1973. *Clinical Orthopaedics and Related Research*, (244):3–6, July 1989.

[20] Keith R. Thulborn. Quantitative sodium MR imaging: A review of its evolving role in medicine. *NeuroImage*, 168:250–268, March 2018. doi: 10.1016/j.neuroimage.2016.11.056.

[21] Guillaume Madelin and Ravinder R. Regatte. Biomedical Applications of Sodium MRI In Vivo. *Journal of magnetic resonance imaging : JMRI*, 38 (3):511–529, September 2013. doi: 10.1002/jmri.24168.

[22] Steven D Wolff and Robert S Balaban. NMR imaging of labile proton exchange. *Journal of Magnetic Resonance (1969)*, 86(1):164–169, January 1990. doi: 10.1016/0022-2364(90)90220-4.

[23] S. D. Wolff and R. S. Balaban. Magnetization transfer contrast (MTC) and tissue water proton relaxation in vivo. *Magnetic Resonance in Medicine*, 10(1):135–144, April 1989. doi: 10.1002/mrm.1910100113.

[24] K. M. Ward, A. H. Aletras, and R. S. Balaban. A new class of contrast agents for MRI based on proton chemical exchange dependent saturation transfer (CEST). *Journal of Magnetic Resonance (San Diego, Calif.: 1997)*, 143(1):79–87, March 2000. doi: 10.1006/jmre.1999.1956.

[25] Joshua M. Goldenberg and Mark D. Pagel. Assessments of tumor metabolism with CEST MRI. *NMR in Biomedicine*, 32(10):e3943, 2019. doi: 10.1002/nbm.3943. _eprint: https://onlinelibrary.wiley.com/doi/pdf/10.1002/nbm.3943.

[26] Benjamin Schmitt, Štefan Zbýň, David Stelzeneder, Vladimir Jellus, Dominik Paul, Lars Lauer, Peter Bachert, and Siegfried Trattnig. Cartilage Quality Assessment by Using Glycosaminoglycan Chemical Exchange Saturation Transfer and 23na MR Imaging at 7 T. *Radiology*, 260(1):257–264, July 2011. doi: 10.1148/radiol.11101841.

[27] Min Deng, Jing Yuan, Wei Tian Chen, Queenie Chan, James F. Griffith, and Yi Xiang Wang. Evaluation of Glycosaminoglycan in the Lumbar Disc

Using Chemical Exchange Saturation Transfer MR at 3.0 Tesla: Reproducibility and Correlation with Disc Degeneration. *Biomedical and environmental sciences: BES*, 29(1):47–55, January 2016. doi: 10.3967/bes2016.005.

[28] Feng Wang, David Kopylov, Zhongliang Zu, Keiko Takahashi, Suwan Wang, C. Chad Quarles, John C. Gore, Raymond C. Harris, and Takamune Takahashi. Mapping murine diabetic kidney disease using chemical exchange saturation transfer MRI. *Magnetic Resonance in Medicine*, 76(5):1531–1541, 2016. doi: 10.1002/mrm.26045.

[29] Zhengwei Zhou, Christopher Nguyen, Yuhua Chen, Jaime L. Shaw, Zixin Deng, Yibin Xie, James Dawkins, Eduardo Marbán, and Debiao Li. Optimized CEST cardiovascular magnetic resonance for assessment of metabolic activity in the heart. *Journal of Cardiovascular Magnetic Resonance*, 19, November 2017. doi: 10.1186/s12968-017-0411-1.

[30] Renhua Wu, Gang Xiao, Iris Yuwen Zhou, Chongzhao Ran, and Phillip Zhe Sun. Quantitative chemical exchange saturation transfer (qCEST) MRI - omega plot analysis of RF-spillover-corrected inverse CEST ratio asymmetry for simultaneous determination of labile proton ratio and exchange rate. *NMR in biomedicine*, 28(3):376–383, March 2015. doi: 10.1002/nbm.3257.

[31] Jan-Eric Meissner, Steffen Goerke, Eugenia Rerich, Karel D. Klika, Alexander Radbruch, Mark E. Ladd, Peter Bachert, and Moritz Zaiss. Quantitative pulsed CEST-MRI using Omega-plots. *NMR in biomedicine*, 28(10):1196–1208, October 2015. doi: 10.1002/nbm.3362.

[32] B. Wu, G. Warnock, M. Zaiss, C. Lin, M. Chen, Z. Zhou, L. Mu, D. Nanz, R. Tuura, and G. Delso. An overview of CEST MRI for non-MR physicists. *EJNMMI Physics*, 3(1):19, August 2016. doi: 10.1186/s40658-016-0155-2.

[33] Olaf Dössel. *Bildgebende Verfahren in der Medizin: von der Technik zur medizinischen Anwendung*. Springer, 2000.

[34] Linda Knutsson, Jiadi Xu, André Ahlgren, and Peter C. M. van Zijl. CEST, ASL, and magnetization transfer contrast: How similar pulse sequences detect different phenomena. *Magnetic Resonance in Medicine*, 80(4):1320–1340, October 2018. doi: 10.1002/mrm.27341.

[35] Susan Francis, Charlotte E. Buchanan, Ben Prestwich, and Maarten W. Taal. Sodium MRI: a new frontier in imaging in nephrology. *Current Opinion in Nephrology and Hypertension*, 26(6):435–441, 2017. doi: 10.1097/MNH.0000000000000370.

[36] A. Biller, S. Badde, A. Nagel, J.-O. Neumann, W. Wick, A. Hertenstein, M. Bendszus, F. Sahm, N. Benkhedah, and J. Kleesiek. Improved Brain

Tumor Classification by Sodium MR Imaging: Prediction of IDH Mutation Status and Tumor Progression. *AJNR. American journal of neuroradiology*, 37(1):66–73, January 2016. doi: 10.3174/ajnr.A4493.

[37] Guillaume Madelin, James Babb, Ding Xia, Gregory Chang, Svetlana Krasnokutsky, Steven B. Abramson, Alexej Jerschow, and Ravinder R. Regatte. Articular cartilage: evaluation with fluid-suppressed 7.0-T sodium MR imaging in subjects with and subjects without osteoarthritis. *Radiology*, 268 (2):481–491, August 2013. doi: 10.1148/radiol.13121511.

[38] Stefan H. Hoffmann, Alexander Radbruch, Michael Bock, Wolfhard Semmler, and Armin M. Nagel. Direct 17O MRI with partial volume correction: first experiences in a glioblastoma patient. *Magnetic Resonance Materials in Physics, Biology and Medicine*, 27(6):579–587, December 2014. doi: 10.1007/s10334-014-0441-8.

[39] Armin M. Nagel, Frank Lehmann-Horn, Marc-André Weber, Karin Jurkat-Rott, Maya B. Wolf, Alexander Radbruch, Reiner Umathum, and Wolfhard Semmler. In Vivo 35Cl MR Imaging in Humans: A Feasibility Study. *Radiology*, 271(2):585–595, February 2014. doi: 10.1148/radiol.13131725. Publisher: Radiological Society of North America.

[40] Falk Miese, Christian Buchbender, Axel Scherer, Hans-Jörg Wittsack, Christof Specker, Matthias Schneider, Gerald Antoch, and Benedikt Ostendorf. Molecular imaging of cartilage damage of finger joints in early rheumatoid arthritis with delayed gadolinium-enhanced magnetic resonance imaging. *Arthritis and Rheumatism*, 64(2):394–399, February 2012. doi: 10.1002/art.33352.

[41] D. R. Roberts, A. R. Chatterjee, M. Yazdani, B. Marebwa, T. Brown, H. Collins, G. Bolles, J. M. Jenrette, P. J. Nietert, and X. Zhu. Pediatric Patients Demonstrate Progressive T1-Weighted Hyperintensity in the Dentate Nucleus following Multiple Doses of Gadolinium-Based Contrast Agent. *AJNR. American journal of neuroradiology*, 37(12):2340–2347, December 2016. doi: 10.3174/ajnr.A4891.

[42] H. Kang, M. Hii, M. Le, R. Tam, A. Riddehough, A. Traboulsee, S. Kolind, M. S. Freedman, and D. K. B. Li. Gadolinium Deposition in Deep Brain Structures: Relationship with Dose and Ionization of Linear Gadolinium-Based Contrast Agents. *AJNR. American journal of neuroradiology*, 39(9): 1597–1603, 2018. doi: 10.3174/ajnr.A5751.

[43] Vikas Gulani, Fernando Calamante, Frank G. Shellock, Emanuel Kanal, Scott B. Reeder, and International Society for Magnetic Resonance in Medicine. Gadolinium deposition in the brain: summary of evidence

and recommendations. *The Lancet. Neurology*, 16(7):564–570, 2017. doi: 10.1016/S1474-4422(17)30158-8.

[44] Javier Perez-Rodriguez, Shenghan Lai, Benjamin D. Ehst, Derek M. Fine, and David A. Bluemke. Nephrogenic systemic fibrosis: incidence, associations, and effect of risk factor assessment–report of 33 cases. *Radiology*, 250 (2):371–377, February 2009. doi: 10.1148/radiol.2502080498.

[45] Robert J. Harris, Jingwen Yao, Ararat Chakhoyan, Catalina Raymond, Kevin Leu, Linda M. Liau, Phioanh L. Nghiemphu, Albert Lai, Noriko Salamon, Whitney B. Pope, Timothy F. Cloughesy, and Benjamin M. Ellingson. Simultaneous pH-sensitive and oxygen-sensitive MRI of human gliomas at 3 T using multi-echo amine proton chemical exchange saturation transfer spin-and-gradient echo echo-planar imaging (CEST-SAGE-EPI). *Magnetic Resonance in Medicine*, 80(5):1962–1978, November 2018. doi: 10.1002/mrm.27204.

[46] R. Martínez-Zaguilán, E. A. Seftor, R. E. Seftor, Y. W. Chu, R. J. Gillies, and M. J. Hendrix. Acidic pH enhances the invasive behavior of human melanoma cells. *Clinical & Experimental Metastasis*, 14(2):176–186, March 1996.

[47] Dario Livio Longo, Juan Carlos Cutrin, Filippo Michelotti, Pietro Irrera, and Silvio Aime. Noninvasive evaluation of renal pH homeostasis after ischemia reperfusion injury by CEST-MRI. *NMR in biomedicine*, 30(7), July 2017. doi: 10.1002/nbm.3720.

[48] Soo Hyun Shin, Michael F. Wendland, Brandon Zhang, An Tran, Albert Tang, and Moriel H. Vandsburger. Noninvasive imaging of renal urea handling by CEST-MRI. *Magnetic Resonance in Medicine*, 83(3):1034–1044, 2020. doi: 10.1002/mrm.27968. _eprint: https://onlinelibrary.wiley.com/doi/pdf/10.1002/mrm.27968.

[49] E. Mark Haacke, Robert W. Brown, Michael R. Thompson, and Ramesh Venkatesan. *MAGNETIC RESONANCE IMAGING: Physical Principles and Sequence Design*. Wiley, 1999.

[50] Thomas J. Vogl, Wolfgang Reith, and Ernst J. Rummeny. *Diagnostische und interventionelle Radiologie*. Springer-Verlag, March 2011. ISBN 978-3-540-87668-7. Google-Books-ID: I8wfBAAAQBAJ.

[51] Matt A. Bernstein, Kevin F. King, and Xiaohong Joe Zhou. *Handbook of MRI Pulse Sequences*. Elsevier, September 2004. ISBN 978-0-08-053312-4. Google-Books-ID: d6PLHcyejEIC.

[52] Moritz Zaiss and Peter Bachert. Chemical exchange saturation transfer (CEST) and MR Z-spectroscopy in vivo: a review of theoretical approaches and methods. *Physics in Medicine and Biology*, 58(22):R221–269, November 2013. doi: 10.1088/0031-9155/58/22/R221.

[53] Jinyuan Zhou, David A. Wilson, Phillip Zhe Sun, Judith A. Klaus, and Peter C. M. Van Zijl. Quantitative description of proton exchange processes between water and endogenous and exogenous agents for WEX, CEST, and APT experiments. *Magnetic Resonance in Medicine*, 51(5):945–952, May 2004. doi: 10.1002/mrm.20048.

[54] Phillip Zhe Sun, Jinyuan Zhou, Judy Huang, and Peter van Zijl. Simplified quantitative description of amide proton transfer (APT) imaging during acute ischemia. *Magnetic Resonance in Medicine*, 57(2):405–410, February 2007. doi: 10.1002/mrm.21151.

[55] Mina Kim, Joseph Gillen, Bennett A. Landman, Jinyuan Zhou, and Peter C. M. van Zijl. Water saturation shift referencing (WASSR) for chemical exchange saturation transfer (CEST) experiments. *Magnetic Resonance in Medicine*, 61(6):1441–1450, June 2009. doi: 10.1002/mrm.21873.

[56] Dario Livio Longo, Walter Dastrù, Giuseppe Digilio, Jochen Keupp, Sander Langereis, Stefania Lanzardo, Simone Prestigio, Oliver Steinbach, Enzo Terreno, Fulvio Uggeri, and Silvio Aime. Iopamidol as a responsive MRI-chemical exchange saturation transfer contrast agent for pH mapping of kidneys: In vivo studies in mice at 7 T. *Magnetic Resonance in Medicine*, 65(1):202–211, January 2011. doi: 10.1002/mrm.22608.

[57] Jinsuh Kim, Yin Wu, Yingkun Guo, Hairong Zheng, and Phillip Zhe Sun. A review of optimization and quantification techniques for chemical exchange saturation transfer MRI toward sensitive in vivo imaging. *Contrast Media & Molecular Imaging*, 10(3):163–178, June 2015. doi: 10.1002/cmmi.1628.

[58] Michael T. McMahon, Assaf A. Gilad, Jinyuan Zhou, Phillip Z. Sun, Jeff W. M. Bulte, and Peter C. M. van Zijl. Quantifying exchange rates in chemical exchange saturation transfer agents using the saturation time and saturation power dependencies of the magnetization transfer effect on the magnetic resonance imaging signal (QUEST and QUESP): Ph calibration for poly-L-lysine and a starburst dendrimer. *Magnetic Resonance in Medicine*, 55(4):836–847, April 2006. doi: 10.1002/mrm.20818.

[59] W. Thomas Dixon, Jimin Ren, Angelo J. M. Lubag, James Ratnakar, Elena Vinogradov, Ileana Hancu, Robert E. Lenkinski, and A. Dean Sherry. A concentration-independent method to measure exchange rates in PARACEST agents. *Magnetic Resonance in Medicine*, 63(3):625–632, March 2010. doi: 10.1002/mrm.22242.

[60] Phillip Zhe Sun. Simplified quantification of labile proton concentration-weighted chemical exchange rate (k(ws)) with RF saturation time dependent ratiometric analysis (QUESTRA): normalization of relaxation and RF irradiation spillover effects for improved quantitative chemical exchange saturation transfer (CEST) MRI. *Magnetic Resonance in Medicine*, 67(4): 936–942, April 2012. doi: 10.1002/mrm.23068.

[61] Moritz Zaiss, Junzhong Xu, Steffen Goerke, Imad S. Khan, Robert J. Singer, John C. Gore, Daniel F. Gochberg, and Peter Bachert. Inverse Z-spectrum analysis for spillover-, MT-, and T1 -corrected steady-state pulsed CEST-MRI–application to pH-weighted MRI of acute stroke. *NMR in biomedicine*, 27(3):240–252, March 2014. doi: 10.1002/nbm.3054.

[62] Julia Stabinska, Tom Cronenberg, Hans-Jörg Wittsack, Rotem Shlomo Lanzman, and Anja Müller-Lutz. Quantitative pulsed CEST-MRI at a clinical 3t MRI system. *Magma (New York, N.Y.)*, 30(5):505–516, October 2017. doi: 10.1007/s10334-017-0625-0.

[63] Moritz Zaiss and Peter Bachert. Exchange-dependent relaxation in the rotating frame for slow and intermediate exchange – modeling off-resonant spin-lock and chemical exchange saturation transfer. *NMR in biomedicine*, 26(5):507–518, May 2013. doi: 10.1002/nbm.2887.

[64] Jun Hua, Craig K. Jones, Jaishri Blakeley, Seth A. Smith, Peter C.M. van Zijl, and Jinyuan Zhou. Quantitative Description of the Asymmetry in Magnetization Transfer Effects around the Water Resonance in the Human Brain. *Magnetic resonance in medicine : official journal of the Society of Magnetic Resonance in Medicine / Society of Magnetic Resonance in Medicine*, 58(4):786–793, October 2007. doi: 10.1002/mrm.21387.

[65] Jae-Seung Lee, Prodromos Parasoglou, Ding Xia, Alexej Jerschow, and Ravinder R. Regatte. Uniform magnetization transfer in chemical exchange saturation transfer magnetic resonance imaging. *Scientific Reports*, 3:1707, 2013. doi: 10.1038/srep01707.

[66] G. A. Morris. The nuclear overhauser effect in structural and conformational analysis. David Neuhaus and Michael P. Williamson. VCH, Weinheim, Basle, Cambridge, New Yok, 1989, £67. *Magnetic Resonance in Chemistry*, 28(8):738–738, 1990. doi: 10.1002/mrc.1260280819.

[67] Moritz Zaiss, Johannes Windschuh, Daniel Paech, Jan-Eric Meissner, Sina Burth, Benjamin Schmitt, Philip Kickingereder, Benedikt Wiestler, Wolfgang Wick, Martin Bendszus, Heinz-Peter Schlemmer, Mark E. Ladd, Peter Bachert, and Alexander Radbruch. Relaxation-compensated CEST-MRI of

the human brain at 7t: Unbiased insight into NOE and amide signal changes in human glioblastoma. *NeuroImage*, 112:180–188, May 2015. doi: 10.1016/j.neuroimage.2015.02.040.

[68] Kyle M. Jones, Edward A. Randtke, Christine M. Howison, and Mark D. Pagel. Respiration gating and Bloch fitting improve pH measurements with acidoCEST MRI in an ovarian orthotopic tumor model. *Proceedings of SPIE–the International Society for Optical Engineering*, 9788, February 2016. doi: 10.1117/12.2216418.

[69] Yi Zhang, Hye-Young Heo, Dong-Hoon Lee, Xuna Zhao, Shanshan Jiang, Kai Zhang, Haiyun Li, and Jinyuan Zhou. Selecting the reference image for registration of CEST series. *Journal of magnetic resonance imaging: JMRI*, 43(3):756–761, March 2016. doi: 10.1002/jmri.25027.

[70] Anja Müller-Lutz, Felix Matuschke, Christoph Schleich, Frithjof Wickrath, Johannes Boos, Benjamin Schmitt, and Hans-Jörg Wittsack. Improvement of water saturation shift referencing by sequence and analysis optimization to enhance chemical exchange saturation transfer imaging. *Magnetic Resonance Imaging*, 34(6):771–778, 2016. doi: 10.1016/j.mri.2016.03.013.

[71] Patrick Schuenke, Johannes Windschuh, Volkert Roeloffs, Mark E. Ladd, Peter Bachert, and Moritz Zaiss. Simultaneous mapping of water shift and B1 (WASABI)-Application to field-Inhomogeneity correction of CEST MRI data. *Magnetic Resonance in Medicine*, 77(2):571–580, 2017. doi: 10.1002/mrm.26133.

[72] Theodor Heinrich Schiebler, Walter Schmidt, and Karl Zilles. *Anatomie*. Springer, 8. auflage edition, 1999. ISBN 3-540-65824.

[73] Ram Sasisekharan, Rahul Raman, and Vikas Prabhakar. Glycomics Approach to Structure-Function Relationships of Glycosaminoglycans. *Annual Review of Biomedical Engineering*, 8(1):181–231, 2006. doi: 10.1146/annurev.bioeng.8.061505.095745.

[74] Demitrios H. Vynios. Metabolism of Cartilage Proteoglycans in Health and Disease, 2014.

[75] G. Lyons, S. M. Eisenstein, and M. B. Sweet. Biochemical changes in intervertebral disc degeneration. *Biochimica Et Biophysica Acta*, 673(4): 443–453, April 1981.

[76] A. P. Hollander, R. M. Atkins, D. M. Eastwood, P. A. Dieppe, and C. J. Elson. Human cartilage is degraded by rheumatoid arthritis synovial fluid but not by recombinant cytokines in vitro. *Clinical and Experimental Immunology*, 83(1):52–57, January 1991.

[77] Falk R. Miese, Benedikt Ostendorf, Hans-Jörg Wittsack, Dorothea C. Reichelt, Tallal C. Mamisch, Christoph Zilkens, Rotem S. Lanzman, Matthias Schneider, and Axel Scherer. Metacarpophalangeal Joints in Rheumatoid Arthritis: Delayed Gadolinium-enhanced MR Imaging of Cartilage—A Feasibility Study. *Radiology*, 257(2):441–447, November 2010. doi: 10.1148/radiol.10100459.

[78] Stephen J. Matzat, Jasper van Tiel, Garry E. Gold, and Edwin H. G. Oei. Quantitative MRI techniques of cartilage composition. *Quantitative Imaging in Medicine and Surgery*, 3(3):162–174, June 2013. doi: 10.3978/j.issn.2223-4292.2013.06.04.

[79] Barbara Herz, Andreas Albrecht, Matthias Englbrecht, Götz H. Welsch, Michael Uder, Nina Renner, Philipp Schlechtweg, Dominik Paul, Lars Lauer, Klaus Engelke, Rolf Janka, Jürgen Rech, Georg Schett, and Stephanie Finzel. Osteitis and synovitis, but not bone erosion, is associated with proteoglycan loss and microstructure damage in the cartilage of patients with rheumatoid arthritis. *Annals of the Rheumatic Diseases*, 73(6):1101–1106, June 2014. doi: 10.1136/annrheumdis-2012-202850.

[80] Anja Müller-Lutz, Christoph Schleich, Gael Pentang, Benjamin Schmitt, Rotem S. Lanzman, Felix Matuschke, Hans-Jörg Wittsack, and Falk Miese. Age-dependency of glycosaminoglycan content in lumbar discs: A 3t gagcEST study. *Journal of magnetic resonance imaging: JMRI*, 42(6):1517–1523, December 2015. doi: 10.1002/jmri.24945.

[81] Anja Müller-Lutz, Christoph Schleich, Benjamin Schmitt, Gerald Antoch, Felix Matuschke, Michael Quentin, Hans-Jörg Wittsack, and Falk Miese. Gender, BMI and T2 dependencies of glycosaminoglycan chemical exchange saturation transfer in intervertebral discs. *Magnetic Resonance Imaging*, 34 (3):271–275, April 2016. doi: 10.1016/j.mri.2015.10.024.

[82] Christoph Schleich, Anja Müller-Lutz, Lisa Zimmermann, Johannes Boos, Benjamin Schmitt, Hans-Jörg Wittsack, Gerald Antoch, and Falk Miese. Biochemical imaging of cervical intervertebral discs with glycosaminoglycan chemical exchange saturation transfer magnetic resonance imaging: feasibility and initial results. *Skeletal Radiology*, 45(1):79–85, January 2016. doi: 10.1007/s00256-015-2251-0.

[83] Daniel B. Abrar, Christoph Schleich, Karl Ludger Radke, Miriam Frenken, Julia Stabinska, Alexandra Ljimani, Hans-Jörg Wittsack, Gerald Antoch, Bernd Bittersohl, Tobias Hesper, Sven Nebelung, and Anja Müller-Lutz. Detection of early cartilage degeneration in the tibiotalar joint using 3 T gagCEST imaging: a feasibility study. *Magnetic Resonance*

Materials in Physics, Biology and Medicine, July 2020. doi: 10.1007/s10334-020-00868-y.

[84] Anja Müller-Lutz, Tom Cronenberg, Christoph Schleich, Frithjof Wickrath, Moritz Zaiss, Johannes Boos, and Hans-Jörg Wittsack. Comparison of glycosaminoglycan chemical exchange saturation transfer using gaussian-shaped and off-resonant spin-lock radiofrequency pulses in intervertebral disks. *Magnetic Resonance in Medicine*, 78(1):280–284, 2017. doi: 10.1002/mrm.26362.

[85] Anja Müller-Lutz, Christoph Schleich, Benjamin Schmitt, Melike Topgöz, Gael Pentang, Gerald Antoch, Hans-Jörg Wittsack, and Falk Miese. Improvement of gagCEST imaging in the human lumbar intervertebral disc by motion correction. *Skeletal Radiology*, 44(4):505–511, April 2015. doi: 10.1007/s00256-014-2034-z.

[86] Anja Müller-Lutz, Alexandra Ljimani, Julia Stabinska, Moritz Zaiss, Johannes Boos, Hans-Jörg Wittsack, and Christoph Schleich. Comparison of B0 versus B0 and B1 field inhomogeneity correction for glycosaminoglycan chemical exchange saturation transfer imaging. *Magma (New York, N.Y.)*, 31(5):645–651, October 2018. doi: 10.1007/s10334-018-0689-5.

[87] Anja Müller-Lutz, Nadia Khalil, Benjamin Schmitt, Vladimir Jellus, Gael Pentang, Georg Oeltzschner, Gerald Antoch, Rotem S. Lanzman, and Hans-Jörg Wittsack. Pilot study of Iopamidol-based quantitative pH imaging on a clinical 3t MR scanner. *Magma (New York, N.Y.)*, 27(6):477–485, December 2014. doi: 10.1007/s10334-014-0433-8.

[88] V. Guivel-Scharen, T. Sinnwell, S. D. Wolff, and R. S. Balaban. Detection of proton chemical exchange between metabolites and water in biological tissues. *Journal of Magnetic Resonance (San Diego, Calif.: 1997)*, 133(1):36–45, July 1998. doi: 10.1006/jmre.1998.1440.

[89] Julia Stabinska, Philipp Neudecker, Alexandra Ljimani, Hans-Jörg Wittsack, Rotem Shlomo Lanzman, and Anja Müller-Lutz. Proton exchange in aqueous urea solutions measured by water-exchange (WEX) NMR spectroscopy and chemical exchange saturation transfer (CEST) imaging in vitro. *Magnetic Resonance in Medicine*, 82(3):935–947, 2019. doi: 10.1002/mrm.27778.

[90] Kyle M. Jones, Alyssa C. Pollard, and Mark D. Pagel. Clinical Applications of Chemical Exchange Saturation Transfer (CEST) MRI. *Journal of magnetic resonance imaging : JMRI*, 47(1):11–27, January 2018. doi: 10.1002/jmri.25838.

[91] Pernilla Peterson, Emma Olsson, and Jonas Svensson. T2 relaxation time bias in gagCEST at 3T and 7T: comparison of saturation schemes. *Magnetic Resonance in Medicine*, 81(2):1044–1051, 2019. doi: 10.1002/mrm.27465.

[92] Vitaliy Khlebnikov, Daniel Polders, Jeroen Hendrikse, Pierre A. Robe, Eduard H. Voormolen, Peter R. Luijten, Dennis W. J. Klomp, and Hans Hoogduin. Amide proton transfer (APT) imaging of brain tumors at 7 T: The role of tissue water T1 -Relaxation properties. *Magnetic Resonance in Medicine*, 77(4):1525–1532, 2017. doi: 10.1002/mrm.26232.

[93] Sander Brinkhof, Razmara Nizak, Vitaliy Khlebnikov, Jeanine J. Prompers, Dennis W. J. Klomp, and Daniel B. F. Saris. Detection of early cartilage damage: feasibility and potential of gagCEST imaging at 7T. *European Radiology*, 28(7):2874–2881, July 2018. doi: 10.1007/s00330-017-5277-y.

[94] Stefan Haneder, Sebastian R. Apprich, Benjamin Schmitt, Henrik J. Michaely, Stefan O. Schoenberg, Klaus M. Friedrich, and Siegfried Trattnig. Assessment of glycosaminoglycan content in intervertebral discs using chemical exchange saturation transfer at 3.0 Tesla: preliminary results in patients with low-back pain. *European Radiology*, 23(3):861–868, March 2013. doi: 10.1007/s00330-012-2660-6.

[95] Tatsuhiro Wada, Osamu Togao, Chiaki Tokunaga, Ryohei Funatsu, Yasuo Yamashita, Kouji Kobayashi, Yasuhiko Nakamura, and Hiroshi Honda. Glycosaminoglycan chemical exchange saturation transfer in human lumbar intervertebral discs: Effect of saturation pulse and relationship with low back pain. *Journal of Magnetic Resonance Imaging*, 45(3):863–871, 2017. doi: 10.1002/jmri.25397. _eprint: https://onlinelibrary.wiley.com/doi/pdf/10.1002/jmri.25397.

[96] Pietro Irrera, Lorena Consolino, Juan Carlos Cutrin, Frank G. Zöllner, and Dario Livio Longo. Dual assessment of kidney perfusion and pH by exploiting a dynamic CEST-MRI approach in an acute kidney ischemia-reperfusion injury murine model. *NMR in biomedicine*, 33(6):e4287, 2020. doi: 10.1002/nbm.4287.

[97] Yunkou Wu, Shanrong Zhang, Todd C. Soesbe, Jing Yu, Elena Vinogradov, Robert E. Lenkinski, and A. Dean Sherry. pH imaging of mouse kidneys in vivo using a frequency-dependent paraCEST agent. *Magnetic Resonance in Medicine*, 75(6):2432–2441, June 2016. doi: 10.1002/mrm.25844.

[98] Esau Poblador Rodriguez, Philipp Moser, Barbara Dymerska, Simon Robinson, Benjamin Schmitt, Andre van der Kouwe, Stephan Gruber, Siegfried Trattnig, and Wolfgang Bogner. A comparison of static and dynamic δ B0 mapping methods for correction of CEST MRI in the presence of temporal

B0 field variations. *Magnetic Resonance in Medicine*, 82(2):633–646, 2019. doi: 10.1002/mrm.27750.

[99] Gizeaddis L. Simegn, Andre J. W. Van der Kouwe, Frances C. Robertson, Ernesta M. Meintjes, and Ali Alhamud. Real-time simultaneous shim and motion measurement and correction in glycoCEST MRI using double volumetric navigators (DvNavs). *Magnetic Resonance in Medicine*, 81(4): 2600–2613, 2019. doi: 10.1002/mrm.27597.

[100] R. L. Ehman and J. P. Felmlee. Adaptive technique for high-definition MR imaging of moving structures. *Radiology*, 173(1):255–263, October 1989. doi: 10.1148/radiology.173.1.2781017.

[101] Liu Qi Chen, Christine M. Howison, Justin J. Jeffery, Ian F. Robey, Phillip H. Kuo, and Mark D. Pagel. Evaluations of extracellular pH within in vivo tumors using acidoCEST MRI. *Magnetic Resonance in Medicine*, 72(5):1408–1417, 2014. doi: 10.1002/mrm.25053. _eprint: https://onlinelibrary.wiley.com/doi/pdf/10.1002/mrm.25053.

[102] Guanshu Liu, Yuguo Li, Vipul R. Sheth, and Mark D. Pagel. Imaging in vivo extracellular pH with a single paramagnetic chemical exchange saturation transfer magnetic resonance imaging contrast agent. *Molecular Imaging*, 11 (1):47–57, February 2012.

[103] Phillip Zhe Sun, Gang Xiao, Iris Yuwen Zhou, Yingkun Guo, and Renhua Wu. A method for accurate pH mapping with chemical exchange saturation transfer (CEST) MRI. *Contrast Media & Molecular Imaging*, 11(3):195–202, 2016. doi: 10.1002/cmmi.1680.

12 Nachdruck der wissenschaftlichen Publikationen

Der Nachdruck der angehängten Publikationen erfolgt mit der freundlichen Genehmigung der jeweiligen Verlage.

Age-Dependency of Glycosaminoglycan Content in Lumbar Discs: A 3T gagCEST Study

Anja Müller-Lutz, PhD,[1] Christoph Schleich, MD,[1]* Gael Pentang, MSc,[1] Benjamin Schmitt, PhD,[2] Rotem S. Lanzman, MD,[1] Felix Matuschke, BSc,[1] Hans-Jörg Wittsack, PhD,[1] and Falk Miese, MD[1]

Purpose: To analyze age-dependency of glycosaminoglycan content using gagCEST (glycosaminoglycan chemical exchange saturation transfer) imaging in lumbar intervertebral discs of healthy volunteers.
Materials and Methods: In all, 70 volunteers without low back pain (mean age 44 ± 14 years, range: 21–69 years) were examined with T_2-weighted and gagCEST imaging with a 3T MR scanner, with approval of the local Ethics Committee after written informed consent was obtained. Pfirrmann grading and classification into discs without bulging and herniation, discs with bulging, and discs with herniation were performed. Only intervertebral discs without bulging and herniation were analyzed. A region-of-interest-based gagCEST analysis of nucleus pulposus (NP) and annulus fibrosus (AF) was performed. Correlation between age and gagCEST was tested within groups of equal Pfirrmann score.
Results: GagCEST effects decreased significantly from 3.09 ± 1.12% in 20–29 years old volunteers to −0.24 ± 1.36% in 50–59 years old volunteers ($P < 0.001$). In the case of Pfirrmann scores 2 and 3, a significant correlation was observed between gagCEST effect and age (Pfirrmann score 2, NP: $\rho = -0.558$, $P < 0.001$; Pfirrmann score 3, NP: $\rho = -0.337$, $P = 0.048$). For Pfirrmann scores 1 and 4, no significant correlation was obtained (Pfirrmann score 1, NP: $\rho = -0.046$, $P = 0.824$; Pfirrmann score 4, NP: $\rho = -0.316$, $P = 0.188$).
Conclusion: We show a decreased gagCEST effect likely corresponding to decreasing glycosaminoglycans with aging. Hence, age-matched analysis of gagCEST imaging may be necessary in future studies.

J. MAGN. RESON. IMAGING 2015;42:1517–1523.

Magnetic resonance imaging (MRI) is a well-established method for imaging of intervertebral disc pathologies.[1] With gagCEST, a noninvasive assessment of glycosaminoglycans (GAG) is possible.[2–5]

Intervertebral discs (IVDs) are composed of collagen and aggrecan, which is a large proteoglycan (PG) molecule. PGs consist of a core protein and one or more covalently attached GAG chains.[6] They are important for vital functions in IVDs like the maintenance of hydroscopic pressure.[6,7] IVDs are composed of two compartments: nucleus pulposus (NP) and annulus fibrosus (AF). Their chemical content is considerably different: AF consists of about 70% collagen and 10–20% aggrecan, whereas NP is comprised of 20–30% collagen and 50% aggrecan.[3,8,9] Therefore, a lower GAG content is expected in normal AF compared to normal NP. The role of collagen in AF is to resist the swelling pressure of NP and to provide shear and tensile strength.[7] In previous studies, a decrease of GAG content was reported to correlate with IVD degeneration, decreased hydration, and decreased disc height.[3,10,11]

Degeneration of IVDs is routinely assessed by Pfirrmann scoring.[1] This scoring is based on signal intensity, disc height, and discriminability of NP and AF and height of IVDs observed on T_2-weighted images. A direct biochemical assessment of the GAG content is not within the scope of Pfirrmann scoring.

Different techniques have been introduced to quantify GAG content, including T_2 relaxometry imaging, dGEMRIC,

View this article online at wileyonlinelibrary.com. DOI: 10.1002/jmri.24945

Received Feb 17, 2015, Accepted for publication Apr 27, 2015.

*Address reprint requests to: C.S., University Dusseldorf, Department of Diagnostic and Interventional Radiology, Moorenstr. 5, D-40225 Düsseldorf, Germany. E-mail: Christoph.Schleich@med.uni-duesseldorf.de

From the [1]University Dusseldorf, Medical Faculty, Department of Diagnostic and Interventional Radiology, Dusseldorf, Germany; and [2]Siemens Australia, Healthcare Sector, Macquarie Park NSW, Australia.

TABLE 1. Detailed Information About the Study Population

Age group	Corresponding age range [years]	Mean age	Minimum age	Maximum age	Number females	Number males
1	20–29	24 ± 2	21	28	7	7
2	30–39	33 ± 3	30	38	7	7
3	40–49	45 ± 4	40	49	9	5
4	50–59	56 ± 2	51	59	11	3
5	60–69	63 ± 3	60	69	8	6

sodium MRI, and gagCEST imaging.[3,12–15] In the present study, gagCEST imaging was chosen since it is directly related to glycosaminoglycan content. It has been successfully applied in previous studies and it does not require contrast agent or dedicated MRI hardware such as sodium coils and special high-frequency equipment. Hence, gagCEST imaging has the key factors that drive broad scientific and clinical use.

The purpose of our work was to investigate if GAG content alters with age in IVDs of healthy volunteers without low back pain.

Materials and Methods

Study Population

The study was approved by the local Ethics Committee, and written informed consent was obtained from all participants. In all, 70 volunteers without low back pain or a history of low back pain (42 females, 28 males, mean age 44 ± 14 years, range: 21–69 years) were enrolled in this study. The volunteers were divided into five age groups, each with 14 volunteers (Table 1). Repeated scans of three additional measured volunteers were acquired and used for assessment of test–retest reproducibility (two males, one female, age 22 ± 1 year). The time interval between the repeated gagCEST measurements was about 40 minutes.

MR Hardware and Sequence Protocol

All volunteers were examined in the year 2014 in supine position using a clinical whole-body 3T MR system (Magnetom Trio, A Tim System, Siemens Healthcare, Erlangen, Germany). Signal reception was performed with a spine matrix coil. Our MR sequence protocol included a localizer, T_2-weighted imaging in sagittal and transversal orientation, and prototype gagCEST and WASSR (water saturation shift referencing[16]) sequences. Sequence details of gagCEST and WASSR sequences are listed in Table 2.

Parameters of the sagittal T_2-weighted turbo spin echo sequence were: number of slices = 15, TE/TR = 105/3100 msec, slice thickness = 3 mm, in-plane resolution = 1.2 × 1.2 mm^2, flip angle = 160°, field of view = 300 × 300 mm^2, two signal averages, number of echoes per slice = 17, a resolution of 256 × 256, and acquisition time of 3 minutes and 39 seconds.

The parameters of the transversal T_2-weighted turbo spin echo sequence were: number of slices = 25, TE/TR = 113/4000 msec, slice thickness = 3 mm, in-plane resolution = 0.8 × 0.6 mm^2, flip angle = 140°, field of view = 240 × 240 mm^2, one signal average, number of echoes per slice = 26, a resolution of 384 × 307, and acquisition time of 3 minutes and 38 seconds.

The T_2-weighted images were acquired in order to enable Pfirrmann scoring and differentiation between intervertebral discs without bulging or herniation, discs with bulging and discs with herniation.

TABLE 2. Detailed Sequence Parameters of the Prototype CEST and WASSR Sequences

		CEST	WASSR
TE/TR	[msec]/[msec]	3.01/1590	3.01/590
Resolution	[mm^3]	1.6 × 1.6 × 5	1.6 × 1.6 × 5
Flip angle	[°]	12	12
Field of View	[mm^2]	300 × 300	300 × 300
Duration	[min:sec]	12:24	7:26
Averages		6	6
Basic Resolution		192 × 192	192 × 192

GagCEST and WASSR sequences were composed of a CEST presaturation module and a segmented 2D RF-spoiled gradient echo module.

The CEST presaturation module of the prototype gagCEST sequence consisted of six Gaussian-shaped RF pulses with a pulse and interpulse duration of 100 msec and a B_1 amplitude of 1.5 μT averaged over time. One reference measurement without CEST presaturation module and 25 measurements with CEST presaturation module were applied to acquire the Z-spectrum in the range of -4 ppm to 4 ppm.

The CEST presaturation module of the prototype WASSR sequence consisted of one Gaussian-shaped RF pulse with a B_1 amplitude of 0.3 μT and a pulse duration of 100 msec. One reference measurement without presaturation module and 41 measurements with CEST presaturation module of the prototype WASSR sequence were performed to cover a frequency range from -1 ppm to 1 ppm.

Bowel movement artifacts and artifacts due to abdominal wall motion were reduced using a saturation band anterior to the spine.

GagCEST imaging provides information about the chemical exchange between hydroxyl protons of glycosaminoglycans and water. With the asymmetry analysis described in the data analysis part, information about the CEST effect can be obtained.

Data Analysis

One radiologist (C.S., 3 years' experience in radiology) scored all lumbar IVDs according to the Pfirrmann grade.[1] In addition, he graded these IVDs into morphological healthy IVDs (no bulging and herniation) and diseased IVDs (bulging or herniation). Diseased IVDs were excluded from statistical analysis.

A subset of 20 randomly selected volunteers was additionally scored to the Pfirrmann grade by a second radiologist (R.S.L., 11 years' experience in radiology) in order to assess the reproducibility of the visual scoring system.

gagCEST and WASSR images were motion-corrected using a diffeomorphic registration approach incorporated in the prototype software fMRLung (Siemens Healthcare).[17,18]

For the analysis of the gagCEST effect an in-house developed MatLab software (MathWorks, Natick, MA, R2012b) was used. As the first step of data processing, an in-plane 3×3 Gaussian filter was applied on each CEST and WASSR image to reduce image noise. To correct the effect of B_0 field inhomogeneity the WASSR maximum symmetry algorithm was used for calculating a frequency offset map.[16] This map was applied to correct acquired CEST curves. The corrected CEST curves divided by the reference signal S_0 are further referred to as Z-spectrum $Z(\omega)$. Based on these data, the magnetization transfer asymmetry ratio (MTR_{asym}) was determined according to $MTR_{asym}(\Delta\omega) = Z(-\Delta\omega) - Z(\Delta\omega)$, where $\Delta\omega$ is the specified frequency shift difference. GagCEST maps were determined using the average MTR_{asym} value in the offset range from 0.9–1.9 ppm comprising the frequency range of resonance signals of GAG hydroxyl protons.[6]

A region of interest (ROI)-based analysis was performed for evaluation of gagCEST values of the nucleus pulposus (NP) and the annulus fibrosus (AF) analog to the method used by Haneder et al.[3] The average size of the ROIs was 38 ± 15 pixels (NP) and 26 ± 11 pixels (AF). The ROIs were drawn by an experienced radiologist (C.S., 4 years of experience). He was blinded to other sequences and to the age of the participants. Mean values and standard deviations were calculated for each ROI.

Statistical Analysis

We compared the means of the gagCEST values for different age groups using a one-way analysis of variance (ANOVA) and Tukey's honestly significant difference (HSD) post-hoc test. *P*-values below 0.05 were considered significant.

We performed correlation analysis for each Pfirrmann score including only IVDs without bulging and herniation using the Spearman correlation coefficient ρ.

A correlation between gagCEST effect and Pfirrmann score and between gagCEST effect and disc level was performed regardless of age.

To assess reproducibility between two gagCEST measurements of the same volunteer, a two-sided paired Student's *t*-test was performed. $P < 0.05$ was considered significant.

A kappa statistic was performed in order to assess the interobserver reliability of Pfirrmann grading.

Spearman correlation analysis between gagCEST effect and age within discs with Pfirrmann grade 2 was additionally performed for each radiologist.

Results

From a total of 350 investigated IVDs, 116 IVDs were excluded from statistical analysis due to bulging or herniation. The majority of IVDs (66%) were scored as Pfirrmann grade 2 (Table 3).

Complete interobserver agreement was achieved in 77%. A difference of one grade occurred in 23%. A difference of two grades and more was not obtained. The kappa coefficient κ for the interobserver agreement was moderate to substantial ($\kappa = 0.60$; $\Delta\kappa = 0.09$).

We observed a loss of gagCEST effect with age for Pfirrmann score 2 (Fig. 1).

As demonstrated in Fig. 2, gagCEST values of IVDs without bulging or herniation decreased significantly between age group 1 and 2 (NP: $MTR_{asym}(\text{group } 1) = 3.09 \pm 1.12$, $MTR_{asym}(\text{group } 2) = 2.40 \pm 1.51$, $P = 0.006$; AF: $MTR_{asym}(\text{group } 1) = 1.51 \pm 1.13$, $MTR_{asym}(\text{group2}) = 0.72 \pm 1.31$, $P = 0.001$;) and age group 2 and 3 (NP: $MTR_{asym}(\text{group } 3) = 1.15 \pm 1.37$, $P < 0.001$; AF: $MTR_{asym}(\text{group } 3) = -0.17 \pm 1.25$, $P < 0.001$). In contrast, we noted no significant differences of MTR_{asym} values between age groups 3 and 4 in NP and AF. A significant decrease of MTR_{asym}-values between age groups 4 and 5 was noted only in NP (NP: $MTR_{asym}(\text{group } 4) = 0.74 \pm 1.11$; $MTR_{asym}(\text{group } 5) = -0.24 \pm 1.36$, $P = 0.001$).

We obtained significant correlation between MTR_{asym} values and age in NP and AF only in case of Pfirrmann grades 2 and 3 (Table 4). Within the subset data of 20 volunteers, gagCEST values again decreased significantly with

TABLE 3. Number of IVDs with Pfirrmann Scores 1, 2, 3, 4, and 5

Age group	Number of IVDs with Pfirrmann score 1	Number of IVDs with Pfirrmann score 2	Number of IVDs with Pfirrmann score 3	Number of IVDs with Pfirrmann score 4	Number of IVDs with Pfirrmann score 5	Number of IVDs without bulging and herniation
1	20	39	3	0	0	62
2	5	43	1	1	0	50
3	1	40	3	3	0	47
4	0	21	18	5	0	44
5	0	11	10	10	0	31
1–5 (all age groups)	26	154	35	19	0	234

age for Pfirrmann grade 2 for both radiologists (Radiologist 1: $\rho = -0.629$, $P < 0.001$ in NP and $\rho = -0.572$, $P < 0.001$ in AF; Radiologist 2: $\rho = -0.537$, $P < 0.001$ in NP and $\rho = -0.537$, $P < 0.001$ in AF). Due to the small number of discs within Pfirrmann grades 1, 3, and 4 (between 6 and 11) no correlation analysis was performed for these grades.

The correlation between MTR_{asym} values and Pfirrmann score was $\rho = -0.649$ ($P < 0.001$) in NP and $\rho = -0.512$ ($P < 0.001$) in AF. The correlation between MTR_{asym} values and disc level was $\rho = 0.397$ ($P < 0.001$) in NP and $\rho = 0.256$ ($P < 0.001$) in AF, thus showing higher gagCEST effect in discs at a lower level.

Average MTR_{asym} values of these IVDs were not significantly different between the two measurements (measurement 1: $MTR_{asym}(NP) = 2.94 \pm 1.16$, $MTR_{asym}(AF) = 1.26 \pm 0.59$; measurement 2: $MTR_{asym}(NP) = 3.17 \pm 1.38$,

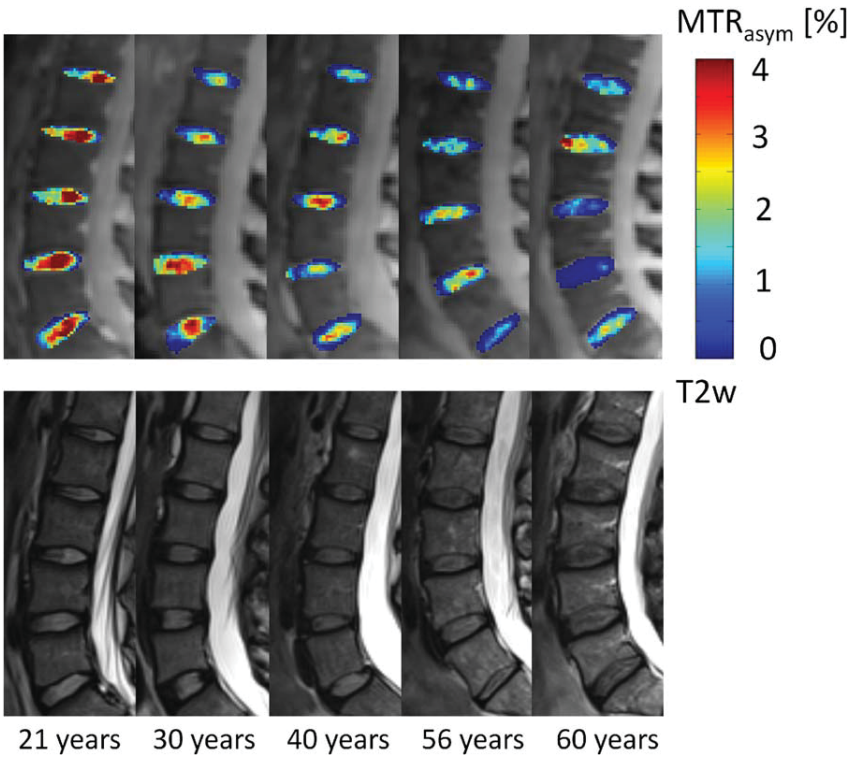

FIGURE 1: Decrease of gagCEST effect with aging in intervertebral discs. CEST images with overlaid MTR_{asym} color map representing the gagCEST effect and sagittal T_2-weighted images are shown in single subjects. Color coding indicates high glycosaminoglycan (GAG) content (red) to low GAG content (blue).

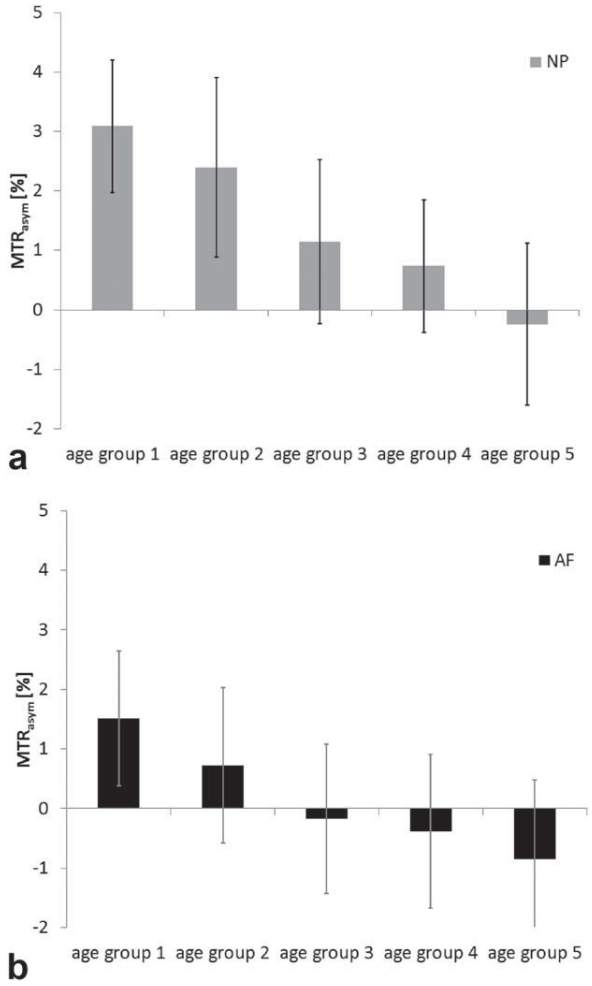

FIGURE 2: MTR_{asym} mean values and standard deviations in NP (a) and AF (b) for five different age groups. A significant decrease of gagCEST effect was obtained in all investigated regions between age groups 1 and 2 and age groups 2 and 3. The *P* for NP are $P = 0.006$ between age groups 1 and 2, $P < 0.001$ between age groups 2 and 3, $P = 0.120$ between age groups 3 and 4, and $P = 0.001$ between age groups 4 and 5. The *P* for AF are $P = 0.001$ between age groups 1 and 2, $P = 0.001$ between age groups 2 and 3, $P = 0.428$ between age groups 3 and 4, and $P = 0.130$ between age groups 4 and 5.

$MTR_{asym}(AF) = 1.71 \pm 1.10$; *P*-value(NP) = 0.22, *P*-value (AF) = 0.11).

Discussion

Our results support the concept of a loss of glycosaminoglycan content in intervertebral discs with age.

Based on the differences of gagCEST values within Pfirrmann grades 2 and 3, we suggest that gagCEST imaging might add information about degeneration even in the absence of bulging or herniation in IVDs. Therefore, gagCEST imaging may be a potential research tool to investigate IVD pathologies related to early cartilage degeneration or damage. We assume that changes of gagCEST effect for Pfirrmann scores 2 and 3 might be caused by biochemical changes with aging, which might be smaller for Pfirrmann scores 1 and 4. Our data suggest that age-matched analyses or age-correction may possibly be necessary in gagCEST studies on normal-appearing intervertebral discs.

A decrease of gagCEST effect has been reported to be related to proteoglycan depletion.[9] Furthermore, there is literature on the correlation of gagCEST effect with glycosaminoglycan concentration.[19] Cartilage degeneration is associated with a loss of aggrecan, which is a large proteoglycan possessing numerous glycosaminoglycan chains.[20] Aggrecan content has been reported to decline with aging due to proteolysis.[20] Taken together, the observed loss of gagCEST effect with age may be explained by a loss of glycosaminoglycans due to physiological IVD degeneration and proteolysis in the aging discs. This finding is consistent with data acquired by Haneder et al[3] and Liu et al,[21] which show a decrease of gagCEST effect with anatomical disc degeneration. Our study is limited by a lack of knowledge of the true glycosaminoglycan content, which might be assessed by histological samples only. Histological proofs were not performed due to ethical considerations. However, the gagCEST technique is an established method for the assessment of glycosaminoglycan content.[9,19]

Next to gagCEST imaging, further biochemical imaging techniques including sodium imaging and dGEMRIC allow for the assessment of glycosaminoglycan content.[22–27] Further, a relation between glycosaminoglycan content and degenerative or symptomatic intervertebral discs has been reported for these techniques.[22,25] Our gagCEST results are consistent with these findings. Of the number of potentially available biochemical MRI techniques, gagCEST imaging is outstanding since no contrast or special MR hardware is necessary. Nevertheless, comparative studies are needed on different biochemical MRI methods for the assessment of glycosaminoglycan content in human intervertebral discs.

In our study, we used the same B_1 amplitude averaged over time as reported by Haneder et al.[3] However, different field strengths have been used previously for gagCEST imaging (Liu et al: 0.8 μT, Saar et al: 1.8 μT, Kim et al: 1.5 μT in phantoms and 0.75 μT in IVDs).[9,19,21] The B_1 amplitude

TABLE 4. Spearman Correlation Analysis Between MTR_{asym} Values and Age.

	NP		AF	
Pfirrmann Score	ρ	***P*-value**	ρ	***P*-value**
1	−0.046	0.824	0.059	0.773
2	−0.558	< 0.001	−0.473	< 0.001
3	−0.337	0.048	−0.393	0.020
4	−0.316	0.188	−0.050	0.838

could have an influence on both, the gagCEST asymmetry as well as the spillover effect. We do not use higher B_1-amplitudes in order to keep the specific absorption rate (SAR) reasonably low and to avoid higher spillover effects.

The gagCEST effect is considered sensitive to changes in pH value, which has been established in an ex vivo porcine model.[28] CEST imaging using the contrast agent iopamidol is a recently developed MRI technique that enables in vivo pH determination using a ratiometric approach.[29,30] The present study is limited by the lack of pH assessment in order to avoid the application of contrast agent. The CEST effect of iopamidol might influence the gagCEST effect due to competing CEST effects, possibly interfering with GAG content assessment.

We obtained a more negative gagCEST effect in the AF with aging. In addition, negative MTR_{asym} values were obtained in NP in older volunteers. This might have several reasons. Z-spectrum analysis might be affected by the NOE-effect, which is positioned at -1 ppm in the Z-spectrum,[9] and thus on the opposite site than the resonance frequency of the –OH groups of glycosaminoglycans. Other explanations are alterations of Z-spectra due to changes in pH value or artifacts due to low signal intensity in the S_0-image (image without presaturation) of CEST data.

One limitation of this study is the large standard deviation obtained for the MTR_{asym} values of each age group. This might be caused by a variation of MTR_{asym} values in dependence on disc level. The standard deviation might be additionally influenced by factors like B_0 and B_1 field inhomogeneity, a low signal in the CEST image S_0 without presaturation, or a high spillover effect. Although B_0 field inhomogeneity correction was performed, no correction for B_1 field inhomogeneity was used in our study. Therefore, development of an improved gagCEST method including B_1 field inhomogeneity correction would be advantageous.

A further limitation is that MTR_{asym} only correlates with concentration of glycosaminoglycans. Therefore, a determination of the GAG concentration is not possible. In addition, MTR_{asym} may differ for different choices of presaturation pulses. Therefore, caution should be exercised when comparing MTR_{asym} values measured with different CEST sequence designs.

The interobserver reliability in Pfirrmann grading was moderate to substantial. In addition, we obtained a similar dependence between gagCEST effect and age exemplary for Pfirrmann grade 2. However, differences in Pfirrmann grading might influence the obtained relation between gagCEST effect and age for each Pfirrmann grade. Therefore, supplementary quantitative T_2 imaging might be advantageous for future gagCEST studies.

In the future, the gagCEST method might be used in order to detect changes due to degeneration early or to start early clinical treatment. If the gagCEST effect is applied in clinical routine, a comparison to reference MTR_{asym} values for the same age is necessary.

In summary, our findings indicate a significant relation between glycosaminoglycan content and aging in healthy human intervertebral discs in volunteers without low back pain. Differences in glycosaminoglycan content with age can be found with the gagCEST technique even in the absence of morphological changes.

References

1. Pfirrmann CW, Metzdorf A, Zanetti M, Hodler J, Boos N. Magnetic resonance classification of lumbar intervertebral disc degeneration. Spine 2001;26:1873–1878.
2. Schmitt B, Zbýò Š, Stelzeneder D, et al. Cartilage quality assessment by using glycosaminoglycan chemical exchange saturation transfer and 23Na MR imaging at 7 T. Radiology 2011;260:257–264.
3. Haneder S, Apprich SR, Schmitt B, et al. Assessment of glycosaminoglycan content in intervertebral discs using chemical exchange saturation transfer at 3.0 Tesla: preliminary results in patients with low-back pain. Eur Radiol 2013;23:861–868.
4. Trattnig S, Marlovits S, Gebetsroither S, et al. Three-dimensional delayed gadolinium-enhanced MRI of cartilage (dGEMRIC) for in vivo evaluation of reparative cartilage after matrix-associated autologous chondrocyte transplantation at 3.0T: Preliminary results. J Magn Reson Imaging JMRI 2007;26:974–982.
5. Tiderius CJ, Sandin J, Svensson J, Dahlberg LE, Jacobsson L. Knee cartilage quality assessed with dGEMRIC in rheumatoid arthritis patients before and after treatment with a TNF inhibitor. Acta Radiol 1987 2010;51:1034–1037.
6. Ling W, Regatte RR, Navon G, Jerschow A. Assessment of glycosaminoglycan concentration in vivo by chemical exchange-dependent saturation transfer (gagCEST). Proc Natl Acad Sci U S A 2008;105:2266–2270.
7. Blumenkrantz G, Li X, Han ET, et al. A feasibility study of in vivo T1rho imaging of the intervertebral disc. Magn Reson Imaging 2006; 24:1001–1007.
8. Eyre DR, Muir H. Quantitative analysis of types I and II collagens in human intervertebral discs at various ages. Biochim Biophys Acta 1977;492:29–42.
9. Saar G, Zhang B, Ling W, Regatte RR, Navon G, Jerschow A. Assessment of glycosaminoglycan concentration changes in the intervertebral disc via chemical exchange saturation transfer. NMR Biomed 2012;25:255–261.
10. Urban JP, McMullin JF. Swelling pressure of the intervertebral disc: influence of proteoglycan and collagen contents. Biorheology 1985; 22:145–157.
11. Lyons G, Eisenstein SM, Sweet MB. Biochemical changes in intervertebral disc degeneration. Biochim Biophys Acta 1981;673: 443–453.
12. Miese F, Buchbender C, Scherer A, et al. Molecular imaging of cartilage damage of finger joints in early rheumatoid arthritis with delayed gadolinium-enhanced magnetic resonance imaging. Arthritis Rheum 2012;64:394–399.
13. Insko EK, Clayton DB, Elliott MA. In vivo sodium MR imaging of the intervertebral disk at 4 T. Acad Radiol 2002;9:800–804.
14. Stelzeneder D, Welsch GH, Kovács BK, et al. Quantitative T2 evaluation at 3.0T compared to morphological grading of the lumbar intervertebral disc: a standardized evaluation approach in patients with low back pain. Eur J Radiol 2012;81:324–330.
15. Trattnig S, Stelzeneder D, Goed S, et al. Lumbar intervertebral disc abnormalities: comparison of quantitative T2 mapping with conventional MR at 3.0 T. Eur Radiol 2010;20:2715–2722.

16. Kim M, Gillen J, Landman BA, Zhou J, van Zijl PCM. Water saturation shift referencing (WASSR) for chemical exchange saturation transfer (CEST) experiments. Magn Reson Med 2009;61:1441–1450.

17. Chefd'Hotel C, Hermosillo G, Faugeras O. A variational approach to multi-modal image matching. In: Proc IEEE Workshop Var Level Set Methods VLSM01. Washington, DC: IEEE Computer Society; 2001:21 [VLSM '01].

18. Hermosillo G, Chefd'hotel C, Faugeras O. Variational methods for multimodal image matching. Int J Comput Vis 2002;50:329–343.

19. Kim M, Chan Q, Anthony M-P, Cheung KMC, Samartzis D, Khong P-L. Assessment of glycosaminoglycan distribution in human lumbar intervertebral discs using chemical exchange saturation transfer at 3 T: feasibility and initial experience. NMR Biomed 2011;24:1137–1144.

20. Sivan SS, Wachtel E, Roughley P. Structure, function, aging and turnover of aggrecan in the intervertebral disc. Biochim Biophys Acta 2014;1840:3181–3189.

21. Liu Q, Jin N, Fan Z, et al. Reliable chemical exchange saturation transfer imaging of human lumbar intervertebral discs using reduced-field-of-view turbo spin echo at 3.0T. NMR Biomed 2013;26:1672–1679.

22. Vaga S, Raimondi MT, Caiani EG, et al. Quantitative assessment of intervertebral disc glycosaminoglycan distribution by gadolinium-enhanced MRI in orthopedic patients. Magn Reson Med 2008;59:85–95.

23. Ciavarro C, Caiani EG, Brayda-Bruno M, et al. Mid-term evaluation of the effects of dynamic neutralization system on lumbar intervertebral discs using quantitative molecular MR imaging. J Magn Reson Imaging JMRI 2012;35:1145–1151.

24. Vaga S, Brayda-Bruno M, Perona F, et al. Molecular MR imaging for the evaluation of the effect of dynamic stabilization on lumbar intervertebral discs. Eur Spine J 2009;18(Suppl 1):40–48.

25. Wang C, McArdle E, Fenty M, et al. Validation of sodium magnetic resonance imaging of intervertebral disc. Spine 2010;35:505–510.

26. Noebauer-Huhmann I-M, Juras V, Pfirrmann CWA, et al. Sodium MR imaging of the lumbar intervertebral disk at 7 T: correlation with T2 mapping and modified Pfirrmann score at 3 T—preliminary results. Radiology 2012;265:555–564.

27. Stelzeneder D, Trattnig S. [Biochemical magnetic resonance imaging of intervertebral discs and facet joints.] Radiology 2010;50:1115–1119.

28. Melkus G, Grabau M, Karampinos DC, Majumdar S. Ex vivo porcine model to measure pH dependence of chemical exchange saturation transfer effect of glycosaminoglycan in the intervertebral disc. Magn Reson Med 2014;71:1743–1749.

29. Longo DL, Busato A, Lanzardo S, Antico F, Aime S. Imaging the pH evolution of an acute kidney injury model by means of iopamidol, a MRI-CEST pH-responsive contrast agent. Magn Reson Med 2013;70:859–864.

30. Müller-Lutz A, Khalil N, Schmitt B, et al. Pilot study of Iopamidol-based quantitative pH imaging on a clinical 3T MR scanner. Magma 2014 [Epub ahead of print].

Magnetic Resonance Imaging 34 (2016) 271–275

Contents lists available at ScienceDirect

Magnetic Resonance Imaging

journal homepage: www.mrijournal.com

Original contribution

Gender, BMI and T2 dependencies of glycosaminoglycan chemical exchange saturation transfer in intervertebral discs

Anja Müller-Lutz [a], Christoph Schleich [a,*], Benjamin Schmitt [b], Gerald Antoch [a], Felix Matuschke [a], Michael Quentin [a], Hans-Jörg Wittsack [a], Falk Miese [a]

[a] University Dusseldorf, Medical Faculty, Department of Diagnostic and Interventional Radiology, D-40225 Dusseldorf, Germany
[b] Siemens Ltd. Australia, Healthcare Sector, 160 Herring Road, Macquarie Park NSW 2113, Australia

ARTICLE INFO

Article history:
Received 12 August 2015
Revised 26 October 2015
Accepted 26 October 2015

Keywords:
Chemical exchange saturation transfer (CEST)
Glycosaminoglycan content
Intervertebral disc
Gender
Body mass index
T2 value

ABSTRACT

Purpose: The purpose was to investigate the dependence of glycosaminoglycan chemical exchange saturation transfer (gagCEST) effect of lumbar intervertebral discs (IVD) on gender, body mass index and T2 value.

Methods: T2 imaging and gagCEST imaging was performed in 34 healthy volunteers (17 males, 17 females) without low back pain at a 3 T MRI system (Magnetom Trio, A Tim System, Siemens Healthcare, Erlangen, Germany). The body mass index was determined for each volunteer. The mean and standard deviation of MTR_{asym} and T2 values were calculated for nucleus pulposus (NP) and annulus fibrosus (AF) as descriptive statistics for females and males. An unpaired student's t-test was applied in order to validate obtained differences. Pearson correlation was determined in order to reveal, if gagCEST effect and T2 values decrease with increasing body mass index (BMI). Pearson correlation analysis was additionally performed between gagCEST and T2 values.

Results: GagCEST effect and T2 values were significantly higher in females compared to males [gagCEST effect (nucleus pulposus, females) = 3.58 ± 1.49 %; gagCEST effect (nucleus pulosus, males) = 3.01 ± 1.63 %, p-value (gagCEST effect, nucleus pulposus) = 0.02); T2 (nucleus pulposus, females) = 134.56 ± 30.27 ms, T2 (nucleus pulposus, males) = 122.35 ± 27.64 ms, p-value (T2, nucleus pulposus) = 0.01)]. Pearson correlation analysis showed a significant negative relation between BMI and gagCEST effect (nucleus pulposus: $\rho = -0.16$, $p = 0.03$) and between BMI and T2 values (nucleus pulposus: $\rho = -0.30$, $p < 0.01$). The correlation between gagCEST effect and T2-values was highly significant (nucleus pulposus: $\rho = 0.59$, $p < 0.01$).

Conclusions: Significantly lower gagCEST effects were found in males compared to females and with increased body mass index. The gagCEST effect was highly correlated with quantitative T2 imaging.

1. Introduction

Glycosaminoglycan loss is an early step in the degeneration process of intervertebral discs (IVDs) and is associated with low back pain (LBP) [1–4]. Glycosaminoglycan chemical exchange saturation transfer (gagCEST) imaging is a non-invasive magnetic resonance (MR) method to assess glycosaminoglycan concentration and which does not need contrast agent or specific hardware [5].

CEST imaging is based on the exchange between solute protons and water protons [6]. If a radiofrequency pulse is applied at the Larmor frequency of the solute proton pool, protons in this pool are excited. The magnetization of solute protons is transferred to the water pool due to chemical exchange. If a long radiofrequency pulse is applied, this exchange process is repeated resulting in a reduction of magnetization of the water pool. During CEST imaging, a so-called Z-spectrum is acquired by applying radiofrequency pulses at different frequency offsets in relation to the Larmor frequency of the water pool. The CEST effect is then determined by an asymmetry analysis of the Z-spectrum.

gagCEST imaging in lumbar intervertebral discs was applied previously in patients with low back pain (LBP) showing a reduced gagCEST effect in discs with morphological degeneration [2]. In addition, a reduced gagCEST effect was reported in patients with spondyloarthritis compared to healthy volunteers [7]. Recently, age-dependency of the gagCEST effect was reported in healthy volunteers of different age [8]. To the best of our knowledge, the

* Corresponding author at: University Dusseldorf, Department of Diagnostic and Interventional Radiology, Moorenstr. 5, D-40225 Düsseldorf, Germany. Tel.: +49 211 81 17752; fax: +49 211 81 16299.
E-mail address: Christoph.Schleich@med.uni-duesseldorf.de (C. Schleich).

http://dx.doi.org/10.1016/j.mri.2015.10.024
0730-725X/

Table 1
Detailed sequence parameters.

		T2-weighted imaging (sagittal)	T2-weighted imaging (transversal)	T2 mapping	CEST	WASSR
TE	[ms]	105.0	113.0	9.1, 18.2, 27.3, 36.4, 45.5, 54.6, 63.7, 72.8, 81.9, 91.0	3.9	3.9
TR	[ms]	3100.0	4510.0	800.0	1760	442.0
Field of view	[mm^2]	300 × 300	300 × 240	300 × 300	300 × 300	300 × 300
Voxel size	[mm^2]	1.2 × 1.2	0.8 × 0.6	1.6 × 1.6	1.6 × 1.6	1.6 × 1.6
Slice thickness	[mm]	3.0	3.0	5.0	5.0	5.0
Flip angle	[°]	160	140	180	12	12
Duration	[min:sec]	3:39	5:13	4:23	9:09	3:43
Averages		2	1	3	2	2
Basic resolution		256 × 256	384 × 307	192 × 192	192 × 192	192 × 192
Number of slices		15	27	1	1	1

dependence of gagCEST effect on other patient properties like gender and body mass index has not been investigated yet.

In a previous study, the gagCEST technique was compared with T2 mapping in the knee of sixty-nine subjects [9]. The authors showed that high gagCEST values were accompanied by high T2-values [9]. T2 mapping and gagCEST imaging has also been applied by Haneder et al. in LBP patients resulting in a weak correlation between gagCEST effect and T2 relaxation time [2].

Several studies have reported an association between body mass index (BMI) and intervertebral disc (IVD) degeneration [10–15]. Further, changes in gagCEST values and T2 values have been reported with IVD degeneration [2,16]. Therefore, we hypothesized a reduced gagCEST effect and T2 values with increased BMI.

In the current study we used gagCEST imaging in young healthy volunteers to investigate the dependence of gagCEST effect on gender. Furthermore, we tested for a correlation between the gagCEST effect and the body mass index. Finally, we aim to validate if gagCEST effect is correlated with T2-value in lumbar intervertebral discs of healthy volunteers.

2. Materials and methods

2.1. Study population

Imaging was performed in 34 volunteers without low back pain (17 females (mean age 26 ± 5 years; minimum age: 21 years; maximum age: 39 years) and 17 males (mean age 26 ± 4 years; minimum age: 20 years; maximum age: 35 years)). Before MR examination, weight and body height were recorded. The study was approved by the local ethics committee and written informed consent was received from all volunteers before enrolment.

2.2. MR measurements

MR experiments were performed on a whole-body 3 T MR system (Magnetom Trio, A Tim System, Siemens Healthcare, Erlangen, Germany) using a spine matrix coil. Our MR protocol included a localizer, T2-weighted imaging in sagittal and transversal direction, a sequence for quantitative T2-mapping, prototype gagCEST and WASSR (Water Saturation Shift Referencing [17]) sequences. Sequence details of T2-weighted imaging, quantitative T2 imaging, CEST, and WASSR are listed in Table 1.

Biochemical imaging was performed using the gagCEST and WASSR sequences. These were composed of a saturation module and a segmented 2D RF-spoiled gradient echo module.

The parameters of the CEST and WASSR saturation module are described elsewhere in detail [7,8,18]. For both gagCEST and WASSR measurements a saturation band was applied anterior to the spine in order to suppress bowel movement artifacts and artifacts due to abdominal wall motion [7,8,18].

2.3. Data analysis

T2-weighted images were analysed to reveal the presence or absence of herniation. The body mass index was calculated for each volunteer following the standard approach: mass/$height^2$.

WASSR and CEST data were analysed as follows: After motion correction using a diffeomorphic registration approach [19] and field inhomogeneity correction [8,17], Z-spectra and corresponding MTR_{asym}

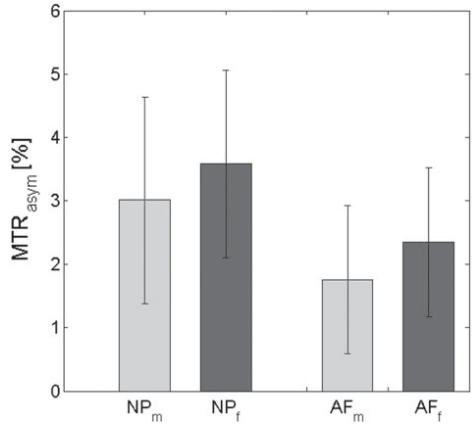

Fig. 1. Magnetization transfer ratio asymmetry (MTR_{asym}) as descriptive parameter for the CEST effect in nucleus pulposus (NP) and annulus fibrosus (AF) in males (m) and females (f).

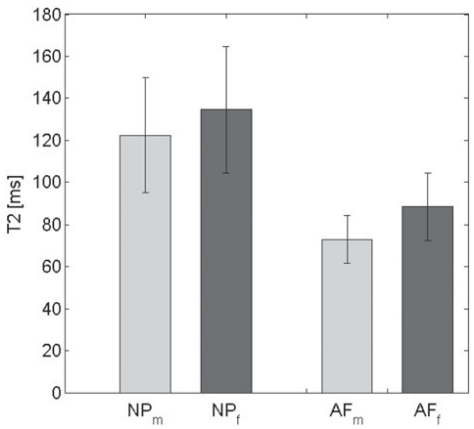

Fig. 2. Transverse relaxation time T2 in nucleus pulposus (NP) and annulus fibrosus (AF) in males (m) and females (f).

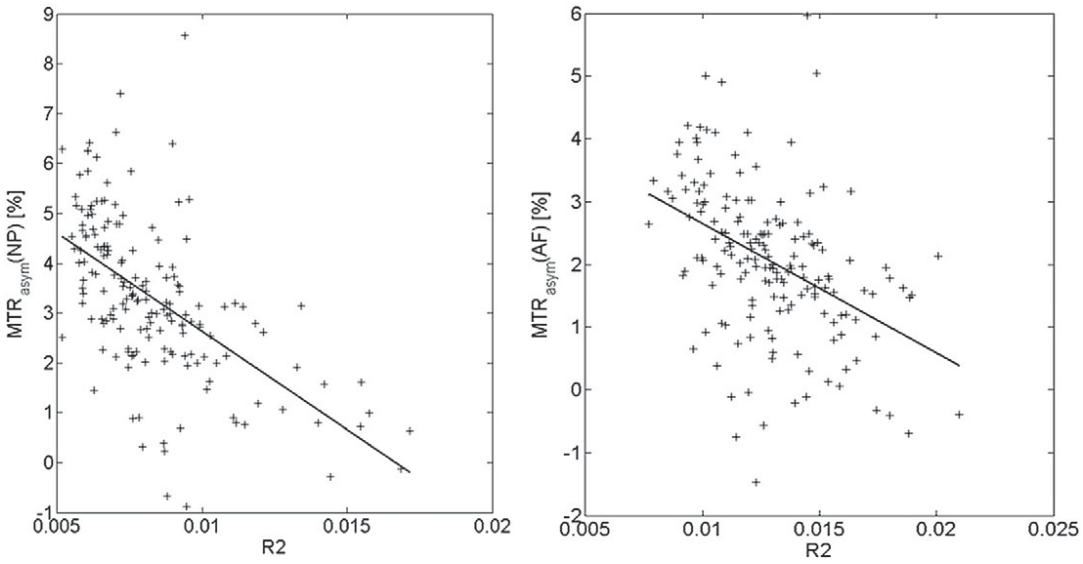

Fig. 3. MTR_{asym} versus R2 = 1/T2 values in NP (left) and AF (right).

curves were determined. MTR_{asym} maps were determined in the irradiation frequency offset range from 0.9 to 1.9 ppm. Nucleus pulposus (NP) and annulus fibrosus (AF) were segmented using in-house-developed MATLAB software based on Bayes classification [7]. The mean and standard deviation of MTR_{asym} were determined for each NP and AF of the lumbar intervertebral disc. T2 values were determined by a fit to the signal at different echo times.

2.4. Statistical analysis

MATLAB (MathWorks, Natick, MA, R2012b) was used for statistical analysis. The mean and standard deviation of MTR_{asym} and T2 values were calculated for NP and AF as descriptive statistics for females and males. Kolmogorov–Smirnov test was applied to verify normal distribution of MTR_{asym} and T2 values over all volunteers, for females and for males in NP and AF. An unpaired student's t-test was applied in order to validate obtained differences. P-values below 0.05 were considered to be significant. Univariate analysis of variance (ANOVA) was applied in order to detect, if there are differences of MTR_{asym} values or T2 values dependent on disc location. Pearson correlation was determined in order to reveal, if gagCEST effect and T2 values decrease with increasing body mass index (BMI). Pearson correlation analysis was additionally performed between gagCEST and T2 values.

3. Results

All MRI measurements were technically successful. No herniations were seen in all healthy volunteers. The number of discs without herniation and protrusion was 72 in males and 79 in females; the number of discs with protrusion was 13 in males and 6 in females.

The average BMI was 24.6 ± 4.4 kg/m^2.

Kolmogorov–Smirnov test verified normal distribution of MTR_{asym} and T2 values over all volunteers, for males and for females.

MTR_{asym} and T2 values were significantly higher in females compared to males in NP and AF (MTR_{asym}(NP, females) = 3.58 ± 1.49 %; MTR_{asym}(NP, males) = 3.01 ± 1.63 %, p-value(MTR_{asym}(NP)) = 0.02; MTR_{asym}(AF, females) = 2.35 ± 1.18 %, MTR_{asym}(AF, males) = 1.75 ±

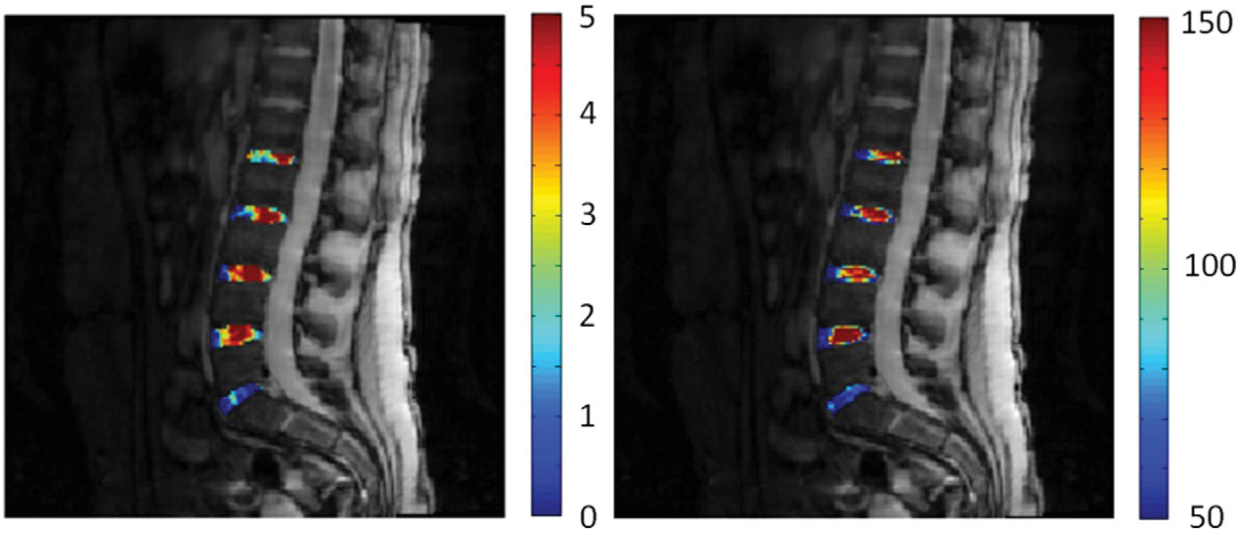

Fig. 4. MTR_{asym} [%] (left) and T2 [ms] (right) map overlaid with anatomical images in lumbar intervertebral discs. In this case, the lowest disc (L5/S1) has lower T2 and MTR_{asym} values compared to higher discs. T2 values and MTR_{asym} values are positively correlated.

1.18 %, p-value(MTR_{asym}(AF)) < 0.01; T2(NP, females) = 134.56 ± 30.27 ms, T2(NP, males) = 122.35 ± 27.64 ms, p-value(NP) = 0.01; T2(AF, females) = 88.51 ± 16.04 ms, T2(AF, males) = 72.92 ± 11.41 ms, p-value(AF) < 0.01) (Figs. 1, 2).

Univariate analysis of variance (ANOVA) revealed no significant difference of MTR_{asym} and T2-values for lumbar discs dependent on their location. Pearson correlation analysis showed a negative relation between BMI and MTR_{asym} values (NP: $\rho = -0.16$, $p = 0.03$; AF: $\rho = -0.13$, $p = 0.09$) and between BMI and T2 values (NP: $\rho = -0.30$, $p < 0.01$; AF: $\rho = -0.29$, $p < 0.01$). In NP, this correlation was significant. In AF, the correlation was only significant between BMI and T2-values.

The correlation between gagCEST effect and T2-values was highly significant (NP: $\rho = 0.59$, $p < 0.01$; AF: $\rho = 0.44$, $p < 0.01$) (Fig. 3). The dependence between gagCEST effect and T2-value is additionally presented in one exemplary volunteer with disc protrusion on disc level L5/S1 (Fig. 4). This disc showed reduced MTR_{asym} and T2-values compared to other discs.

4. Discussion

We showed that the gagCEST effect represented by the asymmetric magnetization transfer ratio (MTR_{asym}) analysis of the Z-spectrum after field inhomogeneity correction is significantly higher in females compared to males. The gagCEST effect decreased significantly with the body mass index. The gagCEST effect is correlated with quantitative T2 evaluation. Females showed significantly higher T2 values compared to males. No differences in MTR_{asym} values were noted between discs at different locations.

The differences in MTR_{asym} values between males and females might be caused by the higher percentage of discs with protrusion in men (15 %) compared to females (7 %) in our volunteer cohort. Discs with protrusion were included in order to keep the mean age over all discs in females and males equal.

The body mass index correlates negatively with T2 values and gagCEST effect. This might indicate a higher degree of degeneration due to overweight. This assumption might be substantiated by the findings of Teraguchi et al. who reported a relation between obesity and disc degeneration using the Pfirrmann scoring system [20,21].

A correlation between gagCEST imaging and T2 mapping was previously reported by Rehnitz et al [9] in the knee. One possible explanation is that the gagCEST effect at 3 T might not only depend on the concentration of glycosaminoglycans, but also on the T2-values of the intervertebral discs [9], which reflects water content and collagen architectural order. An alternative explanation is that glycosaminoglycans are important for the maintenance of fluid content [3,7], so that higher GAG concentrations may be associated with higher water content, which leads to increased T2 values.

In our study, no differences of gagCEST effect were obtained in dependence on disc location. In literature, different findings were obtained. Kim et al. revealed a trend of decreasing gagCEST values from upper to lower discs investigating the discs L3/L4, L4/L5 and L5/S1 [22]. In contrast to our study with 34 volunteers, only twelve volunteers were included in their study. A further difference is that we investigated a younger population (mean age: 26 years; age range: 20–39 years) compared to Kim et al. (mean age: 30 years; age range: 25–53 years) [22]. This might lead to an increased degree of degeneration, especially at lower disc heights due to weight bearing. In addition, our studies are different in regard to the CEST presaturation module.

In a recent study, a correlation between gagCEST effect and age was reported [8]. Our data indicated that both T2 values and MTR_{asym} values also depend on gender. In order to define standard values, a study including a high number of patients should be conducted in the future. In addition, an improvement of the gagCEST method to enable quantitative analysis of glycosaminoglycans might be desirable. A major difficulty might be the fast exchange rate of the hydroxyl group of glycosaminoglycans as well as the presence of high spill-over effect, nuclear overhauser effect, magnetization transfer effect and the CEST effect of the NH-group of glycosaminoglycans.

One limitation of this study is the absence of intervertebral disc biopsy in order to determine the water content and glycosaminoglycan concentration. A histological analysis might reveal, why T2 values and gagCEST effect are correlated. Due to ethical considerations, biopsies were not realized in our study.

A further limitation is that we performed our measurements in 2D in order to decrease image acquisition time. However, 3D gagCEST measurements have been applied previously [2]. Compromises have to be made between data acquisition time, number of measurements at different frequency offsets, additional acquisition of data for water saturation shift referencing, number of signal averages and duration of CEST presaturation module.

In conclusion, significantly lower gagCEST effects were found in males compared to females and with increased body mass index. The gagCEST effect was highly correlated with quantitative T2 imaging. Future studies might reveal if the reduced gagCEST effect with reduced T2 values is caused by a loss of glycosaminoglycans or by a T2-shine-through effect.

References

[1] Cheung KM, Karppinen J, Chan D, Ho DW, Song YQ, Sham P, et al. Prevalence and pattern of lumbar magnetic resonance imaging changes in a population study of one thousand forty-three individuals. Spine (Phila Pa 1976) 2009;34:934–40.
[2] Haneder S, Apprich SR, Schmitt B, Michaely HJ, Schoenberg SO, Friedrich KM, et al. Assessment of glycosaminoglycan content in intervertebral discs using chemical exchange saturation transfer at 3.0 Tesla: preliminary results in patients with low-back pain. Eur Radiol 2013;23:861–8.
[3] Urban JP, Winlove CP. Pathophysiology of the intervertebral disc and the challenges for MRI. J Magn Reson Imaging 2007;25:419–32.
[4] Wu N, Liu H, Chen J, Zhao L, Zuo W, Ming Y, et al. Comparison of apparent diffusion coefficient and T2 relaxation time variation patterns in assessment of age and disc level related intervertebral disc changes. PLoS One 2013;8 [e69052].
[5] Saar G, Zhang B, Ling W, Regatte RR, Navon G, Jerschow A. Assessment of glycosaminoglycan concentration changes in the intervertebral disc via chemical exchange saturation transfer. NMR Biomed 2012;25:255–61.
[6] Ward KM, Aletras AH, Balaban RS. A new class of contrast agents for MRI based on proton chemical exchange dependent saturation transfer (CEST). J Magn Reson 2000;143:79–87.
[7] Schleich C, Müller-Lutz A, Matuschke F, Sewerin P, Sengewein R, Schmitt B, et al. Glycosaminoglycan chemical exchange saturation transfer of lumbar intervertebral discs in patients with spondyloarthritis. J Magn Reson Imaging 2015;42(4):1057–63.
[8] Müller-Lutz A, Schleich C, Pentang G, Schmitt B, Lanzman RS, Matuschke F, et al. Age-dependency of glycosaminoglycan content in lumbar discs: a 3 t gagcEST study. J Magn Reson Imaging 2015.
[9] Rehnitz C, Kupfer J, Streich NA, Burkholder I, Schmitt B, Lauer L, et al. Comparison of biochemical cartilage imaging techniques at 3 T MRI. Osteoarthritis Cartilage 2014;22:1732–42.
[10] Hagiwara H, Shibata H, Sakakibara H, Inoue T. Magnetic resonance imaging evaluation of L5-s1 intervertebral disc degeneration in Japanese women. Asian Spine J 2014;8:581–90.
[11] Law T, Anthony MP, Chan Q, Samartzis D, Kim M, Cheung KM, et al. Ultrashort time-to-echo MRI of the cartilaginous endplate: technique and association with intervertebral disc degeneration. J Med Imaging Radiat Oncol 2013;57:427–34.
[12] Samartzis D, Karppinen J, Mok F, Fong DY, Luk KD, Cheung KM. A population-based study of juvenile disc degeneration and its association with overweight and obesity, low back pain, and diminished functional status. J Bone Joint Surg Am 2011;93:662–70.
[13] Samartzis D, Karppinen J, Chan D, Luk KD, Cheung KM. The association of lumbar intervertebral disc degeneration on magnetic resonance imaging with body mass index in overweight and obese adults: a population-based study. Arthritis Rheum 2012;64:1488–96.
[14] Hangai M, Kaneoka K, Kuno S, Hinotsu S, Sakane M, Mamizuka N, et al. Factors associated with lumbar intervertebral disc degeneration in the elderly. Spine J 2008;8:732–40.
[15] Liuke M, Solovieva S, Lamminen A, Luoma K, Leino-Arjas P, Luukkonen R, et al. Disc degeneration of the lumbar spine in relation to overweight. Int J Obes (Lond) 2005;29:903–8.

[16] Wang YX, Zhao F, Griffith JF, Mok GS, Leung JC, Ahuja AT, et al. T1rho and T2 relaxation times for lumbar disc degeneration: an in vivo comparative study at 3.0-Tesla MRI. Eur Radiol 2013;23:228–34.
[17] Kim M, Gillen J, Landman BA, Zhou J, van Zijl PC. Water saturation shift referencing (WASSR) for chemical exchange saturation transfer (CEST) experiments. Magn Reson Med 2009;61:1441–50.
[18] Müller-Lutz A, Schleich C, Schmitt B, Topgöz M, Pentang G, Antoch G, et al. Improvement of gagCEST imaging in the human lumbar intervertebral disc by motion correction. Skeletal Radiol 2015;44(4):505–11.
[19] Hermosillo G, Chefd'Hotel C, Faugeras O. Variational methods for multimodal image matching. Int J Comput Vis 2002;50:329–43.
[20] Pfirrmann CW, Metzdorf A, Zanetti M, Hodler J, Boos N. Magnetic resonance classification of lumbar intervertebral disc degeneration. Spine (Phila Pa 1976) 2001;26:1873–8.
[21] Teraguchi M, Yoshimura N, Hashizume H, Muraki S, Yamada H, Minamide A, et al. Prevalence and distribution of intervertebral disc degeneration over the entire spine in a population-based cohort: the Wakayama Spine Study. Osteoarthritis Cartilage 2014;22:104–10.
[22] Kim M, Chan Q, Anthony MP, Cheung KM, Samartzis D, Khong PL. Assessment of glycosaminoglycan distribution in human lumbar intervertebral discs using chemical exchange saturation transfer at 3 T: feasibility and initial experience. NMR Biomed 2011;24:1137–44.

Skeletal Radiol (2016) 45:79–85
DOI 10.1007/s00256-015-2251-0

SCIENTIFIC ARTICLE

Biochemical imaging of cervical intervertebral discs with glycosaminoglycan chemical exchange saturation transfer magnetic resonance imaging: feasibility and initial results

Christoph Schleich[1] · Anja Müller-Lutz[1] · Lisa Zimmermann[1] · Johannes Boos[1] · Benjamin Schmitt[2] · Hans-Jörg Wittsack[1] · Gerald Antoch[1] · Falk Miese[1]

Received: 5 May 2015 / Revised: 2 September 2015 / Accepted: 7 September 2015 / Published online: 16 September 2015

Abstract
Objective To evaluate glycosaminoglycan chemical exchange saturation transfer (gagCEST) imaging at 3T in the assessment of the GAG content of cervical IVDs in healthy volunteers.
Materials and Methods Forty-two cervical intervertebral discs of seven healthy volunteers (four females, three males; mean age: 21.4±1.4 years; range: 19–24 years) were examined at a 3T MRI scanner in this prospective study. The MRI protocol comprised standard morphological, sagittal T2 weighted (T2w) images to assess the magnetic resonance imaging (MRI) based grading system for cervical intervertebral disc degeneration (IVD) and biochemical imaging with gagCEST to calculate a region-of-interest analysis of nucleus pulposus (NP) and annulus fibrosus (AF).
Results GagCEST of cervical IVDs was technically successful at 3T with significant higher gagCEST values in NP compared to AF (1.17 %±1.03 % vs. 0.79 %±1.75 %; $p=0.005$). We found topological differences of gagCEST values of the cervical spine with significant higher gagCEST effects in lower IVDs ($r=1$; $p=0$). We could demonstrate a significant, negative correlation between gagCEST values and cervical disc degeneration of NP ($r=-0.360$; $p=0.019$). Non-degenerated IVDs had significantly higher gagCEST effects compared to degenerated IVDs in NP (1.76 %±0.92 % vs. 0.52 %± 1.17 %; $p<0.001$).
Conclusion Biochemical imaging of cervical IVDs is feasible at 3T. GagCEST analysis demonstrated a topological GAG distribution of the cervical spine. The depletion of GAG in the NP with increasing level of morphological degeneration can be assessed using gagCEST imaging.

Keywords Chemical exchange saturation transfer · Glycosaminoglycan · Cervical intervertebral discs · Magnetic resonance imaging

Christoph Schleich and Anja Müller-Lutz have contributed equally.

✉ Anja Müller-Lutz
Anja.Lutz@med.uni-duesseldorf.de

[1] University Dusseldorf, Medical Faculty, Department of Diagnostic and Interventional Radiology, 40225 Dusseldorf, Germany

[2] Siemens Ltd. Australia, Healthcare Sector, 160 Herring Road, Macquarie Park, NSW 2113, Australia

Introduction

Neck pain is a common symptom in humans [1] and often occurs in combination with intervertebral disc (IVD) degeneration [2]. The pathophysiology of IVD degeneration is not yet completely understood, the most researchers assume a multifactorial origin such as environmental factors, physiological consequences of aging or correlation with mechanical loading [3].

Morphological magnetic resonance imaging (MRI) is a well established and the most sensitive method for the clinical assessment of IVD degeneration [4]. Degenerative changes of the disc are characterized by a decrease of the water content, which can be morphologically visualized by T2-weighted images in MRI [5, 6].

A semi-quantitative, five-point-Likert-classification system (grade 1–5) for the assessment of cervical disc degeneration was presented by Miyazaki et al. according to nucleus signal intensity, nucleus structure, distinction between nucleus pulposus and annulus fibrosus, and disc height in midsagittal T2-weighted images with classification of severe degenerated cervical IVDs in grades 4 or 5 [7]. Although this classification system showed a very good intra- and interobserver reliability, it did not provide

reliable quantification of the changes in the early stages of IVD degeneration which are characterized by a loss of glycosaminoglycans (GAG) or water in a morphologically intact disc [8].

To quantify the biochemical changes that develop during the early stages of IVD degeneration, a more sensitive technique is needed. Glycosaminoglycan chemical exchange saturation transfer (gagCEST) is a novel technique which facilitates visualization and quantification of GAGs in joint cartilage or IVDs [9, 10].

The different parts of the human IVD, annulus fibrosus (AF) and nucleus pulposus (NP), vary substantially in the content of the two main macromolecular components, collagen and aggrecan [11]. Aggrecan is a large proteoglycan attached with approximately 100 GAG side chains [12]. The proteoglycan content is about 50 % in the NP and 10–20 % in the AF [13], whereas the distribution of collagen is the opposite with 20–30 % in the NP and 70 % in the AF [14]. GAGs are important to maintain IVD tissue fluid content and a deficit is associated with the development of degenerative disc disease [12]. With gagCEST, it is possible to acquire molecule-specific saturation information on bulk water protons for the indirect detection of glycosaminoglycans in IVDs [15].

To the best of our knowledge, the measurement of GAG content with gagCEST of cervical IVDs has not yet been investigated adequately to date. Our hypothesis was that gagCEST of cervical IVDs is feasible and the GAG content of cervical IVDs is decreased in MRI-morphologically degenerated discs compared to MRI-morphologically healthy discs.

Materials and methods

Study population

The study was approved by the local ethics committee. Written informed consent was obtained from all volunteers for this prospective study. Seven healthy volunteers (four females, three males; mean age 21.4±1.4 years; range: 19–24 years) without neck pain, overweight or previous surgery of the cervical spine were prospectively enrolled in this study.

MR hardware and sequence protocol

All volunteers were examined in supine position using a clinical whole-body 3T MR system (Magnetom Trio, A Tim System, Siemens Healthcare, Erlangen, Germany). Signal reception was performed using a 12-channel head coil, a dedicated neck coil and a spine-matrix coil. Our MR sequence protocol included a localizer, a T2-weighted sequence in sagittal orientation and the prototype gagCEST (glycosaminoglycan chemical exchange saturation transfer) and WASSR (water saturation shift referencing) sequences. WASSR and CEST sequences were composed of a presaturation module and a segmented 2D RF-spoiled gradient echo module. Detailed parameters are provided in Table 1. Figure 1 shows an example of biochemical gagCEST imaging and morphological T2w image of the cervical spine.

Parameters of the sagittal T2-weighted turbo spin echo (TSE) sequence were: number of slices=12, TE/TR=111 ms/4870 ms, slice thickness=3 mm, in-plane resolution=0.8×0.8 mm^2, flip angle=140°, field of view=150×150 mm^2, number of excitations (NEX)=2, number of echoes per slice=25, a basic resolution of 192×192 and acquisition time of 1 min and 15 s.

One radiologist, blinded to the gagCEST values, with 4 years of experience in musculoskeletal radiology scored all cervical intervertebral discs according to the Miyazaki scoring system [7]. The scoring system is based on a five-steps Likert scale with grade 1 and 2 for non-degenerative discs and grade 3–5 for degenerative IVDs according to nucleus signal intensity, nucleus structure, distinction between nucleus pulposus and annulus fibrosus, and disc height in midsagittal T2-weighted images. To analyze degenerated from non-degenerated discs, we divided the IVDs into two, pooled groups: group A is composed of IVDs with Miyazaki score 1 or 2, group B is composed of IVDs with Miyazaki score 3 to 5.

WASSR and CEST images were motion-corrected using a diffeomorphic registration approach incorporated in the prototype software fMRLung (Siemens Healthcare, Erlangen, Germany) [10, 16]. The following data analysis was performed with an in-house-developed MATLAB software (The Mathworks, Inc., Natick, MA, USA, R2012b). A reduction of image noise was performed using an in-plane 3×3 Gaussian filter. B0 field inhomogeneities were corrected using the WASSR maximum symmetry algorithm [17]. The offset-corrected CEST-curves divided by the signal without CEST presaturation S0 are defined as $Z(\omega)$. The magnetisation transfer asymmetry was defined as $MTR_{asym}(\Delta\omega)=Z(-\Delta\omega)-Z(\Delta\omega)$, where $\Delta\omega$ is the specified frequency shift difference. The evaluation of glycosaminoglycan CEST effect was determined using the MTR_{asym} value in the frequency range $\Delta\omega$ from 1.1 to 1.5 ppm, which comprises the chemical exchange resonances of GAG hydroxyl protons.

A region-of-interest analysis was performed for MTR_{asym} evaluation of the nucleus pulposus (NP) and annulus fibrosus (AF) using an in-house developed IVD segmentation (MATLAB software; The Mathworks, Inc., Natick, MA, USA, R2012b). All cervical IVDs were detected automatically. The disc segmentation was based on Bayes-classification to divide bone and ligament from disc tissue of the cervical spine. The defined ROIs were

Table 1 Detailed sequence parameters for the prototype gagCEST and WASSR sequence

		WASSR	CEST
2D RF-spoiled GRE module			
T_E/T_R	ms/ms	5.56/575	5.56/1990
In-plane resolution	mm^2	0.8×0.8	0.8×0.8
Basic resolution		256×256	256×256
Slice thickness	mm	5	5
Flip angle	°	12	12
Field of view	mm^2	150×150	150×150
Duration	min:sec	10:40	17:36
NEX (number of excitations)		2	2
Presaturation module			
Number of measured frequency offsets		42	26
Maximum frequency offset $\Delta\omega_{max}$	ppm	1	4
B1-CWAE	μT	1.5	0.3
Number of CEST presaturation pulses		1	8
PD/IPD	ms/ms	100/6	100/100

divided into NP (the innermost 60 % of the IVD) and AF (the remaining region of the IVD), as reported in the preceding studies [18–20].

Mean and standard deviation of MTR_{asym} were determined. Additionally, mean MTR_{asym} values of NP and AF were analyzed according to significant difference; furthermore, we appropriated NP- and AF-MTR_{asym} values to calculate significant differences between group 1 (non-degenerative discs) and group 2 (degenerative discs). Statistical significance was evaluated using a two-tailed student's t-test. Spearman correlation analysis was performed between MTR_{asym} values and the morphological grading, as well as the corresponding disc location. *p*-values below 0.05 were considered to be significant.

Results

All measurements were technically successful and there were no drop outs. A total of 42 IVDs were analyzed. One IVD was scored Miyazaki score 1, 21 IVDs were graded Miyazaki 2, 18 IVDs were scored Miyazaki score 3, two IVDs were graded Miyazaki 4 and no IVDs were scored Miyazaki score 5. The mean gagCEST values of NP were significantly higher

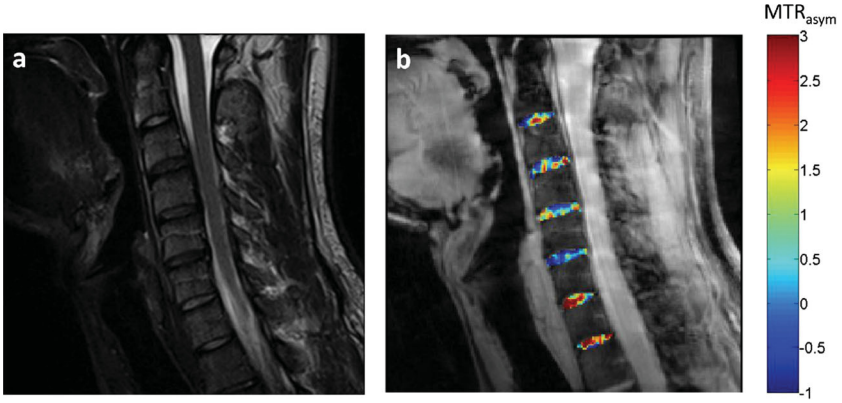

Fig. 1 Morphological T2w image and gagCEST imaging of the cervical spine. **a** Picture represents morphological T2-weighted images for Miyazaki classification. The cervical spine was scored according to Miyazaki classification: grade 2 for C2/3, grade 3 for C3/4, grade 3 for C4/5, grade 3 for C5/6, grade 2 for C6/7 and grade 2 for C7/Th1. **b** Picture demonstrates sagittal T2-weighted images with an overlaid MTR_{asym} color map illustrating the corresponding gagCEST effect of the cervical IVDs. *Color coding* indicates high glycosaminoglycan (GAG) content in *red* to low GAG content in *blue*. We found significantly lower gagCEST values in degenerative discs compared with non-degenerative discs. Additionally, higher GAG values could be demonstrated in lower located cervical IVDs

Table 2 Detailed summary of the 42 analyzed *IVDs* with morphological grading according to Miyazaki and colleagues, number of IVDs, percentage of total IVDs, mean MTR_{asym} values of *NP* and *AF* in % and *p-value* of the comparison between NP and AF

Miyazaki grading	No. of IVDs	Percentage of total IVDs	Mean MTR_{asym} [%]		NP vs. AF
			NP	AF	*p*-value
1	1	2.38	0.88±0.00	0.03±0.00	–
2	21	50.00	1.74±0.94	1.15±1.01	0.006
3	18	42.86	0.45±1.21	0.34±1.49	0.523
4	2	4.76	1.16±0.01	1.02±0.63	0.806
Pooled 1/2	22	52.38	1.76±0.92	1.14±0.99	0.003
Pooled 3/4	20	47.62	0.52±1.17	0.40±1.43	0.473

compared to AF (1.17 %±1.03 % vs. 0.79 %±1.75 %; p=0.005). The descriptive statistic is summarized in Table 2.

GagCEST values compared with morphological grading

Morphological grading of cervical IVDs was performed according to the five-steps scoring system of Miyazaki and colleagues with grade 1 and 2 of non-degenerated discs and grade 3–5 of degenerated discs. MTR_{asym} values of NP were significantly higher in non-degenerated discs compared to degenerated discs (1.76 %±0.92 % vs. 0.52±1.17; p<0.001; Fig. 2). In the AF, there was a borderline significant difference between non-degenerated discs compared with degenerated discs (1.14 %±0.99 % vs. 0.40±1.14; p<0.1; Fig. 2).

There was a significant, negative correlation between mean gagCEST values and morphological grading in the NP (r=−0,360; p=0.019). In non-degenerated cervical IVDs (Miyazaki grade 1/2), significantly higher mean MTR_{asym} values were found in the NP compared with the AF (1.76 %±0.92 % vs. 1.14 %±0.99 %; p=0.003), but there were non-significant differences between these two components in degenerated IVDs (Miyazaki grade 3/4; 0.52 %±1.17 % vs. 0.40 %±1.43 %; p=0.473).

Topological distribution of gagCEST along the cervical spine

We found higher gagCEST values in the lower cervical IVDs compared with higher located discs in the NP (r=1; p<0.001). In the AF, there was a positive, borderline significant trend towards higher MTR_{asym} values in lower located cervical IVDs (r=0.771; p<0.1) (Fig. 3; Table 3).

Reproducibility calculation

For the intra-subject reproducibility, two of the seven volunteers (one female, one male) were examined twice. The two examinations were acquired consecutively, between the measurements the volunteers were moved out of the MRI scanner and were positioned again. We built an average of the gagCEST effect of NP and AF and compared the two data sets. Between both measurements no significant differences of NP- and AF-gagCEST effects were seen (p=0.436).

Discussion

Biochemical changes are considered as the early manifestations of IVD degeneration [21]. GAGs were identified as playing a central role in the degenerative processes of IVDs [12]. Disc degeneration seems to associated with the incapacity of disc cells to maintain a highly hydrated proteoglycan-rich matrix in the NP to which GAGs are bound [22]. The

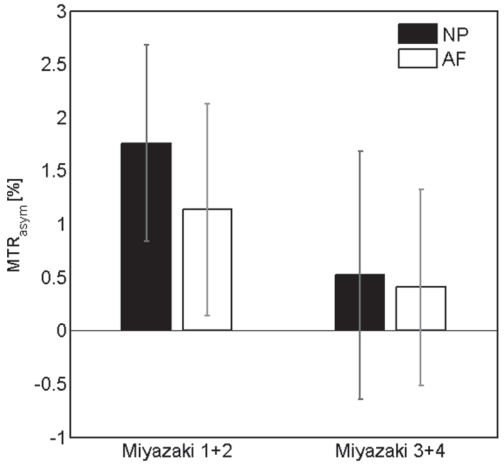

Fig. 2 Pooled MTR_{asym} of non-degenerative cervical discs compared with degenerative cervical discs. Pooled MTR_{asym} of non-degenerative cervical discs (Miyazaki score 1 and 2) revealed significantly higher gagCEST values compared with degenerative cervical discs (Miyazaki score 3 and 4) for *NP* (1.76 %±0.92 % vs. 0.52±1.17; p<0.001). For *AF*, no significant difference between non-degenerative and degenerative discs could be detected (1.14 %±0.99 % vs. 0.40±1.14; p=0.065). Negative MTR_{asym} values may be explained by side effects such as the nuclear Overhauser effect and the magnetization transfer effect

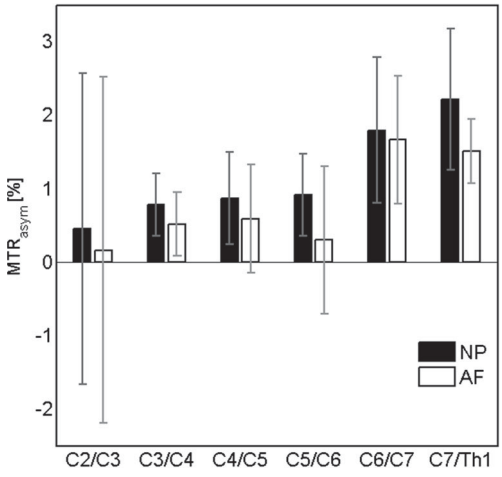

Fig. 3 GAG distribution of different localizations of the cervical spine. GAG distribution of different localizations of the cervical spine. The MTR_{asym} values of *NP* were significantly higher in lower located discs ($r=1$; $p<0.001$). For *AF*, we found a positive but not significant trend towards higher GAG content in lower located cervical discs ($r=0.771$; $p=0.072$). Negative MTR_{asym} values may be explained by side effects such as the nuclear Overhauser effect and the magnetization transfer effect

complete details of the complex and multifaceted disc degeneration process is not yet understood [8].

Feasibility studies report on successful differentiation of degenerative and non-degenerative IVDs with gagCEST [11, 23]. The CEST dataset consists of several images acquired with presaturation impulses at different offset frequencies around the water resonance, and one reference image without saturation. The normalized signal as a function of the presaturation offset (z-spectrum) can then be utilized to determine and quantify the CEST effect according to the MTR_{asym} values with respect to the water resonance due to the −OH protons of GAG appearing in a frequency range of 0.9 −1.9 ppm from the water resonance. The magnitude of the measured MTR_{asym} values correlates directly with the underlying concentration of GAG [24].

In our young, healthy collective, 47 % (20/42 discs) of the analyzed cervical IVDs showed morphological disc changes. IVD degeneration is known to be common among asymptomatic patients and is prevalent in cervical discs of young, healthy adults [8, 25]. As expected from histological analyses and previous imaging studies [13, 15] demonstrating higher GAG content in NP compared with AF, the gagCEST content in the non-degenerated NP (Miyazaki grade 1/2) was significantly higher than for AF; however, in degenerated cervical IVDs (Miyazaki grade 3/4) the gagCEST effects for NP and AF were not significantly different. The diminished difference between NP and AF in degenerated discs as a result of reduced gagCEST signal may indicate a loss of GAG compared with healthy IVDs, which supports the concept of GAG loss in degenerative IVDs [11, 12]. Especially in the NP, we could demonstrate a significant GAG depletion in degenerated discs (Miyazaki grade 3/4) compared with non-degenerated discs (Miyazaki grade 1/2). These findings are corroborated by published data identifying changes in the GAG content in the NP as one of the central points in early IVD degeneration [11, 26]. In the AF, we found a borderline significant difference between degenerated and non-degenerated cervical discs, which may be due to the a priori low GAG content of the AF [13] and the small sample size in this study. These results indicated that the NP may be the appropriate compartment of cervical IVDs to detect early disc alterations. The significant correlation between gagCEST values and morphological grading supported that it may be possible to distinguish degenerated from non-degenerated cervical IVDs with gagCEST, which had been demonstrated for lumbar IVDs in the literature [11].

Additionally, we assumed a topological distribution of higher GAG content in lower located cervical IVDs. Sowa et al. were able to demonstrate higher T2 signals in lower located cervical discs. The authors believed that this reflects an increasing water and proteoglycan content in the lower cervical IVDs to resist the stronger mechanical load in this part of the spine [8, 27].

Our study had some limitations. The main limitation of this study was the restricted number of volunteers participating in cervical gagCEST imaging. With our analysis, we could demonstrate that gagCEST of cervical IVDs was feasible at 3T, taking into account the assessment of GAGs in the cervical spine is much more challenging compared with lumbar IVDs, due to motion artifacts caused by respiration or artery pulsation [28]. During postprocessing management, we established several techniques to achieve an optimal setting for GAG measurements by using magnetic field inhomogeneity (WASSR) or motion corrections (diffeomorphic registration algorithm). The current results seem to be promising for evaluating the initial results in a larger population. We believe that the strength of this study is the homogeneous, asymptomatic population of young adults. In further evaluations, patients with neck pain or neurological symptoms should be included. The absence of cartilage biopsies was a further limitation. Biopsies were not performed due to

Table 3 Mean gagCEST values in % of *NP* and *AF* among the cervical spine

Disc height	Mean MTR_{asym} values [%]	
	NP	AF
C2/C3	0.45±0.95	0.16±1.43
C3/C4	0.77±0.99	0.51±1.69
C4/C5	0.87±0.77	0.59±1.53
C5/C6	0.91±1.00	0.30±1.74
C6/C7	1.79±1.06	1.66±1.93
C7/Th1	2.21±1.42	1.50±2.18

ethical considerations; also we did not analyse gender and race effects in this study.

Additionally no consensus analysis by a second reader for gagCEST and morphological analysis according to Miyazaki was performed. For Miyazaki scoring, we think that this is a minor limitation because of the good intra- and interobserver agreement, given in the literature [7]. The gagCEST values for cervical IVDs were detected automatically with the algorithm described in the previous, making an inter-observer analysis obsolete. Our intra-observer calculation of gagCEST analysis revealed no significant differences between the two measurements of the same volunteer in two of the seven volunteers; thus, these data have to be confirmed in future studies.

In summary, gagCEST of cervical IVDs on a clinical 3 Tesla MRI system may be a powerful, non-invasive research tool to investigate early disc degeneration in future studies. GagCEST of non-degenerative IVDs demonstrated significantly higher GAG values compared with degenerative discs, especially in the NP. Supporting our findings, GAG content of NP was higher in non-degenerative discs compared with AF. In degenerative cervical IVDs, the characteristic difference of the GAG content between NP and AF disappeared. The topological distribution of gagCEST along the cervical spine demonstrated higher GAG content in lower cervical IVDs.

Conflict of interest The authors declare that there is no conflict of interest.

References

1. Hanvold TN, Veiersted KB, Waersted M. A prospective study of neck, shoulder, and upper back pain among technical school students entering working life. J Adolesc Health. 2010;46(5):488–94.
2. Williams FM, Sambrook PN. Neck and back pain and intervertebral disc degeneration: role of occupational factors. Best Pract Res Clin Rheumatol. 2011;25(1):69–79.
3. Adams MA, Roughley PJ. What is intervertebral disc degeneration, and what causes it? Spine (Phila Pa 1976). 2006;31(18):2151–61.
4. Pfirrmann CW, Metzdorf A, Zanetti M, Hodler J, Boos N. Magnetic resonance classification of lumbar intervertebral disc degeneration. Spine (Phila Pa 1976). 2001;26(17):1873–8.
5. Weidenbaum M, Foster RJ, Best BA, Saed-Nejad F, Nickoloff E, Newhouse J, et al. Correlating magnetic resonance imaging with the biochemical content of the normal human intervertebral disc. J Orthop Res. 1992;10(4):552–61.
6. Panagiotacopulos ND, Pope MH, Krag MH, Block R. Water content in human intervertebral discs: part I, measurement by magnetic resonance imaging. Spine (Phila Pa 1976). 1987;12(9):912–7.
7. Miyazaki M, Hong SW, Yoon SH, Morishita Y, Wang JC. Reliability of a magnetic resonance imaging-based grading system for cervical intervertebral disc degeneration. J Spinal Disord Tech. 2008;21(4):288–92.
8. Chen C, Huang M, Han Z, Shao L, Xie Y, Wu J, et al. Quantitative T2 magnetic resonance imaging compared to morphological grading of the early cervical intervertebral disc degeneration: an evaluation approach in asymptomatic young adults. PLoS One. 2014;9(2):e87856.
9. Schmitt B, Zbýn S, Stelzeneder D, Jellus V, Paul D, Lauer L, et al. Cartilage quality assessment by using glycosaminoglycan chemical exchange saturation transfer and (23)Na MR imaging at 7 T. Radiology. 2011;260(1):257–64.
10. Müller-Lutz A, Schleich C, Schmitt B, Topgöz M, Pentang G, Antoch G, et al. Improvement of gagCEST imaging in the human lumbar intervertebral disc by motion correction. Skeletal Radiol. 2015;44(4):505–11.
11. Haneder S, Apprich SR, Schmitt B, Michaely HJ, Schoenberg SO, Friedrich KM, et al. Assessment of glycosaminoglycan content in intervertebral discs using chemical exchange saturation transfer at 3.0 Tesla: preliminary results in patients with low-back pain. Eur Radiol. 2013;23(3):861–8.
12. Urban JP, Winlove CP. Pathophysiology of the intervertebral disc and the challenges for MRI. J Magn Reson Imaging. 2007;25(2):419–32.
13. Saar G, Zhang B, Ling W, Regatte RR, Navon G, Jerschow A. Assessment of glycosaminoglycan concentration changes in the intervertebral disc via chemical exchange saturation transfer. NMR Biomed. 2012;25(2):255–61.
14. Eyre DR, Muir H. Quantitative analysis of types I and II collagens in human intervertebral discs at various ages. Biochim Biophys Acta. 1977;492(1):29–42.
15. Kim M, Chan Q, Anthony MP, Cheung KM, Samartzis D, Khong PL. Assessment of glycosaminoglycan distribution in human lumbar intervertebral discs using chemical exchange saturation transfer at 3 T: feasibility and initial experience. NMR Biomed. 2011;24(9):1137–44.
16. Chefd'hotel C, Hermosillo G, Faugeras O. A variational approach to multi-modal image matching. Proceedings of the IEEE Workshop on Variational and Level Set Methods (VLSM'01). VLSM '01. Washington DC: IEEE Computer Society; 2001. p. 21.
17. Kim M, Gillen J, Landman BA, Zhou J, van Zijl PC. Water saturation shift referencing (WASSR) for chemical exchange saturation transfer (CEST) experiments. Magn Reson Med. 2009;61(6):1441–50.
18. Schleich C, Müller-Lutz A, Matuschke F, Sewerin P, Sengewein R, Schmitt B, et al. Glycosaminoglycan chemical exchange saturation transfer of lumbar intervertebral discs in patients with spondyloarthritis. J Magn Reson Imaging. 2015. doi:10.1002/jmri.24877.
19. Stelzeneder D, Welsch GH, Kovács BK, Goed S, Paternostro-Sluga T, Vlychou M, et al. Quantitative T2 evaluation at 3.0T compared to morphological grading of the lumbar intervertebral disc: a standardized evaluation approach in patients with low back pain. Eur J Radiol. 2012;81(2):324–30.
20. Trattnig S, Stelzeneder D, Goed S, Reissegger M, Mamisch TC, Paternostro-Sluga T, et al. Lumbar intervertebral disc abnormalities: comparison of quantitative T2 mapping with conventional MR at 3.0 T. Eur Radiol. 2010;20(11):2715–22.
21. Stelzeneder D, Messner A, Vlychou M, Welsch GH, Scheurecker G, Goed S, et al. Quantitative in vivo MRI evaluation of lumbar facet joints and intervertebral discs using axial T2 mapping. Eur Radiol. 2011;21(11):2388–95.
22. An HS, Anderson PA, Haughton VM, Iatridis JC, Kang JD, Lotz JC, et al. Introduction: disc degeneration—summary. Spine (Phila Pa 1976). 2004;29(23):2677–8.
23. Rehnitz C, Kupfer J, Streich NA, Burkholder I, Schmitt B, Lauer L, et al. Comparison of biochemical cartilage imaging techniques at 3 T MRI. Osteoarthr Cartil. 2014;22(10):1732–42.
24. Ling W, Regatte RR, Navon G, Jerschow A. Assessment of glycosaminoglycan concentration in vivo by chemical exchange-dependent saturation transfer (gagCEST). Proc Natl Acad Sci U S A. 2008;105(7):2266–70.
25. Siivola SM, Levoska S, Tervonen O, Ilkko E, Vanharanta H, Keinänen-Kiukaanniemi S. MRI changes of cervical spine in

asymptomatic and symptomatic young adults. Eur Spine J. 2002;11(4):358–63.
26. Urban JP, McMullin JF. Swelling pressure of the intervertebral disc: influence of proteoglycan and collagen contents. Biorheology. 1985;22(2):145–57.
27. Sowa G, Vadalà G, Studer R, Kompel J, Iucu C, Georgescu H, et al. Characterization of intervertebral disc aging: longitudinal analysis of a rabbit model by magnetic resonance imaging, histology, and gene expression. Spine (Phila Pa 1976). 2008;33(17):1821–8.
28. Figley CR, Yau D, Stroman PW. Attenuation of lower-thoracic, lumbar, and sacral spinal cord motion: implications for imaging human spinal cord structure and function. AJNR Am J Neuroradiol. 2008;29(8):1450–4.

Magnetic Resonance Materials in Physics, Biology and Medicine
https://doi.org/10.1007/s10334-020-00868-y

RESEARCH ARTICLE

Detection of early cartilage degeneration in the tibiotalar joint using 3 T gagCEST imaging: a feasibility study

Daniel B. Abrar[1] · Christoph Schleich[1] · Karl Ludger Radke[1] · Miriam Frenken[1] · Julia Stabinska[1] · Alexandra Ljimani[1] · Hans-Jörg Wittsack[1] · Gerald Antoch[1] · Bernd Bittersohl[2] · Tobias Hesper[2] · Sven Nebelung[1] · Anja Müller-Lutz[1]

Received: 31 March 2020 / Revised: 10 July 2020 / Accepted: 14 July 2020

Abstract

Objective To establish and optimize a stable 3 Tesla (T) glycosaminoglycan chemical exchange saturation transfer (gagCEST) imaging protocol for assessing the articular cartilage of the tibiotalar joint in healthy volunteers and patients after a sustained injury to the ankle.

Methods Using Bloch–McConnell simulations, we optimized the sequence protocol for a 3 T MRI scanner for maximum gagCEST effect size within a clinically feasible time frame of less than 07:30 min. This protocol was then used to analyze the gagCEST effect of the articular cartilage of the tibiotalar joint of 17 healthy volunteers and five patients with osteochondral lesions of the talus following ankle trauma. Reproducibility was tested with the intraclass correlation coefficient.

Results The mean magnetization transfer ratio asymmetry (MTR_{asym}), i.e., the gagCEST effect size, was significantly lower in patients than in healthy volunteers ($0.34 \pm 1.9\%$ vs. $1.49 \pm 0.11\%$; $p < 0.001$ [linear mixed model]). Intra- and inter-rater reproducibility was excellent with an average measure intraclass correlation coefficient (ICC) of 0.97 and a single measure ICC of 0.91 ($p < 0.01$).

Discussion In this feasibility study, pre-morphological tibiotalar joint cartilage damage was quantitatively assessable on the basis of the optimized 3 T gagCEST imaging protocol that allowed stable quantification gagCEST effect sizes across a wide range of health and disease in clinically feasible acquisition times.

Keywords Cartilage · Magnetic resonance imaging · Proteoglycans · Osteoarthritis · Molecular imaging

Introduction

To this day and age, several magnetic resonance imaging (MRI) techniques have emerged that go beyond mere morphological depiction of joint cartilage. Such compositional MRI techniques allow the detection of early degenerative changes of the articular cartilage, e.g., loss of proteoglycans, that precede morphological damage and hence are considered an early, and more importantly, reversible, stage of osteoarthritis (OA) [1]. Because of its proteoglycan-specifity, the gold-standard technique of compositional MRI of cartilage is delayed gadolinium-enhanced MRI of cartilage (dGEMRIC) [2, 3]. However, due to recent restrictions imposed on gadolinium-based contrast agents, alternative compositional MRI techniques that do not rely on the administration of contrast agents have received ever-increasing scientific and clinical attention [4]. Among these techniques, glycosaminoglycan chemical

Daniel B. Abrar and Christoph Schleich have contributed equally to this work.

Sven Nebelung and Anja Müller-Lutz have contributed equally to this work.

Electronic supplementary material The online version of this article (https://doi.org/10.1007/s10334-020-00868-y) contains supplementary material, which is available to authorized users.

✉ Daniel B. Abrar
DanielBenjamin.Abrar@med.uni-duesseldorf.de

[1] Department of Diagnostic and Interventional Radiology, Medical Faculty, University Hospital Düsseldorf, University Dusseldorf, Moorenstraße 5, 40225 Düsseldorf, Germany

[2] Department of Orthopedic and Trauma Surgery, Medical Faculty, Heinrich-Heine University Düsseldorf, Düsseldorf, Germany

Published online: 28 July 2020

exchange saturation transfer (gagCEST) imaging assesses the specific GAG content in human articular cartilage and its depletion, which is considered an early sign of cartilage degeneration [5].

GagCEST imaging is based upon the chemical exchange of water protons between GAG and bulk water molecules. To induce a CEST effect, solute protons are saturated by a frequency-specific radiofrequency (RF) pulse and then transferred to bulk water by chemical exchange, which consequently reduces its signal. The normalized signal can then be used to quantify the CEST effect at a GAG -specific frequency range of 0.9–1.9 ppm via analysis of the magnetization transfer ratio asymmetry (MTR_{asym}), which correlates with the GAG concentration [5, 6]. For additional details on the basic principles of CEST imaging, the interested reader is referred to earlier excellent reviews.[7, 8]. Several studies showed promising results using gagCEST imaging at the spine [9–12]. However, data on the joints of the lower extremity with substantially thinner cartilage are sparse. In 2016, our group demonstrated promising results for the application of gagCEST at the knee joint [13]. Kogan et al. applied gagCEST imaging on a 7 T MRI scanner to assess the ankle joint of healthy volunteers [14]. Even though these results were promising, gagCEST imaging of the ankle joint has not yet been established on a 3 T MRI scanner. To achieve a more widespread scientific and clinical adaptation of the technique, the clinical utility has to be demonstrated on a broader scale, which -given the limited availability of 7 T MRI scanners- necessitates the technique's implementation on more widely available 3 T MRI scanners.

Tibiotalar joint injuries are common [15]. Osteochondral lesions of the talus (OLT), defined as an injury of the cartilage layer and the underlying subchondral bone, are frequent injuries in active populations that can be seen in up to 73% of all traumatic ankle injuries [16]. OLTs may predispose the joint to premature OA and ought to be diagnosed in an early and reliable manner as a timely diagnosis is a pre-requisite for appropriate treatment [17].

The aim of this study was (a) to develop and optimize a gagCEST imaging protocol for the articular cartilage of the tibiotalar joint that is clinically feasible and fits into diagnostic workflows and (b) to apply this imaging protocol to a population of healthy volunteers and patients with OLT after an ankle injury to prove clinical utility and validity. We hypothesized that -based on the developed and optimized gagCEST imaging protocol- (a) imaging of the articular cartilage of the tibiotalar joint would be possible in a clinical population and in clinically feasible time frames and (b) patients after variable ankle injuries (representative of the patient population undergoing MRI diagnostics in the clinic) demonstrate lower gagCEST effects compared to healthy volunteers.

Methods

Simulations

In a first step, simulations using the two-pool (water and GAG (–OH and –NH) Bloch–McConnell equation [18, 19] and a customized script (implemented in MATLAB [R2018a, The MathWorks, MA, USA] and to be downloaded at https://github.com/cest-sources/BM_sim_fit/) [20] were applied for the optimization of a pulsed gagCEST sequence [20–22]. The equations were solved analytically [19]. Based on this script, the CEST effect was simulated without the application of a saturation pulse. The radiofrequency field strength B1, the pulse duration t_p and the number of CEST saturation pulses n_p were varied using a constant duty cycle (DC) of 0.5. To keep the specific absorption rate (SAR) within the safe range, local SAR was restricted accordingly. Therefore, the maximum pulse duration was secondarily restricted by ther scanner to a maximum of 300 ms. For water, simulations were performed with relaxation times as reported earlier, i.e., T1 = 1.2 s and T2 = 0.039 s and a concentration of 88 M [23, 24]. The following parameters were used for GAG-OH protons: exchange rate = 1000 Hz, concentration 0.3 M, T1 = 1 s, T2 = 0.01 s and chemical shift = 1 ppm, and for GAG-NH protons: exchange rate = 50 Hz, concentration = 0.1 M, T1 = 1 s, T2 = 0.01 s and chemical shift = 3.2 ppm [24, 25]. The different variations of the parameters used in the simulation are displayed in Table 1; output parameters were z-spectra and MTR_{asym} curves. For each parameter, the maximum MTR_{asym} value was analytically determined at a step size of 0.01, 0.02 and 0.05 ppm at frequency offsets of 0.9–1.9 ppm, 0.5–1.5 ppm and 1–1.5 ppm. The optimized protocol in terms of the largest gagCEST effect at a reasonable acquisition time was used for the subsequent in-vivo studies.

Table 1 Details of sequence parameters used for simulating each parameter's contribution to quantitatively assess GAG exchange processes based on Bloch–McConnell simulations

Experiment	n_p	t_p (ms)	B_1 [µT]
1	6	100	0.2; 0.4; 0.6; 0.8; 1.0; 1.2; 1.4
2	6	100; 200; 300	1.0
3	2; 4; 6; 8; 10; 12; 14	100	1.0

In each experiment, one of the three parameters (number of pulses n_p, pulse duration t_p, and radiofrequency-field strength B_1) was systematically varied

In-vivo study

Study population

19 healthy volunteers (mean age 23.0 ± 3.8, range 20–37 years, 11 males, 8 females) and six patients (mean age 31.7 ± 9.3, range 20–44 years, two males, four females) after earlier ankle injury were recruited from 06/2018 to 01/2019 via dedicated specialist consultations at our Department of Orthopedic and Trauma Surgery. The predefined inclusion criterion for patients was an isolated traumatic OLT lesion as diagnosed in earlier MRI studies. At the time of recruitment, patients were graded according to the Anderson modification of the Berndt and Harty classification and four patients had grade 1 and two patients grade 2b OLT lesions [15, 16]. Predefined exclusion criteria for healthy volunteers included all forms of primary or secondary OA of the ankle as well as other bone and joint disorders such as OLT, rheumatoid arthritis, avascular necrosis, gouty arthritis, septic arthritis, Paget disease or osteochondritis dissecans. Volunteers were also excluded if they had acute or chronic ankle pain or a history of serious trauma or surgery to the index ankle joint.

The MRI data sets of one patient and two healthy volunteers had to be excluded from image analysis due to excessive motion artifacts. The mean disease duration of patients was 22 ± 30 months (range 1–60 months). Written and informed consent was obtained from all patients before the initiation of the study. The study was approved by the local ethics committee (Ethical Committee of the University Hospital Düsseldorf, study number: 3980).

MRI studies

All imaging studies were performed on a 3 T MRI scanner (Magnetom Prisma, Siemens Healthineers, Erlangen, Germany) using a dedicated receive-only 16-channel foot–ankle coil (Foot/Ankle 16, Siemens Healthineers). Patients and volunteers were scanned in the supine position with a neutral ankle position of 90° dorsiflexion. Positioning aids, sandbags and medical tape were used to reduce motion artifacts.

The MRI protocol included standard morphological sequences, i.e., sagittal (sag) and coronal (cor) Proton Density-weighted (PDw) fat-saturated (fs) sequences, transversal (tra) T2-weighted turbo-spin echo (TSE), and cor T1-weighted TSE sequences. In addition to the actual gagCEST sequence as detailed below, water saturation shift referencing (WASSR), T1 mapping gradient echo (GE) and T2 multi-spin- echo (SE) mapping sequences with five different echo times (13.8, 27.6, 41.4, 55.2 and 69 ms) were acquired. Of note, the latter two sequences were only acquired in the healthy volunteers and not in the patients. GagCEST imaging was performed using a two-dimensional (2D) radiofrequency (RF)-spoiled GE sequence with a pulsed CEST pre-saturation module consisting of 8 Gaussian-shaped RF pulses with a duty cycle of 0.5. 26 images with pre-saturation pulses at different offset frequencies around the bulk water resonance were obtained. Among these images was one reference image with a frequency offset of 300 ppmThe maximum frequency offset (Δω) was 4 ppm with a step size of 0.33 ppm. In a fraction of the healthy volunteer cohort ($n = 10$, mean age 22.4 ± 1.8, range 20–25 years, seven males, three females) radiofrequency field strengths and pulse durations were systematically varied to optimize the protocol at the beginning of the study. More specifically, three different radiofrequency field strengths ($B_1 = 0.6$, 0.8 and 1.0 µT) and three different pulse durations ($t_p = 100$, 200 and 300 ms) were used. Based on the results of the simulations, i.e., the largest measured MTR_{asym} values, we used a radiofrequency field strength of $B_1 = 0.8$ and a pulse duration $t_p = 300$ ms in the remaining healthy volunteer and patient cohorts. For the WASSR sequence, 22 images with pre-saturation and a reduced radiofrequency field strength ($B_1 = 0.25$ µT) were obtained. The maximum frequency offset was decreased to $\Delta\omega = 1$ ppm with a step size of 0.1 ppm. For WASSR and CEST sequences, motion correction was applied. The acquisition time was 5:01 min for the CEST and 2:22 min for the WASSR sequence. The total acquisition times for the compositional MRI sequences were: 24:21 min for the initial 10 healthy volunteers (3 × 5:05 min CEST, 1 × 2:22 min WASSR, 6 × 1:14 min T1) and 7:27 min for the remaining 7 healthy volunteers and the 5 patients (1 × 5:05 min CEST and 1 × 2:22 min WASSR). The acquisition time for the morphological sequences was 18 min, resulting in a total scan time of 42:21 min for the initial 10 volunteers and 25:27 min for the consecutive 7 volunteers and the 5 patients.

Detailed parameters of the morphological and compositional sequences are given in Tables 2 and 3.

Image analysis

All images were independently analyzed by two radiologists (DBA, 3 years of training in musculoskeletal imaging; CS, 8 years of training in musculoskeletal imaging) who were blinded to the volunteers' or patients' data. First, all studies were read to determine the individual joint's overall status with a particular focus on the integrity of tibiotalar cartilage. Also, OLTs were -if present- classified according to Hepple et al. [26]. Second, using the unsaturated WASSR image, both readers independently identified the cartilage layers of the tibiotalar joint and quantified its biophysical properties in a standardized manner by placing an ellipsoid-shaped region-of-interest (ROI) in the median plane onto both cartilage layers at the central load-bearing region of the tibiotalar joint. Each ROI was placed distant to the tibial and talar bone cortex and the anterior and posterior joint

Table 2 Detailed sequence parameters of morphological MRI sequences

Imaging parameter	Sagittal fs PDw	Coronal fs PDw	Transversal T2w TSE	Coronal T1w TSE
FOV (mm)	160 × 160	160 × 160	160 × 160	160 × 160
Slice thickness (mm)	3	3	3	3
TE (ms)	40	40	78	17
TR (ms)	4000	4000	4600	700
Resolution (mm/pixel)	0.31 × 0.42	0.31 × 0.42	0.31 × 0.39	0.28 × 0.4
Flip angle (°)	150	150	150	140
Acquisition matrix	512 × 384	512 × 384	512 × 410	576 × 403

Field of view (FOV), slice thickness, echo time (TE), repetition time (TR), resolution, flip angle, and acquisition matrix are given for sagittal and coronal fat-saturated proton-density-weighted (fs PDw), transversal T2-weighted turbo spin echo (T2w TSE) and coronal T1-weighted TSE (T1w TSE) sequences

Table 3 Detailed sequence parameters of compositional MRI sequences

Imaging parameter	WASSR	gagCEST	T1 map	T2 map
FOV (mm)	160 × 160	160 × 160	160 × 160	160 × 160
Slice thickness (mm)	5	5	7	3 mm
TE (ms)	3.5	3.5	11	13.8/27.6, 41.4/55.2/69
TR (ms)	7.2	7.2	6000	1000
TI (ms)			25/50/100/500/1000/2000	
Resolution (mm/pixel)	0.6 × 0.6	0.6 × 0.6	0.6 × 0.6	0.4 × 0.4
Flip angle (°)	15	15	180	180
Pulsed CEST saturation module				
Frequency range (ppm – ppm)	− 1 to 1	− 3 to 3		
Number of Dynamic Scans	21 + 1	25 + 1 reference image		
Number of saturation pulses	1	8		
Pulse Duration t_p (ms)	54	300 (100, 200)		
Interpulse Duration (ms)	–	300		
B_1 amplitude (μT)	0.2	0.8 (0.6, 1.0)		

In healthy volunteers, pulse duration t_p and B_1 amplitude were evaluated at 100, 200, and 300 ms and at 0.6, 0.8, and 1.0 μT, respectively, while in patients, the following parameter settings were used: 300 ms and 0.8 μT

WASSR water saturation, *gagCEST* glycosaminoglycan chemical exchange saturation transfer imaging, *FOV* field of view, *TE* echo time, *TR* repetition time, *TI* inversion time

areas to reduce partial volume artifacts due to the presence of cortical bone and potentially excessive amounts of joint fluid (Fig. 1). The second reader repeated the ROI placement at a different time point to allow for the assessment of inter-rater reliability.

For the analysis of the MTR_{asym} curve, i.e., the CEST effect, we used an in-house script implemented in Matlab (MATLAB R2018a, The MathWorks, Inc., MA, USA). Prior to further evaluation, B_0 field inhomogeneities were corrected by the WASSR maximum-symmetry algorithm with the calculation of a pixel-wise frequency offset curve [27, 28]. These offset-corrected CEST-curves divided by the signal without pre-saturation (S_0) were defined as the so-called z-spectrum ($Z(\omega)$). The maximum frequency offset of each z-spectrum was $\Delta\omega = 3$ ppm. Next, we used the magnetization transfer asymmetry (MTR_{asym}) (defined as $MTR_{asym}(\Delta\omega) = Z(-\Delta\omega) - Z(\Delta\omega)$) for the evaluation of the gagCEST effect [29]. MTR_{asym} maps were calculated using the average value of MTR_{asym} in the GAG-specific range of $\Delta\omega = 0.9 - 1.9$ ppm [30]. In addition, the B_{0}- corrected and -normalized spectra were fitted using Lorentzian function analysis to account for the GAG-OH, GAG-NH, water pools at − 1 ppm, the nuclear Overhauser effect at − 1 and − 2.8 ppm and the magnetization transfer pool at − 2.43 ppm [31, 32]. In the following, the Lorentzian-fitted gagCEST effect is given as GAG-OH amplitude.

T1 and T2 relaxation times calculations in ten healthy volunteers were also performed in Matlab. In a pixel-wise manner, acquired data was fitted and calculated based on the following equations:

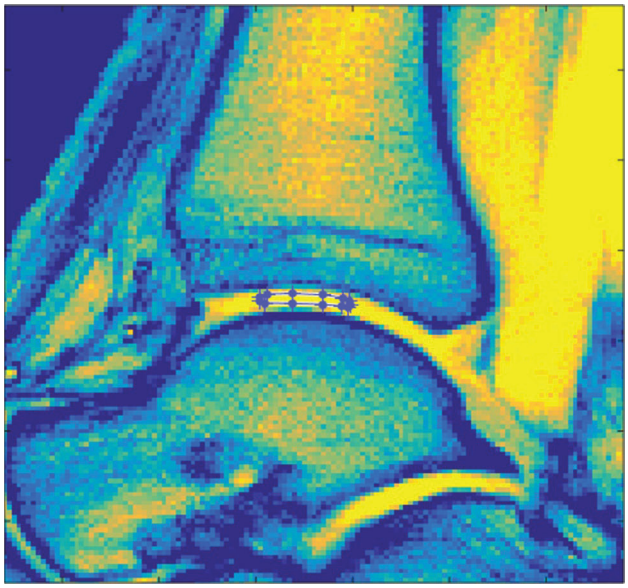

Fig. 1 Exemplary image detailing the region-of-interest (ROI) definition. Water saturation shift referencing sequence (WASSR) image of the tibiotalar joint of a 29-year-old healthy male. Manual definition of the ROI in the central weight-bearing region of the tibiotalar joint was performed individually by two radiologists to include the cartilage layers of the tibiotalar joints while reducing partial volume artifacts due to cortical bone and/or joint fluid

$$T1\colon M_z(t) = M_z^0 - \left(M_z^0 - M_z(0)\right) exp(\frac{-t}{T_1})$$

$$T2\colon M_{xy}(t) = M_{xy}(0) exp(\frac{-t}{T_2})$$

with T1 and T2 being the sought relaxation times, $M_z(t)$ the total magnetization in the z-direction, and $M_{xy}(t)$ the total magnetization in the xy-plane at time point t.

Statistical analysis

SPSS software (IBM, version 22, Armonk, NY, USA) was used for all statistical analyses by KLR and DBA. For descriptive analysis, mean gagCEST values ± standard deviation, median, and range (minimum–maximum) were calculated for healthy volunteers and patients. For optimization of the imaging protocol radiofrequency field strength and pulse duration were systematically varied and then compared using a multivariate analysis of variance (MANOVA) and a post-hoc Scheffé-test. For the comparison of gagCEST values between both cohorts, a multivariable statistical analysis was performed using a linear mixed model (LMM). The established model included a subject-specific random intercept, the factors healthy volunteer/patient, age, gender and the interaction of these factors assuming a fixed linear effect on the gagCEST values. Results of this model are given in Table 1 of the Supplementary Material. The LMM was fitted using a restricted maximum likelihood approach (REML). Based on this final model, the mean differences of gagCEST values were calculated and evaluated for significance. For correlation analyses of MTRasym values and GAG-OHamplitudes, Pearson's correlation was determined and quantified using the correlation coefficient r. Correlation strength was graded as suggested by Cohen [33]: small (0.1–0.3), moderate (0.3–0.5), and large (> 0.5). p values < 0.05 were considered significant. For the evaluation of inter- and intrarater reliability, single and average measure intraclass correlation coefficients (sICC and aICC) were calculated based on the ROIs drawn by the two raters.

Results

Simulations

The results of the systematic simulations are illustrated in Figs. 2 and 3.

a. Variation of t_p.
   Maximum MTRasym values were 1.33 % at 0.9–1.9 ppm with t_p = 200 ms, 1.07 % at 0.5–1.5 ppm with t_p = 100 ms and 1.37 % at 1.0–1.5 ppm with t_p = 100 ms (Fig. 3a).
b. Variation of n_p.
   The CEST effect increases with the number of applied saturation pulses (n_p) (Fig. 3b). Eight applied pulses reach 98% of the maximum gagCEST effect that could be obtained with 14 pulses at all ranges (0.9–1.9 ppm, 0.5–1.5 ppm and 1.0–1.5 ppm). Maximum MTR_{asym} values with eight applied pulses were 1.33 % at 0.9–1.9 ppm, 1.02 % at 0.5–1.5 ppm and 1.33 % at 1.0–1.5 ppm.
c. Variation of B_1.

The CEST effect increases with increasing B_1 until it reaches a maximum (Fig. 3c). Due to the spillover effect, MTR_{asym} values decrease beyond the maximum. Maximum MTR_{asym} values were 1.33 % at 0.9–1.9 ppm and a B_1 of 1 µT, 1.17 % at 0.5–1.5 ppm and a B_1 of 0.8 µT and 1.37 % at 1.0–1.5 ppm and a B_1 of 1 µT.

In-vivo studies

Morphological MRI of patients and healthy volunteers

Apart from the presence of OLTs as outlined below and a moderate joint effusion, the overall joint status of three of

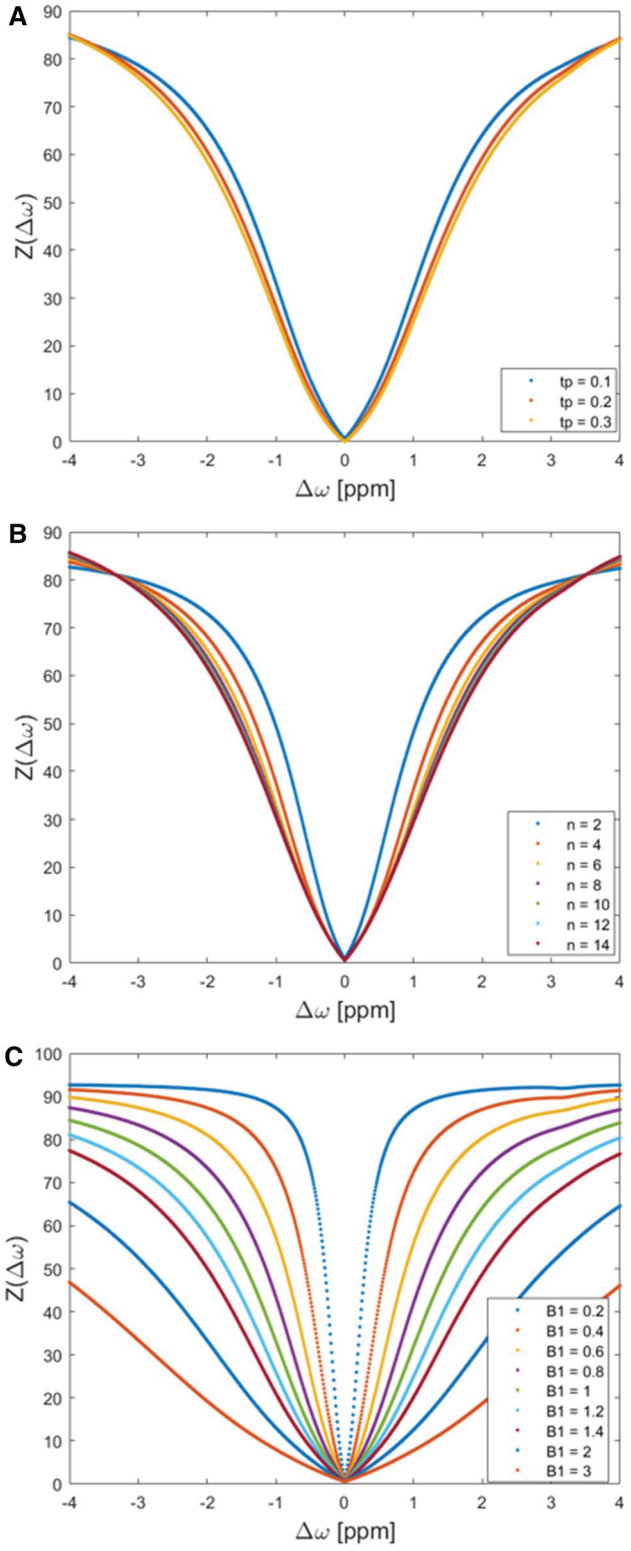

Fig. 2 Simulations results detailing the effects of variations in CEST framework conditions. Pulse durations t_p (100, 200, and 300 ms) (**a**), number of applied pulses n_p ($n = 2 - 14$) (**b**), and radiofrequency field strengths B_1 (0.2–3 μT) (**c**) were systematically varied. Each colored curve represents a simulated parameter value and gives the z-spectrum at different offset frequencies (0–4 ppm)

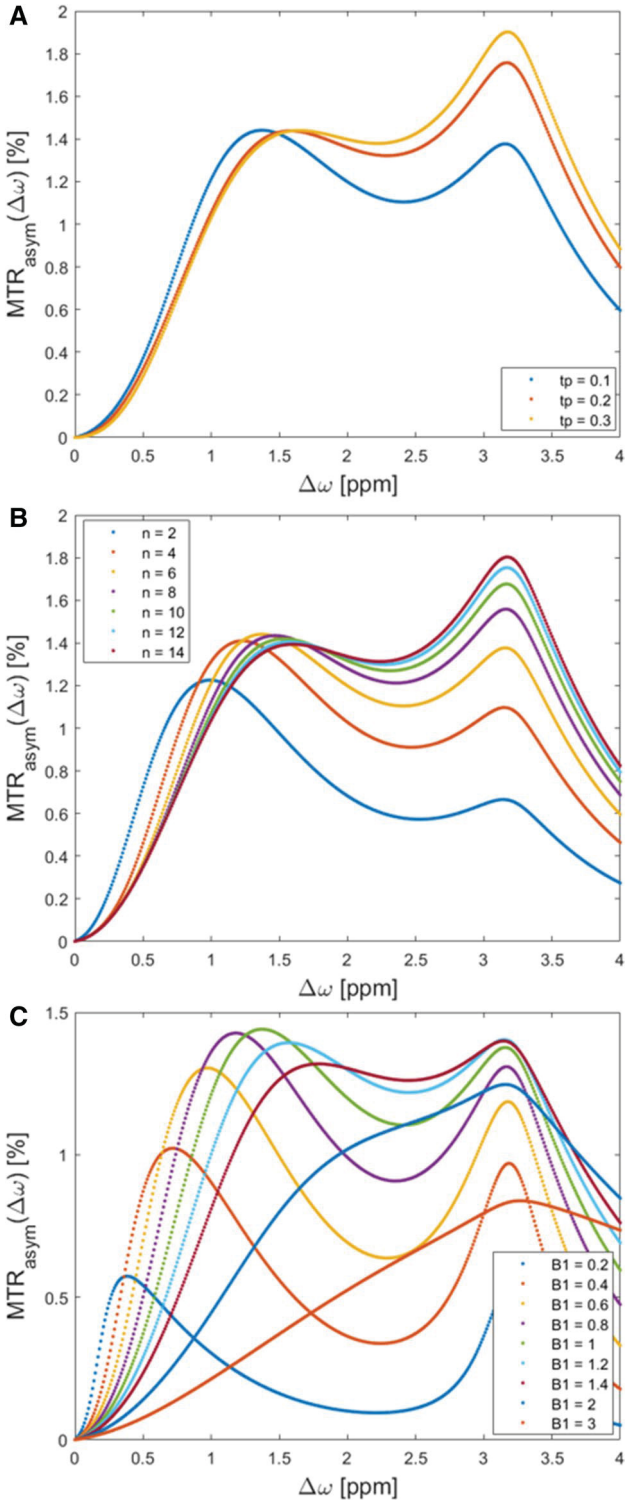

Fig. 3 Simulations results detailing the effects of variations in CEST framework conditions. Pulse durations t_p (100, 200, and 300 ms) (**a**), number of applied pulses n_p ($n = 2 - 14$) (**b**), and radiofrequency field strengths B_1 (0.2–1.4 μT) (**c**) were systematically varied. Each colored curve represents a simulated parameter value and gives the maximum magnetization transfer ratio asymmetry at different offset frequencies (0–4 ppm)

five patients was unremarkable. In them, we did not find any bone marrow lesions, subchondral thickening, osteophytes or joint space narrowing. In two patients, we noted signs of secondary OA with osteophytes, joint space narrowing, subchondral sclerosis, and moderate joint effusion. The joint status of healthy volunteers was unremarkable without any structural alterations. Within the entire study population, the following accessory ossicles were found: Os tibiale externum in six individuals, Os trigonum in three individuals, Os supratalare in one individual.

Staging of OLTs was performed according to the Heppner classification (stages 1–5, 1: articular cartilage damage only, 2a: cartilage injury with underlying fracture and surrounding edema, 2b: 2a without surrounding edema, 3: detached, but undisplaced fragment, 4: detached and displaced fragment, 5: subchondral cyst). The following stages were observed in the patient cohort: one individual with stage 2a, one individual with stage 3, one individual with stage 4 and two individuals with stage 5.

Implementation of the optimized protocol in 10 healthy volunteers

Table 4 gives the details of the MTRasym values in 10 healthy volunteers as a function of systematically varied parameter settings of B_1 (0.6, 0.8, and 1.0 µT) and tp (100, 200, and 300 ms).

a. Variation of B_1.

The mean MTR_{asym} values had a maximum of 1.7 ± 1.4 % at 0.8 µT and tended to be -even though non-significantly- numerically higher than at 1.0 µT (0.5 ± 1.0 %, $p = 0.073$) and at 0.6 µT (1.3 ± 1.1 %, $p = 0.759$).

b. Variation of t_p.

The highest mean MTR_{asym} values were found at $t_p = 300$ ms that were significantly higher than at $t_p = 100$ ms (1.67 vs. 0.12 %, $p < 0.004$) and tended to be higher than at $t_p = 200$ ms (1.67 vs 0.71 %, $p = 0.092$).

Implementation of the optimized protocol in all healthy volunteers and patients

a. MTR_{asym} values and GAG-OH amplitude of healthy volunteers vs. patients.

Using the optimized imaging protocol (with the following framework conditions: radiofrequency-field strength $B_1 = 0.8$, pulse duration $t_p = 300$ ms and number of pulses $n_p = 8$), the mean MTR_{asym} value of the tibiotalar joint cartilage in patients was 0.3 ± 0.2 % (95 % confidence interval [CI] 0–0.7) and in healthy volunteers was 1.5 ± 0.9 % (95 % CI 1.3–1.7) ($p < 0.001$). MTR_{asym} values are visualized in Fig. 3. Corresponding gagCEST maps are given in Fig. 4.

Gag-OH amplitudes of the tibiotalar joint cartilage in patients were 0.8±0.4 % (95% CI 0–1.6) and in healthy volunteers 2.0±0.2 % (CI 1.6–2.4) ($p = 0.013$). We found strong and significant correlations between mean MTR_{asym} values and gagOH amplitudes ($r = 0.56$, $p = 0.006$).

No significant differences were found between the volunteers that were used for protocol optimization and the remaining volunteers (volunteer cohort 1: MTRasym: 1.5 ± 0.9 %, volunteer cohort 2: MTRasym: 1.4 ± 0.9 %, $p = 0.715$).

The reproducibility of the MTR_{asym} values of all ROIs was excellent (aICC= 0.97, 95% confidence intervals 0.82/0.95, $p < 0.001$ and sICC= 0.91, 95% CI 0.93/0.98, $p < 0.001$).

b. T1 and T2 relaxation times in healthy volunteers.

The in-vivo measurements in healthy volunteers showed a mean T1 relaxation time of 940 ± 120 ms (range 720–1080 ms) and a mean T2 relaxation time of 35± 7 ms (range 26–48 ms) (Figs. 5, 6).

Table 4 Magnetization transfer ratio asymmetry (MTR_{asym}) values as a function of systematically varied B_1 and t_p in 10 healthy volunteers

Offset frequency [ppm]	B_1 (µT)	t_p (ms)	MTRasym (%)	p value
0.9–1.9	0.6	100	0.37 ± 0.78	100 vs. 200 ms: < **0.001**
		200	0.75 ± 0.65	100 vs. 300 ms: < **0.001**
		300	1.34 ± 1.05	200 vs. 300 ms: **0.016**
	0.8	100	0.12 ± 0.47	0.6 vs. 0.8:
		200	0.71 ± 0.81	1.0
		300	1.67 ± 1.35	0.6 vs. 1.0: **0.001**
	1.0	100	0.27 ± 0.78	0.8 vs. 1.0: < **0.001**
		200	0.94 ± 1.02	
		300	0.49 ± 0.95	

MTR_{asym} values are given as mean ± standard deviation

Means were compared using a multivariate analysis of variance (MANOVA) followed by a post-hoc Scheffé test

p values < 0.05 were considered significant and are given in bold type

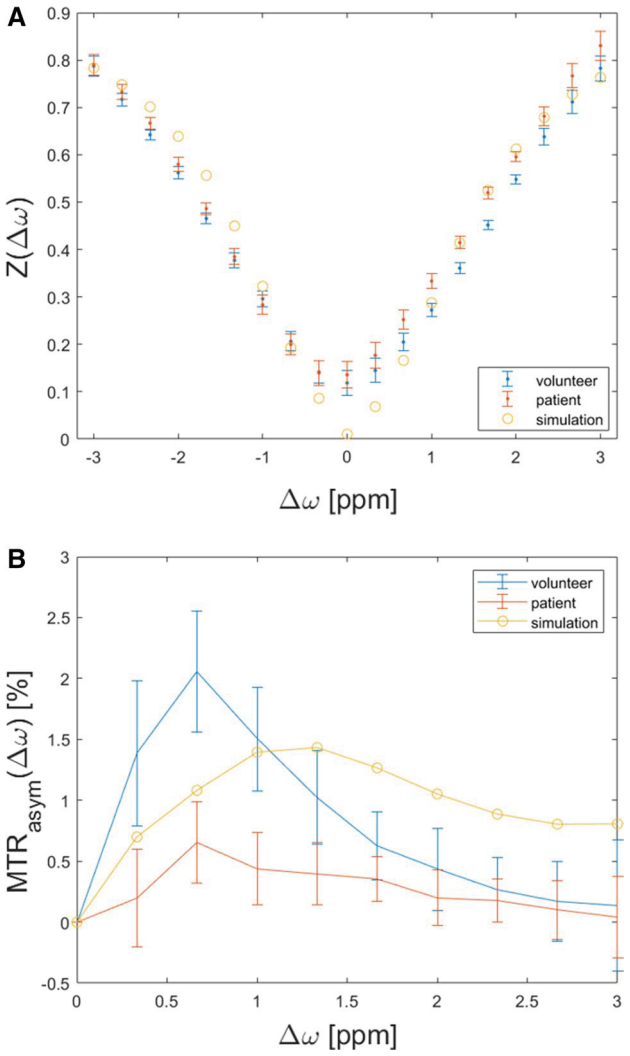

Fig. 4 Illustration of Z-spectra (**a**) and MTRasym (**b**) curves of the simulation (blue), a volunteer (yellow) and a patient (orange)**.** CEST framework conditions were $B_1 = 0.8$, $t_p = 300$ ms and np = 8. Simulations results For the patient's and volunteer's curves means (dots) and standard deviations (whiskers) are given.Of note, the GAG-NH peak is only visible in the simulation, but not in-vivo

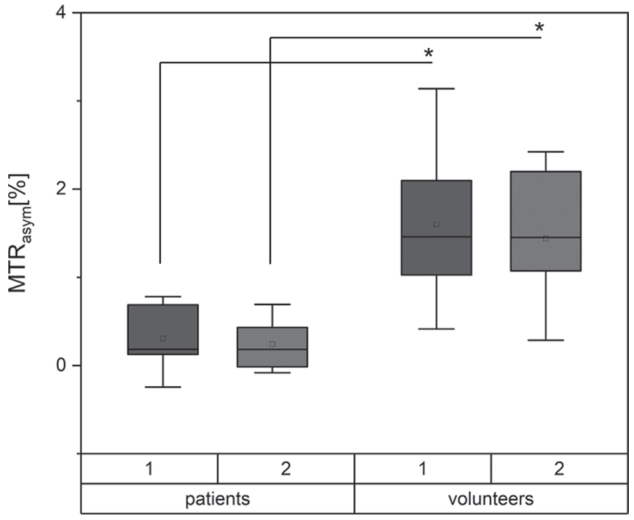

Fig. 5 Comparison of MTR_{asym} values in patients and healthy volunteers. Data are presented as means (thick line), medians (square boxes), standard deviation (boxes), and ranges (whiskers). For each cohort, two separate boxes are presented: 1 gives the MTRasym values of the ROI defined by rater 1. Box 2 depict the MTR_{asym} values of the corresponding ROIs of rater 2. p values < 0.05 were considered significant and are highlighted with an asterisk

Discussion

The most important finding of this study is that -following comprehensive and systematic sequence optimization- gagCEST imaging of the tibiotalar joint is feasible using a clinical standard 3 T MRI scanner, fits into clinical workflows with an acquisition time of less than 07:30 min, and yields stable and reproducible results that allow compositional cartilage assessment. In addition, we demonstrated that the tibiotalar joint cartilage of patients with known tibiotalar joint injury, especially OLT, have significantly lower gagCEST values than healthy volunteers.

Compositional MRI exceeds the mere morphological depiction of cartilage and allows for the detection of early cartilage changes that precede morphological alterations, i.e., loss of proteoglycans, as an early, potentially treatable stage of OA. GagCEST can be used for the detection and treatment monitoring of very early OA [34]. Despite this great clinical need, research on gagCEST imaging in general has been limited by the numerous technical complexities involved such as homogeneous magnetic field properties, long scan times, low SNR, and high field strengths (optimally ≥ 7.0 T) that are considered necessary for cartilage imaging [35]. Moreover, with the majority of imaging studies focusing on the knee joint, data on the tibiotalar joint is sparse [14]. This is mainly due to the joint's limited cartilage thickness, measuring only about 2 mm in healthy individuals and the known limited spatial resolution of gagCEST imaging [36, 37]. In this study, we set out to establish and optimize a gagCEST imaging protocol with reasonable scan times, sufficient SNR, and high reproducibility at 3.0 T for the potential implementation in the clinical setting.

GagCEST imaging can be modified by altering the number of applied saturation pulses, pulse durations and radiofrequency field strengths. To find the optimal setting of these parameters that allow for both a high gagCEST effect size and reasonable acquisition time, we used the Bloch–McConnell simulation before proceeding with the *in-vivo* measurements [38]. The simulation experiments showed a maximum effect size at a radiofrequency field strength of 0.8 µT.

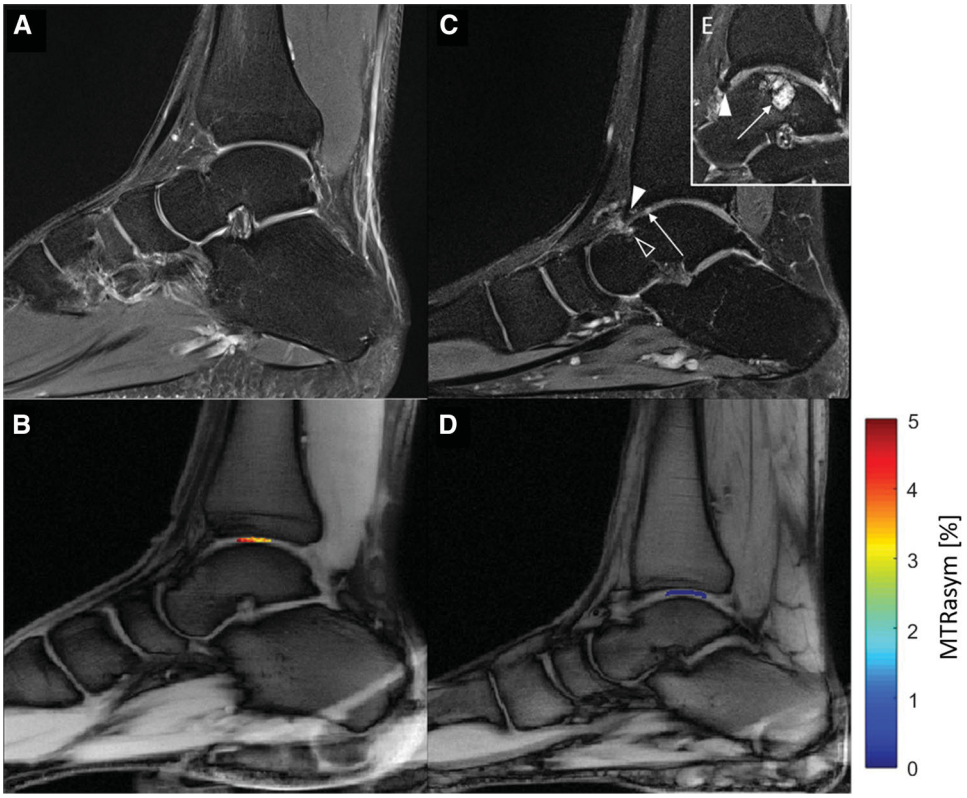

Fig. 6 Sagittal proton-density weighted (PDw) images and corresponding glycosaminoglycan chemical exchange saturation transfer (gagCEST) maps of a 29-year-old healthy male (**a** and **b**) and an age-matched male patient with an established osteochondral lesion of the talus (OLT; **c**, **d**, **e**). **a** Unremarkable tibiotalar joint with no sign of cartilage damage, osteoarthritis or OLT. **c** Osteochondral lesion of the anterior talus (black arrowhead), osteophyte of the anterior tibia (white arrowhead), and intra-tissue signal hyperintensity of the anterior tibiotalar joint cartilage indicative of focal cartilage damage (long arrow). **e** More medial to (**c**), presence of a large cystic OLT in the weight-bearing aspect of the talus (long arrow) representing a stage 5 OLT according to the Hepple classification and an osteophyte of the anterior tibia (arrowhead). Overall, the tibiotalar joint cartilage is focally thinned, inhomogeneous, and irregular. **b** and **d** The tibiotalar joint cartilage of the healthy volunteer has higher gagCEST values than the patient (color-coded gagCEST maps overlaid onto T1w morphological image)

The effect size decreased at higher field strengths due to the *'spillover effect'*: With an increasing B_1 amplitude, the spillover effect leads to direct saturation of the water pool instead of the soluble proton pool and hence results in decreases of the gagCEST effect [39]. When tested in healthy volunteers, we noted numerically higher MTR_{asym} values and GAG-OH amplitudes at 0.8 than at 1.0 µT, but not than at 0.6 µT. The effect size increased with the applied number of pulses with a MTR_{asym} of 0.98% at 14 pulses; however, at eight applied pulses, the MTR_{asym} reached 0.98% of the maximum effect size. To keep the acquisition time as short as possible at a maximum gagCEST effect size, we decided to use eight pulses. Moreover, the effect size was found to be increased with increasing pulse durations. Due to limitations secondary to the specific absorption rate (SAR); however, the maximum pulse durations to be used in vivo were limited to 300 ms [40]. By trend, we found higher MTR_{asym} values in vivo at a pulse duration of 300 ms (as compared to 100 and 200 ms)—even though these differences were only partially significant.

After simulations and in-vivo experiments, our final gagCEST protocol consisted of 8 applied pulses with a pulse duration of 300 ms at a radiofrequency field strength of 0.8 µT and a constant duty cycle of 0.5 aiming for a minimized scan time. We used WASSR to improve the differentiation of the water and GAG peak as well as to correct for B_0 field inhomogeneities [27]. Using this protocol, we found excellent reproducibility of gagCEST values as measured by one individual rater and between two independent raters (aICC = 0.97 and sICC = 0.91). These values for reproducibility were even higher than presented in previous studies focusing on gagCEST of peripheral joints [34]. A good reproducibility is beneficial not only for future studies, but also for the perspective of clinical implementation of the technique [41].

The acquisition time of the optimized gagCEST sequence was 5:01 min, followed by an additional 2:22 min for the WASSR sequence. Thus, the sequence requires 7:23 min. Hence, our scan time is comparable to the one presented

by Kogan et al., who conducted the only previous study on gagCEST imaging of the ankle joint, and even shorter than several gagCEST studies focusing on the knee joint [13, 14, 42]. Additionally, the gagCEST imaging protocol was designed for 3 T scanners, which is the commonly used field strength for musculoskeletal imaging in clinical practice [43]. Thus, our protocol may be applied in both research and clinical contexts to further advance the clinical utility of gagCEST imaging of the tibiotalar joint. However, it still has to be considered less sensitive at detecting early cartilage changes than imaging protocols applied at 7 T scanners, especially if the latter are designed as volumetric multi-slice approaches [14]. Volumetric protocols have been implemented at 3 T scanners for gagCEST imaging of the knee joint and generally allow for better localization of cartilage changes. Consequently, future adaptation of volumetric protocols for gagCEST imaging of the tibiotalar joint seems of great scientific and clinical interest.

In addition to providing a stable and reproducible protocol, we observed significant differences between healthy volunteers and patients with OLTs. Since this study was the first of its kind comparing healthy individuals with patients using gagCEST at the ankle joint, we chose a patient cohort with morphologically damaged cartilage to demonstrate feasibility of this technique. In the future, we intend to study patients after ankle trauma without morphological apparent cartilage lesions to assess the presence of pre-morphological tissue damage.

Despite its strengths, our study has limitations. Our measured T1 and T2 relaxation times were shorter than the ones used for the simulations, but were overall comparable to the current literature [44].

Synovial fluid in general and joint effusion in particular are known to interfere with gagCEST imaging due to the presence of GAGs [1, 45]. Therefore, we placed our ROIs in the center of the tibiotalar joint at a distance to the anterior and posterior anatomical recesses, where joint fluid may collect and distort our measurements. Á priori, we excluded patients with manifest joint effusion as visible in the morphological sequences. However, since we included both cartilage layers, i.e., both tibial and talar, in one single ROI, the odds are high that synovial fluid might have contaminated our gagCEST measures. Future studies should, therefore, use sequences that use fluid suppression. Moreover, our study population was small, which may be explained by the fact that we set out to implement a clinically applicable imaging protocol for gagCEST imaging. Nonetheless, future studies need to be conducted to corroborate our findings in larger patient numbers. Furthermore, we did not compare our findings to the gold-standard technique dGEMRIC. Since dGEMRIC relies on gadolinium-based contrast agents and its use is restricted due to ethical reasons, we consider this only a minor limitation. Last, we used a two-pool exchange model considering only the water- and the GAG-OH pool for the simulation. This model might be partially inaccurate for *in-vivo* applications, because of other influencing factors such as the GAG-NH pool, the nuclear Overhauser effect (NOE), and the magnetization transfer (MT) that were not included in our simulation because of lacking application-specific-framework fitting parameters for the NOE and MT. However, for the eventual quantification of the *in-vivo* measurements we used both the MTRasym values and the Lorentzian fit analyses. While the former accounts only for the water and the GAG-OH pool the latter also takes the GAG-NH, NOE and magnetization transfer pools into consideration. As both were strongly correlated, we consider the morge simple two-pool exchange model to be sufficient for *in-vivo* quantification purposes.

In this feasibility study, pre-morphological tibiotalar joint cartilage damage was quantitatively assessable on the basis of an optimized 3 T gagCEST imaging protocol that allowed a stable gagCEST effect quantification both in normal and degenerated cartilage in clinically feasible acquisition times.

Acknowledgements Open Access funding provided by Projekt DEAL. DBA was supported by the local research committee of the medical faculty. SN has been supported by grants from the "Deutsche Forschungsgemeinschaft" (DFG) (NE 2136/3-1).

Author contributions DBA: study conception and design. Acquisition of data. Analysis and interpretation of data. Drafting of manuscript. CS: study conception and design. Acquisition of data. Analysis and interpretation of data. Critical revision. KLR: study conception and design. Acquisition of data. Analysis and interpretation of data. Critical revision. MF: study conception and design. Analysis and interpretation of data. Critical revision. JS: study conception and design. Analysis and interpretation of data. Critical revision. AL: study conception and design. Analysis and interpretation of data. Critical revision. H-JW: study conception and design. Analysis and interpretation of data. Critical revision. GA: study conception and design. Critical revision. BB: study conception and design. Critical revision. TH: study conception and design. Acquisition of data. Critical revision. SN: study conception and design. Analysis and interpretation of data. Critical revision. AM-L: study conception and design. Acquisition of data. Analysis and interpretation of data. Critical revision.

Compliance with ethical standards

Conflict of interest The authors declare that they have no conflict of interest.

Ethical standards All procedures performed in studies involving human participants were in accordance with the ethical standards of the institutional and/or national research committee and with the 1964 Helsinki Declaration and its later amendments or comparable ethical standards.

References

1. Guermazi A, Alizai H, Crema Md et al (2015) Compositional mri techniques for evaluation of cartilage degeneration in osteoarthritis. Osteoarthr Cartil 23(10):1639–1653
2. Matzat SJ, Van Tiel J, Gold GE et al (2013) Quantitative mri techniques of cartilage composition. Quant Imaging Med Surg 3(3):162–174
3. Matzat J, Kogan F, Fong W et al (2014) Imaging strategies for assessing cartilage composition in osteoarthritis. Curr Rheumatol Rep 16(11):1–9. https://doi.org/10.1007/S11926-014-0462-3
4. Kanda T (2019) The new restrictions on the use of linear gadolinium-based contrast agents In Japan. Magn Reson Med Sci 18(1):1–3
5. Ling W, Regatte RR, Navon G et al (2008) Assessment of glycosaminoglycan concentration in vivo by chemical exchange-dependent saturation transfer (Gagcest). Proc Natl Acad Sci USA 105(7):2266–2270
6. Williamson DC, Närväinen J, Hubbard PI et al (2006) Effects of radiation damping on Z-spectra. J Magn Reson 183(2):203–212
7. Vinogradov E, Sherry AD, Lenkinski RE (2013) Cest: from basic principles to applications, challenges and opportunities. J Magn Reson 229:155–172
8. Kogan F, Hariharan H, Reddy R (2013) Chemical exchange saturation transfer (cest) imaging: description of technique and potential clinical applications. Curr Radiol Rep 1(2):102–114
9. Müller-Lutz A, Schleich C, Schmitt B et al (2016) Gender, bmi and T2 dependencies of glycosaminoglycan chemical exchange saturation transfer in intervertebral discs. Magn Reson Imaging 34(3):271–275
10. Pulickal T, Boos J, Konieczny M et al (2019) Mri identifies biochemical alterations of intervertebral discs in patients with low back pain and radiculopathy. Eur Radiol 29(12):6443–6446
11. Schleich C, Müller-Lutz A, Blum K et al (2016) Facet tropism and facet joint orientation: risk factors for the development of early biochemical alterations of lumbar intervertebral discs. Osteoarthr Cartil 24(10):1761–1768
12. Schleich C, Müller-Lutz A, Eichner M et al (2016) Glycosaminoglycan chemical exchange saturation transfer of lumbar intervertebral discs in healthy volunteers. Spine 41(2):146–152
13. Schleich C, Bittersohl B, Miese F et al (2016) Glycosaminoglycan chemical exchange saturation transfer at 3t mri in asymptomatic knee joints. Acta Radiol 57(5):627–632
14. Kogan F, Hargreaves BA, Gold GE (2017) Volumetric multislice gagCEST imaging of articular cartilage: optimization and comparison with T1rho. Magn Reson Med 77(3):1134–1141
15. Jr Steele, Tj D, Ae F et al (2018) Osteochondral lesions of the talus. Foot Ankle Orthop 3(3):247301141877955
16. Posadzy M, Desimpel J, Vanhoenacker F (2017) Staging of osteochondral lesions of the talus: mri and cone beam Ct. J Belg Soc Radiol 101(Suppl 2):1
17. Looze CA, Capo J, Ryan MK et al (2017) Evaluation and management of osteochondral lesions of the talus. Cartilage 8(1):19–30
18. Zaiss M, Bachert P (2013) Chemical exchange saturation transfer (Cest) And Mr Z-spectroscopy in vivo: a review of theoretical approaches and methods. Phys Med Biol 58(22):R221–R269
19. Zaiss M, Zu Z, Xu J et al (2014) A Combined analytical solution for chemical exchange saturation transfer and semi-solid magnetization transfer. Nmr Biomed 28(2):217–230
20. Zaiss M, Angelovski G, Demetriou E et al (2018) Quesp and quest revisited—fast and accurate quantitative cest experiments. Magn Reson Med 79(3):1708–1721
21. Schmitt B, Zaiss M, Zhou J et al (2011) Optimization of pulse train presaturation for cest imaging in clinical scanners. Magn Reson Med 65(6):1620–1629
22. Roeloffs V, Meyer C, Bachert P et al (2015) Towards quantification of pulsed spinlock and cest at clinical mr scanners: an analytical interleaved saturation-relaxation (isar) approach. Nmr Biomed 28(1):40–53
23. Stanisz GJ, Odrobina EE, Pun J et al (2005) T1, T2 relaxation and magnetization transfer in tissue at 3T. Magn Reson Med 54(3):507–512
24. Singh A, Haris M, Cai K et al (2012) Chemical exchange saturation transfer magnetic resonance imaging of human knee cartilage at 3 T and 7 T. Magn Reson Med 68(2):588–594
25. Saar G, Zhang B, Ling W et al (2012) Assessment of glycosaminoglycan concentration changes in the intervertebral disc via chemical exchange saturation transfer. Nmr Biomed 25(2):255–261
26. Hepple S, Winson IG, Glew D (1999) Osteochondral lesions of the talus: a revised classification. Foot Ankle Int 20(12):789–793
27. Kim M, Gillen J, Landman BA et al (2009) Water saturation shift referencing (wassr) for chemical exchange saturation transfer (cest) experiments. Magn Reson Med 61(6):1441–1450
28. Müller-Lutz A, Schleich C, Schmitt B et al (2015) Improvement of gagCEST imaging in the human lumbar intervertebral disc by motion correction. Skeletal Radiol 44(4):505–511
29. Müller-Lutz A, Schleich C, Pentang G et al (2015) Age-dependency of glycosaminoglycan content in lumbar discs: a 3T gagCEST study. J Magn Reson Imaging 42(6):1517–1523
30. Müller-Lutz A, Cronenberg T, Schleich C et al (2017) Comparison of glycosaminoglycan chemical exchange saturation transfer using gaussian-shaped and off-resonant spin-lock radiofrequency pulses in intervertebral disks. Magn Reson Med 78(1):280–284
31. Zaiss M, Schmitt B, Bachert P (2011) Quantitative separation of cest effect from magnetization transfer and spillover effects by lorentzian-line-fit analysis of Z-spectra. J Magn Reson 211(2):149–155
32. Deng M, Yuan J, Chen WT et al (2016) Evaluation of glycosaminoglycan in the lumbar disc using chemical exchange saturation transfer mr at 30 tesla: reproducibility and correlation with disc degeneration. Biomed Environ Sci 29(1):47–55
33. Cohen J (1992) A power primer. Psychol Bull 112(1):155–159
34. Brinkhof S, Nizak R, Khlebnikov V et al (2018) Detection of early cartilage damage: feasibility and potential of gagcest imaging at 7T. Eur Radiol 28(7):2874–2881
35. Martín Noguerol T, Raya JG, Wessell DE et al. (2019) Functional mri for evaluation of hyaline cartilage extracelullar matrix, a physiopathological-based approach. Br J Radiol 92(1103):20190443. https://Www.Ncbi.Nlm.Nih.Gov/Pmc/Articles/Pmc3473592/Pdf/Bjr-83-476.Pdf.
36. Millington SA, Li B, Tang J et al (2007) Quantitative and topographical evaluation of ankle articular cartilage using high resolution mri. J Orthop Res 25(2):143–151

37. Krusche-Mandl I, Schmitt B, Zak L et al (2012) Long-term results 8 years after autologous osteochondral transplantation: 7 T gagcest and sodium magnetic resonance imaging with morphological and clinical correlation. Osteoarthr Cartil 20(5):357–363
38. Abergel D, Palmer AG (2004) Approximate solutions of the bloch-mcconnell equations for two-site chemical exchange. ChemPhysChem 5(6):787–793
39. Zaiss M, Xu J, Goerke S et al (2014) Inverse Z-spectrum analysis for spillover-, Mt-, and T1 -corrected steady-state pulsed cest-mri–application to Ph-weighted mri of acute stroke. Nmr Biomed 27(3):240–252
40. Wang Z, Collins CM (2010) Effect of Rf pulse sequence on temperature elevation for a given time-average Sar. Concepts Magn Reson Part B Magn Reson Eng 37b(4):215–219
41. Dickersin K, Mayo-Wilson E (2018) Standards for design and measurement would make clinical research reproducible and usable. Proc Natl Acad Sci USA 115(11):2590–2594
42. Krishnamoorthy G, Nanga RPR, Bagga P et al (2016) High quality 3d gagcest imaging of in vivo human knee cartilage at 7T. Magn Reson Med 77(5):1866–1873
43. Tp F, Nc A, Jp W et al (2018) Musculoskeletal imaging: current practice and future directions. Semin Musculoskelet Radiol 22(5):564–581
44. Wiener E, Pfirrmann CWA, Hodler J (2010) Spatial variation in T1 of healthy human articular cartilage of the knee joint. Br J Radiol 83(990):476–485 **(Accessed 23 Mar 2020)**
45. Kulkarni P, Deshpande S, Koppikar S et al (2016) Glycosaminoglycan measured from synovial fluid serves as a useful indicator for progression of osteoarthritis and complements Kellgren-Lawrence score. Bba Clin 6:1–4

Skeletal Radiol (2015) 44:505–511
DOI 10.1007/s00256-014-2034-z

SCIENTIFIC ARTICLE

Improvement of gagCEST imaging in the human lumbar intervertebral disc by motion correction

Anja Müller-Lutz · Christoph Schleich · Benjamin Schmitt · Melike Topgöz · Gael Pentang · Gerald Antoch · Hans-Jörg Wittsack · Falk Miese

Received: 14 July 2014 / Revised: 8 September 2014 / Accepted: 8 October 2014 / Published online: 23 October 2014

Abstract
Objective To investigate whether motion correction improves glycosaminoglycan chemical exchange saturation transfer imaging (gagCEST imaging) of intervertebral discs (IVDs).
Materials and methods Magnetic resonance gagCEST imaging of 12 volunteers was obtained in lumbar IVDs at 3 T using a prototype pulse sequence. The data were motion-corrected using a prototype diffeomorphism-based motion compensation technique. For both the data with and that without motion correction ($data_c$, $data_{uc}$), CEST evaluation was performed using the magnetisation transfer ratio asymmetry (MTR_{asym}) as a means of quantifying CEST effects. MTR_{asym} and the signal-to-noise ratio (SNR) of the MTR_{asym} map in the nucleus pulposus (NP) were compared for $data_c$ and $data_{uc}$. A visual grading analysis was performed by a radiologist in order to subjectively quantify the quality of the MTR_{asym} analysis (score 1: best quality, score 5: worst quality). Furthermore, a landmark analysis was performed in order to objectively quantify the motion between CEST images using the mean landmark distance d_{mean}.
Results MTR_{asym} and SNR were significantly higher for the motion-corrected data than for the uncorrected CEST data ($MTR_{asym}(data_c)$ = 3.77 % ± 0.95 %, $MTR_{asym}(data_{uc})$ = 3.41 % ± 1.54 %, p value=0.001; $SNR(data_c)$ = 3.88± 2.04, $SNR(data_{uc})$ = 2.77±1.55, p value<0.001, number of IVDs = 48). The visual grading analysis revealed a higher reliability for $data_c$ (maximum score = 2) compared with $data_{uc}$ (maximum score = 5). The landmark analysis demonstrated the superiority of the motion-corrected data ($d_{mean}(data_c)$ =0.08 mm ±0.09 mm, $d_{mean}(data_{uc})$ = 0.36 mm ±0.09 mm, p value=0.001).
Conclusion Our study showed significant improvements in the ability to quantify CEST imaging in IVDs after the application of motion correction compared with uncorrected datasets.

Keywords Chemical exchange saturation transfer · Motion correction · Glycosaminoglycans · Intervertebral disk · Magnetic resonance imaging

Introduction

Low back pain (LBP) occurs in all age groups [1–4] and has a significant negative effect on the quality of life [5]. Intervertebral disc (IVD) degeneration has been assumed to be one of the causes of LBP [6, 7], for which a loss of glycosaminoglycans has been reported to be an initiating factor [5].

Magnetic resonance imaging plays an important role in the assessment of cartilage degradation owing to the ability to non-invasively assess the biochemical composition of cartilage with different MRI techniques such as dGEMRIC, T_2 relaxometry imaging, ^{23}NA imaging and glycosaminoglycan chemical exchange saturation transfer imaging (gagCEST) imaging [1, 8–11]. GagCEST imaging is a biomarker of cartilage GAG composition that has been applied in the human lumbar IVD in prior studies. GagCEST imaging is directly related to the content of glycosaminoglycans.

GagCEST imaging exploits the accumulation of molecule-specific saturation information on bulk water protons for the indirect detection of glycosaminoglycans [12]. In CEST imaging, several measurements are performed with a CEST

A. Müller-Lutz · C. Schleich (✉) · M. Topgöz · G. Pentang · G. Antoch · H.-J. Wittsack · F. Miese
Medical Faculty, Department of Diagnostic and Interventional Radiology, University Dusseldorf, Moorenstrasse 5, 40225 Dusseldorf, Germany
e-mail: christoph.schleich@med.uni-duesseldorf.de

B. Schmitt
Healthcare Sector, Siemens Ltd. Australia, 160 Herring Road, Macquarie Park, NSW 2113, Australia

presaturation module at different frequency offsets. These measurements yield the Z-spectrum, which enables an asymmetry analysis for the evaluation of the gagCEST effect [13]. Owing to the consecutive acquisition of several scans, the CEST sequence is subject to motion artefacts arising from patient movement during the acquisition time. In various MRI fields such as dynamic MRI, dGEMRIC and functional magnetic resonance imaging, motion correction techniques have been established to improve the quality of the desired parameter outcome [14–17].

A promising approach in CEST imaging would be to apply an algorithm that has proven its quality for multimodal image registration. In multimodal image processing, registration methods are usually built upon statistical similarity measures instead of using image intensity differences [18]. This approach was extended by an infinite-dimensional variational framework with a linear elastic regularization, which had the main drawback of a limited capture range and slow convergence [19]. These problems could be solved by the use of an approximation of a continuous flow of diffeomorphism [18].

We used a non-rigid registration method, which has previously been shown to improve registration results in cardiac MRI image registration [20]. A non-rigid motion correction technique was assumed to be beneficial for the intervertebral discs because IVDs are slightly deformable during motion and displacement can take place in any direction.

The aim of the present study was to test whether motion correction by a non-rigid diffeomorphism-based registration improves gagCEST evaluation in human IVDs.

Materials and methods

Study population

The study was approved by the local ethics committee, and written informed consent was obtained from all participants. Twelve healthy volunteers (7 female, 5 male; mean age 25± 5 years; range: 21–32 years) were enrolled in this study.

MR hardware and sequence protocol

Magnetic resonance imaging was performed on a clinical whole-body 3 T MRI system (Magnetom Trio, A Tim System, Siemens Healthcare, Erlangen, Germany), equipped with the spine matrix coil for signal reception. The patient was in a supine position. The MR protocol acquired consisted of a localizer, a T2-weighted sequence in sagittal orientation, the prototype gagCEST sequence in sagittal orientation and the prototype water saturation shift referencing (WASSR) sequence [21] in sagittal orientation.

GagCEST and WASSR images were centred in the middle of the spine. The positions of the gagCEST and WASSR images were identical. The images were obtained using a segmented 2D RF-spoiled gradient echo sequence with a CEST pre-saturation module. For gagCEST imaging, the pre-saturation module consisted of a series of six Gaussian-shaped radiofrequency pulses with B_1 amplitude of 1.5 μT averaged over time (B_1 continuous wave amplitude equivalent). The duration of each saturation pulse and interpulse delay was 100 ms. One reference measurement without presaturation and 25 measurements with presaturation at different frequency offsets $\Delta\omega$ from the bulk water resonance were acquired during the gagCEST measurement. The sampled frequency range was between $-\Delta\omega_{max}$ and $\Delta\omega_{max}$, where $\Delta\omega_{max}$ was 4 ppm. The duration of the gagCEST imaging sequence was 12 min and 24 s.

For WASSR imaging, the pre-saturation module consisted of one Gaussian-shaped RF pulse with a B_1 amplitude of 0.3 μT and a pulse duration of 100 ms. Forty-one measurements with presaturation at different frequency offsets ranging from −1 ppm to 1 ppm and one reference image without presaturation were acquired. The duration of the WASSR imaging sequence was 7 min and 26 s.

In order to supress bowel movement artefacts, the signal of the abdomen was supressed with a saturation band in CEST and WASSR data acquisitions in the same position. The sequence details of the T2-weighted sequence as well as the gagCEST and WASSR sequence were summarized in Table 1.

Data analysis

The T2-weighted images were scored by a radiologist (CS; 3 years' experience in musculoskeletal radiology) according to the Pfirrmann score [22]. Before data analysis, motion correction was performed for the CEST and WASSR datasets using a prototype diffeomorphic registration approach [19, 23]

Table 1 Detailed sequence parameters of the T2-weighted imaging in sagittal orientation (T2w sag), chemical exchange saturation transfer imaging (CEST) and water saturation shift referencing (WASSR) sequences

	T2w sag	CEST	WASSR
Repetition time T_R (ms)	3,100	1,590	590
Echo time T_E (ms)	105	3.01	3.01
Spatial resolution (mm × mm)	1.2 × 1.2	1.6 × 1.6	1.6 × 1.6
Slice thickness (mm)	3.0	5.0	5.0
Flip angle (°)	160	12	12
Field of view (mm × mm)	300 × 300	300 × 300	300 × 300
Duration (min:s)	3:39	12:24	7:26
Averages	2	6	6
Basic resolution	256	192	192
Number of slices	15	1	1

incorporated into the prototype software fMRLung (Siemens Healthcare, Erlangen, Germany). This registration approach was initially introduced in order to register multimodal images using statistical criteria in a variational setting [23]. In the following, the uncorrected data were denoted as $data_{uc}$ and the corrected data were denoted as $data_c$.

The CEST evaluation was performed using in-house developed Matlab software (Mathworks, Natick, MA, USA, R2012b). For efficiency of data processing, a rectangular region of interest (ROI) was placed around the lumbar intervertebral discs. Before analysis, a 3×3 Gaussian filter was applied to each CEST and WASSR image to reduce image noise. In order to reduce the influence of B0 field heterogeneities, a pixel-by-pixel frequency offset was calculated using the WASSR maximum-symmetry algorithm introduced by Kim et al. [21]. The calculated frequency shifts were used to correct the acquired CEST curves. From the corrected CEST curves, the magnetisation transfer asymmetry ratio (MTR_{asym}) was calculated according to

$$MTR_{asym}(\Delta\omega) = \frac{S(-\Delta\omega) - S(\Delta\omega)}{S_0},$$

where S is the signal intensity at the specified frequency shift difference and S_0 is the signal intensity without presaturation. Finally, the average MTR_{asym} in the offset range 1–1.5 ppm, which comprises resonance frequencies of GAG hydroxyl protons, was used for the creation of gagCEST maps.

Four ROIs for the four lower lumbar IVDs were manually drawn on the reference gagCEST image, which was used for motion correction. Thereby, the complete visible nucleus pulposus (NP) and the annulus fibrosus (AF) were covered. The defined volume was divided automatically into the AF (anterior and posterior 20 % of the intervertebral space) and the NP (inner 60 %) according to the method used by Haneder et al. [1]. The mean, standard deviation and signal-to-noise ratio (SNR) of the MTR_{asym} image was calculated for each region of interest. The ratio between the MTR_{asym} values in AF and NP -M_{ratio}—as well as the difference in the MTR_{asym} values in AF and NP -M_{diff}—were calculated. In total, 48 IVDs were analysed for $data_c$ as well as for $data_{uc}$.

The MTR_{asym} maps on the IVDs were overlaid with the anatomical images. On these images, a blinded visual grading analysis was performed by a radiologist (CS; 3 years' experience in musculoskeletal radiology). Thereby, the position of the highest MTR_{asym} values was investigated. If the highest MTR_{asym} values were in the middle of the IVD in all the investigated IVDs, the score was 1. For each IVD where the highest MTR_{asym} values were detected to be at the margin of the IVD, the score was increased by one. In the following, this score is denoted as the MTR_{asym} score. This scoring is based on the results of Haneder et al., who obtained higher MTR_{asym} values in NP compared with AF [1].

In addition to the MTR_{asym} analysis, a landmark analysis was performed. The landmarks were positioned at the superior anterior, inferior anterior, superior posterior and inferior posterior margins of the IVDs. In order to evaluate displacements, the distance between the landmarks and the corresponding reference landmarks were calculated. The mean and maximum distance over all landmarks d_{mean} and d_{max} were determined for each volunteer. The percentage of landmarks with decreased/increased/equal distances (λ_d, λ_i, λ_e) with motion correction compared with no image registration was determined.

Statistical analysis

Statistical data analysis was performed using the software SPSS (version 22; SPSS, Chicago, IL, USA). The mean and standard deviations were calculated as descriptive statistics. To quantify statistically significant differences, the Wilcoxon test was used. p values below 0.05 were considered to be significant.

A box plot was generated for the MTR_{asym} values of NP, AF and wIVD (whole IVD) with and without motion correction. Outliers were defined as values with a distance from the 25th percentile or the 75th percentile of more than 1.5 times and less than 3 times the box height. Outliers with a distance more than 3 times the box height were defined as extreme outliers.

Results

Forty-eight lumbar IVDs were scored using the Pfirrmann score. 24 IVDs had Pfirrmann score 1 and 24 IVDs had Pfirrmann score 2. With and without motion correction, MTR_{asym} values in NP were highest, followed by wIVD. The lowest MTR_{asym} values were obtained in AF. These differences were statistically significant ($p \leq 0.001$).

The values obtained for MTR_{asym} in NP, AF and wIVD are listed in Table 2. Significantly higher MTR_{asym} values were noted in the data with motion correction ($p < 0.001$, Fig. 1). Only one outlier was detected for the motion-corrected data, whereas 10 outliers and one extreme outlier were seen for the data without motion correction. Higher values of NP compared with wIVD and AF were noted.

Significantly higher SNR values were obtained with motion correction than without motion correction for all regions: NF, AF and wIVD (p values < 0.001, Table 2, Fig. 2). In both motion-corrected and uncorrected data, the SNR in AF was lowest followed by the SNR in wIVD. The SNR in the NP

Table 2 Magnetisation transfer ratio asymmetry (MTR_{asym}) and signal-to-noise ratio (SNR) values and their standard deviations ΔMTR_{asym} and ΔSNR in nucleus pulposus (NP), annulus fibrosus (AF) and whole intervertebral discs (wIVD) obtained with and without motion correction. The MTR_{asym} difference is the mean difference between MTR_{asym} values obtained with and without motion correction, the SNR difference is the mean difference between the SNR values with and without motion correction. The *p* values indicate if the differences are statistically significant

	NP		AF		wIVD	
	Without motion correction	Motion correction	Without motion correction	Motion correction	Without motion correction	Motion correction
MTR_{asym} (%)	3.41	3.77	1.41	1.84	2.53	2.90
ΔMTR_{asym} (%)	1.54	0.95	1.55	0.99	1.39	0.86
SNR	2.77	3.88	1.06	1.43	1.43	1.86
ΔSNR	1.55	2.04	0.86	0.89	0.71	0.74
MTR_{asym} difference (%)	0.36±0.94		0.43±1.02		0.37±0.86	
p value (MTR_{asym} difference)	0.001		< 0.001		< 0.001	
SNR difference	1.11±1.26		0.37±0.47		0.43±0.44	
p value (SNR difference)	< 0.001		< 0.001		< 0.001	

was highest. These differences were statistically significant (*p* values<0.001).

M_{ratio}=−1.60±11.57 was calculated without motion correction and M_{ratio} =0.49±0.23 was obtained with motion correction. The standard deviation over all investigated IVDs is significantly decreased with motion correction (*p* value<0.001). The difference between M_{ratio} with and without motion correction was statistically significant (*p* value=0.016).

For M_{diff}, no statistically significant differences were obtained (M_{diff} without motion correction: 1.99±1.13; M_{diff} with motion correction: 1.92±0.96, *p* value=0.209). As an illustrative example, in Fig. 3 the MTR_{asym} maps in the investigated IVDs of one volunteer were overlaid onto the anatomical image. Whereas the slightly reduced MTR_{asym} values are only visible after close consideration, the decreased SNR can be easily observed. In addition, the highest MTR_{asym} values representing the NP are slightly displaced to the borders of the IVDs in this patient.

Whereas the maximum MTR_{asym} score for $data_c$ was 2, the maximum MTR_{asym} score for $data_{uc}$ was 5. The mean MTR_{asym} score for $data_c$ was significantly lower than for $data_{uc}$ ($data_c$: MTR_{asym} score = 1.3±0.5; $data_{uc}$: MTR_{asym} score = 2.4±1.4, *p* value=0.02).

The averaged value of d_{mean} over all volunteers was 0.36 mm ± 0.28 mm without motion correction and 0.08 mm ± 0.09 mm with motion correction. This difference was statistically significant (*p* value=0.001). No significant

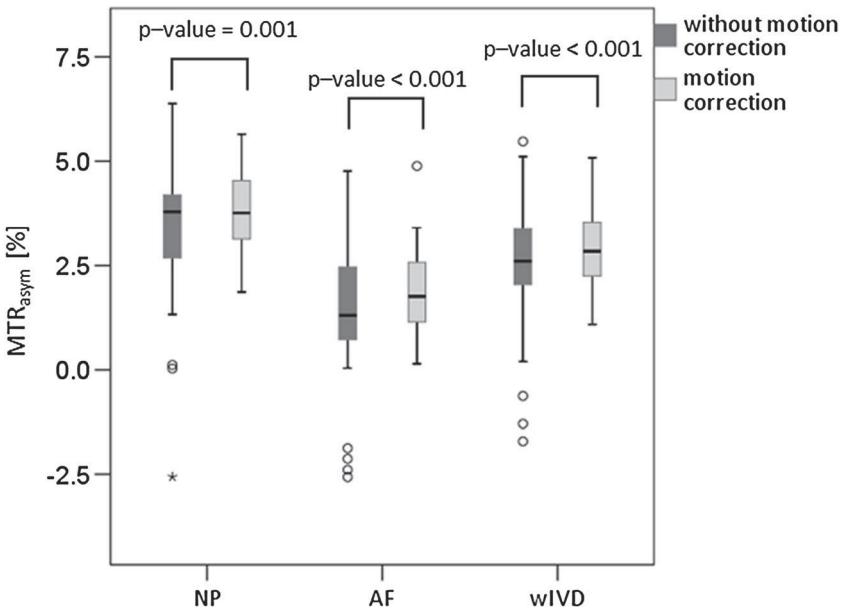

Fig. 1 Magnetisation transfer ratio asymmetry (MTR_{asym}) values in nucleus pulposus (NP), annulus fibrosus (AF) and whole intervertebral discs (wIVD) obtained with and without motion correction. Significantly higher MTR_{asym} values were obtained with motion correction. In addition, fewer outliers were obtained for $data_c$ compared with $data_{uc}$

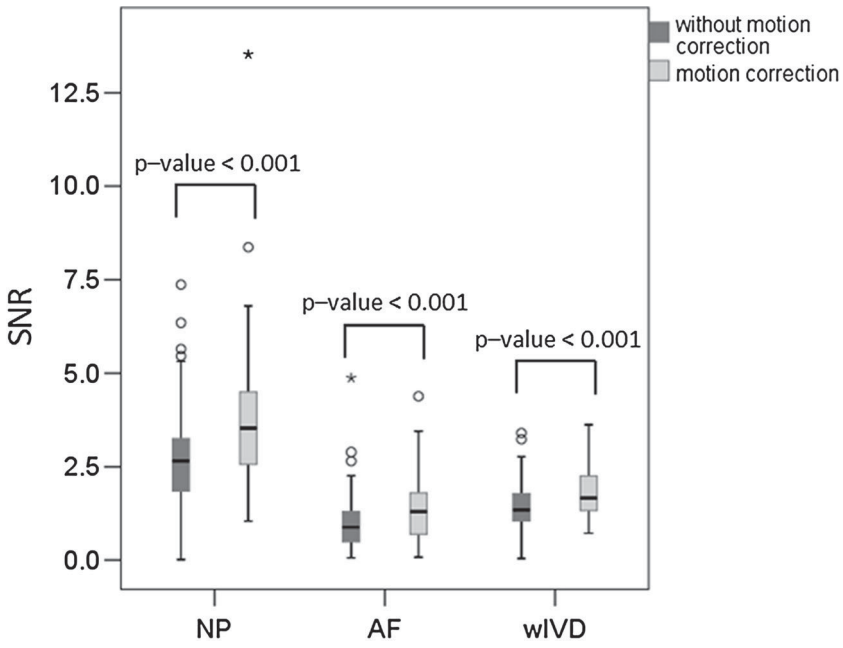

Fig. 2 Signal-to-noise ratio (SNR) values in NP, AF and wIVD obtained with and without motion correction. Significantly higher SNR values were obtained for $data_c$ compared with $data_{uc}$

difference was obtained for the averaged value of d_{max} (d_{max} = 3.49 mm ±1.53 mm without motion correction; d_{max} = 2.70 mm ±1.17 mm with motion correction, *p* value= 0.055).

For most landmarks (λ_e = 79.74 %), the distance to the reference frame was identical with and without motion correction. λ_d was 18.10 % and λ_i was 2.16 %, thus indicating that more landmarks are in better accordance with the reference frame in the case of image registration. The difference between λ_d and λ_i was significant (*p* value=0.001).

Discussion

This is the first study demonstrating the value of motion correction for gagCEST imaging in the lumbar IVDs. With image registration, an increased SNR in the MTR_{asym} images was obtained, thus emphasizing the improvement of CEST analysis with motion correction. The application of motion correction for gagCEST imaging may enhance the reliability and accuracy of future studies.

With motion correction higher SNR values of the MTR_{asym} images were obtained. One possible explanation for these

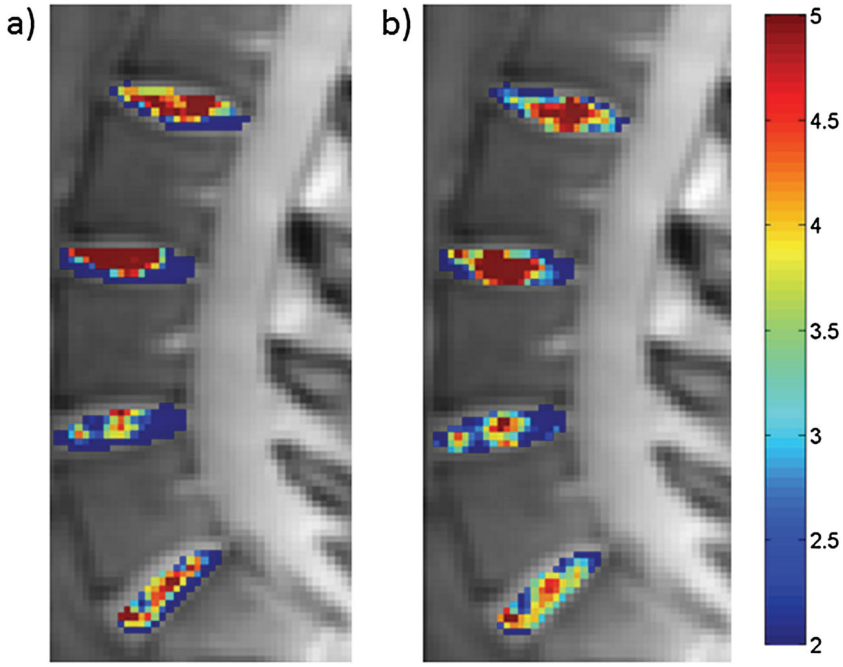

Fig. 3 MTR_{asym} maps overlaid with the anatomical images **a** without motion correction and **b** with motion correction. The higher SNR obtained with motion correction is clearly visible. The signal in the NP is higher than in the AF with and without motion correction

increased SNR values is that without motion correction the signal of vertebral body or tissue may affect the WASSR or CEST curves of the intervertebral discs owing to motion. This would affect the correction of field heterogeneities or the Z-spectrum.

In this study, only a single slice in the middle of the spine was acquired to keep the acquisition time within a reasonable range. By decreasing the number of measurements with presaturation at different frequency offsets or decreasing the number of averages, the imaging time may be reduced, thus enabling a 3D acquisition in a clinically acceptable examination time. The 3D approach has the advantage that motion correction can be applied in a through-plane and an in-plane direction. However, decreased image quality may be obtained because of the reduced number of measurements and signal averages.

The landmark analysis clearly shows that motion artefacts are successfully suppressed if image registration is applied. The blinded visual grading analysis of the MTR_{asym} images overlaid with the anatomical images substantiates the assumption of improvement of the quality of CEST analysis with the application of motion correction.

Prior to this study, bowel movement artefacts were shown to be effectively suppressed by a reduced-field-of-view (rFOV) method [24]. Higher reproducibility and reliability were shown with rFOV compared with acquisition without the application of rFOV. No motion correction was performed in the post-processing in order to correct motion artefacts arising from the motion of the IVDs itself. The range of MTR_{asym} values with the rFOV method is consistent with the values obtained in our study, which may be caused by the suppression of motion artefacts in both techniques.

In our study, a 3x3 Gaussian filter was applied to each image of the CEST and WASSR sequence. This filter was primarily applied to reduce image noise. Since this filter was not applied in the frequency direction, no effect is expected for Z-spectrum analysis. Because of the small size of the filter, the offset map based on the filtered WASSR images is reasonable because of the locally similar field heterogeneities in each intervertebral disc.

As in the study by Haneder et al. [1], who investigated the lumbar IVDs of 16 patients, the MTR_{asym} signal in NP was higher than in AF for Pfirrmann grades 1 and 2. In contrast to their study, our study yielded lower MTR_{asym} values. In addition, our study revealed lower standard deviations of about 1 % in NP compared with 5 % in the study by Haneder et al. for Pfirrmann grades 1 and 2. There may be several reasons for the differences obtained for the MTR_{asym} values. First, Haneder et al. used a different phase error correction algorithm shifting the minimum of the Z-spectra as determined by smoothing spline interpolation to 0 ppm [1], whereas in our study the WASSR method introduced by Kim et al. was used [21]. Second, the bowel motion was not suppressed in the study by Haneder et al., whereas in our study a saturation slab was applied to suppress intestinal peristalsis and abdominal wall motion. Third, no motion correction was applied in their study. Without motion correction, the standard deviation in the NP increased 1.5-fold compared with the value with motion correction in our study.

A robust contrast between NP and AF was also shown in the study by Kim et al. [5]. They also obtained higher MTR_{asym} values compared with our study. In contrast to the study by Haneder and his coworkers, Kim et al. used the WASSR maximum symmetry algorithm [5, 21]. In the study by Kim et al., no rFOV method or suppression of peristaltic and abdominal motion was applied. The standard deviations obtained in their study were also higher than in our study, even though they were lower than the standard deviations obtained by Haneder et al. These findings may indicate that the application of both WASSR and suppression of bowel and abdominal wall motion increase the reliability and applicability of CEST analysis in lumbar IVDs.

In the study by Melkus et al., it was observed that the gagCEST effect is dependent on both the concentration of GAG and pH values [25]. In chondroitin sulphate phantom measurements they showed a dependence of MTR_{asym} on the pH value. Highest MTR_{asym} values were obtained at pH = 7.0 to 7.2, whereas lower and higher pH values showed decreased MTR_{asym} values. The pH of the IVDs in our study as well as in the studies by Haneder et al. and Kim et al. was not determined. Future studies should be performed to determine the dependence of MTR_{asym} and pH in the human IVD. For this purpose, CEST imaging using the contrast agent iopamidol could be used, which was recently shown to be applicable in vivo [26, 27].

Recently, gagCEST imaging was performed in the knee [12, 28, 29]. Future studies need to be performed in order to investigate whether motion correction using the diffeomorphism algorithm [23] improves CEST analysis in the cartilage of the knee too.

The GAG content of ex vivo IVDs measured by CEST imaging has been reported to correlate with the fixed charged density (FCD) [30]. In addition, a dependence of CEST imaging on GAG and sodium imaging was noted [30]. An in vivo comparison of cartilage quality using gagCEST and sodium imaging was recently performed by Schmitt et al. in human knee cartilage on a 7-T MRI system [12]. Future studies could be performed comparing CEST imaging and sodium imaging in vivo in human IVDs at 3 T.

This study shows an improvement in gagCEST evaluation in the IVDs after proper compensation for subject motion during image acquisition. In future, this technique could be applied in order to improve knowledge of disc degeneration. This may complement the information obtained about disc degeneration with T2 relaxation time measurements [31].

Our study has limitations. The small number of 12 volunteers leading to 48 investigated IVDs and the absence of cartilage biopsy are drawbacks. The latter was not performed because of ethical considerations. In addition, no patients with LBP or with IVD degeneration were included, where even higher degrees of movement due to pain and discomfort may be expected.

In summary, our findings indicate that gagCEST evaluation in human lumbar IVDs can be significantly improved using motion correction. The improvement due to motion correction is reflected by an increased SNR of CEST images and a smaller scattering of the MTR_{asym} values.

Acknowledgements We gratefully acknowledge Erika Rädisch for her expert assistance with data acquisition.

Conflict of interest No conflict of interest.

References

1. Haneder S, Apprich SR, Schmitt B, et al. Assessment of glycosaminoglycan content in intervertebral discs using chemical exchange saturation transfer at 3.0 Tesla: preliminary results in patients with low-back pain. Eur Radiol. 2013;23:861–8.
2. Balagué F, Mannion AF, Pellisé F, Cedraschi C. Non-specific low back pain. Lancet. 2012;379:482–91.
3. Deyo RA, Mirza SK, Martin BI. Back pain prevalence and visit rates: estimates from U.S. national surveys, 2002. Spine. 2006;31:2724–7.
4. Hart LG, Deyo RA, Cherkin DC. Physician office visits for low back pain. Frequency, clinical evaluation, and treatment patterns from a U.S. national survey. Spine. 1995;20:11–9.
5. Kim M, Chan Q, Anthony M-P, Cheung KMC, Samartzis D, Khong P-L. Assessment of glycosaminoglycan distribution in human lumbar intervertebral discs using chemical exchange saturation transfer at 3 T: feasibility and initial experience. NMR Biomed. 2011;24:1137–44.
6. Luoma K, Riihimäki H, Luukkonen R, Raininko R, Viikari-Juntura E, Lamminen A. Low back pain in relation to lumbar disc degeneration. Spine. 2000;25:487–92.
7. De Schepper EIT, Damen J, van Meurs JBJ, et al. The association between lumbar disc degeneration and low back pain: the influence of age, gender, and individual radiographic features. Spine. 2010;35:531–6.
8. Miese F, Buchbender C, Scherer A, et al. Molecular imaging of cartilage damage of finger joints in early rheumatoid arthritis with delayed gadolinium-enhanced magnetic resonance imaging. Arthritis Rheum. 2012;64:394–9.
9. Insko EK, Clayton DB, Elliott MA. In vivo sodium MR imaging of the intervertebral disk at 4 T. Acad Radiol. 2002;9:800–4.
10. Stelzeneder D, Welsch GH, Kovács BK, et al. Quantitative T2 evaluation at 3.0 T compared to morphological grading of the lumbar intervertebral disc: a standardized evaluation approach in patients with low back pain. Eur J Radiol. 2012;81:324–30.
11. Trattnig S, Stelzeneder D, Goed S, et al. Lumbar intervertebral disc abnormalities: comparison of quantitative T2 mapping with conventional MR at 3.0 T. Eur Radiol. 2010;20:2715–22.
12. Schmitt B, Zbýň Š, Stelzeneder D, et al. Cartilage quality assessment by using glycosaminoglycan chemical exchange saturation transfer and 23Na MR imaging at 7 T. Radiology. 2011;260:257–64.
13. Guivel-Scharen V, Sinnwell T, Wolff SD, Balaban RS. Detection of proton chemical exchange between metabolites and water in biological tissues. J Magn Reson. 1998;133:36–45.
14. Miese F, Kröpil P, Ostendorf B, et al. Motion correction improves image quality of dGEMRIC in finger joints. Eur J Radiol. 2011;80:e427–31.
15. Friston KJ, Williams S, Howard R, Frackowiak RS, Turner R. Movement-related effects in fMRI time-series. Magn Reson Med. 1996;35:346–55.
16. Eddy WF, Fitzgerald M, Noll DC. Improved image registration by using Fourier interpolation. Magn Reson Med. 1996;36:923–31.
17. Herrmann K-H, Wurdinger S, Fischer DR, et al. Application and assessment of a robust elastic motion correction algorithm to dynamic MRI. Eur Radiol. 2007;17:259–64.
18. Chefd'hotel C, Hermosillo G, Faugeras O. Flows of diffeomorphisms for multimodal image registration. IEEE Int Symp Biomed Imaging 2002 Proc 2002;753–6.
19. Chefd'Hotel C, Hermosillo G, Faugeras O. A Variational Approach to Multi-Modal Image Matching. Proc. IEEE Workshop Var. Level Set Methods VLSM01. Washington, DC, USA: IEEE Computer Society; 2001. Accessed 12 September 2013. Available at http://dl.acm.org/citation.cfm?id=832286.835648.
20. Kellman P, Viallon M, Chefd'hotel C, Stemmer A, Croisille P. Improved image reconstruction incorporating non-rigid motion correction for cardiac MRI using BLADE acquisition. J Cardiovasc Magn Reson. 2009;11:P227.
21. Kim M, Gillen J, Landman BA, Zhou J, van Zijl PCM. Water saturation shift referencing (WASSR) for chemical exchange saturation transfer (CEST) experiments. Magn Reson Med. 2009;61:1441–50.
22. Pfirrmann CW, Metzdorf A, Zanetti M, Hodler J, Boos N. Magnetic resonance classification of lumbar intervertebral disc degeneration. Spine. 2001;26:1873–8.
23. Hermosillo G, Chefd'hotel C, Faugeras O. Variational methods for multimodal image matching. Int J Comput Vis. 2002;50:329–43.
24. Liu Q, Jin N, Fan Z, et al. Reliable chemical exchange saturation transfer imaging of human lumbar intervertebral discs using reduced-field-of-view turbo spin echo at 3.0 T. NMR Biomed. 2013;26:1672–9.
25. Melkus G, Grabau M, Karampinos DC, Majumdar S. Ex vivo porcine model to measure pH dependence of chemical exchange saturation transfer effect of glycosaminoglycan in the intervertebral disc. Magn Reson Med. 2014;71:1743–9.
26. Müller-Lutz A, Khalil N, Schmitt B, et al. Pilot study of iopamidol-based quantitative pH imaging on a clinical 3T MR scanner. MAGMA 2014;10.1007/s10334-014-0433-8.
27. Longo DL, Busato A, Lanzardo S, Antico F, Aime S. Imaging the pH evolution of an acute kidney injury model by means of iopamidol, a MRI-CEST pH-responsive contrast agent. Magn Reson Med. 2013;70:859–64.
28. Wei W, Jia G, Flanigan D, Zhou J, Knopp MV. Chemical exchange saturation transfer MR imaging of articular cartilage glycosaminoglycans at 3 T: accuracy of B0 Field Inhomogeneity corrections with gradient echo method. Magn Reson Imaging. 2014;32:41–7.
29. Singh A, Haris M, Cai K, et al. Chemical exchange saturation transfer magnetic resonance imaging of human knee cartilage at 3 T and 7 T. Magn Reson Med. 2012;68:588–94.
30. Saar G, Zhang B, Ling W, Regatte RR, Navon G, Jerschow A. Assessment of glycosaminoglycan concentration changes in the intervertebral disc via chemical exchange saturation transfer. NMR Biomed. 2012;25:255–61.
31. Takashima H, Takebayashi T, Yoshimoto M, et al. Correlation between T2 relaxation time and intervertebral disk degeneration. Skeletal Radiol. 2012;41:163–7.

Magnetic Resonance Imaging 34 (2016) 771–778

Contents lists available at ScienceDirect

Magnetic Resonance Imaging

journal homepage: www.mrijournal.com

Original contribution

Improvement of water saturation shift referencing by sequence and analysis optimization to enhance chemical exchange saturation transfer imaging

Anja Müller-Lutz [a], Felix Matuschke [a], Christoph Schleich [a,*], Frithjof Wickrath [a], Johannes Boos [a], Benjamin Schmitt [b], Hans-Jörg Wittsack [a]

[a] University Dusseldorf, Medical Faculty, Department of Diagnostic and Interventional Radiology, D-40225 Dusseldorf, Germany
[b] Siemens Healthcare Pty Ltd, Magnetic Resonance, 160 Herring Road, Macquarie Park NSW, 2113, Australia

ARTICLE INFO

Article history:
Received 17 December 2015
Revised 18 February 2016
Accepted 3 March 2016

Keywords:
Chemical exchange saturation transfer
Water saturation shift referencing
Monte-Carlo-simulations
Field inhomogeneity correction
Brain
Intervertebral disks

ABSTRACT

Purpose: To optimize B_0-field inhomogeneity correction for chemical exchange saturation transfer (CEST) imaging by investigating different water saturation shift referencing (WASSR) Z-spectrum shapes and different frequency correction techniques.
Methods: WASSR Z-spectra were simulated for different B_1-fields and pulse durations (PD). Two parameter settings were used for further simulations and experiments (WASSR1: $B_1 = 0.1\,\mu T$, PD = 50 ms; WASSR2: $B_1 = 0.3\,\mu T$, PD = 40 ms). Four frequency correction techniques were investigated: 1) MinW: Minimum of the spline-interpolated WASSR-spectrum; 2) MSCF: maximum symmetry center frequency algorithm; 3) PMSCF: further development of MSCF algorithm; 4) BFit: fit with Bloch equations. Performance of frequency correction was assessed with Monte-Carlo simulations and in-vivo MR examinations in the brain and intervertebral disks.
Results: Different shapes of WASSR-Z-spectra were obtained by changing B_1 and PD including spectra with one (1-Peak) or two (2-Peak) minima. WASSR1 resulted in 1-Peak WASSR-spectrum, whereas WASSR2 resulted in 2-Peak WASSR-spectrum. Both Monte-Carlo simulations and in-vivo MR examinations revealed highest accuracy of field-inhomogeneity correction with WASSR1 combined with PMSCF or BFit.
Conclusion: Using a WASSR sequence, which results in a Z-spectrum with a single absorption peak, in combination with advanced postprocessing algorithms enables improved B_0-field inhomogeneity correction for CEST imaging.

1. Introduction

Biochemical imaging using chemical exchange saturation transfer (CEST) contrast is highly sensitive to magnetic field inhomogeneities [1,2]. These field inhomogeneities can shift the center of the Z-spectrum [2] and cause false results of CEST analysis.

Different methods to correct field inhomogeneities have been introduced. These methods include field maps, field inhomogeneity corrections using the minimum of either the Z-spectrum itself or of a fitted Z-spectrum (e.g. Lorentzian-shape fit, cubic spline fit or polynomial fit), and the maximum symmetry center frequency algorithm applied to a separately acquired water saturation shift referencing (WASSR) sequence [1,3–10]. WASSR has demonstrated the ability to be easily incorporated into CEST protocols along with robust performance across a variety of CEST applications [1,11–14].

A well-known phenomenon of CEST Z-spectra is that they can have different shapes including single or multiple minima due to different amount of direct water saturation (DWS) in dependence on pulse irradiation properties and different relaxation times [15–17]. The CEST effect depends on the field strength of the main magnetic field. Although the CEST effect is higher at high B_0 fields (7 T or higher), CEST measurements at lower field strengths have successfully detected exchangeable protons such as amide protons, amine protons and hydroxyl protons [12,18,19]. If human subjects are involved, measurements are usually realized at clinical MR systems. These clinical MR systems often have specific absorption rate (SAR) and hardware limitations and therefore pulsed CEST is used [17,20]. For WASSR data acquisition, it is not necessary to apply a pulsed acquisition scheme, since small B_1-fields and short durations of the radiofrequency irradiation keep SAR and hardware requirements in a feasible range. However, CEST imaging at clinical MR systems

* Corresponding author at: University Dusseldorf, Department of Diagnostic and Interventional Radiology, Moorenstr. 5, D-40225 Düsseldorf, Germany.
E-mail address: Christoph.Schleich@med.uni-duesseldorf.de (C. Schleich).

http://dx.doi.org/10.1016/j.mri.2016.03.013
0730-725X/

requires higher B_1-fields and therefore pulsed CEST acquisition has to be considered.

In this study, we aim to optimize the WASSR sequence and analysis software for an improved B_0 inhomogeneity correction on a clinical 3 T MRI system.

2. Materials and methods

Simulations and data analysis were performed using MATLAB (MathWorks, Natick, MA, R2012b).

2.1. Field inhomogeneity correction techniques

Four different field correction techniques were applied to the WASSR [1] data in our study:

i. The frequency offset was determined according to the minimum of the spline-interpolated WASSR data (*MinW*).
ii. The frequency offset was calculated with the *MSCF*-algorithm introduced by Kim et al. [1] (*MSCF*)
iii. A self-developed, enhanced version of the MSCF-algorithm was used: periodic MSCF-algorithm (*PMSCF*). Compared with the regular MSCF algorithm introduced by Kim et al. [1] the PMSCF algorithm includes all WASSR data to calculate the offset frequency. We aim to improve the accuracy of the algorithm by this method. Using the primary introduced WASSR algorithm, problems will occur including data at the boundaries. To avoid this problems, we extended the data according to
$Z(\omega_i + P) = Z(\omega_i) \mid P = \omega_{i=N} + \omega_{i=1} + \delta\omega;\ \delta\omega = \omega_{i+1} - \omega_i$ for all i
Thereby, $Z(\omega)$ is the normalized signal intensity at the offset frequency ω.
iv. The frequency offset was determined using a Bloch-fit (*BFit*). We fit the determined WASSR data using the method “nonlinear bisquare”. As fit model we used solution of the Bloch equations for our pulse sequence. We used the solution algorithm of Bloch equations as introduced by Murase et al. [21].

2.2. Numerical simulations

For all numerical simulations a magnetic field strength of 3 T was assumed. WASSR-spectra were calculated by solving the time course of spin magnetization using the Bloch equations [21,22]. Relaxation parameters for simulations were chosen representative of gray matter as $T_1 = 1331$ ms and $T_2 = 110$ ms [23].

WASSR-curves were simulated with $B_1 = 0.1$ μT and $B_1 = 0.3$ μT with varying pulse durations (PD) in the range of 0 ms to 50 ms with a step size of 1 ms. We used one Gaussian-shaped pulse for the simulation. The shape of the WASSR-curves were analyzed regarding the number of minima.

Two WASSR-curves with different shapes were used for further simulations: a) PD = 50 ms, $B_1 = 0.1$ μT (WASSR1); b) PD = 40 ms, $B_1 = 0.3$ μT (WASSR2). Z-spectra for these WASSR simulations were simulated in a range of −1.0 ppm to 1.0 ppm with a step size of 0.05 ppm.

To verify the accuracy of the above mentioned field inhomogeneity correction algorithms, $n_{simWASSR} = 10{,}000$ noisy frequency shifted WASSR-spectra were created by Monte-Carlo simulations. WASSR spectra with normally distributed offset ($\sigma_O = 0.1$ ppm) were calculated. Rician noise according to ref.[24, 25] was added with $\sigma_N = 0.025$, $\sigma_N = 0.05$ and $\sigma_N = 0.1$.

2.3. Accuracy of frequency correction

The frequency shift of each Monte-Carlo-simulated WASSR-spectrum was determined by the four techniques MinW, MSCF, PMSCF and BFit for WASSR1 and WASSR2. The residual error Δ (difference between calculated and original simulated frequency shift) was determined. Descriptive analysis of the residual error Δ was performed for both presaturation modules and for each frequency correction algorithm, respectively. Statistical analysis was performed using the Wilcoxon signed rank test. P-values below 0.05 were considered to be significant.

2.4. MR measurements

Two volunteers underwent MRI to show the transferability of our theoretically obtained results to in vivo measurements. The study was approved by the local ethics committee, and written informed consent was obtained from both volunteers. The examinations were performed on a clinical whole-body 3 T MR system (Magnetom Trio, A Tim System, Siemens Healthcare, Erlangen, Germany).

The first volunteer underwent an MRI examination of the brain. Signal reception was performed with a 12-channel birdcage head coil. The MR protocol (protocol 1) included a localizer, a CEST sequence for APT-CEST imaging, two WASSR data acquisitions with different B_1-amplitudes of the Gaussian-shaped presaturation pulse and, to differentiate white matter (WM) and gray matter (GM), a quantitative T_2-sequence. Single-slice turbo gradient echo imaging was used as host sequence for CEST and WASSR data acquisitions. Details of theses sequences are listed in Table 1. Parameters of the quantitative T_2 sequence were: FOV = 230 × 230 mm^2, basic resolution = 192 × 192, slice thickness = 6 mm, TE = [9.1, 18.2, 27.3, 36.4, 45.5, 54.6, 63.7, 72.8, 81.9, 91.0] ms, TR = 800 ms, flip angle = 180°, number of signal averages = 2, GRAPPA acceleration factor = 2.

The second volunteer underwent an MRI examination of lumbar intervertebral disks. Signal reception was performed with a spine matrix coil. The MR protocol (protocol 2) included a localizer, gagCEST imaging and two WASSR data acquisitions with different B_1-amplitudes of the presaturation module (Table 1).

In both examinations (brain and intervertebral disks), no shimming was performed between the CEST and both WASSR sequences, thus leading to the same center frequency of CEST and WASSR sequences.

For each acquired WASSR data, the four previously introduced algorithms (MinW, MSCF, PMSCF and BFit) were applied to obtain an offset map. These offset maps were further used to correct the acquired CEST spectra. MTR_{asym} maps were determined based on the corrected CEST spectra. Thereby, MTR_{asym} was evaluated in a range of 3.25 ppm to 3.75 ppm for APT-CEST imaging corresponding to the resonance frequency range of amide protons (resonance frequency at 3.5 ppm [26,27]) and in a range of 0.9 ppm to 1.1 ppm for gagCEST imaging corresponding to the resonance frequency range of hydroxyl protons (resonance frequency at 1 ppm [7]). MTR_{asym} was calculated according to

$$MTR_{asym}\left(\omega_{pool}, \Delta\omega\right) = mean\left(MTR_{asym}(\omega_i)\right)$$
$$\omega_i \in \left[\omega_{pool} - \frac{\Delta\omega}{2}, \omega_{pool} + \frac{\Delta\omega}{2}\right]$$

where ω_{pool} is the pool position (1 ppm for gagCEST imaging and 3.5 ppm for APT-CEST imaging) and $\Delta\omega$ is the frequency range (0.2 ppm for gagCEST imaging and 0.5 ppm for APT-CEST imaging). We used a sample step size of $h = \omega_{i+1} - \omega_i = 0.01$ ppm.

Table 1
MR parameters of the in-vivo APT-CEST and in-vivo gagCEST measurements and their corresponding WASSR sequences.

	APT-CEST (brain)	WASSR1 (brain)	WASSR2 (brain)	gagCEST (IVD)	WASSR1 (IVD)	WASSR2 (IVD)
Acquisition duration [min:sec]	5:53	2:19	2:16	11:13	3:18	3:13
Host Sequence Parameters						
Basic Resolution	192 × 192	192 × 192	192 × 192	192 × 192	192 × 192	192 × 192
Field of View [mm x mm]	230 × 230	230 × 230	230 × 230	300 × 300	300 × 300	300 × 300
Slice thickness [mm]	6	6	6	5	5	5
k-space lines per shot	34	34	34	64	64	64
TE/TR [ms/ms]	3.03/1400	3.03/550	3.03/540	3.93/1650	3.93/392	3.93/382
Flip angle [°]	12	12	12	12	12	12
Number of Signal Averages	2	2	2	2	2	2
Presaturation Pulse Train Parameters						
Number of measured frequency offsets	41	41	41	33	41	41
Frequency range [ppm]	−5.0 – 5.0	−1.0 – 1.0	−1.0 – 1.0	−4.8 – 4.8	−1.0 – 1.0	1.0–1.0
B_1-continous wave amplitude equivalent (B_1-CWAE) [μT]	1.5	0.1	0.3	0.7	0.1	0.3
Number of presaturation pulses	5	1	1	7	1	1
Pulse-shape	Gaussian	Gaussian	Gaussian	Gaussian	Gaussian	Gaussian
Pulse duration [ms]	100	50	40	100	50	40
Interpulse delay [ms]	100	No	No	100	No	No

MTR_{asym} values were determined in GM and WM of the brain and in the nucleus pulposus (NP) and annulus fibrosus (AF) in all five lumbar intervertebral disks.

To determine the quality of the obtained MTR_{asym} maps with the two different WASSR sequences and the four offset correction techniques, respectively, the standard deviation was determined for regions of interest (ROI). The standard deviation was chosen as a measure of homogeneity since similar MTR_{asym} values would be expected in each selected ROI.

For brain MRI, 20 regions of interests were automatically delineated by an in-house developed MATLAB script in each GM and WM. To draw ROIs, seed points were selected randomly in GM and WM. Afterwards, region growing was performed until the ROI reached a pixel number of 25.

For MRI of the lumbar intervertebral disks, each disk was automatically segmented into NP and AF as described by Schleich and co-workers [28]. For further analysis, each NP and each AF was split into left and right parts.

Descriptive analysis of the standard deviation of the MTR_{asym} values (averaged over all ROIs) was performed. Data were tested for normal distribution using the Kolmogorov–Smirnov-test. Wilcoxon (for non-normally distributed data) or the paired Student's t-test (for normally distributed data) was applied. P-values below 0.05 were considered significant.

3. Results

3.1. Numerical Simulations

The simulation showed different shapes of WASSR curves for different B_1-amplitudes and pulse durations. For the low B_1-amplitude of 0.1 μT only a single minimum was found in WASSR spectra, whereas for a B_1-amplitude of 0.3 μT either a single minimum or two minima were found depended on the PD. Two minima were more pronounced for higher pulse durations (Fig. 1).

The WASSR sequence with PD = 50 ms, B_1 = 0.1 μT (WASSR1) resulted in a WASSR-spectrum with one minimum, whereas the WASSR sequence with PD = 40 ms and B_1 = 0.3 μT (WASSR2) resulted in a WASSR-spectrum with two minima. These WASSR-curves were utilized for further Monte-Carlo simulations.

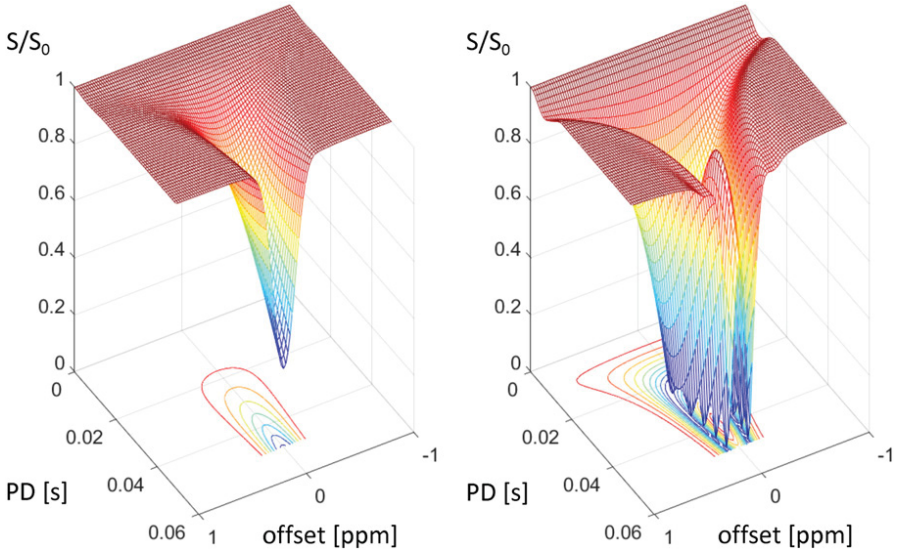

Fig. 1. WASSR curves with B_1 amplitude of 0.1 μT (left) and 0.3 μT (right) with different pulse durations (PD).

Table 2
Descriptive analysis of the residual error Δ for 1-peak and 2-peak WASSR spectra.

sequence	algorithm	σ	Mean [ppm]	Median [ppm]	standard deviation [ppm]	Minimum [ppm]	Maximum [ppm]
WASSR1	MinW	0.025	0.014	0.013	0.010	<0.001	0.055
		0.050	0.019	0.016	0.014	<0.001	0.075
		0.100	0.026	0.022	0.019	<0.001	0.118
	MSCF	0.025	0.002	0.002	0.002	<0.001	0.012
		0.050	0.005	0.004	0.003	<0.001	0.032
		0.100	0.011	0.009	0.012	<0.001	0.316
	PMSCF	0.025	0.002	0.002	0.002	<0.001	0.011
		0.050	0.004	0.004	0.003	<0.001	0.024
		0.100	0.011	0.009	0.008	<0.001	0.068
	BFit	0.025	0.002	0.002	0.002	<0.001	0.024
		0.050	0.004	0.003	0.003	<0.001	0.037
		0.100	0.009	0.007	0.007	<0.001	0.077
WASSR2	MinW	0.025	0.137	0.137	0.007	0.121	0.156
		0.050	0.137	0.137	0.008	0.099	0.159
		0.100	0.135	0.136	0.013	0.089	0.183
	MSCF	0.025	0.002	0.001	0.002	<0.001	0.016
		0.050	0.003	0.002	0.003	<0.001	0.029
		0.100	0.006	0.004	0.008	<0.001	0.158
	PMSCF	0.025	0.001	0.001	0.001	<0.001	0.005
		0.050	0.002	0.002	0.002	<0.001	0.009
		0.100	0.004	0.004	0.003	<0.001	0.025
	BFit	0.025	0.001	0.001	0.001	<0.001	0.013
		0.050	0.002	0.001	0.002	<0.001	0.044
		0.100	0.005	0.004	0.006	<0.001	0.109

3.2. Accuracy of frequency correction

Kolmogorov–Smirnov-test revealed a non-normal distribution of the data. Therefore, the Wilcoxon test was applied in order to analyze significances.

Descriptive analysis of the determined residual error Δ of the Monte-Carlo-simulated WASSR-spectra with the four algorithms MinW, MSCF, PMSCF and BFit (Table 2) revealed significant higher residual errors Δ for 2-Peak WASSR spectra compared to 1-Peak WASSR spectra for the same noise level. Investigating all noise levels, the method MinW resulted in highest residual errors Δ (1-Peak WASSR: 0.020 ± 0.016; 2-Peak WASSR: 0.137 ± 0.010). Smaller residual errors Δ were obtained with the methods MSCF, PMSCF and BFit. BFit resulted in lower Δ values (1-Peak WASSR: 0.005 ppm ± 0.005 ppm; 2-Peak WASSR: 0.003 ppm ± 0.004 ppm), followed by PMSCF (1-Peak WASSR: 0.006 ppm ± 0.006 ppm; 2-Peak WASSR: 0.002 ppm ± 0.002 ppm) and MSCF (1-Peak WASSR: 0.006 ppm ± 0.008 ppm; 2-Peak WASSR: 0.003 ppm ± 0.005 ppm). The residual errors Δ found for the different algorithms were significantly different from each other.

3.3. MR measurements

CEST and two WASSR sequences were successfully acquired in the brain and in lumbar intervertebral disks. Offset maps

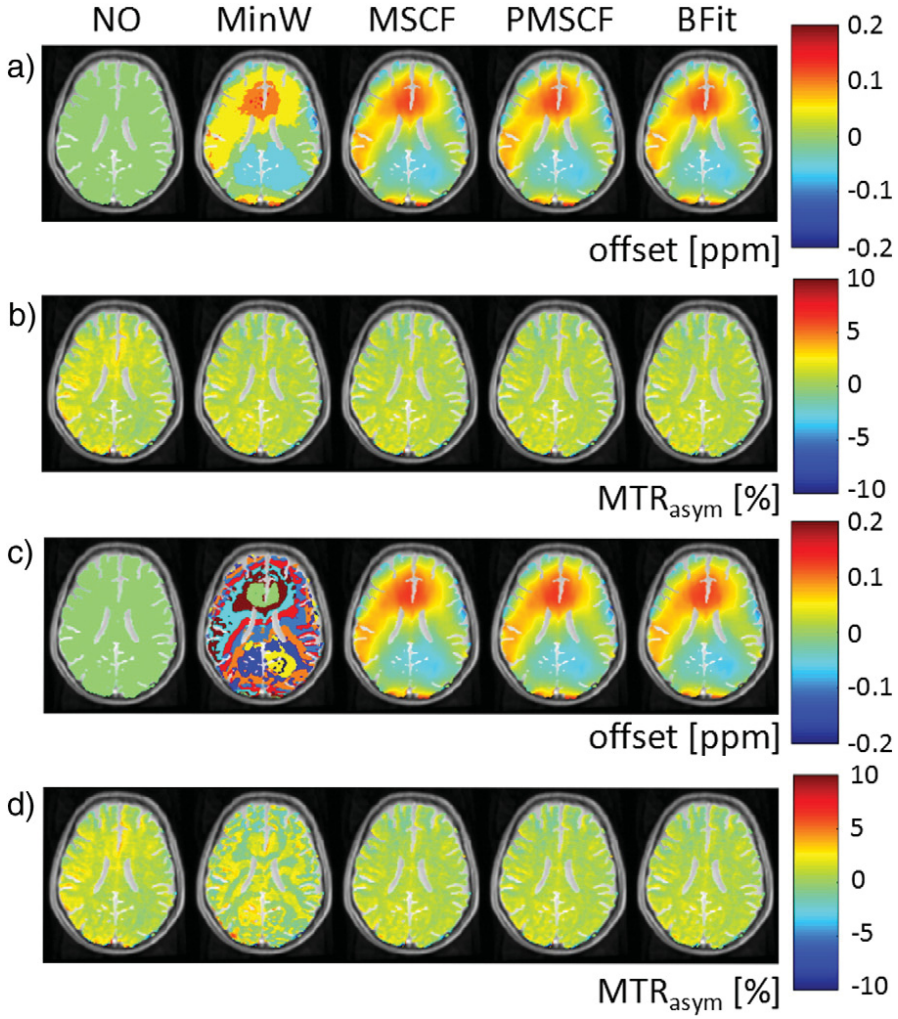

Fig. 2. Offset [ppm] (a,c) and MTR_{asym} [%] (b,d) maps obtained in the brain of one volunteer without offset correction (NO) and with the four offset correction techniques MinW, MSCF, PMSCF and BFit. Thereby, a and b are based on the WASSR1 sequence, whereas c and d are based on WASSR2 sequence. Similar results in both, offset maps and MTR_{asym} maps were obtained with MSCF, PMSCF and BFit. The results obtained without correction and with the correction method MinW applied to 2-Peak WASSR Z-spectra showed large deviations compared to the other techniques.

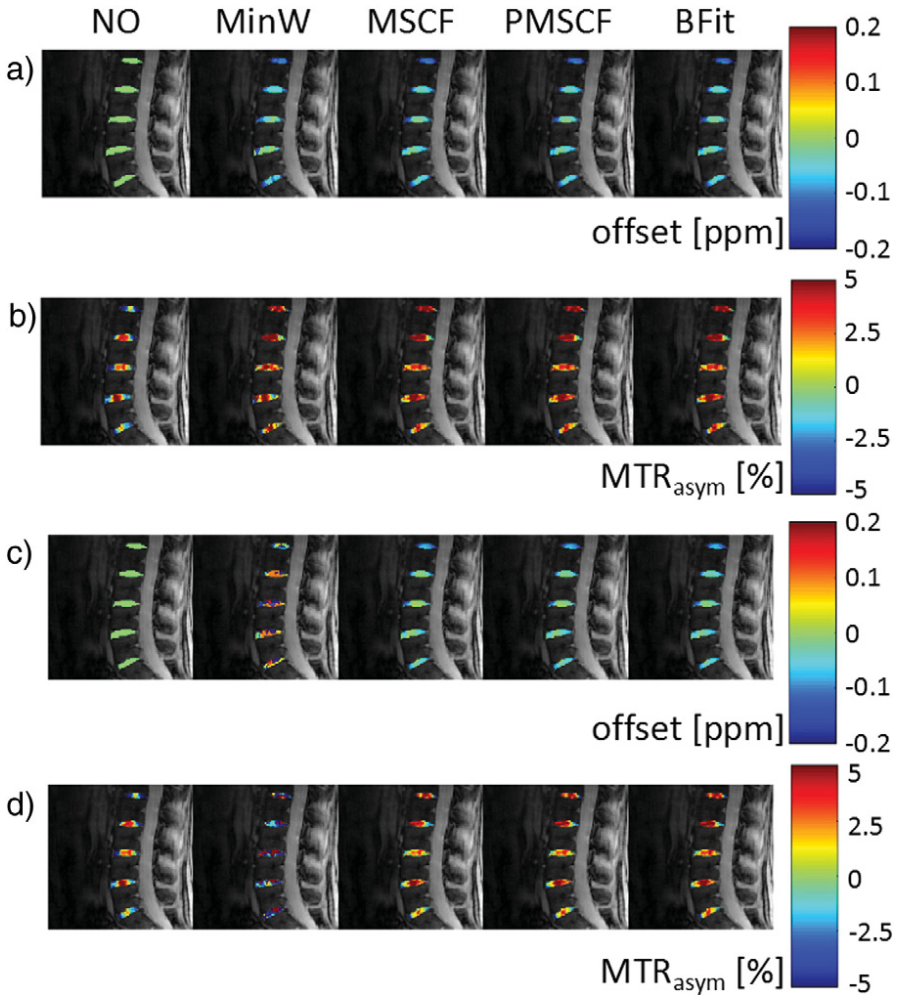

Fig. 3. Offset [ppm] (a,c) and MTR_{asym} [%] (b,d) maps obtained in lumbar intervertebral disks of one volunteer without offset correction (NO) and with the four offset correction techniques MinW, MSCF, PMSCF and BFit. Thereby, a and b are based on the WASSR1 sequence, whereas c and d are based on the WASSR2 sequence. Similar results in both offset maps and MTR_{asym} maps were obtained with MSCF, PMSCF and BFit. The results obtained without correction and with the correction method MinW applied to 2-Peak WASSR Z-spectra showed large deviations compared to the other techniques.

were successfully determined without any correction and with the four offset correction techniques MinW, MSCF, PMSCF and BFit (Figs. 2, 3). After calculation of CEST and MTR_{asym} curves (Supplementary Material S1), MTR_{asym} maps were determined (Figs. 2, 3). The offset map obtained with WASSR2 combined with an offset analysis using the MinW algorithm illustrated high differences from the offset maps obtained with the algorithms MSCF, PMSCF and BFit and from the offset map obtained with WASSR1. Offset maps obtained with WASSR1 and the MinW algorithm were more similar to the results obtained by the algorithms MSCF, PMSCF and BFit with the same presaturation pulse parameters, but the offsets were less continuously distributed. Visually, MTR_{asym} maps obtained with WASSR1 and WASSR2 were similar for the algorithms MSCF, PMSCF and BFit in both in-vivo measurements (Figs. 2, 3).

CEST analysis showed higher MTR_{asym} values in GM compared to WM and higher MTR_{asym} values in NP compared to AF (Table 3).

In both, GM and NP, WASSR1 resulted in a WASSR spectrum with a single minimum (1-Peak WASSR), whereas WASSR2 resulted in a spectrum with two minima (2-Peak WASSR) (Fig. 4).

Kolmogorov–Smirnov analysis revealed normal distribution of ΔMTR_{asym} values for each region and all investigated offset correction techniques combined with either WASSR1 or WASSR2.

Table 3
Mean and standard deviation of MTR_{asym} values over all pixels in GM, WM, NP and AF.

	MTR_{asym} (GM) [%]	MTR_{asym} (WM) [%]	MTR_{asym} (NP) [%]	MTR_{asym} (AF) [%]
1-Peak, MinW	**1.124 ± 1.581**	**0.941 ± 0.727**	**4.875 ± 2.201**	**2.898 ± 3.074**
1-Peak, MSCF	**1.069 ± 1.598**	**0.882 ± 0.688**	**4.635 ± 1.714**	**2.859 ± 2.383**
1-Peak, PMSCF	**1.071 ± 1.598**	**0.882 ± 0.687**	**4.645 ± 1.716**	**2.936 ± 2.372**
1-Peak, BFit	**1.097 ± 0.808**	**0.890 ± 0.592**	**4.769 ± 1.755**	**2.875 ± 2.420**
2-Peak, MinW	**1.013 ± 2.602**	**0.849 ± 1.458**	**4.861 ± 8.530**	**−0.001 ± 6.844**
2-Peak, MSCF	**1.032 ± 1.631**	**0.839 ± 0.695**	**3.394 ± 1.759**	**1.335 ± 2.511**
2-Peak, PMSCF	**1.036 ± 1.632**	**0.844 ± 0.695**	**3.670 ± 1.808**	**1.581 ± 2.499**
2-Peak, BFit	**1.072 ± 0.817**	**0.863 ± 0.603**	**4.152 ± 1.789**	**1.959 ± 2.531**

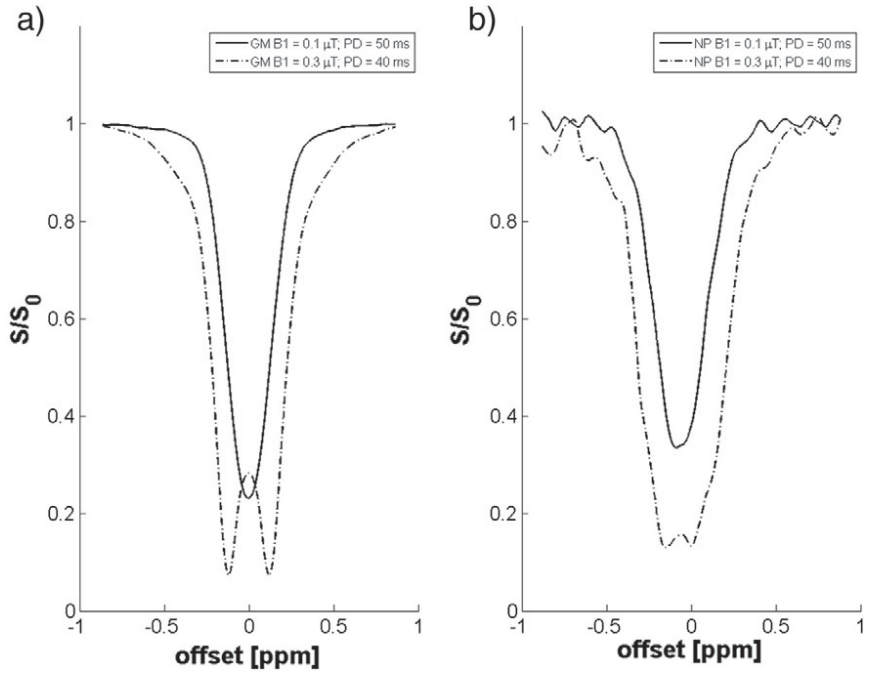

Fig. 4. WASSR spectra obtained in gray matter GM (a) and in nucleus pulposus NP (b) with different WASSR parameters. Similar to the results obtained in the simulations, $B_1 = 0.1\ \mu T$ and PD = 50 ms resulted in a 1-Peak WASSR spectrum in both GM and NP, whereas $B_1 = 0.3\ \mu T$ and PD = 40 ms resulted in a double-Peak (2-Peak) WASSR spectrum. The double-Peak was less pronounced in the NP compared to the GM.

Therefore, Student's t-test was applied for further analysis of statistical significance.

Descriptive analysis of the standard deviation obtained for the regions of interest is provided in Table 4.

Descriptive and statistical analysis demonstrated significant higher ΔMTR_{asym} values for regions of interest in NP and AF for the WASSR2 sequence compared to the WASSR1 sequence when MinW was applied as offset correction method (Tables 4, 5). No significant differences were found for ΔMTR_{asym} values between WASSR1 and WASSR2 when using PMSCF and BFit, respectively (Tables 4, 5). (See Table 6).

For both sequences WASSR1 and WASSR2, MinW resulted in higher ΔMTR_{asym} values compared to ΔMTR_{asym} values obtained with MSCF, PMSCF or BFit except for WASSR2 in WM (Table 4). These differences were significant. No significant differences were found between ΔMTR_{asym} values obtained with the algorithms PMSCF and BFit except for WASSR1 in NP, where lower ΔMTR_{asym} values were obtained with PMSCF compared to BFit. No significant difference of ΔMTR_{asym} values were obtained between the algorithm MSCF and PMSCF and MSCF and BFit (Tables 4, 6).

4. Discussion

In this study we determined the influence of different shapes of WASSR spectra for the assessment of field inhomogeneities in CEST MRI. Furthermore we compared four different techniques to

Table 4
Standard deviation of MTR_{asym} [%] calculated for the ROIs using the 1-Peak or 2-Peak WASSR sequence in GM, WM, NP and AF.

	Mean [%]	Median [%]	Standard deviation [%]	Minimum [%]	Maximum [%]	Mean [%]	Median [%]	Standard deviation [%]	Minimum [%]	Maximum [%]
	GM, 1-Peak					GM, 2-Peak				
MinW	1.189	1.208	0.444	0.165	1.987	1.159	1.230	0.900	−0.527	2.728
MSCF	1.141	1.234	0.442	0.1505	2.043	1.108	1.200	0.471	−0.004	2.051
PMSCF	1.142	1.273	0.444	0.107	2.046	1.113	1.197	0.472	−0.002	2.072
BFit	1.147	1.239	0.443	0.115	2.060	1.120	1.205	0.464	0.033	2.067
	WM, 1-Peak					WM, 2-Peak				
MinW	1.068	1.034	0.398	0.457	1.971	0.940	0.980	0.957	−0.444	2.618
MSCF	0.993	1.007	0.341	0.432	1.772	0.967	0.981	0.341	0.341	1.706
PMSCF	0.991	1.006	0.340	0.444	1.770	0.973	0.986	0.343	0.342	1.720
BFit	0.995	1.003	0.339	0.444	1.776	0.993	1.006	0.342	0.365	1.755
	NP, 1-Peak					NP, 2-Peak				
MinW	1.925	1.874	0.854	0.673	3.007	7.135	7.369	3.057	0.496	11.528
MSCF	1.267	1.205	0.499	0.672	2.033	1.252	1.222	0.392	0.560	1.926
PMSCF	1.262	1.258	0.508	0.651	2.014	1.318	1.286	0.426	0.534	2.004
BFit	1.328	1.320	0.545	0.659	2.138	1.291	1.221	0.465	0.589	2.110
	AF, 1-Peak					AF, 2-Peak				
MinW	2.557	2.767	0.892	1.268	3.895	6.549	6.819	1.489	4.230	8.256
MSCF	1.738	1.582	0.686	0.861	3.074	1.859	1.642	0.782	1.128	3.236
PMSCF	1.799	1.571	0.743	0.889	3.187	1.894	1.771	0.797	1.099	3.280
BFit	1.794	1.558	0.707	1.007	3.212	1.953	1.678	0.821	1.137	3.487

Table 5
P-values between ΔMTR_{asym} obtained with the 1-Peak and 2-Peak WASSR sequences for each offset correction technique.

	GM	WM	NP	AF
p_{MinW} (1-Peak, 2-Peak)	<0.001	<0.001	<0.001	<0.001
p_{MSCF} (1-Peak, 2-Peak)	0.431	0.012	0.869	<0.001
p_{PMSCF} (1-Peak, 2-Peak)	0.565	0.130	0.523	0.176
p_{BFit} (1-Peak, 2-Peak)	0.826	0.456	0.693	0.035

acquire offset maps and evaluated these offset maps using simulations and measured MRI data of the human brain and intervertebral lumbar disks. These four techniques are the frequently used algorithms MinW and MSCF [1,5,29,30], the self-developed refinement of the MSCF algorithm (PMSCF) algorithm and the processing-time-intensive algorithm BFit, which fits the Bloch equations to the WASSR spectra to determine the frequency offset. Results with low residual error in the simulations and low ΔMTR_{asym} values in the in-vivo measurements were found for WASSR spectra with only one minimum (1-Peak WASSR) and for the algorithms PMSCF and BFit. It should be noted, that the low residual error with the algorithm BFit during the simulation might in part be due to the generation of the curves with Bloch equations overlaid by noise.

In our study we obtained higher MTR_{asym} values in GM compared to WM and higher MTR_{asym} values in NP compared to AF. These results are consistent with previous findings [5,12,31,32].

Our in vivo results were in good agreement with the findings from our simulation study. The results found in both studies illustrate the necessity to consider both, the WASSR pulse sequence and an appropriate postprocessing method for frequency offset correction. The applicability of a 1-Peak WASSR sequence combined with PMSCF or BFit in a large number of volunteers or patients in different body regions and for different CEST contrast agents was beyond the scope of this article, but should be addressed in future studies.

In our study, we applied different offset correction techniques to the brain and to intervertebral disks. The brain served as an example for a region with weak field inhomogeneities, whereas the human lumbar intervertebral disks served as an example for a region with strong field inhomogeneities. In the brain, we used APT-CEST imaging at an offset frequency of 3.5 ppm, whereas in the lumbar intervertebral disks we investigated gagCEST imaging at an offset frequency of 1 ppm. GagCEST imaging is very sensitive to magnetic field inhomogeneities due to the small offset frequency of the hydroxyl protons to water [7]. In both regions, we could show a high performance of the offset frequency algorithms MSCF, PMSCF and BFit.

Our study was performed at a field strength of 3 T. We expect to obtain different WASSR pulse shapes in dependence on B_1 field strength and pulse duration at other field strengths such as 1.5 T or 7 T. At higher field strengths, the width of the WASSR peak will decrease according to the Bloch equations.

In the past, different pulse shapes have been used to acquire CEST data including rectangular [33], gaussian-shaped [17,34], sinc-shaped [35] or Fermi pulses [36,37]. Performing experiments with other pulse shapes will require finding optimal parameters for the respective pulse shapes in order to obtain a 1-Peak WASSR Z-spectrum.

The shape of the WASSR-Z-spectra depends on different parameters such as longitudinal and transversal relaxation time as well as the irradiation flip angle (Supplementary Material S2). In order to obtain only one minimum of the WASSR-Z-spectrum, an irradiation flip angle less than 90° is desirable. Ideally, the B_1 field strength and irradiation duration should be optimized for the expected relaxation times. It should be borne in mind that in real data acquisition the preset B_1 value might not be identical with the B_1 value in a specific voxel. Systematic deviations of the B_1 value as well as a distribution around this systematically changed B_1 value are expected. Application of a preset irradiation flip angle of 90° might therefore result in little lower or higher flip angles, which might change the WASSR-Z-spectrum shape.

One limitation in the present study is that we do not evaluate the signal to noise ratio for specific anatomic locations in the brain. The signal to noise ratio might be used as quantity to assess the applicability of each method in relevant anatomic regions. However, in our study we measured only one slice position in one volunteer. For statistical analysis of relevant anatomic regions, 3D data sets of more volunteers would be necessary.

One question might be if the improved offset correction techniques are always necessary in order to quantify the CEST effect with high accuracy. Our results indicate that a simple determination of the minimum of the spline-interpolated WASSR spectrum might be sufficient in case of high frequency offsets and low field inhomogeneities (WM, APT-CEST). With higher frequency offsets of the CEST-visible protons - which is the case in PARACEST agents [11] – field inhomogeneity correction might become less important. However, several endogenous CEST-visible protons resonate very close to water. Substances most prone to field inhomogeneity artifacts are for example glycogen and glycosaminoglycans [1,12]. For these substances an appropriate field inhomogeneity correction is essential.

Table 6
P-values between ΔMTR_{asym} obtained with different offset correction techniques (MinW, MSCF, PMSCF and BFit) obtained with 1-Peak or 2-Peak WASSR sequences.

	GM	WM	NP	AF
$P_{1\text{-Peak}}$ (MinW, MSCF)	0.019	0.008	0.009	0.008
$P_{1\text{-Peak}}$ (MinW, PMSCF)	0.022	0.007	0.006	0.015
$P_{1\text{-Peak}}$ (MinW, BFit)	0.022	0.005	0.008	0.006
$P_{1\text{-Peak}}$ (MSCF, PMSCF)	0.502	0.224	0.789	0.176
$P_{1\text{-Peak}}$ (MSCF, BFit)	0.569	0.180	0.098	0.183
$P_{1\text{-Peak}}$ (PMSCF, BFit)	0.753	0.474	0.019	0.922
$P_{2\text{-Peak}}$ (MinW, MSCF)	<0.001	<0.001	<0.001	<0.001
$P_{2\text{-Peak}}$ (MinW, PMSCF)	<0.001	<0.001	<0.001	<0.001
$P_{2\text{-Peak}}$ (MinW, BFit)	<0.001	<0.001	<0.001	<0.001
$P_{2\text{-Peak}}$ (MSCF, PMSCF)	0.758	0.619	0.018	0.305
$P_{2\text{-Peak}}$ (MSCF, BFit)	0.807	0.166	0.416	0.085
$P_{2\text{-Peak}}$ (PMSCF, BFit)	0.935	0.196	0.516	0.263

5. Conclusion

An improvement of field inhomogeneity correction on a voxel-by-voxel basis is feasible using an optimized WASSR sequence which results in a Z-spectrum with only one minimum. In the brain and the intervertebral disks, lowest standard deviation of MTR_{asym} can be achieved using the algorithms MSCF, PMSCF or BFit to determine the offset frequency of water. For optimal offset correction, a determination of the minimum of the spline-interpolated Z-spectrum results in a lower performance compared to the offset correction techniques MSCF, PMSCF and BFit. Out of the four investigated techniques, PMSCF and BFit led to the highest accuracy of offset correction in both, simulations and in-vivo. An appropriate WASSR sequence with a single WASSR Z-spectrum minimum in combination with either PMSCF or BFit offset correction technique should be chosen for CEST imaging.

Appendix A. Supplementary data

Supplementary data to this article can be found online at http://dx.doi.org/10.1016/j.mri.2016.03.013.

References

[1] Kim M, Gillen J, Landman BA, Zhou J, van Zijl PC. Water saturation shift referencing (WASSR) for chemical exchange saturation transfer (CEST) experiments. Magn Reson Med 2009;61(6):1441–50.

[2] Dula AN, Asche EM, Landman BA, Welch EB, Pawate S, Sriram S, et al. Development of chemical exchange saturation transfer at 7 T. Magn Reson Med 2011;66(3):831–8.

[3] Togao O, Hiwatashi A, Keupp J, Yamashita K, Kikuchi K, Yoshiura T, et al. Scan-rescan reproducibility of parallel transmission based amide proton transfer imaging of brain tumors. J Magn Reson Imaging 2015.

[4] Webb P, Spielman D, Macovski A. Inhomogeneity correction for in vivo spectroscopy by high-resolution water referencing. Magn Reson Med 1992; 23(1):1–11.

[5] Haneder S, Apprich SR, Schmitt B, Michaely HJ, Schoenberg SO, Friedrich KM, et al. Assessment of glycosaminoglycan content in intervertebral discs using chemical exchange saturation transfer at 3.0 Tesla: preliminary results in patients with low-back pain. Eur Radiol 2013;23(3):861–8.

[6] Liu G, Qin Q, Chan KW, Li Y, Bulte JW, McMahon MT, et al. Non-invasive temperature mapping using temperature-responsive water saturation shift referencing (T-WASSR) MRI. NMR Biomed 2014;27(3):320–31.

[7] Wei W, Jia G, Flanigan D, Zhou J, Knopp MV. Chemical exchange saturation transfer MR imaging of articular cartilage glycosaminoglycans at 3 T: Accuracy of B0 Field Inhomogeneity corrections with gradient echo method. Magn Reson Imaging 2014;32(1):41–7.

[8] Zhou J, Payen JF, Wilson DA, Traystman RJ, van Zijl PC. Using the amide proton signals of intracellular proteins and peptides to detect pH effects in MRI. Nat Med 2003;9(8):1085–90.

[9] Zhou J, Lal B, Wilson DA, Laterra J, van Zijl PC. Amide proton transfer (APT) contrast for imaging of brain tumors. Magn Reson Med 2003;50(6):1120–6.

[10] Stancanello J, Terreno E, Castelli DD, Cabella C, Uggeri F, Aime S. Development and validation of a smoothing-splines-based correction method for improving the analysis of CEST-MR images. Contrast Media Mol Imaging 2008;3(4):136–49.

[11] Wu Y, Zhang S, TC Soesbe, J Yu, Vinogradov E, RE Lenkinski, et al. pH imaging of mouse kidneys in vivo using a frequency-dependent paraCEST agent. Magn Reson Med 2015.

[12] Müller-Lutz A, Schleich C, Pentang G, Schmitt B, Lanzman RS, Matuschke F, et al. Age-dependency of glycosaminoglycan content in lumbar discs: A 3t gagcEST study. J Magn Reson Imaging 2015.

[13] Liu Q, Jin N, Fan Z, Natsuaki Y, Tawackoli W, Pelled G, et al. Reliable chemical exchange saturation transfer imaging of human lumbar intervertebral discs using reduced-field-of-view turbo spin echo at 3.0 T. NMR Biomed 2013;26(12): 1672–9.

[14] Müller-Lutz A, Schleich C, Schmitt B, Antoch G, Matuschke F, Quentin M, et al. Gender, BMI and T2 dependencies of glycosaminoglycan chemical exchange saturation transfer in intervertebral discs. Magn Reson Imaging 2015.

[15] Xu J, Yadav NN, Bar-Shir A, Jones CK, Chan KW, Zhang J, et al. Variable delay multi-pulse train for fast chemical exchange saturation transfer and relayed-nuclear overhauser enhancement MRI. Magn Reson Med 2014;71(5):1798–812.

[16] Sun PZ, Wang E, Cheung JS, Zhang X, Benner T, Sorensen AG. Simulation and optimization of pulsed radio frequency irradiation scheme for chemical exchange saturation transfer (CEST) MRI-demonstration of pH-weighted pulsed-amide proton CEST MRI in an animal model of acute cerebral ischemia. Magn Reson Med 2011;66(4):1042–8.

[17] Schmitt B, Zaiss M, Zhou J, Bachert P. Optimization of pulse train presaturation for CEST imaging in clinical scanners. Magn Reson Med 2011;65(6):1620–9.

[18] Heo HY, Zhang Y, Jiang S, Lee DH, Zhou J. Quantitative assessment of amide proton transfer (APT) and nuclear overhauser enhancement (NOE) imaging with extrapolated semisolid magnetization transfer reference (EMR) signals: II. Comparison of three EMR models and application to human brain glioma at 3 Tesla. Magn Reson Med 2015.

[19] Harris RJ, Cloughesy TF, Liau LM, RM Prins, JP Antonios, D Li, et al. pH-weighted molecular imaging of gliomas using amine chemical exchange saturation transfer MRI. Neuro Oncol 2015.

[20] Sun PZ, Benner T, Kumar A, Sorensen AG. Investigation of optimizing and translating pH-sensitive pulsed-chemical exchange saturation transfer (CEST) imaging to a 3T clinical scanner. Magn Reson Med 2008;60(4):834–41.

[21] Murase K, Tanki N. Numerical solutions to the time-dependent Bloch equations revisited. Magn Reson Imaging 2011;29(1):126–31.

[22] Bloch F. Nuclear Induction. Phys Rev; 1946. p. 460–74.

[23] Wansapura JP, Holland SK, Dunn RS, Ball WS. NMR relaxation times in the human brain at 3.0 tesla. J Magn Reson Imaging 1999;9(4):531–8.

[24] Gudbjartsson H, Patz S. The Rician distribution of noisy MRI data. Magn Reson Med 1995;34(6):910–4.

[25] Zaiss M, Schmitt B, Bachert P. Quantitative separation of CEST effect from magnetization transfer and spillover effects by Lorentzian-line-fit analysis of z-spectra. J Magn Reson 2011;211(2):149–55.

[26] Zhou J, Blakeley JO, Hua J, Kim M, Laterra J, Pomper MG, et al. Practical data acquisition method for human brain tumor amide proton transfer (APT) imaging. Magn Reson Med 2008;60(4):842–9.

[27] Zhou J, Hong X, Zhao X, Gao JH, Yuan J. APT-weighted and NOE-weighted image contrasts in glioma with different RF saturation powers based on magnetization transfer ratio asymmetry analyses. Magn Reson Med 2013;70(2):320–7.

[28] Schleich C, Müller-Lutz A, Matuschke F, Sewerin P, Sengewein R, Schmitt B, et al. Glycosaminoglycan chemical exchange saturation transfer of lumbar intervertebral discs in patients with spondyloarthritis. J Magn Reson Imaging 2015.

[29] Müller-Lutz A, Khalil N, Schmitt B, Jellus V, Pentang G, Oeltzschner G, et al. Pilot study of Iopamidol-based quantitative pH imaging on a clinical 3T MR scanner. MAGMA 2014;27(6):477–85.

[30] Kim M, Chan Q, Anthony MP, Cheung KM, Samartzis D, Khong PL. Assessment of glycosaminoglycan distribution in human lumbar intervertebral discs using chemical exchange saturation transfer at 3 T: feasibility and initial experience. NMR Biomed 2011;24(9):1137–44.

[31] Saar G, Zhang B, Ling W, Regatte RR, Navon G, Jerschow A. Assessment of glycosaminoglycan concentration changes in the intervertebral disc via chemical exchange saturation transfer. NMR Biomed 2012;25(2):255–61.

[32] Tee YK, Harston GW, Blockley N, Okell TW, Levman J, Sheerin F, et al. Comparing different analysis methods for quantifying the MRI amide proton transfer (APT) effect in hyperacute stroke patients. NMR Biomed 2014;27(9):1019–29.

[33] SZ Chen, Yuan J, Deng M, Wei J, Zhou J, YJ Wáng. Chemical exchange saturation transfer (CEST) MR technique for in-vivo liver imaging at 3.0 tesla. Eur Radiol 2015.

[34] van Zijl PC, Jones CK, Ren J, Malloy CR, Sherry AD. MRI detection of glycogen in vivo by using chemical exchange saturation transfer imaging (glycoCEST). Proc Natl Acad Sci U S A 2007;104(11):4359–64.

[35] Jones CK, Polders D, Hua J, Zhu H, Hoogduin JH, Luijten P, et al. In vivo three-dimensional whole-brain pulsed steady-state chemical exchange saturation transfer at 7 T. Magn Reson Med 2012;67(6):1579–89.

[36] Dixon WT, Ren J, Lubag AJ, Ratnakar J, Vinogradov E, Hancu I, et al. A concentration-independent method to measure exchange rates in PARACEST agents. Magn Reson Med 2010;63(3):625–32.

[37] Dixon WT, Hancu I, Ratnakar SJ, Sherry AD, Lenkinski RE, Alsop DC. A multislice gradient echo pulse sequence for CEST imaging. Magn Reson Med 2010;63(1): 253–6.

Magnetic Resonance Materials in Physics, Biology and Medicine (2018) 31:645–651
https://doi.org/10.1007/s10334-018-0689-5

RESEARCH ARTICLE

Comparison of B_0 versus B_0 and B_1 field inhomogeneity correction for glycosaminoglycan chemical exchange saturation transfer imaging

Anja Müller-Lutz[1] · Alexandra Ljimani[1] · Julia Stabinska[1] · Moritz Zaiss[2] · Johannes Boos[1] · Hans-Jörg Wittsack[1] · Christoph Schleich[1]

Received: 5 February 2018 / Revised: 26 April 2018 / Accepted: 3 May 2018 / Published online: 14 May 2018

Abstract

Purpose The study compares glycosaminoglycan chemical exchange saturation transfer (gagCEST) imaging of intervertebral discs corrected for solely B_0 inhomogeneities or both B_0 and B_1 inhomogeneities.

Methods Lumbar intervertebral discs of 20 volunteers were examined with T_2-weighted and gagCEST imaging. Field inhomogeneity correction was performed with B_0 correction only and with correction of both B_0 and B_1. GagCEST effects measured by the asymmetric magnetization transfer ratio (MTR_{asym}) and signal-to-noise ratio (SNR) were compared between both methods.

Results Significant higher MTR_{asym} and SNR values were obtained in the nucleus pulposus using B_0 and B_1 correction compared with B_0-corrected gagCEST. The GagCEST effect was significantly different in the nucleus pulposus compared with the annulus fibrosus for both methods.

Conclusion The B_0 and B_1 field inhomogeneity correction method leads to an improved quality of gagCEST imaging in IVDs compared with only B_0 correction.

Keywords Chemical exchange saturation transfer · Field inhomogeneity correction · WASSR · WASABI · Glycosaminoglycans · Intervertebral disks

Introduction

Magnetic resonance (MR) glycosaminoglycan chemical exchange saturation transfer (gagCEST) imaging is a valuable method to assess the content of glycosaminoglycans [1, 2], which are one of the main matrix contents of hyaline and fibrous cartilage [2, 3].

Recent studies reported a relation between the gagCEST effect and intervertebral disc (IVD) degeneration, decreased IVD hydration and decreased height of the discs [4–7].

The gagCEST effect can be influenced by artefacts from motion or field inhomogeneity [8, 9]. Up to now, different methods have been applied to correct B_0 field inhomogeneity including frequency shift correction of the CEST curve before gagCEST analysis, the water saturation shift referencing (WASSR) field inhomogeneity correction algorithm or gradient echo methods using different echo times [5, 10, 11].

Recently, the new water saturation and B_1 correction (WASABI) method has been introduced by Schuenke et al. [12]. The WASABI method enables the assessment of both B_0 and B_1 field inhomogeneities [12]. Instead of a Gaussian-shaped presaturation pulse with low B_1 field strength—which is used in the WASSR technique—the WASABI method uses a short rectangular radiofrequency pulses with a high B_1 field strength resulting in a Z spectrum with several oscillations. In this WASABI Z spectrum, information about B_0 is encoded in the shift of the symmetry axis, whereas information about the radiofrequency (RF) amplitude B_1 is encoded in the periodicity of the oscillations [12]. WASABI has been applied in investigations of the head at a magnetic field strength of 7 T [12], but might also be of relevance for CEST applications in other regions and at clinically available magnetic field strengths.

✉ Alexandra Ljimani
Alexandra.Ljimani@med.uni-duesseldorf.de

[1] Department of Diagnostic and Interventional Radiology, University Dusseldorf Medical Faculty, 40225 Düsseldorf, Germany

[2] High-Field MR Center, Max Planck Institute for Biological Cybernetics, Tübingen, Germany

In our study we use the WASABI method to verify whether considering both B_0 and B_1 correction improves image quality compared with B_0 correction only for gagCEST imaging in IVDs. Correction of both B_0 and B_1 field inhomogeneities with the WASABI method is compared with correction of solely B_0 field inhomogeneities with the WASSR technique, which has already been shown to be applicable for gagCEST imaging [8]. We chose IVDs to evaluate field inhomogeneity corrected gagCEST imaging because of the IVD thickness and discoid shape. IVDs can be divided into two parts: the nucleus pulposus (NP), representing the core of the disc, and the annulus fibrosus (AF), which is the outer ring of the disc [2]. NP and AF have different content compositions including proteoglycans (PG) to which GAG is attached and thus show a different amount of gagCEST effect [2]. Therefore, we sought to investigate whether NP can be differentiated from AF because of the gagCEST effect obtained by both methods. We further compared the amount of gagCEST effect and signal-to-noise ratio (SNR) of the gagCEST effect between both methods and hypothesized that WASABI will lead to an increased SNR because of correction of both B_0 and B_1 inhomogeneities.

Materials and methods

Study population

This prospective study was approved by the local ethics committee. Twenty volunteers without any history of lower back pain or previous spine surgery (12 females, 8 males, 29 ± 9 years, 21–57 years) were included. Written informed consent was obtained prior to examination from all volunteers.

MR measurements

All MR measurements were performed of lumbar IVDs using a whole-body MRI system with static magnetic field strength of 3 T (Magnetom Trio, Siemens Healthcare, Erlangen, Germany) and a spine matrix coil for signal reception. The sequence protocol consisted of sagittal and transversal T_2-weighted imaging [13], T_2 mapping [13], T_1 mapping, WASSR and WASABI sequences, and three CEST sequences with different B_1 field strengths for imaging of GAG.

For quantitative T_1 mapping, a 3D fast low-angle shot sequence was applied with two different flip angles ($\alpha_1 = 5°$ and $\alpha_2 = 26°$). Sequence parameters of the T_1 mapping sequence were: field of view, 300×300 mm^2; voxel size, $1.6 \times 1.6 \times 2.5$ mm^3; basic resolution, 192 × 192; repetition time, 15 ms; echo time, 1.29 ms.

WASSR, WASABI and CEST sequences were performed with a single-shot gradient echo sequence with field of view 300×300 mm^2; voxel size $2.3 \times 2.3 \times 5$ mm^3; basic resolution, 128×128; flip angle, 10°; repetition time, 10 ms; echo time, 3.64 ms.

Before imaging, a saturation module was applied at different frequency offsets to obtain the Z spectrum. For WASSR, the saturation module consisted of a single Gaussian-shaped RF pulse with $B_1 = 0.1$ µT and pulse duration PD = 58 ms. The WASSR-Z spectrum was acquired in a frequency range from − 1 to 1 ppm using 41 frequency offsets. The WASABI-Z spectrum was obtained using 49 frequency offsets in a frequency range from − 2.4 to 2.4 ppm with one rectangular-shaped RF pulse ($B_1 = 4$ µT and PD = 5 ms) for the presaturation module. Three CEST sequences with different B_1 field strengths of 0.5, 1.0 and 1.5 µT were applied using ten spin-lock pulses with PD = 100 ms and a duty cycle of 50%. CEST Z spectra were acquired with 33 frequency offsets in a range from − 4.8 to 4.8 ppm.

For each WASSR, WASABI and CEST sequence, a reference scan was acquired at a frequency offset of − 300 ppm.

Total acquisition time of all imaging sequences was 34 min.

Data analysis

The degree of morphological degeneration was classified using the Pfirrmann scoring system [14]. Only discs without degeneration (Pfirrmann grades one and two) and without protrusion or herniation were analysed.

The T_1 map was determined for the two middle slices of the 3D T_1 mapping FLASH sequence using the formula

$$T_1(x,y) = \frac{\mathrm{TR}}{\ln\left(\frac{\sin(\alpha 1)\cos(\alpha 2) - F(x,y)\sin(\alpha 2)\cos(\alpha 1))}{\sin(\alpha 1) - F(x,y)\sin(\alpha 2)}\right)}$$

where

$$F(x,y) = \frac{S_{\alpha 1}(x,y)}{S_{\alpha 2}(x,y)}$$

$S_{\alpha 1}(x, y)$ and $S_{\alpha 2}(x, y)$ are the signal intensities of the images obtained with the two different flip angles α_1 and α_2. The final T_1 map was built by averaging the T_1 maps of the two investigated slices.

Before analysis of WASABI, WASSR and CEST data, Gaussian filtering with a 3×3 matrix was applied to each image of each sequence. Frequency correction with WASSR is described in detail elsewhere [11]. WASABI B_0 and B_1 maps were obtained as described in the manuscript of Schuenke et al. [12]. Z spectra were shifted pixel-wise according to the obtained frequency offset maps with WASABI or WASSR. For WASABI, an additional B_1 correction

was performed according to Windschuh et al. [15] using the B_0 inhomogeneity corrected Z spectra with $B_1 = 0.5$ µT, $B_1 = 1.0$ µT and $B_1 = 1.5$ µT. The final asymmetry analysis was performed for Z spectra at $B_1 = 1.0$ µT. MTR_{asym} maps were calculated by averaging the asymmetry effect in the offset frequency range of GAG resonances (0.9–1.9 ppm) [1, 4].

Outliers were removed from statistical analysis. Therefore, pixels were excluded from further analysis if MTR_{asym} was outside the range:

$25\text{th percentile}(MTR_{asym}) - 1.5(75\%\ \text{percentile}(MTR_{asym}) - 25\%\ \text{percentile}(MTR_{asym})) < MTR_{asym} < 75\text{th percentile}(MTR_{asym}) + 1.5(75\%\ \text{percentile}(MTR_{asym}) - 25\%\ \text{percentile}(MTR_{asym}))$.

Total IVDs were omitted from further analysis if more than half of the pixels of the corresponding IVD were excluded.

After automatic segmentation of NP and AF [16], mean MTR_{asym}, $SNR(MTR_{asym})$, T_2 and B_1 values were determined for these regions. Thereby, $SNR(MTR_{asym})$ is defined as $mean(MTR_{asym})$ divided by the standard deviation of MTR_{asym} in the investigated region.

Statistical analysis

Statistical analysis was performed using MATLAB (MathWorks, Natick, MA, R2015a).

The number of discs without degeneration and without protrusion or herniation was determined.

MTR_{asym}, SNR, T_1 and T_2 values obtained in NP and AF were tested for normal distribution using the Kolmogorov-Smirnov test. Descriptive analysis was performed providing the mean, standard deviation, median, minimum and maximum of the investigated parameter. The Wilcoxon test was used to compare MTR_{asym} and SNR values obtained with WASSR and WASABI as well as differences between NP and AF.

Spearman correlation analysis was performed to reveal whether gagCEST correlated with T_1 and T_2 values.

Results

All MRI examinations were performed successfully. Eighty-four discs were classified as non-degenerative (Pfirrmann grade one or two) without degeneration or herniation. Six further discs were excluded because of erroneous data (outliers in MTR_{asym} values in more than half of the pixels). Therefore, 78 discs remained for further data analysis.

Figure 1 displays offset ($\Delta\omega$) and relative B_1 (rB_1) maps as well as the difference of $\Delta\omega$ maps obtained with B_0 correction only (B_0c) and B_0 and B_1 correction (B_0c and B_1c) exemplary for two volunteers. Similar $\Delta\omega$ maps were obtained with WASSR and WASABI (difference of $\Delta\omega$ with WASSR and WASABI: 0.007 ppm ± 0.028 ppm).

The mean relative B_1 value in the IVDs was below one (IVD: $rB_1 = 0.78 \pm 0.07$), thus indicating reduced radiofrequency reception in this region.

Descriptive analysis of MTR_{asym}, SNR, T_1 and T_2 values is presented in Table 1. Table 2 provides evaluation of statistically significant differences in the NP and AF of the MTR_{asym} and SNR obtained with B_0c or B_0c and B_1c.

MTR_{asym}(NP, B_0c and B_1c), MTR_{asym}(NP, B_0c), MTR_{asym}(AF, B_0c and B_1c) and MTR_{asym}(AF, B_0c) were non-normally distributed. Figures 2 and 3 show the MTR_{asym} values in NP and AF of two exemplary selected volunteers. In NP, significantly higher MTR_{asym} values were obtained with B_0c and B_1c compared with solely B_0c ($p = 0.019$), whereas in AF statistical analysis revealed an equal distribution. With B_0c and B_1c significantly higher MTR_{asym} values were observed in NP compared with AF (B_0c and B_1c: $p = 0.004$). Nevertheless, a large irregular variability of MTR_{asym} was observed, which was more pronounced in AF compared with NP (see Figs. 2 and 3).

Figure 2 and 3 show lower gagCEST values in one of the two selected volunteers with the WASSR technique (a, c) (NP: $p = 0.048$, AF: $p = 0.008$), but not with the WASABI technique (b, d) (NP: $p = 0.234$, AF: $p = 0.170$).

SNR (MTR_{asym}, NP, B_0c and B_1c), SNR (MTR_{asym}, NP, B_0c), SNR (MTR_{asym}, AF, B_0c and B_1c) and SNR (MTR_{asym}, AF, B_0c) were non-normally distributed. Significantly higher SNR was obtained in both NP and AF with B_0c and B_1c compared with B_0c (NP: $p = 0.002$; AF: $p = 0.012$). With both methods, SNR was significantly higher in NP compared with AF (B_0c and B_1c: $p < 0.001$; B_0c: $p < 0.001$).

T_1 and T_2 values were not normally distributed. A significant correlation between T_1 and MTR_{asym} was only obtained with WASSR in NP but not in AF (NP: $p = 0.019$; AF: $p = 0.239$). Using WASABI, no correlation between T_1 and MTR_{asym} was observed (NP: $p = 0.678$; AF: $p = 0.980$).

There was a significant correlation between T_2 and MTR_{asym} with WASABI (NP: $p = 0.036$; WASABI, AF: $p = 0.047$) but not with WASSR (NP: $p = 0.167$; AF: $p = 0.776$).

Discussion

We demonstrated the application of B_0 and B_1 field inhomogeneity correction using the WASABI correction method for gagCEST imaging of IVDs. WASABI-corrected evaluation led to a higher gagCEST effect and an increased SNR compared with gagCEST imaging using WASSR-based B_0 correction only.

Our results regarding the increased SNR indicate that gagCEST imaging can be improved by using both B_0 and B_1

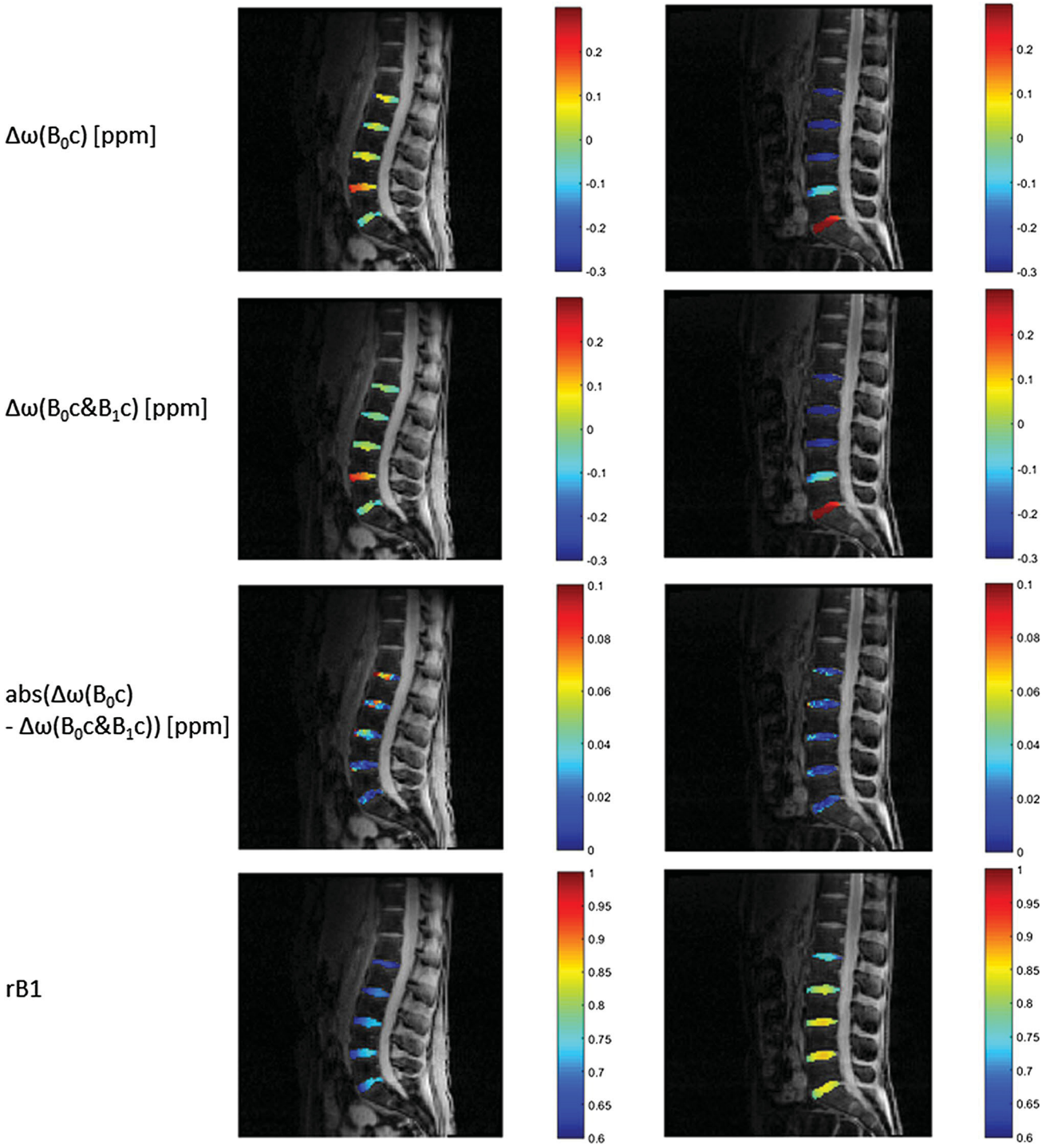

Fig. 1 $\Delta\omega$ maps obtained with B_0c, B_0c and B_1c; absolute difference of these $\Delta\omega$ maps and relative the B_1 map are shown exemplarily for two volunteers

correction. We used the SNR as a quality feature since similar glycosaminoglycan content can be expected for regions with similar composition. Due to alterations as a consequence of cartilage degeneration or destruction, this assumption might be queried. Therefore, our study population was restricted to healthy volunteers without previously known cartilage diseases.

MTR_{asym} maps and SNR analysis revealed a high variability of MTR_{asym} especially in AF. This might have several reasons: In our study, we used a 3-T MRI system to analyse

Table 1 Descriptive analysis of MTR_{asym}, SNR, T_2, T_1 and relative B_1 field rB_1 for both nucleus pulposus (NP) and annulus fibrosus (AF)

	Mean	Sd	Median	Min	Max
MTR_{asym}(NP, B_0c and B_1c) [%]	1.99	2.41	2.50	− 5.32	7.22
MTR_{asym}(AF, B_0c and B_1c) [%]	1.14	2.06	1.24	− 4.14	4.75
MTR_{asym}(NP, B_0c) [%]	1.45	2.05	1.51	− 3.01	7.02
MTR_{asym}(AF, B_0c) [%]	0.90	1.74	0.95	− 2.52	5.52
SNR(MTR_{asym}, NP, B_0c and B_1c)	3.22	2.10	2.82	0.06	9.52
SNR(MTR_{asym}, AF, B_0c and B_1c)	1.19	0.86	0.97	0.02	3.47
SNR(MTR_{asym}, NP, B_0c)	2.42	2.18	1.85	0.02	13.23
SNR(MTR_{asym}, AF, B_0c)	0.82	0.61	0.71	0.02	2.79
T_2(NP) [ms]	134.13	37.50	139.62	57.25	211.69
T_2(AF) [ms]	88.83	27.45	85.50	8.19	181.89
T_1(NP) [ms]	1306.45	317.29	1291.28	683.45	2146.38
T_1(AF) [ms]	930.23	326.57	863.74	517.74	2826.47
rB_1(NP)	0.79	0.07	0.78	0.64	1.02
rB_1(AF)	0.77	0.07	0.76	0.62	1.00

rB_1 multiplied by the transmitted B_1 field of the RF presaturation during CEST experiments represents the effective B_1 field of the RF presaturation pulses

Table 2 Evaluation of statistical significances of MTR_{asym} and SNR

p value [MTR_{asym} B_0c and B_1c, NP), MTR_{asym}(B_0c, NP)]	0.019
p value [MTR_{asym}(B_0c and B_1c, AF), MTR_{asym}(B_0c, AF)]	0.192
p value [MTR_{asym}(B_0c and B_1c, NP), MTR_{asym}(B_0c and B_1c, AF)]	0.004
p value [MTR_{asym}(B_0c, NP), MTR_{asym}(B_0c, AF)]	0.055
p value [SNR(B_0c and B_1c, NP), SNR(B_0c, NP)]	0.002
p value [SNR(B_0c and B_1c, AF), SNR(B_0c, AF)]	0.012
p value [SNR(B_0c and B_1c, NP), SNR(B_0c and B_1c, AF)]	< 0.001
p value [SNR(B_0c, NP), SNR(B_0c, AF)]	< 0.001

gagCEST. Nevertheless, the gagCEST effect at 3 T is very low, and less glycosaminoglycan content is expected in AF compared with NP. In addition, AF is more prone to artefacts due to field inhomogeneities and partial volume artefacts because of its proximity to vertebral bodies. We assume that the high variability of MTR_{asym} in AF probably arises from technical constraints rather than from large physiological variations of the glycosaminoglycan content.

With increasing B_1 amplitude, an enhanced but broadened CEST effect is expected. Therefore, higher gagCEST values obtained by WASABI-corrected gagCEST compared with WASSR-corrected gagCEST might be explained by the observation of reduced B_1 values compared with the transmitted B_1 amplitude in IVDs. Additional B_1 field inhomogeneity correction increases the SNR and gagCEST effect; however, the measurement time is prolonged since the performance of B_1 field inhomogeneity correction depends on a high number of CEST measurements [15]. The duration of the WASABI sequence used in this article is approximately equal to the duration of the WASSR sequence (WASABI: 3 min 34 s, WASSR: 3 min 2 s). Windschuh et al. [15] reported a different method to assess B_1 field inhomogeneities using one additional single-shot gradient echo sequence with an acquisition time of 10 s to create a flip angle map. An alternative approach to perform both B_0 and B_1 field inhomogeneity correction is therefore to combine the WASSR B_0 field inhomogeneity correction with a correction of B_1 field inhomogeneity using a flip angle map.

Sixteen discs were excluded because of degeneration and protrusion or herniation to concentrate on technical aspects.

Six further discs were excluded from our study because of an unrealistically low or high CEST effect. The reason might be large B_0 or B_1 field inhomogeneities, which might worsen the WASSR or WASABI technique or make the applied spin-lock gagCEST imaging method inapplicable.

B_0- and B_1-corrected gagCEST data show higher CEST values in NP compared with AF. Higher gagCEST values in NP compared with AF were also reported in the literature [8, 9] and are expected because of the larger amount of PG in NP compared with AF [2]. Thus, the increased gagCEST effect in NP compared with AF substantiates the applicability of WASABI correction to gagCEST imaging.

A correlation between T_2 values and gagCEST values was obtained with B_0 and B_1 field inhomogeneity correction but not with B_0 correction only. Previously, a relation between T_2 values and disc degeneration was reported [17]. Therefore, our findings might be a hint for increased sensibility to detect degeneration using both B_0 and B_1 correction.

In this work, we confirmed our hypothesis of an improvement of gagCEST imaging using correction of both B_0 and B_1 field inhomogeneities with the WASABI correction method at a main magnetic field strength of 3 T in NP, which enables the application of this technique to clinical MR systems. In AF, the variability of the

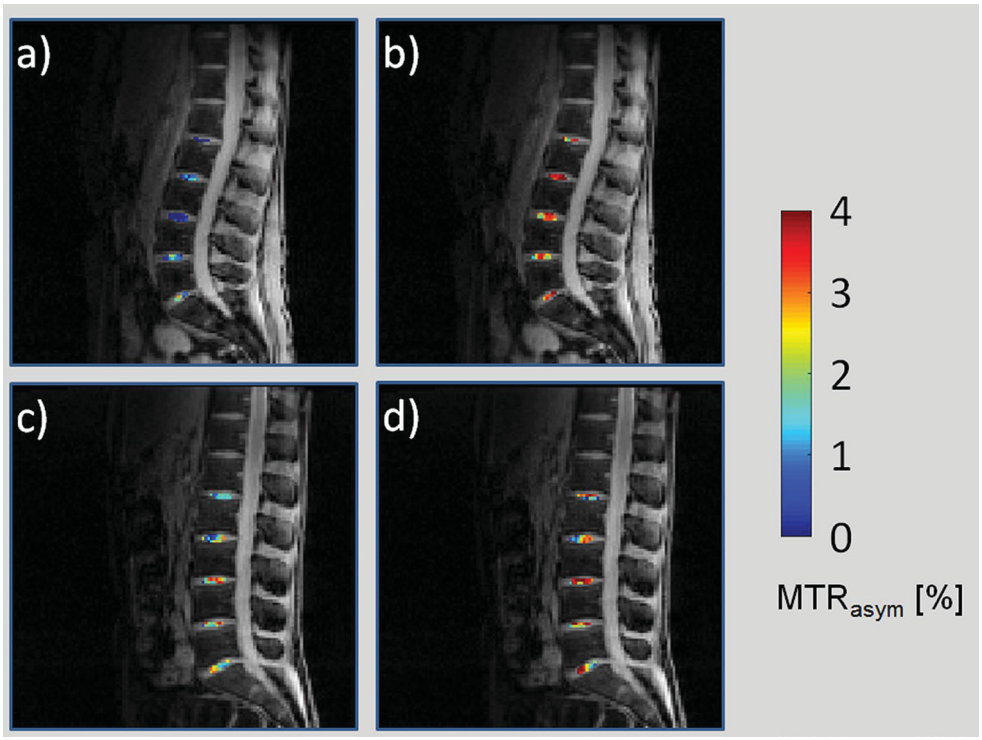

Fig. 2 MTR_{asym} maps in NP obtained with B_0 correction only (**a**, **c**) and with B_0 and B_1 correction (**b**, **d**) of two exemplary selected volunteers

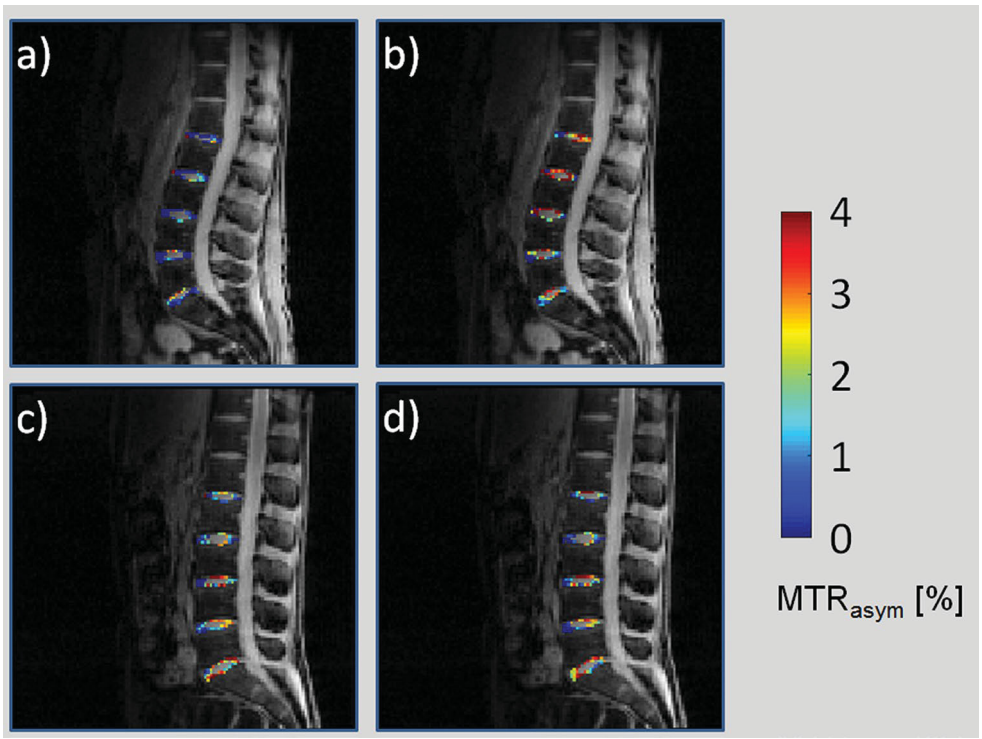

Fig. 3 MTR_{asym} maps in AF obtained with B_0 correction only (**a**, **c**) and with B_0 and B_1 correction (**b**, **d**) of two exemplary selected volunteers

gagCEST effect is high, thus indicating technical limitations of the gagCEST effect. At higher field strengths, the CEST effect increases but is also more prone to B_0 and B_1 inhomogeneities [12, 18]. Therefore, field inhomogeneity correction is more important, and the WASABI correction

method may help to improve gagCEST imaging at higher field strengths.

Conclusions

An improved quality of gagCEST imaging in IVDs can be achieved using both B_0 and B_1 field inhomogeneity correction. Compared with simple B_0 correction, B_0 and B_1 correction yielded an increased SNR and increased relation to T_2 values. Future studies in patients have to be performed to verify whether B_0 and B_1 correction leads to improved diagnostics with biochemical cartilage imaging.

Authors contribution Study conception and design: A.M.-L., J.S., M.Z., H.-J.W., C.S. Acquisition of data: A.M.-L. Analysis and interpretation of data: A.M.-L., A.L., J.S., M.Z., J.B., H.-J.W., C.S. Drafting of manuscript: A.M.-L., A.L., J.S., J.B., H.-J.W., C.S. Critical revision: A.M.-L., A.L., J.S., J.B., H.-J.W., C.S.

Compliance with ethical standards

Conflict of interest All authors declare that they have no conflicts of interest.

Ethical standards The study was performed in compliance with ethical standards.

References

1. Ling W, Regatte RR, Navon G, Jerschow A (2008) Assessment of glycosaminoglycan concentration in vivo by chemical exchange-dependent saturation transfer (gagCEST). Proc Natl Acad Sci U S A 105(7):2266–2270
2. Saar G, Zhang B, Ling W, Regatte RR, Navon G, Jerschow A (2012) Assessment of glycosaminoglycan concentration changes in the intervertebral disc via chemical exchange saturation transfer. NMR Biomed 25(2):255–261
3. Roughley PJ, Lee ER (1994) Cartilage proteoglycans: structure and potential functions. Microsc Res Tech 28(5):385–397
4. Müller-Lutz A, Schleich C, Pentang G, Schmitt B, Lanzman RS, Matuschke F, Wittsack HJ, Miese F (2015) Age-dependency of glycosaminoglycan content in lumbar discs: a 3t gagcEST study. J Magn Reson Imaging 42(6):1517–1523
5. Haneder S, Apprich SR, Schmitt B, Michaely HJ, Schoenberg SO, Friedrich KM, Trattnig S (2013) Assessment of glycosaminoglycan content in intervertebral discs using chemical exchange saturation transfer at 3.0 Tesla: preliminary results in patients with low-back pain. Eur Radiol 23(3):861–868
6. Urban JP, McMullin JF (1985) Swelling pressure of the intervertebral disc: influence of proteoglycan and collagen contents. Biorheology 22(2):145–157
7. Lyons G, Eisenstein SM, Sweet MB (1981) Biochemical changes in intervertebral disc degeneration. Biochim Biophys Acta 673(4):443–453
8. Kim M, Chan Q, Anthony MP, Cheung KM, Samartzis D, Khong PL (2011) Assessment of glycosaminoglycan distribution in human lumbar intervertebral discs using chemical exchange saturation transfer at 3 T: feasibility and initial experience. NMR Biomed 24(9):1137–1144
9. Müller-Lutz A, Schleich C, Schmitt B, Topgöz M, Pentang G, Antoch G, Wittsack HJ, Miese F (2015) Improvement of gagCEST imaging in the human lumbar intervertebral disc by motion correction. Skeletal Radiol 44(4):505–511
10. Wei W, Jia G, Flanigan D, Zhou J, Knopp MV (2014) Chemical exchange saturation transfer MR imaging of articular cartilage glycosaminoglycans at 3 T: accuracy of B_0 field inhomogeneity corrections with gradient echo method. Magn Reson Imaging 32(1):41–47
11. Kim M, Gillen J, Landman BA, Zhou J, van Zijl PC (2009) Water saturation shift referencing (WASSR) for chemical exchange saturation transfer (CEST) experiments. Magn Reson Med 61(6):1441–1450
12. Schuenke P, Windschuh J, Roeloffs V, Ladd ME, Bachert P, Zaiss M (2016) Simultaneous mapping of water shift and B_1 (WASABI)-application to field-inhomogeneity correction of CEST MRI data. Magn Reson Med. https://doi.org/10.1002/mrm.26133
13. Müller-Lutz A, Schleich C, Schmitt B, Antoch G, Matuschke F, Quentin M, Wittsack HJ, Miese F (2016) Gender, BMI and T_2 dependencies of glycosaminoglycan chemical exchange saturation transfer in intervertebral discs. Magn Reson Imaging 34(3):271–275
14. Pfirrmann CW, Metzdorf A, Zanetti M, Hodler J, Boos N (2001) Magnetic resonance classification of lumbar intervertebral disc degeneration. Spine 26(17):1873–1878 **(Phila Pa 1976)**
15. Windschuh J, Zaiss M, Meissner JE, Paech D, Radbruch A, Ladd ME, Bachert P (2015) Correction of B_1-inhomogeneities for relaxation-compensated CEST imaging at 7 T. NMR Biomed 28(5):529–537
16. Schleich C, Müller-Lutz A, Matuschke F, Sewerin P, Sengewein R, Schmitt B, Ostendorf B, Wittsack HJ, Stanke K, Antoch G, Miese F (2015) Glycosaminoglycan chemical exchange saturation transfer of lumbar intervertebral discs in patients with spondyloarthritis. J Magn Reson Imaging 42(4):1057–1063
17. Yoon MA, Hong SJ, Kang CH, Ahn KS, Kim BH (2016) T_1rho and T2 mapping of lumbar intervertebral disc: correlation with degeneration and morphologic changes in different disc regions. Magn Reson Imaging 34(7):932–939
18. van Zijl PC, Yadav NN (2011) Chemical exchange saturation transfer (CEST): what is in a name and what isn't? Magn Reson Med 65(4):927–948

Comparison of Glycosaminoglycan Chemical Exchange Saturation Transfer Using Gaussian-Shaped and Off-Resonant Spin-Lock Radiofrequency Pulses in Intervertebral Disks

Anja Müller-Lutz,[1] Tom Cronenberg,[1] Christoph Schleich,[1]* Frithjof Wickrath,[1] Moritz Zaiss,[2] Johannes Boos,[1] and Hans-Jörg Wittsack[1]

Purpose: To investigate, if a train of spin-lock pulses (chemical exchange saturation transfer with spin-lock pulses = CESL) improves biochemical glycosaminoglycan imaging compared with conventional chemical exchange saturation transfer with Gaussian-shaped pulses (CEST) in lumbar intervertebral discs.
Methods: T_2, CEST, and CESL imaging was performed in lumbar intervertebral discs of 15 healthy volunteers at 3 Tesla. Mean and standard deviation of the asymmetric magnetization transfer ratio (MTR_{asym}), the asymmetric spin-lock ratio (SLR_{asym}) and T_2 values were calculated for nucleus pulposus (NP) and annulus fibrosus (AF). Wilcoxon test was used to analyze differences between MTR_{asym} and SLR_{asym}. Pearson correlation was used to determine the relationship between MTR_{asym}, SLR_{asym} and T_2.
Results: Data showed no significant difference between MTR_{asym} and SLR_{asym} (NP: $P = 0.35$; AF: $P = 0.34$). MTR_{asym} and SLR_{asym} values differed significantly between NP and AF (MTR_{asym}: $P = 0.014$, SLR_{asym}: $P = 0.005$). T_2 values correlated significantly with MTR_{asym} (NP: $\rho = 0.76$, $P < 0.001$; AF: $\rho = 0.60$, $P < 0.001$) and SLR_{asym} (NP: $\rho = 0.73$, $P < 0.001$; AF: $\rho = 0.47$, $P < 0.001$).
Conclusion: CESL does not improve the chemical exchange asymmetry effect compared with conventional CEST, but leads to comparable results. **Magn Reson Med 78:280–284, 2017.**

Key words: chemical exchange saturation transfer; spin-lock; glycosaminoglycans; intervertebral disks

INTRODUCTION

Glycosaminoglycans (GAG) is a major component of intervertebral discs (IVDs) (1). The amount of GAG content correlates with disc degeneration making the biochemical imaging of GAG desirable (2). Conventional chemical exchange saturation transfer with Gaussian-shaped radiofrequency (RF) pulses (CEST), a biochemical MR imaging technique, has been shown to be sensitive to the amount of hydroxyl protons of GAG molecules (3).

At clinical MR systems, pulsed CEST presaturation has to be applied due to hardware limitations and specific absorption rate (SAR) limits (4). The most common pulsed CEST presaturation scheme is comprised by Gaussian-shaped RF pulses (4) and has been used for biochemical imaging of GAG in several studies (5–8). One major difficulty of gagCEST imaging at 3 Tesla (T) is the small CEST effect at 3T. Therefore, an effective and reliable presaturation scheme is especially important.

Recently, spin-lock pulses have been introduced for pulsed chemical exchange MR imaging (9,10). Subsequently, this approach is denoted as CESL (Chemical Exchange saturation transfer imaging using the spin-lock technique). The spin-lock saturation block is comprised of three RF pulses (10,11): The first RF pulse flips the magnetization away from the direction of the main magnetic field to the effective field at a specific frequency offset. The second RF pulse is a rectangular pulse, during which the chemical exchange saturation transfer process takes place. The third RF pulse flips the magnetization back to the direction of the main magnetic field.

Pulsed CESL has some advantages over pulsed CEST: Spin-lock presaturation is known to provide a higher signal-to-noise ratio by restoring magnetization along the axis of the effective field (9,12). The direct water saturation (DWS) is broader in the Z-Spectrum using CEST compared with CESL (12). In addition, the saturation efficiency increases with CESL compared with CEST (10). Therefore, we aim to investigate the performance of CESL for biochemical imaging of GAG. We hypothesize that CESL leads to an increased chemical exchange asymmetry effect compared with CEST.

METHODS

Study Population

Fifteen healthy volunteers without lower back pain and without any history of back problems (9 females, 6 males; 29 ± 10 years; range, 19–58 years) were enrolled in this prospective study. The study was approved by the local ethics committee and written informed consent was received from all volunteers.

MR Measurements

MR imaging of lumbar IVDs was performed on a 3T whole-body MRI system (Magnetom Trio, A Tim System,

[1]University Dusseldorf, Medical Faculty, Department of Diagnostic and Interventional Radiology, Dusseldorf, Germany.
[2]Department of Medical Physics in Radiology, Deutsches Krebsforschungszentrum (DKFZ), Heidelberg, Germany.
*Correspondence to: Christoph Schleich, Dr.Med., University Dusseldorf, Department of Diagnostic and Interventional Radiology, Moorenstr. 5, D-40225 Düsseldorf, Germany. E-mail: christoph.schleich@med.uni-duesseldorf.de

Received 14 March 2016; revised 6 July 2016; accepted 8 July 2016
DOI 10.1002/mrm.26362
Published online 3 August 2016 in Wiley Online Library (wileyonlinelibrary.com).

Table 1
Sequence Parameter of Qualitative and Quantitative T_2 Imaging.

	T_2-weighted imaging (sagittal)	T_2-weighted imaging (transversal)	T_2 mapping
Sequence type	Turbo spin echo	Turbo spin echo	Spin echo
Turbo factor	31	18	No
FOV [mm^2]	300×300	240×240	300×300
Voxel size [mm^2]	1.2×1.2	0.8×0.6	1.6×1.6
Slice thickness [mm]	3.0	3.0	5.0
Number of slices	15	27	1
Basic resolution	256×256	384×307	192×192
Flip angle [°]	160	140	180
TE [ms]	105.0	113.0	9.1, 18.2, 27.3, 36.4, 45.5, 54.6, 63.7, 72.8, 81.9, 91.0
Repetition time [ms]	3100.0	4510.0	800.0
Acquisition duration [min:s]	3:39	5:13	4:23

Siemens Healthcare, Erlangen, Germany) using a spine matrix coil. Patients were scanned in supine position. After a localizer, images for T_2 weighting and T_2 quantification were acquired (Table 1). GAG biochemical imaging sequences were acquired in sagittal direction. Three sequences were performed for biochemical imaging of GAG: CEST, CESL and a water saturation shift referencing (WASSR) sequence, which enables field inhomogeneity correction.

Each CEST, CESL, and WASSR sequence consisted of a presaturation module and an imaging module. Imaging was performed in a single slice using a single-shot gradient echo sequence with following parameters: field of view (FOV) = $300 \times 300\,mm^2$, voxel size = $2.3 \times 2.3\,mm^2$, slice thickness = 5.0 mm, basic resolution = 128×128, flip angle = 10 °, echo time (TE) = 3.64 ms and repetition time = 10.0 ms. The presaturation module of CEST and CESL was comprised of 10 Gaussian or spin-lock pulses with a pulse duration of 100 ms, a mean B_1 amplitude of 1.6 μT and a duty cycle of 50%. The entire Z-spectrum was acquired with 33 frequency offsets in intervals of 0.3 ppm from -4.8 to 4.8 ppm. In addition, one reference scan with a frequency offset of -300 ppm was acquired for CEST-spectrum and CESL-spectrum normalization. The WASSR presaturation module consisted of one single Gaussian-shaped RF pulse with a pulse duration of 100 ms and a mean B_1 amplitude of 0.2 μT. The entire WASSR-spectrum was acquired with 41 frequency offsets in intervals of 0.05 ppm from -1.0 to 1.0 ppm. One reference scan at -300 ppm was acquired for WASSR-spectrum normalization.

Data Analysis

Pfirrmann analysis (13) was performed to analyze the degree of degeneration. Pfirrmann grades 1 and 2 describe nondegenerative IVDs with clear distinction of nucleus pulposus (NP) and annulus fibrosus (AF), whereas Pfirrmann grades 3, 4, and 5 describe degenerative IVDs with unclear or visually undetectable delineation between NP and AF. T_2 values of IVDs were determined by an exponential fit to the signal of the quantitative T_2 imaging sequence at different ETs.gagCEST analysis was performed as follows: Field inhomogeneity correction was applied by shifting the Z-spectrum data by the shift determined pixel-wise using the maximum symmetry center frequency (MSCF) approach on the WASSR data (14). For CEST, the asymmetric magnetization transfer ratio (MTR_{asym}) curve and for CESL, the asymmetric spin-lock ratio (SLR_{asym}) curve were determined using the difference in the normalized signal intensities at the label frequencies $\Delta\omega$ and $-\Delta\omega$ of the CEST-spectrum or CESL-spectrum. MTR_{asym} and SLR_{asym} maps were determined by calculating the average value of MTR_{asym} or SLR_{asym} curves in the irradiation frequency offset range from 0.9 – 1.9 ppm for each pixel. NP and AF were segmented automatically using in-house developed MATLAB software based on Bayes classification (7). MTR_{asym} and SLR_{asym} values were determined for AF and NP in all lumbar discs, respectively.

Statistical Analysis

MATLAB (MathWorks, Natick, MA, R2015a) was used for statistical analysis. Descriptive statistics including mean and standard deviation of MTR_{asym}, SLR_{asym}, and T_2 values for NP and AF were calculated. Data are given as mean ± standard deviation. Median and ranges are provided. *P*-values below 0.05 were considered to be significant. The Kolmogorov-Smirnov test was used to test for normal distribution of MTR_{asym}, SLR_{asym}, and T_2 values in our collective as well as for each Pfirrmann score separately. The Wilcoxon test was used to compare MTR_{asym} and SLR_{asym} values between NP and AF for the whole collective as well as for different Pfirrmann scores. Kruskal-Wallis analysis was performed to assess a dependence of MTR_{asym} and SLR_{asym} values on Pfirrmann score. Spearman correlation was performed to investigate if MTR_{asym} and SLR_{asym} depend on T_2-values for both all data and for different Pfirrmann scores.

RESULTS

Two volunteers had to be excluded from further analysis due to motion during MRI acquisitions. The remaining 13 volunteers successfully underwent the MRI examination. MTR_{asym} and SLR_{asym} maps of one volunteer are exemplarily presented in Figure 1. Visually, both maps are similar and show a higher degree of asymmetry in NP compared with AF. For all but MTR_{asym} and SLR_{asym}

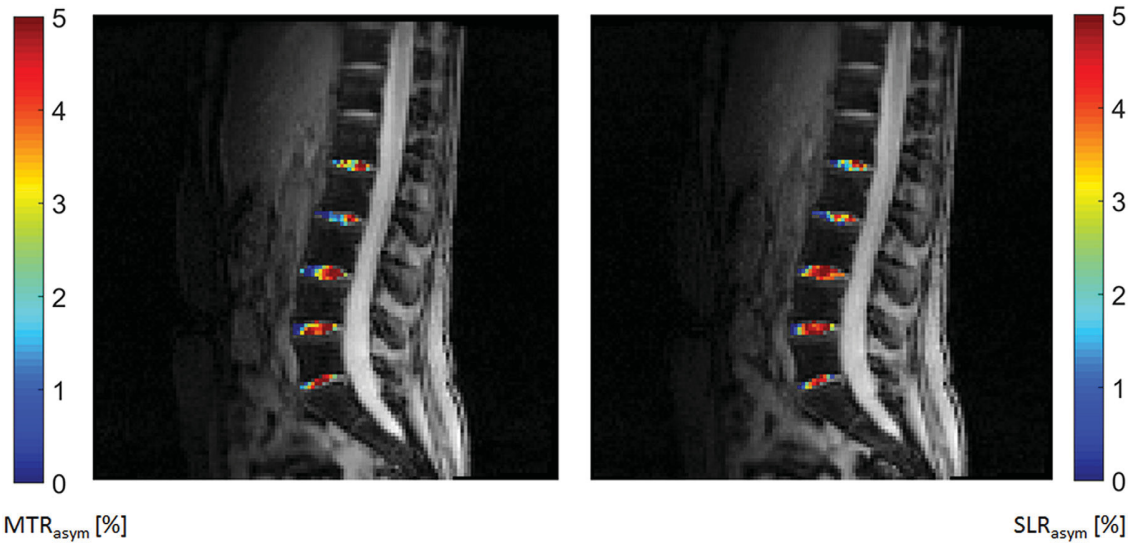

FIG. 1. MTR$_{asym}$ [%] (left) and SLR$_{asym}$ [%] (right) maps overlaid with anatomical imaging in lumbar intervertebral discs of one volunteer. Higher MTR$_{asym}$ and SLR$_{asym}$ values were obtained in NP compared with AF.

calculated for Pfirrmann score four, Kolmogorov-Smirnov test revealed a nonnormal distribution of MTR$_{asym}$, SLR$_{asym}$ and T_2 values. Therefore, the Wilcoxon test was performed to compare MTR$_{asym}$ and SLR$_{asym}$. Descriptive analysis of MTR$_{asym}$ and SLR$_{asym}$ is provided in Table 2. There was no significant difference between MTR$_{asym}$ and SLR$_{asym}$ in both NP and AF (NP: $P = 0.35$; AF: $P = 0.34$) over the whole collective. The analysis for each Pfirrmann score revealed a significant difference between the asymmetry effect obtained with MTR$_{asym}$ and SLR$_{asym}$ for Pfirrmann score 3 in NP only ($P < 0.01$).

CEST and CESL asymmetry maps are provided for two exemplarily selected volunteers with a degenerative disc adjacent to a nondegenerative disc (Fig. 2). Both volunteers show an apparent increase of asymmetry effect for CESL compared with CEST in degenerative discs, whereas in the nondegenerative disc, this effect is only detectable in one of both volunteers. There was a significant difference for both MTR$_{asym}$ and SLR$_{asym}$ between NP and AF, with a higher level of significance for SLR$_{asym}$ (MTR$_{asym}$: $P = 0.014$, SLR$_{asym}$: $P = 0.005$). MTR$_{asym}$ and T_2 (NP: $\rho = 0.76$, $P < 0.001$; AF: $\rho = 0.60$, $P < 0.001$) as well as SLR$_{asym}$ and T_2 correlated significantly in both NP and AF (NP: $\rho = 0.73$, $P < 0.001$; AF: $\rho = 0.47$, $P < 0.001$) over the whole collective. Considering all Pfirrmann scores separately, a significant correlation to T_2 was only obtained for Pfirrmann score 2 with both SLR$_{asym}$ (NP: $\rho = 0.70$, $P < 0.001$; AF: $\rho = 0.42$, $P = 0.002$) and MTR$_{asym}$ in NP and AF (NP: $\rho = 0.64$, $P < 0.001$; AF: $\rho = 0.53$, $P < 0.001$) and for Pfirrmann score 1 with SLR$_{asym}$ in NP ($\rho = 0.69$, $P = 0.035$).

Eight of 65 IVDs were classified as Pfirrmann score 1 (approximately 12.3%), 45 discs as Pfirrmann score 2 (approximately 69.2%), 9 discs as Pfirrmann score 3 (approximately 13.8%) and 3 as Pfirrmann score 4 (4.6%). MTR$_{asym}$ and SLR$_{asym}$ decreased with increasing Pfirrmann scores (Table 3). The Kruskal-Wallis analysis revealed significant differences in MTR$_{asym}$ values between Pfirrmann scores for both NP and AF (NP: $P < 0.001$; AF: $P < 0.004$). For SLR$_{asym}$ the Kruskal-Wallis analysis revealed significant differences in NP only (NP: $P = 0.010$; AF: $P = 0.104$).

DISCUSSION

In this study, we demonstrated that both MTR$_{asym}$ and SLR$_{asym}$ analysis can be used to study the GAG content of IVDs at 3T and lead to comparable results. Both techniques showed significant differences between NP and AF, with a higher level of significance for SLR$_{asym}$. This difference between NP and AF is caused by a higher GAG concentration and higher T1 values in NP compared with AF and has been previously reported by different research groups (2,3,5,6,15).

For hydroxyl proton exchange, an increased saturation effect is expected for CESL compared with CEST (10). We hypothesized a significant increase in the chemical

Table 2
Descriptive Analysis of MTR$_{asym}$, SLR$_{asym}$, and T_2 Values in NP and AF.

	Mean	Median	σ	Minimum	Maximum
MTR$_{asym}$(NP) [%]	4.19	3.86	2.63	−0.89	9.47
MTR$_{asym}$(AF) [%]	3.03	3.14	2.03	−1.37	7.85
SLR$_{asym}$(NP) [%]	4.56	4.32	2.75	−3.69	11.14
SLR$_{asym}$(AF) [%]	3.38	2.97	2.35	−1.95	10.46
T_2 (NP) [ms]	129.44	127.05	50.32	48.23	247.50
T_2 (AF) [ms]	89.34	85.32	25.93	41.61	154.59

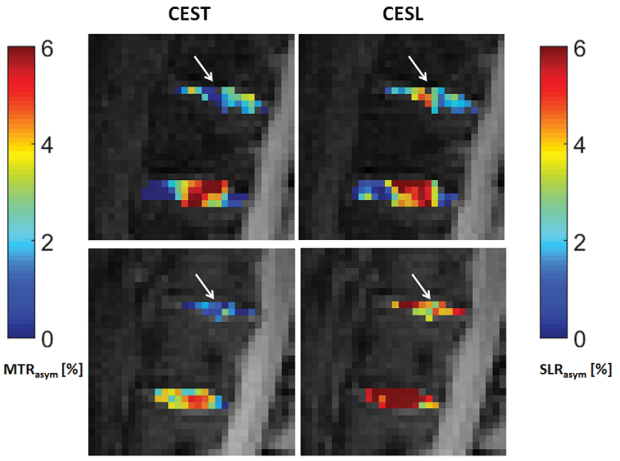

FIG. 2. MTR_{asym} [%] and SLR_{asym} [%] maps overlaid with anatomical imaging in lumbar intervertebral discs of two volunteer with a degenerative disc adjacent to a nondegenerative disc. Degenerative discs are indicated by white arrows. Upper row: Intervertebral discs L2/L3 (Pfirrmann score 4) and L3/L4 (Pfirrmann score 2) of the first selected volunteer. Lower row: Intervertebral discs L1/L2 (Pfirrmann score 3) and L2/L3 (Pfirrmann score 2) of the second volunteer.

exchange dependent asymmetry effect measured with CESL compared with CEST. In our study, there was no significant difference between these two techniques over the whole collective, whereas a significant difference was obtained for discs with Pfirrmann score 3. For practical applications, B_0 and B_1 inhomogeneity might lead to an imperfect SL presaturation scheme and reduce the sensitivity gain of CESL over CEST (10). Therefore, we expect that further optimization of B_0 and B_1 inhomogeneity correction might be necessary to reveal a sensitivity gain of CESL over CEST. Furthermore, adiabatic spin-lock approaches might overcome the limitations of field inhomogeneities (16). In our study, we performed higher-order manual shimming. However, the investigated FOV included several materials including IVDs and vertebral bodies, which may have led to B_0 and B_1 inhomogeneities and possibly influenced our results.

MTR_{asym} and SLR_{asym} showed T_2-dependency. In the present study, this was observed by quantitative analysis comparing asymmetry values directly with T_2 as well as with a semi-quantitative analysis using the Pfirrmann scoring system. For MTR_{asym}, a T_2-shine-through effect was suggested previously (17–19). The strength of T_2-shine-through effect on MTR_{asym} and SLR_{asym} might be investigated in future studies, both theoretically and experimentally. Additionally, it would be desirable to correlate histologically determined GAG content from cartilage samples to chemical exchange asymmetry analysis. Gathering of histological specimens to correlate GAG content of IVDs with biochemical imaging was not performed in this study due to ethical considerations.

In our study, SLR_{asym} and MTR_{asym} were determined with the same saturation power of the CE presaturation module to produce optimal similarity of conditions. SLR_{asym} was reported to be less sensitive to DWS compared with MTR_{asym} (10). Hence, further optimization with higher saturation power and shorter irradiation duration might improve the CESL sequence.

One limitation of our study was the long acquisition time of approximately half an hour leading to motion during MR acquisitions in two volunteers. In addition, the long acquisition time impedes data acquisition of orthopedic patients. Methods to reduce the protocol duration are the acquisition of either the CEST or the CESL sequence, a reduced number of acquired frequency offsets during the WASSR sequence, or the application of parallel imaging techniques like GRAPPA or SENSE (20,21).

One difficulty of the present study is the limited sensitivity of 3T MR for the assessment of GAG content resulting in a low CEST or CESL contrast (22). To enhance this sensitivity, MR systems with higher magnetic fields are favorable (23). However, high-field MR systems are not used in clinical routine.

CONCLUSIONS

In summary, CESL was shown to be applicable for biochemical GAG imaging in vivo, however, no sensitivity gain compared with CEST was observed. CESL shows an increased significant difference between NP and AF.

ACKNOWLEDGMENTS

We gratefully acknowledge K. Bousabarah and E. Rädisch for assistance with data acquisition.

REFERENCES

1. Urban JP, Winlove CP. Pathophysiology of the intervertebral disc and the challenges for MRI. J Magn Reson Imaging 2007;25:419–432.
2. Haneder S, Apprich SR, Schmitt B, Michaely HJ, Schoenberg SO, Friedrich KM, Trattnig S. Assessment of glycosaminoglycan content in intervertebral discs using chemical exchange saturation transfer at 3.0 Tesla: preliminary results in patients with low-back pain. Eur Radiol 2013;23:861–868.
3. Saar G, Zhang B, Ling W, Regatte RR, Navon G, Jerschow A. Assessment of glycosaminoglycan concentration changes in the

Table 3
MTR_{asym} [%] and SLR_{asym} [%] in NP and AF for Each Pfirrmann Score.

	Pfirrmann score			
	1	2	3	4
Percentage [%]	12.3	69.2	13.8	4.6
MTR_{asym} (NP) [%]	5.58 ± 2.27	4.70 ± 2.44	1.71 ± 1.30	0.21 ± 1.16
SLR_{asym} (NP) [%]	5.81 ± 1.07	4.83 ± 3.03	3.06 ± 0.93	1.69 ± 1.43
MTR_{asym} (AF) [%]	3.39 ± 1.85	3.47 ± 1.92	1.44 ± 1.35	0.13 ± 1.52
SLR_{asym} (AF) [%]	3.74 ± 1.37	3.63 ± 2.59	2.77 ± 1.08	0.53 ± 1.55

intervertebral disc via chemical exchange saturation transfer. NMR Biomed 2012;25:255–261.
4. Schmitt B, Zaiss M, Zhou J, Bachert P. Optimization of pulse train presaturation for CEST imaging in clinical scanners. Magn Reson Med 2011;65:1620–1629.
5. Müller-Lutz A, Schleich C, Pentang G, Schmitt B, Lanzman RS, Matuschke F, Wittsack HJ, Miese F. Age-dependency of glycosaminoglycan content in lumbar discs: a 3T gagcEST study. J Magn Reson Imaging 2015;42:1517–1523.
6. Müller-Lutz A, Schleich C, Schmitt B, Antoch G, Matuschke F, Quentin M, Wittsack HJ, Miese F. Gender, BMI and T2 dependencies of glycosaminoglycan chemical exchange saturation transfer in intervertebral discs. Magn Reson Imaging 2016;34:271–275.
7. Schleich C, Müller-Lutz A, Matuschke F, et al. Glycosaminoglycan chemical exchange saturation transfer of lumbar intervertebral discs in patients with spondyloarthritis. J Magn Reson Imaging 2015;42:1057–1063.
8. Schleich C, Müller-Lutz A, Eichner M, Schmitt B, Matuschke F, Bittersohl B, Zilkens C, Wittsack HJ, Antoch G, Miese F. Glycosaminoglycan chemical exchange saturation transfer of lumbar intervertebral discs in healthy volunteers. Spine (Phila Pa 1976) 2016;41:146–152.
9. Roeloffs V, Meyer C, Bachert P, Zaiss M. Towards quantification of pulsed spinlock and CEST at clinical MR scanners: an analytical interleaved saturation-relaxation (ISAR) approach. NMR Biomed 2015;28:40–53.
10. Jin T, Kim SG. Advantages of chemical exchange-sensitive spin-lock (CESL) over chemical exchange saturation transfer (CEST) for hydroxyl- and amine-water proton exchange studies. NMR Biomed 2014;27:1313–1324.
11. Zaiss M, Bachert P. Chemical exchange saturation transfer (CEST) and MR Z-spectroscopy in vivo: a review of theoretical approaches and methods. Phys Med Biol 2013;58:R221–R269.
12. Jin T, Autio J, Obata T, Kim SG. Spin-locking versus chemical exchange saturation transfer MRI for investigating chemical exchange process between water and labile metabolite protons. Magn Reson Med 2011;65:1448–1460.
13. Pfirrmann CW, Metzdorf A, Zanetti M, Hodler J, Boos N. Magnetic resonance classification of lumbar intervertebral disc degeneration. Spine (Phila Pa 1976) 2001;26:1873–1878.
14. Kim M, Gillen J, Landman BA, Zhou J, van Zijl PC. Water saturation shift referencing (WASSR) for chemical exchange saturation transfer (CEST) experiments. Magn Reson Med 2009;61:1441–1450.
15. Kim M, Chan Q, Anthony MP, Cheung KM, Samartzis D, Khong PL. Assessment of glycosaminoglycan distribution in human lumbar intervertebral discs using chemical exchange saturation transfer at 3 T: feasibility and initial experience. NMR Biomed 2011;24:1137–1144.
16. Santyr GE, Fairbanks EJ, Kelcz F, Sorenson JA. Off-resonance spin locking for MR imaging. Magn Reson Med 1994;32:43–51.
17. Zaiss M, Windschuh J, Paech D, et al. Relaxation-compensated CEST-MRI of the human brain at 7T: unbiased insight into NOE and amide signal changes in human glioblastoma. Neuroimage 2015;112:180–188.
18. Rehnitz C, Kupfer J, Streich NA, Burkholder I, Schmitt B, Lauer L, Kauczor HU, Weber MA. Comparison of biochemical cartilage imaging techniques at 3 T MRI. Osteoarthritis Cartilage 2014;22:1732–1742.
19. Zaiss M, Xu J, Goerke S, Khan IS, Singer RJ, Gore JC, Gochberg DF, Bachert P. Inverse Z-spectrum analysis for spillover-, MT-, and T1-corrected steady-state pulsed CEST-MRI--application to pH-weighted MRI of acute stroke. NMR Biomed 2014;27:240–252.
20. Griswold MA, Jakob PM, Heidemann RM, Nittka M, Jellus V, Wang J, Kiefer B, Haase A. Generalized autocalibrating partially parallel acquisitions (GRAPPA). Magn Reson Med 2002;47:1202–1210.
21. Pruessmann KP, Weiger M, Scheidegger MB, Boesiger P. SENSE: sensitivity encoding for fast MRI. Magn Reson Med 1999;42:952–962.
22. Liu Q, Jin N, Fan Z, Natsuaki Y, Tawackoli W, Pelled G, Bae H, Gazit D, Li D. Reliable chemical exchange saturation transfer imaging of human lumbar intervertebral discs using reduced-field-of-view turbo spin echo at 3.0 T. NMR Biomed 2013;26:1672–1679.
23. Deng M, Yuan J, Chen WT, Chan Q, Griffith JF, Wang YX. Evaluation of glycosaminoglycan in the lumbar disc using chemical exchange saturation transfer MR at 3.0 Tesla: reproducibility and correlation with disc degeneration. Biomed Environ Sci 2016;29:47–55.

Magn Reson Mater Phy (2014) 27:477–485
DOI 10.1007/s10334-014-0433-8

RESEARCH ARTICLE

Pilot study of Iopamidol-based quantitative pH imaging on a clinical 3T MR scanner

Anja Müller-Lutz · Nadia Khalil · Benjamin Schmitt · Vladimir Jellus · Gael Pentang · Georg Oeltzschner · Gerald Antoch · Rotem S. Lanzman · Hans-Jörg Wittsack

Received: 20 September 2013 / Revised: 24 January 2014 / Accepted: 27 January 2014 / Published online: 26 February 2014

Abstract
Objective The objective of this study was to show the feasibility to perform Iopamidol-based pH imaging via clinical 3T magnetic resonance imaging (MRI) using chemical exchange saturation transfer (CEST) imaging with pulse train presaturation.
Materials and methods The pulse train presaturation scheme of a CEST sequence was investigated for Iopamidol-based pH measurements using a 3T magnetic resonance (MR) scanner. The CEST sequence was applied to eight tubes filled with 100-mM Iopamidol solutions with pH values ranging from 5.6 to 7.0. Calibration curves for pH quantification were determined. The dependence of pH values on the concentration of Iopamidol was investigated. An in vivo measurement was performed in one patient who had undergone a previous contrast-enhanced computed tomography (CT) scan with Iopamidol. The pH values of urine measured with CEST MRI and with a pH meter were compared.
Results In the measured pH range, pH imaging using CEST imaging with pulse train presaturation was possible. Dependence between the pH value and the concentration of Iopamidol was not observed. In the in vivo investigation, the pH values in the human bladder measured by the Iopamidol CEST sequence and in urine were consistent.
Conclusion Our study shows the feasibility of using CEST imaging with Iopamidol for quantitative pH mapping in vitro and in vivo on a 3T MR scanner.

Keywords Chemical exchange saturation transfer (CEST) · pH quantification · Iopamidol · pH-responsive contrast agent · Magnetic resonance imaging (MRI)

The concepts and information presented in this paper are based on research and are not commercially available.

A. Müller-Lutz (✉) · N. Khalil · G. Pentang · G. Oeltzschner · G. Antoch · R. S. Lanzman · H.-J. Wittsack
Department of Diagnostic and Interventional Radiology, Medical Faculty, University Dusseldorf, Moorenstrasse 5, 40225 Düsseldorf, Germany
e-mail: Anja.Lutz@med.uni-duesseldorf.de

B. Schmitt
Healthcare Sector, Siemens Ltd. Australia, 160 Herring Road, Macquarie Park, NSW 2113, Australia

V. Jellus
Healthcare Sector, Siemens AG, Allee am Röthelheimpark 2, 91052 Erlangen, Germany

Introduction

Alteration in pH values can be observed in different pathologies, such as in cancer or renal diseases [1–9]. For example, the anaerobic glycolysis in cancer cells results in an acidic pH in cancer tissue [1–3], which might result in an increased resistance to radio- and chemotherapies [3, 4]. Tissue pH can be determined noninvasively in vivo using several magnetic resonance (MR) techniques such as MR spectroscopy (MRS) and magnetic resonance spectroscopic imaging (MRSI) [7, 10–23], MRI with T1-shortening contrast agents [3, 24–27], or with the pH-dependent chemical exchange saturation transfer (CEST) effect [6, 28–33].

pH measurements with MRS and MRSI are based on differences in chemical shifts between pH-dependent and pH-independent resonances [34]. Different methods of MRS and MRSI have been used including ^{31}P and ^{19}F spectroscopy [7, 10–18], ^{1}H spectroscopic imaging [19–21], and the use of hyperpolarized ^{13}C bicarbonate [22, 23].

While these techniques have been applied successfully in several studies for pH imaging, their main disadvantage is their limited spatial resolution.

MR relaxometry represents another approach for pH-imaging and is based on the injection of Gd-based pH-sensitive contrast agents [25, 26]. Since the pH contrast agents are both pH-dependent and concentration-dependent, Raghunand et al. [3] have introduced a two-phase injection method with two contrast agents, one being pH sensitive and the other one pH insensitive for pH quantification. The main disadvantages of Gd-based approaches are that at least two contrast agents have to be injected in order to obtain concentration-independent pH determination and the need to perform calibration measurements in vivo. Furthermore, Martinez et al. [35] observed that a reliable pH quantification in the core of the tumor is not possible with this method.

A promising approach for tissue pH quantification is the use of pH-sensitive chemical exchange-dependent saturation transfer (CEST) imaging. CEST describes the indirect saturation of bulk water due to chemical exchange with labile protons, which are previously saturated by an on-resonance irradiation pulse [36]. In general, CEST contrast depends on several factors such as tissue pH, concentration of labile protons, and temperature. One method enabling pH quantification with CEST is the pHWI technique, which exploits the dependence of the APT–CEST effect on the proton exchange constant, which itself depends on the pH value [31–33]. In order to perform concentration-independent CEST measurements, ratiometric methods using the CEST effect of two labile proton groups have been introduced [6, 30, 37, 38], showing that in vivo pH quantification is possible in animals at high field strengths (7T) using a continuous wave saturation pulse [6, 9].

However, continuous-wave (CW) saturation pulses cannot be used on clinical MR scanners mainly due to technical and hardware constraints. Therefore, a pulse train presaturation scheme was introduced for CEST imaging at clinical MR systems [39, 40]. The use of a pulse train presaturation scheme has the additional benefit compared with the CW CEST method of a reduced specific absorption rate over the whole CEST presaturation module. This approach combined with a pH-sensitive CEST contrast agent might therefore be used for pH measurements on clinical MR scanners.

One potential CEST contrast agent enabling ratiometric pH quantification is Iopamidol [6, 41], a well-established and approved contrast agent for computed tomography (CT) [41]. It possesses labile protons and contains two types of amide functionalities, which cause a CEST effect at two different frequencies [6].

Therefore, the aim of the present study was to show the feasibility of quantitative pH imaging via the use of Iopamidol as a ratiometric CEST contrast agent on a clinical 3T MR scanner.

Materials and methods

Magnetic resonance imaging was performed on a whole-body 3T MRI system (Magnetom Trio A Tim System, Siemens Healthcare, Erlangen, Germany). CEST imaging was performed in a 2D acquisition mode using an acquisition matrix (M × P) of 192 × 192 and a slice thickness of 8 mm. The repetition time was 145 ms, the echo time 2.85 ms, and the flip angle was 10°. In order to accelerate data acquisition, the parallel imaging method GRAPPA with a factor of 2 was applied.

In-vitro MRI studies

All in-vitro experiments were performed with a standard twelve-channel receive-only head coil. A CEST preparation module was applied with pulsed saturation radio frequency (RF) pulses followed by an RF-spoiled segmented-gradient echo (GRE) readout. The maximum CEST offset was 9 ppm. The field of view was adjusted to the phantom size and amounts to 180 mm^2, thus resulting in a resolution of 0.94 × 0.94 mm^2. Thirteen shots per slice were used in the GRE sequence.

Three in-vitro studies were performed. Iopamidol solutions were heated to 37 °C before each study and embedded in a warm water bath with a temperature of 38 °C, which served as a temperature stabilizer. The first study was performed in order to maximize the CEST effect with respect to the CEST parameters (sequence design study). The second study was undertaken to obtain calibration curves for pH quantification (pH calibration study). The third study addressed the dependence of the method on the concentration of the contrast agent (concentration dependence study).

- Sequence design study

This study was performed using a potassium phosphate-buffered 100-mM Iopamidol solution with a constant pH value of 6.4. The Iopamidol solution was transferred into a tube with a diameter of 5 cm, embedded in a water cylinder with a diameter of 10 cm and a length of 9 cm. The B_1 continuous-wave amplitude equivalent (B_1-CWAE), the pulse duration and interpulse delay (PD and IPD), and the number of CEST pulses (NP) were investigated regarding their influence on the CEST effect. Here, B_1-CWAE is the time average B_1 amplitude [42, 43]. The parameters used for optimization of the CEST presaturation module as well as the corresponding acquisition times are listed in Table 1.

Table 1 Parameters of the CEST presaturation module in the sequence design study

B_1-CWAE (μT)	NP	PD = IPD (ms)	Number of acquired points in the CEST spectrum	Duration of CEST sequence (min:s)
0.2, 0.4, 0.6, 0.8	10	100	34	13:20
0.4	6, 8, 10	100	34	8:08, 10:44, 13:20
0.4	10	60, 80, 100	34	8:24, 10:52, 13:20

- pH calibration study

We added 100 mM Iopamidol to an aqueous potassium phosphate-buffered solution with pH values ranging from 5.6 to 7.0 (interval 0.2 pH). The eight Iopamidol solutions with different pH values were transferred into eight different tubes with a diameter of 1.4 cm. All tubes were placed into a cylinder with a diameter of 12 cm and a length of 9 cm, which was filled with water. The CEST sequence with the parameters determined by the sequence design study was applied for CEST imaging.

- Concentration dependence study

This study was performed with Iopamidol in aqueous potassium phosphate-buffered solution with a pH value of 6.8 ± 0.01. Eight different concentrations of Iopamidol were imaged. The Iopamidol concentration was varied from 20 to 160 mM in steps of 20 mM. The concentration dependence study was performed with the same phantom and CEST sequence as in the pH calibration study.

In-vivo MRI studies

A first in-vivo measurement was performed in a 63-year-old female patient who had undergone a previous contrast-enhanced CT with Iopamidol. The time between the CT and Iopamidol-CEST acquisition was about 1 h and 15 min. Using the Iopamidol kinetics described by McKinstry et al. [44] and a bladder volume in women of about 250–550 ml, the Iopamidol concentration in the bladder can be estimated to be in the range of 50–130 mM. MR imaging of the urinary bladder was performed with a 6-channel array body coil in combination with a 24-channel array spine coil integrated into the scanner. A CEST preparation module was applied with pulsed saturation RF pulses followed by a 2D RF-spoiled segmented GRE readout of a single slice analogous to the phantom measurements. The maximum CEST offset was 10 ppm. The field of view was adjusted to 380 mm^2, thus resulting in a resolution of 2.0×2.0 mm^2. Six shots per slice were used in the GRE sequence. The CEST preparation module parameters obtained by the in-vitro study were used. The acquisition duration of the in-vivo Iopamidol-CEST examination was 13 min and 57 s.

The study was approved by the local ethics committee and written informed consent was obtained from the patient prior to the MR examination.

Data analysis

All data were evaluated using in-house-developed MATLAB software (The Mathworks, Inc., Natick, MA, USA, R2011b). The Z-spectra were obtained by interpolating data points on a voxel-by-voxel basis with cubic splines in order to determine the exact location of bulk water, which was assigned to 0 ppm. Furthermore, based on the offset-corrected Z-spectra, the MRT_{asym} curves were determined by

$$\mathrm{MTR}_{\mathrm{asym}}(\Delta\omega) = \frac{I(-\Delta\omega) - I(\Delta\omega)}{I_0},$$

where $\Delta\omega$ ranges from 0 ppm to the maximum offset in the offset-corrected Z-spectra.

The analysis of the sequence design study includes the investigation, if the CEST effect of both amide functionalities of Iopamidol is differentiable for different CEST pre-pulse parameters, as well as a the quantitative analysis of the saturation transfer effect.

For saturation transfer analysis, the saturation transfer was calculated voxel-by-voxel for both CEST peaks at the frequencies $\Delta\omega_1 = 4.2$ ppm and $\Delta\omega_2 = 5.4$ ppm according to

$$\mathrm{ST}(\Delta\omega)[\%] = \frac{I(-\Delta\omega) - I(\Delta\omega)}{I(-\Delta\omega)} * 100,$$

where ST is an abbreviation for saturation transfer. High saturation transfer effects for both peaks are desirable, since the CEST effect should be clearly identifiable.

Based on the criteria that the CEST effect is as high as possible under the condition that the CEST effects of the two types of amide functionalities are differentiable, the optimal sequence parameters were determined.

To evaluate the pH calibration study, the ratiometric saturation transfer RST was calculated by the following equation:

$$\mathrm{RST} = \frac{(100 - \mathrm{ST}(\Delta\omega_1)) \cdot \mathrm{ST}(\Delta\omega_2)}{(100 - \mathrm{ST}(\Delta\omega_2)) \cdot \mathrm{ST}(\Delta\omega_1)}$$

RST values were plotted versus the pH value. The data were fitted by a third-order polynomial function.

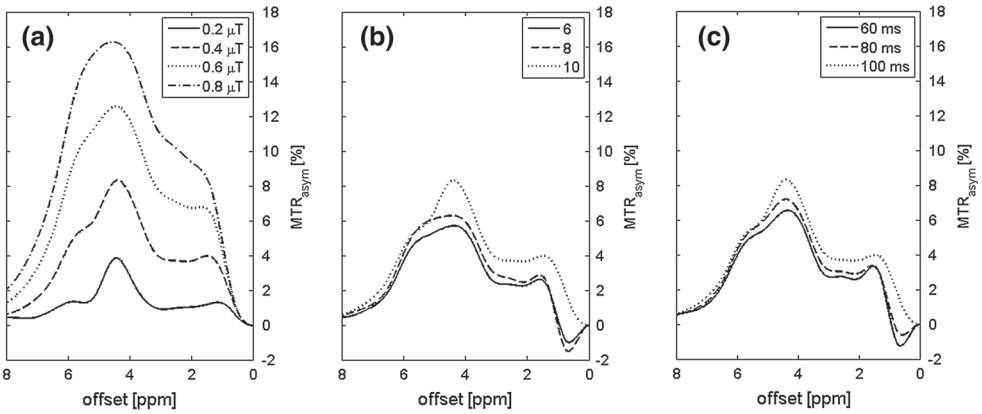

Fig. 1 MTR_{asym} curves of the Iopamidol solution measured with different B_1-CWAE field strengths (**a**), different number of pulses (**b**), and different pulse durations (**c**)

The calibration curve was further used in the concentration dependence measurement and in vivo measurement for pH quantification.

The evaluation of concentration dependence was performed in the phantom filled with eight different concentrations at a pH value of 6.8 by calculation of pH maps based on the third-order polynomial fit.

For the in-vivo study, pH quantification was applied based on the third-order polynomial fit. First, the bladder was selected manually. For all pixels inside this region of interest, the pH value was determined. Afterwards, the mean and standard deviation of the pH value of the bladder was determined. The pH of the human bladder was compared with the pH value measured with a pH meter (Mettler Toledo) in the patient's urine.

For the evaluation of statistical significance, a two-tailed, unpaired Student's t test was performed. Values below 0.05 were considered to be significant.

Results

Sequence design study

Figure 1 shows the MTR_{asym} curves for different B_1-CWAE, different numbers of presaturation pulses, and different pulse and interpulse durations. MTR_{asym} increases strongly with increasing B_1-CWAE. The two MTR_{asym} peaks at 4.2 and 5.4 ppm merge with increasing B_1-CWAE, so that they are not differentiable for B_1-CWAE ≥ 0.6 μT.

The increasing number of presaturation pulses and the increasing pulse and interpulse duration tend to promote saturation transfer effects. Therefore, and due to the absence of a tendency to merge, high pulse and interpulse durations and a high number of saturation pulses have been chosen.

Figure 2 shows the saturation transfer effects of both amide functionalities. Increasing STs of both CEST peaks were obtained with increasing B_1-CWAE amplitude. This increase was statistically significant (p value <0.0001). Increasing NP and PD resulted in slightly increasing ST values, which was significant for the first Iopamidol peak (p value <0.0001). For the second Iopamidol peak, the increase was only significant for an increase from six to eight saturation pulses, and for a prolongation of the pulse duration from 60 to 80 ms (p value <0.0001). No significant increase of the second Iopamidol peak was obtained by increasing the number of saturation pulses to ten (p value = 0.12) or a prolongation of pulse duration to 100 ms (p value = 0.15).

Due to the tendency of increased saturation transfer effects for increasing NP and PD aligned with the observation of two differentiable MTR_{asym} effects, the selection of NP = 10 and PD = IPD = 100 ms has proven to be optimal. For B_1-CWAE, an increase in saturation effect was paired with the tendency of both CEST effects to merge. Therefore, an intermediate value of B1-CWAE of 0.4 μT was used. This parameter setting ensures high saturation transfer effects without merging at 3T.

In summary, B_1-CWAE = 0.4 μT, NP = 10 and IPD = PD = 100 ms resulted in the best saturation transfer effects, enabling the detection of both CEST peaks.

pH calibration study

Figure 3 shows the results of the pH calibration study: RST is shown as parametric image (a) and is plotted versus the pH value (b). The third-order polynomial fit is shown as grey solid line. The fit equation was given by

$$\mathrm{RST} = a_0 + a_1(\mathrm{pH} - b) + a_2(\mathrm{pH} - b)^2 + a_3(\mathrm{pH} - b)^3,$$

with $a_0 = 0.28$, $a_1 = 0.68$, $a_2 = 1.99$, $a_3 = 0.48$ and $a = 7.11$.

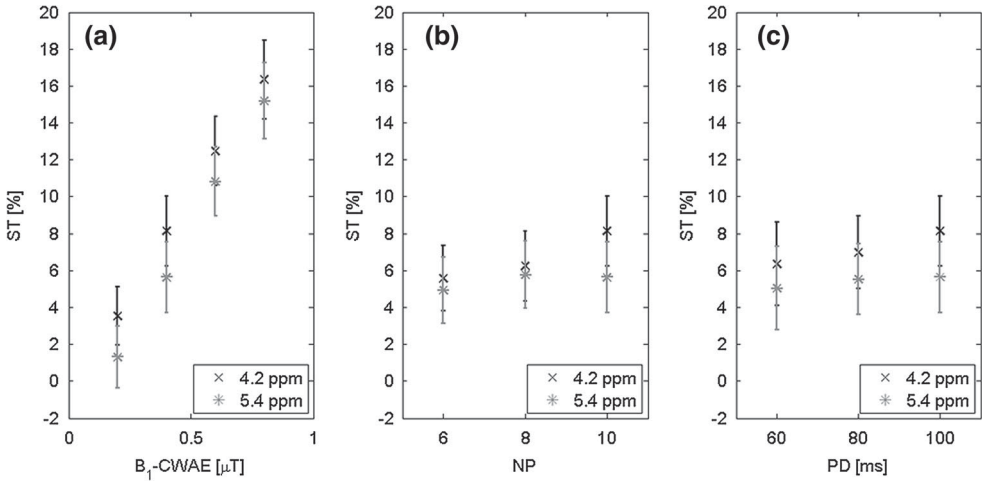

Fig. 2 Saturation transfer (ST) dependence on the B_1-CWAE field strength (**a**), the number of pulses (**b**), and the pulse duration (**c**)

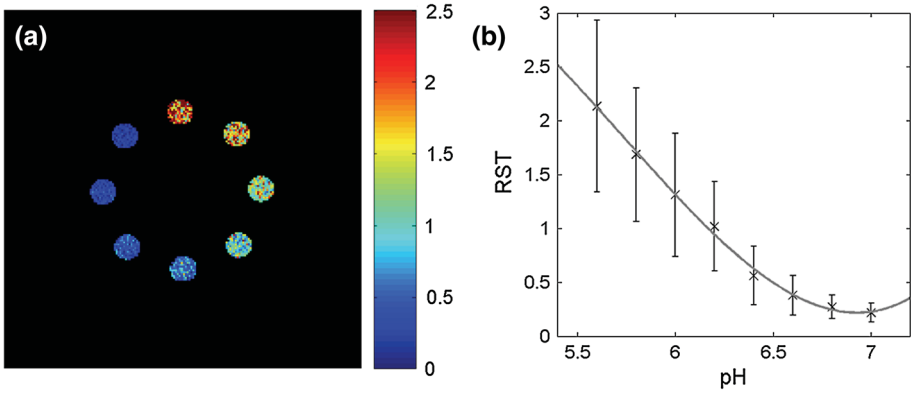

Fig. 3 **a** RST map of the eight different tubes filled with Iopamidol solution, with pH values ranging from 5.6 (*top tube*) to 7.0 (*upper left corner*) arranged in a clockwise direction. **b** RST is plotted versus the pH value. The *grey line* represents the curve fit using a third-order polynomial function

Concentration dependence study

Figure 4 shows the pH dependence on the concentration. For all concentrations ranging from 20 to 160 mM, the pH value determined by CEST MRI was in good accordance with the pH value determined by the pH meter. Only the standard deviation of the low-concentration pH CEST-measurements was slightly increased at low concentrations.

In-vivo measurement

Figure 5 shows the CEST curve and MTR_{asym} curve measured in the human bladder. The saturation effect of Iopamidol is clearly visible in both the CEST curve and the MTR_{asym} curve. In addition, a second peak between 1 and 1.5 ppm can be observed, which can be assigned to the CEST effect of urea. The pH value determined by the Iopamidol-CEST sequence was 6.65 ± 0.34. This value was in good accordance with the pH value measured after the examination of the patient's urine, which was 6.72 ± 0.01.

Discussion

The present study demonstrates the feasibility of using Iopamidol-CEST to quantify pH values in vitro as well as in vivo on a clinical 3T system.

The considered pH range in our study was from 5.6 to 7.0. This range includes the extracellular pH values measured in human tumors (extracellular pH = 6.8–6.9), but not the normal extracellular pH value of 7.4 and intracellular pH value of tumors (intracellular pH = 7.0–7.4) [7, 25, 27, 45–47]. Future studies using Iopamidol as a pH-responsive contrast agent might therefore be of interest in investigating the influence of different CEST presaturation modules on the measureable pH range.

Longo et al. [9] observed an entire pH of the mouse kidney of 6.73 ± 0.11 and found lower values in the inner and outer medulla. However, increased values in the kidney were observed after glycerol injection (7.09 ± 0.10). Differentiating renal cortex and medulla using our imaging method should be possible and has to be investigated in the future. Reliable measurement of pH values >7.0 might be difficult due to the reduced influence of the chemical exchange process of the second Iopamidol peak. In order to

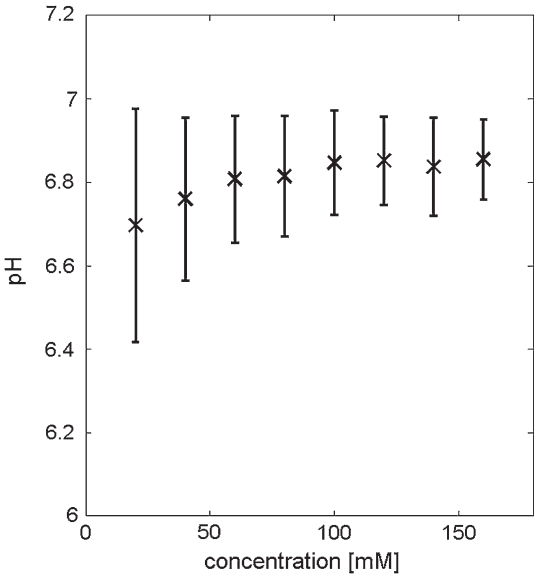

Fig. 4 Dependence of the Iopamidol concentration on the measured pH value. Thereby, the mean and standard deviation of the pH values from all pixels inside the tube with a specific concentration was plotted versus the concentration. The pH value of the Iopamidol solution was 6.8 ± 0.01. The Iopamidol concentration varied from 20 to 160 mM in steps of 20 mM. Notice that the real pH value was inside the standard deviation of the measured pH value for all concentrations

enable pH quantification in vivo in humans at higher pH values, the Iopamidol-CEST method would have to be set up at a human 7T MRI system, thus enabling a similar imaging sequence as used by Longo et al. [9].

One main drawback using a field strength of 3T is an increased CEST effect overlap of the two types of amide functionalities compared to high-field systems, which prohibits B_1-CWAE field strengths higher than 0.4 μT, although higher field strengths result in higher saturation transfer effects. Earlier studies investigating Iopamidol at higher field strengths have used higher B_1 amplitudes, which enable higher saturation transfer effects [6, 9]. The smaller saturation transfer effects at 3T might be prone to errors due to signal noise. However, despite the small B_1-CWAE amplitude used in our study, a clear dependence on pH value for the relation of both CEST peaks was observed.

The ratiometric saturation transfer parameter RST determined in our study at a field strength of 3T shows a similar pH dependence as the RST calculated by Longo et al. [6] at a field strength of 7T, an irradiation time of 5 s, and a irradiation power of 3 μT. In our study, as well as in the study of Longo et al. [6], the RST value is between 0 and 2.5. In both studies, RST is highest at low pH values, and decreases with increasing pH value [6]. These results confirm the transferability of the Iopamidol-CEST imaging sequence for pH mapping to 3T MR systems.

A further disadvantage of 3T MR systems compared to higher field strengths is the increased spill-over effect of water. By keeping B_1-CWAE low, spill-over effects for offset values higher than 3 ppm can be kept low. One possibility to further decrease the influence of spill-over effects is the use of paramagnetic instead of diamagnetic contrast agents. pH quantification with paramagnetic contrast agents have been performed previously by Sheth et al. [37] with a spectrometer operating at 600 MHz. Future studies might be performed in order to investigate the feasibility of paramagnetic contrast agents for pH quantification with CEST imaging at clinical 3T MR systems.

In our study, a pulsed CEST preparation module was applied. In the study of Zu et al. [48], it was stated that the B_1-CWAE is the appropriate B_1 norm to obtain a similar behavior of labeling and spillover effects compared to the continuous wave experiment [48]. Future studies might be performed in order to compare the continuous wave and pulsed CEST method for pH quantification using Iopamidol at 3T MRI systems.

Our study clearly shows the concentration independence of the pH quantification method for all examined concentrations, although the standard deviation is slightly increased for concentrations below 40 mM. Thus, pH quantification with Iopamidol is possible, even for low concentrations, but an SNR decrease in the pH map can be expected. Since the expected concentration for the human in-vivo study is inside the investigated range of the concentration independence study, the application of Iopamidol-CEST for in-vivo pH imaging is justified.

The pH value measured in the in-vivo measurement of the human bladder was in good accordance with pH determined in the urine by the pH meter, thus reinforcing the hypothesis that pH imaging is possible at clinical 3T scanners.

In our in-vitro study, pH quantification was performed at a temperature of 37 °C. Next to concentration, temperature might also influence the obtained CEST effects. The temperature dependence has to be taken into account in the pH quantification in patients suffering from fever. Furthermore, temperature differences in tissue might arise due to inflammation. Therefore, Iopamidol-CEST imaging in combination with temperature measurements might be performed in the future.

In the present work, field inhomogeneity correction was performed by shifting the interpolated CEST curves in order to match the exact location of bulk water, which was assigned to 0 ppm. Alternatively, other field inhomogeneity correction algorithms like offset correction by the acquisition of an additional B_0 field map or water saturation shift referencing (WASSR) might be used [49, 50]. Nevertheless, additional acquisition time is needed to perform these B_0 inhomogeneity correction processes. The effect of

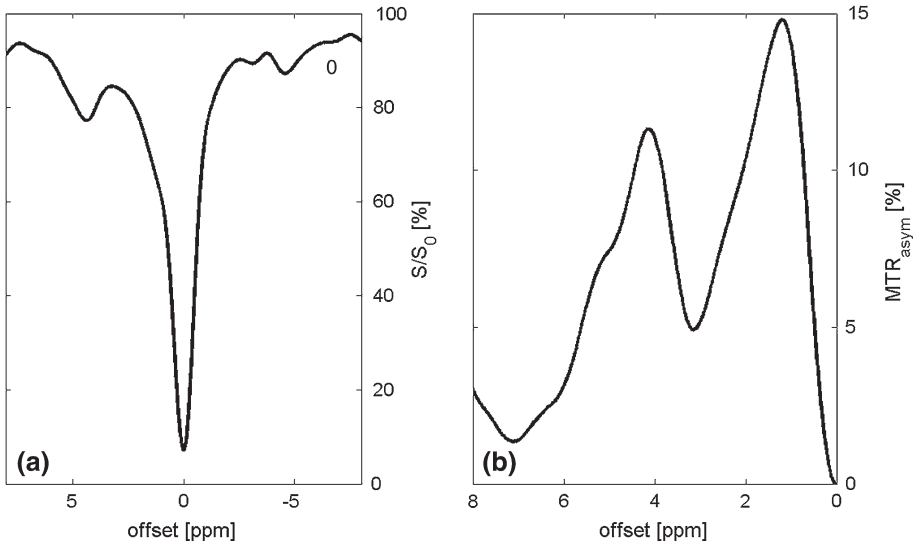

Fig. 5 CEST (**a**) and MTR_{asym} (**b**) curve in the bladder

different field inhomogeneity correction algorithms on the dependence of the ratiometric saturation transfer should be investigated in the future. In particular, it would be of interest if the standard deviation in the pH map can be reduced by field inhomogeneity correction with the WASSR technique or the B_0 field map.

In contrast to the study of Longo et al. [6, 9], CEST presaturation was performed in the present study using a pulse train instead of a continuous wave presaturation pulse due to SAR demands and due to technical constraints of the 3T MR system. However, high-saturation effects could be achieved with our CEST presaturation pulses. Nevertheless, future studies might be performed on an experimental MR system without technical constraints regarding pulse width and duty cycle in order to compare Iopamidol-CEST imaging with continuous and pulsed train presaturation.

Previously, imaging of pH value was performed using APT–CEST imaging, which was also referred to as pHWI [31–33, 42]. With pHWI, Sun et al. [31] showed that a differentiation between ischemic penumbra and benign oligemia was possible in Wister rats. In the future, the pH imaging technique presented in our work might be applied to stroke patients in order to investigate whether the ischemic penumbra can be differentiated from other tissue with Iopamidol-CEST imaging. The advantage of Iopamidol-CEST imaging compared to pHWI is that pH quantification by Iopamidol-CEST imaging is independent of the concentration [6], whereas the CEST contrast in APT–CEST imaging also varies with the proton concentrations of the bulk water and labile groups [42]. In order to perform concentration-independent pH mapping, the use of Iopamidol-CEST imaging might be preferable.

One drawback of this study is the limited application of the Iopamidol-CEST sequence in only one patient. This was due to external circumstances: the patient undergoing a CT examination with Iopamidol has to agree to a follow-up MR examination, and the MR scanner, which is used heavily in clinical routine, must be available within a narrow time frame. Nevertheless, studies involving more patients should be performed in the future.

Future areas of application of the presented method could include the pH imaging of neoplasia or of renal pathologies. Depending on the anatomic regions, the applied CEST method would have to be modified to include respiratory gating of the sequence.

Conclusion

In summary, it can be stated that pH quantification with Iopamidol-CEST imaging, using pulsed train presaturation, is possible on clinical 3T systems for the pH range of 5.6–7.0. Our in-vivo results obtained in the human bladder were congruent with pH values measured externally in the urine by a pH meter. A linear relationship between ST_{log} and pH value was obtained. pH quantification with Iopamidol-CEST imaging is independent of the concentration of Iopamidol.

Acknowledgments We gratefully acknowledge E. Rädisch for assistance with data acquisition.

Conflict of interest BS and VJ are employed by Siemens. For the remaining authors, no conflicts of interest or funding sources are declared.

References

1. Lim E-K, Huh Y-M, Yang J et al (2011) pH-triggered drug-releasing magnetic nanoparticles for cancer therapy guided by molecular imaging by MRI. Adv Mater 23:2436–2442

2. Stubbs M, Bhujwalla ZM, Tozer GM et al (1992) An assessment of 31P MRS as a method of measuring pH in rat tumours. NMR Biomed 5:351–359
3. Raghunand N, Howison C, Sherry AD et al (2003) Renal and systemic pH imaging by contrast-enhanced MRI. Magn Reson Med 49:249–257
4. Raghunand N, Mahoney B, van Sluis R et al (2001) Acute metabolic alkalosis enhances response of C3H mouse mammary tumors to the weak base mitoxantrone. Neoplasia 3:227–235
5. Raghunand N, He X, van Sluis R et al (1999) Enhancement of chemotherapy by manipulation of tumour pH. Br J Cancer 80:1005–1011
6. Longo DL, Dastrù W, Digilio G et al (2011) Iopamidol as a responsive MRI-chemical exchange saturation transfer contrast agent for pH mapping of kidneys: in vivo studies in mice at 7 T. Magn Reson Med 65:202–211
7. Gillies RJ, Raghunand N, Garcia-Martin ML, Gatenby RA (2004) pH imaging. A review of pH measurement methods and applications in cancers. IEEE Eng Med Biol Mag 23:57–64
8. Pereira PCB, Miranda DM, Oliveira EA, Silva ACSE (2009) Molecular pathophysiology of renal tubular acidosis. Curr Genomics 10:51–59
9. Longo DL, Busato A, Lanzardo S et al (2013) Imaging the pH evolution of an acute kidney injury model by means of iopamidol, a MRI-CEST pH-responsive contrast agent. Magn Reson Med 70:859–864
10. Gillies RJ, Liu Z, Bhujwalla Z (1994) 31P-MRS measurements of extracellular pH of tumors using 3-aminopropylphosphonate. Am J Physiol 267:C195–C203
11. Soto GE, Zhu Z, Evelhoch JL, Ackerman JJ (1996) Tumor 31P NMR pH measurements in vivo: a comparison of inorganic phosphate and intracellular 2-deoxyglucose-6-phosphate as pHnmr indicators in murine radiation-induced fibrosarcoma-1. Magn Reson Med 36:698–704
12. Gillies RJ, Ogino T, Shulman RG, Ward DC (1982) 31P nuclear magnetic resonance evidence for the regulation of intracellular pH by Ehrlich ascites tumor cells. J Cell Biol 95:24–28
13. Madden A, Glaholm J, Leach MO (1990) An assessment of the sensitivity of in vivo 31P nuclear magnetic resonance spectroscopy as a means of detecting pH heterogeneity in tumours: a simulation study. Br J Radiol 63:120–124
14. Szwergold BS (1992) NMR spectroscopy of cells. Annu Rev Physiol 54:775–798
15. Bhujwalla ZM, McCoy CL, Glickson JD et al (1998) Estimations of intra- and extracellular volume and pH by 31P magnetic resonance spectroscopy: effect of therapy on RIF-1 tumours. Br J Cancer 78:606–611
16. Raghunand N, Altbach MI, van Sluis R et al (1999) Plasmalemmal pH-gradients in drug-sensitive and drug-resistant MCF-7 human breast carcinoma xenografts measured by 31P magnetic resonance spectroscopy. Biochem Pharmacol 57:309–312
17. Hunjan S, Mason RP, Mehta VD et al (1998) Simultaneous intracellular and extracellular pH measurement in the heart by 19F NMR of 6-fluoropyridoxol. Magn Reson Med 39:551–556
18. Ojugo AS, McSheehy PM, McIntyre DJ et al (1999) Measurement of the extracellular pH of solid tumours in mice by magnetic resonance spectroscopy: a comparison of exogenous (19)F and (31)P probes. NMR Biomed 12:495–504
19. Van Sluis R, Bhujwalla ZM, Raghunand N et al (1999) In vivo imaging of extracellular pH using 1H MRSI. Magn Reson Med 41:743–750
20. García-Martín ML, Hérigault G, Rémy C et al (2001) Mapping extracellular pH in rat brain gliomas in vivo by 1H magnetic resonance spectroscopic imaging: comparison with maps of metabolites. Cancer Res 61:6524–6531
21. Provent P, Benito M, Hiba B et al (2007) Serial in vivo spectroscopic nuclear magnetic resonance imaging of lactate and extracellular pH in rat gliomas shows redistribution of protons away from sites of glycolysis. Cancer Res 67:7638–7645
22. Gallagher FA, Kettunen MI, Day SE et al (2008) Magnetic resonance imaging of pH in vivo using hyperpolarized 13C-labelled bicarbonate. Nature 453:940–943
23. Schroeder MA, Swietach P, Atherton HJ et al (2010) Measuring intracellular pH in the heart using hyperpolarized carbon dioxide and bicarbonate: a 13C and 31P magnetic resonance spectroscopy study. Cardiovasc Res 86:82–91
24. Mikawa M, Miwa N, Bräutigam M et al (2000) Gd(3+)-loaded polyion complex for pH depiction with magnetic resonance imaging. J Biomed Mater Res 49:390–395
25. Lowe MP, Parker D, Reany O et al (2001) pH-dependent modulation of relaxivity and luminescence in macrocyclic gadolinium and europium complexes based on reversible intramolecular sulfonamide ligation. J Am Chem Soc 123:7601–7609
26. Zhang S, Wu K, Sherry A (1999) A novel pH-sensitive MRI contrast agent. Angew Chem Int Ed Engl 38:3192–3194
27. Garcia-Martin ML, Martinez GV, Raghunand N et al (2006) High resolution pH(e) imaging of rat glioma using pH-dependent relaxivity. Magn Reson Med 55:309–315
28. Gillies RJ, Raghunand N, Karczmar GS, Bhujwalla ZM (2002) MRI of the tumor microenvironment. J Magn Reson Imaging JMRI 16:430–450
29. Ward KM, Balaban RS (2000) Determination of pH using water protons and chemical exchange dependent saturation transfer (CEST). Magn Reson Med 44:799–802
30. Aime S, Barge A, Delli Castelli D et al (2002) Paramagnetic lanthanide(III) complexes as pH-sensitive chemical exchange saturation transfer (CEST) contrast agents for MRI applications. Magn Reson Med 47:639–648
31. Sun PZ, Zhou J, Sun W et al (2007) Detection of the ischemic penumbra using pH-weighted MRI. J Cereb Blood Flow Metab 27:1129–1136
32. McMahon MT, Gilad AA, Zhou J et al (2006) Quantifying exchange rates in chemical exchange saturation transfer agents using the saturation time and saturation power dependencies of the magnetization transfer effect on the magnetic resonance imaging signal (QUEST and QUESP): Ph calibration for poly-L-lysine and a starburst dendrimer. Magn Reson Med 55:836–847
33. Zhou J, Payen J-F, Wilson DA et al (2003) Using the amide proton signals of intracellular proteins and peptides to detect pH effects in MRI. Nat Med 9:1085–1090
34. Hashim AI, Zhang X, Wojtkowiak JW et al (2011) Imaging pH and metastasis. NMR Biomed 24:582–591
35. Martinez GV, Zhang X, García-Martín ML et al (2011) Imaging the extracellular pH of tumors by MRI after injection of a single cocktail of T1 and T2 contrast agents. NMR Biomed 24:1380–1391
36. Sherry AD, Woods M (2008) Chemical exchange saturation transfer contrast agents for magnetic resonance imaging. Annu Rev Biomed Eng 10:391–411
37. Sheth VR, Liu G, Li Y, Pagel MD (2012) Improved pH measurements with a single PARACEST MRI contrast agent. Contrast Media Mol Imaging 7:26–34
38. Terreno E, Castelli DD, Cravotto G et al (2004) Ln(III)-DOTAMGly complexes: a versatile series to assess the determinants of the efficacy of paramagnetic chemical exchange saturation transfer agents for magnetic resonance imaging applications. Investig Radiol 39:235–243
39. Schmitt B, Zaiß M, Zhou J, Bachert P (2011) Optimization of pulse train presaturation for CEST imaging in clinical scanners. Magn Reson Med 65:1620–1629

40. Sun PZ, Benner T, Kumar A, Sorensen AG (2008) Investigation of optimizing and translating pH-sensitive pulsed-chemical exchange saturation transfer (CEST) imaging to a 3T clinical scanner. Magn Reson Med 60:834–841
41. Aime S, Calabi L, Biondi L et al (2005) Iopamidol: exploring the potential use of a well-established x-ray contrast agent for MRI. Magn Reson Med 53:830–834
42. Sun PZ, Benner T, Kumar A, Sorensen AG (2008) Investigation of optimizing and translating pH-sensitive pulsed-chemical exchange saturation transfer (CEST) imaging to a 3T clinical scanner. Magn Reson Med 60:834–841
43. Haneder S, Apprich SR, Schmitt B et al (2013) Assessment of glycosaminoglycan content in intervertebral discs using chemical exchange saturation transfer at 3.0 Tesla: preliminary results in patients with low-back pain. Eur Radiol 23:861–868
44. McKinstry DN, Rommel AJ, Sugerman AA (1984) Pharmacokinetics, metabolism, and excretion of Iopamidol in healthy subjects. Investig Radiol 19:S171
45. Zhang X, Lin Y, Gillies RJ (2010) Tumor pH and its measurement. J Nucl Med 51:1167–1170
46. Lutz NW, Le Fur Y, Chiche J et al (2013) Quantitative in vivo characterization of intracellular and extracellular pH profiles in heterogeneous tumors: a novel method enabling multiparametric pH analysis. Cancer Res 73:4616–4628
47. Arnold DL, Shoubridge EA, Feindel W, Villemure JG (1987) Metabolic changes in cerebral gliomas within hours of treatment with intra-arterial BCNU demonstrated by phosphorus magnetic resonance spectroscopy. Can J Neurol Sci 14:570–575
48. Zu Z, Li K, Janve VA et al (2011) Optimizing pulsed-chemical exchange saturation transfer imaging sequences. Magn Reson Med 66:1100–1108
49. Sun PZ, Farrar CT, Sorensen AG (2007) Correction for artifacts induced by B(0) and B(1) field inhomogeneities in pH-sensitive chemical exchange saturation transfer (CEST) imaging. Magn Reson Med 58:1207–1215
50. Kim M, Gillen J, Landman BA et al (2009) Water saturation shift referencing (WASSR) for chemical exchange saturation transfer (CEST) experiments. Magn Reson Med 61:1441–1450

Magn Reson Mater Phy (2017) 30:505–516
DOI 10.1007/s10334-017-0625-0

RESEARCH ARTICLE

Quantitative pulsed CEST-MRI at a clinical 3T MRI system

Julia Stabinska[1] · Tom Cronenberg[1] · Hans-Jörg Wittsack[1] · Rotem Shlomo Lanzman[1] · Anja Müller-Lutz[1]

Received: 16 January 2017 / Revised: 28 April 2017 / Accepted: 12 May 2017 / Published online: 31 May 2017

Abstract
Objectives The goal of this study was to quantify CEST related parameters such as chemical exchange rate and fractional concentration of exchanging protons at a clinical 3T scanner. For this purpose, two CEST quantification approaches—the AREX metric (for 'apparent exchange dependent relaxation'), and the AREX-based Ω-plot method were used. In addition, two different pulsed RF irradiation schemes, using Gaussian-shaped and spin-lock pulses, were compared.
Materials and methods Numerical simulations as well as MRI measurements in phantoms were performed. For simulations, the Bloch–McConnell equations were solved using a two-pool exchange model. MR experiments were performed on a clinical 3T MRI scanner using a cylindrical phantom filled with creatine solution at different pH values and different concentrations.
Results The validity of the Ω-plot method and the AREX approach using spin-lock preparation for determination of the quantitative CEST parameters was demonstrated. Especially promising results were achieved for the Ω-plot method when the spin-lock preparation was employed.
Conclusion Pulsed CEST at 3T could be used to quantify parameters such as exchange rate constants and concentrations of protons exchanging with free water. In the future this technique might be used to estimate the exchange rates and concentrations of biochemical substances in human tissues in vivo.

Keywords Chemical exchange saturation transfer (CEST) · Magnetic resonance imaging (MRI) · Creatine

Introduction

Chemical exchange saturation transfer (CEST) represents a new molecular MRI technique that enables indirect detection of labile solute protons through bulk water signal changes following selective saturation of exchangeable protons at different frequencies [1–3]. Several CEST MRI approaches have been shown capable of measuring dilute CEST agents and microenvironmental properties such as pH and temperature [4–6].

Since the CEST effect varies with labile proton ratio, exchange rate, and experimental conditions such as field strength and radiofrequency (RF) irradiation scheme, there is a need to develop quantitative CEST analysis for defining underlying CEST parameters [7, 8]. Several analytical and numerical methods have been established to determine labile proton concentration and exchange rate from the CEST-weighted data [9–12]. Two approaches to measure the labile proton ratio-weighted exchange rate as a function of saturation time (QUEST) and saturation power (QUESP) have been proposed by McMahon et al. [10]. The exchange rates are determined by fitting the changes in the intensity of the water signal after application of different saturation powers (QUESP) or saturation times (QUEST) to the modified Bloch–McConnell equations. Dixon et al. extended the QUESP method and showed that the CEST effect can be represented as a linear function of $1/B_1^2$ (the so-called Ω-plot) and that the proton exchange

Julia Stabinska and Tom Cronenberg contributed equally to this work.

✉ Julia Stabinska
Julia.Stabinska@med.uni-duesseldorf.de

[1] Department of Diagnostic and Interventional Radiology, Medical Faculty, University Dusseldorf, Moorenstr. 5, 40225 Düsseldorf, Germany

rate and labile proton ratio can be determined independently by linear regression of the CEST effect [11]. However, this method is limited to paramagnetic CEST agents (PARACEST) that exhibit large chemical shifts. As a result, the selective RF pulse is applied far from the free water resonance frequency, which reduces direct water saturation (spillover) and magnetization transfer effects [3]. The QUEST ratiometric analysis (QUESTRA) has been shown to correct the influence of confounding factors, such as relaxation and spillover effects [12]. Nevertheless, it provides only the labile proton ratio-weighted exchange rate. More recently, it has been presented that the spillover factor is not sensitive to the labile proton ratio and exchange rate, and therefore can be estimated and efficiently corrected by the inverse metric [13, 14]. Sun et al. demonstrated that the RF spillover-factor Ω-plot method provides good quantification in the case of endogenous CEST agents with small chemical shifts [7, 15]. However, they performed their experiments using continuous-wave (CW) saturation, which is usually not feasible on clinical scanners due to the hardware and specific absorption rate (SAR) limitations. Thus, the pulsed train pre-saturation scheme must be used instead [16, 17]. Sun et al. compared pulsed- and continuous wave—RF irradiation schemes for CEST and showed that the maximal pulsed-CEST contrast is approximately 95% of CW-CEST and that their optimal saturation RF power is approximately equal [18]. A theoretical model for pulsed-CEST experiments and optimized saturation scheme was defined by Schmitt et al. [16]. To translate quantitative CEST to clinical MRI systems, the pulsed quantitative CEST approaches such as AREX ('apparent exchange dependent relaxation') and AREX-based Ω-plots method have been proposed [19, 20]. Zaiss et al. introduced a novel metrics, MTR_{Rex}, which eliminates spillover and semi-solid MT effects and then extended it to the AREX, a T_1 relaxation-compensated metric, which in turn facilitates quantification of the CEST effect [21]. The analytic description of the spillover corrected Ω-plot method in the case of pulsed CEST was proposed by Meissner et al. [20]. However, they performed the CEST MRI experiments at high field strength (7T). Although higher magnetic field strengths are beneficial to the CEST phenomenon, the commonly used field strengths on clinical MR usually do not surpass 3T.

Recently, spin-lock (SL) saturation preparation for pulsed chemical exchange MR imaging has been introduced [22, 23]. Pulsed SL may provide several advantages over the conventional pulsed CEST: (1) higher signal-to-noise ratio (SNR) by restoring magnetization along the longitudinal axis of the rotating frame [22, 24]; (2) less direct water saturation because of the suppression of the magnetization rotations in the transversal plane [22]; and (3) increase of the saturation efficiency compared with the conventional CEST [23]. Chemical exchange imaging with spin-lock technique has also been shown to better characterize the chemical exchange processes when the resonant frequency offsets are small (e.g., <2 ppm) and the exchange is in the intermediate to fast regime compared with the CEST in the case of saturation by a train of Gaussian-shaped RF pulses [25, 26].

The aim of this study was (1) to evaluate quantitative CEST parameters using the AREX metric and the AREX-based Ω-plot method and (2) to compare two different saturation schemes at a clinical 3T MRI system.

Materials and methods

Quantitative parameter determination

Zaiss et al. proposed a novel magnetization transfer ratio, which eliminates spillover and semi-solid macromolecular magnetization transfer (MT) [21]:

$$\mathrm{MTR_{Rex}} = \frac{1}{Z_{\mathrm{lab}}} - \frac{1}{Z_{\mathrm{ref}}} = \frac{R_{\mathrm{ex}} \cdot \mathrm{DC}}{R_{1\mathrm{w}}}, \tag{1}$$

where $Z_{\mathrm{lab}} = Z(+\Delta\omega)$ is the label scan around the resonance of the CEST pool (s) and $Z_{\mathrm{ref}} = Z(-\Delta\omega)$, the reference scan at the opposite frequency with respect to water; R_{ex} is the exchange-dependent relaxation in the rotating frame; DC is the duty cycle and $R_{1\mathrm{w}}$ is the relaxation rate of the water pool (w). The $\mathrm{MTR_{Rex}}$ metric could be extended to an apparent exchange dependent relaxation metric—AREX [21]:

$$\mathrm{AREX} = \mathrm{MTR_{Rex}} R_{1\mathrm{w}}. \tag{2}$$

In the full saturation limit (1) $\omega_1 \gg R_{2\mathrm{s}} + k_{\mathrm{sw}}$ and in the large-shift limit (2) $\delta\omega_{\mathrm{s}} \gg \omega_1$, when applying RF pulse at the CEST pool resonance, $R_{\mathrm{ex}} = f \cdot k_{\mathrm{ws}}$ and, hence:

$$\mathrm{AREX} = k_{\mathrm{ws}} \cdot \mathrm{DC}, \tag{3}$$

where ω_1 is the RF irradiation amplitude; $R_{2\mathrm{s}}$ the relaxation rate of the pool s; $\delta\omega_{\mathrm{s}}$ is the chemical shift of the pool s; k_{sw} and k_{ws} are the exchange rate between pool s and w and back exchange rate, respectively, and f is the labile proton ratio.

Assuming the f is known, we can calculate the chemical exchange rate k_{sw}:

$$k_{\mathrm{sw}} = \frac{\mathrm{AREX}}{\mathrm{DC} \cdot f}. \tag{4}$$

The relaxation-compensated Ω-plot analysis can be applied to the AREX signal. For this purpose, a stack of the AREX maps for different RF amplitudes B_1 is created and then fitted with the equation [20]:

$$\frac{1}{\mathrm{AREX}}\left(\frac{1}{\omega^2}\right) = p_0 + p_1 \cdot \frac{1}{\omega^2}, \tag{5}$$

where p_0 is an intersection p_1, the slope of the linear function.

For shaped pulses (e.g., Gaussian), a time dependent $\omega_1(t)$ has to be taken into account. Meissner et al. calculated the average longitudinal relaxation rate in the rotating frame $R_{1\rho}$ as a function of the pulse shape [20]. This method allows the calculation of form factors for the modified CEST signals and the B_1 dispersion of the CEST effect in the case of using a pulsed saturation scheme. For the Gaussian-shaped pulse, the form factors are defined as follows [20]:

$$c_1 = \frac{\sqrt{2\pi}\sigma}{t_p} \tag{6}$$

$$c_2 = c_1 \cdot \sqrt{\sqrt{2}}. \tag{7}$$

For the experiment with spin-lock pulses: $c_1 = c_2 = 1$.

The exchange-dependent relaxation R_{ex} in the case of pulsed pre-saturation can be approximated as:

$$R_{\mathrm{ex}}^{\mathrm{shaped}} = f k_{\mathrm{sw}} c_1 \frac{\omega_1^2}{\omega_1^2 + k_{\mathrm{sw}}(k_{\mathrm{sw}} + R_{2\mathrm{s}})c_2^2}. \tag{8}$$

Using Eqs. (1), (2) and (8) as well as p_1 and p_0 values determined from the linear Eq. (5) enables quantification of k_{sw} and f with the following equations:

$$k_{\mathrm{sw}} = -\frac{R_{2\mathrm{s}}}{2} + \sqrt{\frac{(R_{2\mathrm{s}})^2}{4} + \frac{p_1}{p_0 \cdot c_2^2}}. \tag{9}$$

$$f = \frac{1}{c_1 \cdot \mathrm{DC} \cdot p_0 \cdot \left(-\frac{R_{2\mathrm{s}}}{2} + \sqrt{\frac{(R_{2\mathrm{s}})^2}{4} + \frac{p_1}{p_0 \cdot c_2^2}}\right)}. \tag{10}$$

Both considered methods use a Z-spectrum model in the pulsed CEST experiment given by Zaiss et al. [21]. This model is valid if several key conditions defined by Meissner et al. are met [20]: (1) small CEST pool ($f < 1\%$), (2) sufficiently long saturation times ($t_{\mathrm{sat}} > T_{2\mathrm{w}}$), (3) exchange dynamic is faster than the pulse dynamic ($k_{\mathrm{sw}} > 1/t_p$), (4) exchange dynamic in the interpulse delay can be neglected ($k_{\mathrm{sw}} < 1/t_d$), (5) analytical integral of $R_{1\rho}$ is valid ($\Delta\omega > \omega_1$), (6) the approximation of the analytical derived form factors of a Gaussian-shaped pulse is satisfactory ($\sigma/t_p < 0.5$), where σ is the width of the pulse. In contrast to the original Ω-plot method proposed by Dixon et al., there are two other limitations for the AREX-based Ω-plot method; (7) $R_{1\rho}t_p \ll 1$ and $R_{1\mathrm{w}}t_d \ll 1$ and (8) $\omega_1^2 < 0.5 \cdot k_{\mathrm{sw}}.(k_{\mathrm{sw}} + R_{2\mathrm{s}})$. Last but not least, the steady-state condition as for the AREX method has to be fulfilled (9) $t_{\mathrm{sat}} \geq 5 \cdot T_{1\mathrm{w}}$.

Numerical simulations

For simulations, the Bloch–McConnell (BM) equations were solved using Matlab (Matlab R2012a, Mathworks, Natick, MA, USA) by a two-pool exchange model as proposed by Murase et al. [27], assuming representative $T_{1\mathrm{w}} = 2.473$ s and $T_{2\mathrm{w}} = 1.676$ s for the bulk water, and $T_{1\mathrm{s}} = 0.5$ s and $T_{2\mathrm{s}} = 0.015$ s for labile protons at 1.9 ppm at 3T, respectively [21]. The saturation scheme consisted either of 50 Gaussian-shaped, or 50 spin-lock pulses with pulse duration and inter-pulse delay $t_p = t_d = 100$ ms. The spin-lock magnetization preparation pulse was obtained by using the rotation matrix:

$$M(\alpha) = \begin{pmatrix} 1 & 0 & 0 \\ 0 & \cos\alpha & -\sin\alpha \\ 0 & \sin\alpha & \cos\alpha \end{pmatrix}, \tag{11}$$

where $\alpha = \Theta$ or $-\Theta$.

The quantitative CEST analysis was applied to the simulated data, to assess the accuracy of the methods over a wide range of B_1, f and k_{sw} values. The results were then normalized to the theoretical values from the BM simulations, giving the normalized exchange rate $k_{\mathrm{sw}}^{\mathrm{norm}}$ and the normalized labile proton ratio f^{norm} maps.

General simulation parameters are listed in Table 2 in the "Appendix".

Phantom

For MR experiments, three sets of phantoms were employed, each containing four 60 mL tubes (Table 1). Eleven samples, using phosphate buffer and creatine solution (Creatine anhydrous, Alfa Aesar GmbH & Co KGm Karlsruhe, Germany), were prepared at room temperature. Three phantoms either consisting of creatine solutions with varying pH values (Phantom 1&2) or varying molar concentration (Phantom 3) were obtained. The labile proton ratio f was calculated using the equation: $N \cdot [\mathrm{Cr}]/2 \cdot [\mathrm{H_2O}]$, where N is the number of labile protons per creatine molecule, and $[\mathrm{H_2O}]$ and [Cr] are water and creatine molar concentration, respectively. The number of exchangeable protons per creatine molecule was assumed to be four [19, 28]. To assess the accuracy of the determined chemical exchange rate from labile protons s to bulk water w, the reference k_{sw} value for creatine was calculated from the empirical equation [28]:

Table 1 Phantoms employed with the reference $k_{sw,ref}$ value obtained from the empirical relation given in Eq. (12), reference labile proton ratio f_{ref} and k_{sw} and f values determined using quantitative CEST analysis

					AREX method		Ω-plot method			
					Pulsed SL	Gaussian-shaped pulses	Pulsed SL		Gaussian-shaped pulses	
Phantom	pH	c (Mm)	$k_{sw,ref}$ (Hz)	f_{ref} (‰)	k_{sw} (Hz)	k_{sw} (Hz)	k_{sw} (Hz)	f (‰)	k_{sw} (Hz)	f (‰)
1	6.15	50	23.17	1.8	38.48 ± 2.73	33.58 ± 2.82	41.21 ± 7.63	1.8 ± 0.34	56.32 ± 11.02	1.9 ± 0.39
1	6.31	50	33.50	1.8	49.58 ± 3.33	41.44 ± 2.95	49.88 ± 7.34	1.9 ± 0.27	65.76 ± 11.11	2.0 ± 0.32
1	6.52	50	54.32	1.8	69.99 ± 4.53	56.00 ± 3.59	68.86 ± 8.66	2.0 ± 0.2	81.78 ± 11.62	2.2 ± 0.26
1	6.70	50	82.22	1.8	94.41 ± 4.36	71.14 ± 3.60	93.28 ± 10.24	2.0 ± 0.17	98.28 ± 9.84	2.3 ± 0.21
2	6.83	50	110.91	1.8	133.87 ± 5.68	92.2 ± 4.61	116.94 ± 8.46	2.3 ± 0.17	141.68 ± 11.16	2.2 ± 0.17
2&3	7.02	50	171.78	1.8	174.81 ± 8.90	117.15 ± 6.56	162.18 ± 10.67	2.3 ± 0.14	173.30 ± 12.55	2.3 ± 0.17
2	7.21	50	266.06	1.8	243.54 ± 11.62	157.67 ± 7.62	259.83 ± 21.72	2.3 ± 0.12	249.92 ± 17.29	2.3 ± 0.14
2	7.51	50	530.86	1.8	312.88 ± 19.47	213.57 ± 10.29	492.72 ± 63.89	2.3 ± 0.16	413.60 ± 27.65	2.2 ± 0.11
3	7.02	25	171.78	0.9	182.04 ± 9.43	124.67 ± 7.08	185.35 ± 46.10	1.2 ± 0.10	160.73 ± 22.29	1.3 ± 0.14
3	7.02	75	171.78	2.7	172.30 ± 7.77	118.76 ± 5.70	163.76 ± 17.20	3.4 ± 0.18	167.91 ± 12.12	3.6 ± 0.22
3	7.02	100	171.78	3.6	174.38 ± 9.70	119.02 ± 5.36	161.20 ± 12.52	4.7 ± 0.27	267.20 ± 8.68	4.9 ± 0.25

$$k_{sw}(298.15\text{K}) \approx k_{b,eff}(298.15\text{K}) \cdot \frac{\text{mol}}{\text{L}} \cdot 10^{\text{pH}-14+\frac{E_{A,b,eff}+\Delta H_R^0}{R\cdot\ln 10}\left(\frac{1}{298.15\text{K}}-\frac{1}{T}\right)}, \quad (12)$$

where $k_{b,eff}$ (298.15 K) = 3.009 × 10^9 Hz L mol^{-1}, $E_{A,b,eff}$ = 32.27 kJ mol^{-1}, ΔH_R^0 = 55.84 kJ mol^{-1} and R = 8.314 $mol^{-1}K^{-1}$. Recently, the effective base-catalyzed rate constant $k_{b,eff}$ and the effective activation energy $E_{A,b,eff}$ were estimated by Goerke et al. [28] by means of water-exchange (WEX)-filtered 1H NMR spectroscopy. Thus, this method served us as a reference method for measuring the exchange rate of creatine. The k_{sw} values derived from Eq. (12) formed our 'ground truth' and are listed in Table 1.

MRI experiments

All measurements were performed on a clinical 3T MR scanner (Magentom Trio A Tim System, Siemens Healthcare, Erlangen, Germany) with a 12-channel birdcage coil. A 2-D single-shot gradient echo sequence (GRE) as described in [16] was used for CEST image data acquisition. The following parameters were chosen: field of view FOV = 130 mm × 130 mm, image matrix = 64 × 64, slice thickness = 8 mm, repetition time T_R = 7.3 ms, echo time T_E = 3.41 ms, and flip angle = 10°. Sampling was performed equidistantly at 41 various frequency offsets between −3.5 and 3.5 ppm. An additional scan at frequency offset −300 ppm was acquired for normalization. The saturation module consisted either of 50 Gaussian-shaped, or 50 spin lock pulses with $t_p = t_d$ = 100 ms and RF pulse amplitudes B_1 of 0.25, 0.5, 1.0, 1.25, 1.65, and 2.1 μT. Each of the spin lock pulses is flanked by two Gaussian-shaped RF pulses with the flip angle θ and opposite phase, where θ is the angle between the effective field and the z-axis. A simplified schematic CEST pulse sequence diagram (Fig. 1) is included in the appendix. The water saturation shift referencing (WASSR) method for B_0 inhomogeneity correction was used [29]. Here, a single Gaussian pulse with t_{pd} = 56 ms and RF amplitude B_1 = 0.1 μT was employed. Additionally, T1-weighted MR images were acquired by a turbo-inversion-recovery sequence. Altogether, 13 contrasts at different inversion delays (TI) ranging from 25 ms to 3.2 s were fitted to obtain T1 maps.

Data processing

All data were processed using Matlab. The T_1 maps were obtained by least-squares fitting of the IR measurements data as a function of the inversion delay (TI): S (TI) ∝ S_0 (1–2·exp(−TI/T_1)), where S_0 is the equilibrium signal. To reduce noise, a 5 × 5 Gaussian filter was applied to each CEST and WASSR image. Based on the WASSR images, an offset map were calculated using the WASSR maximum

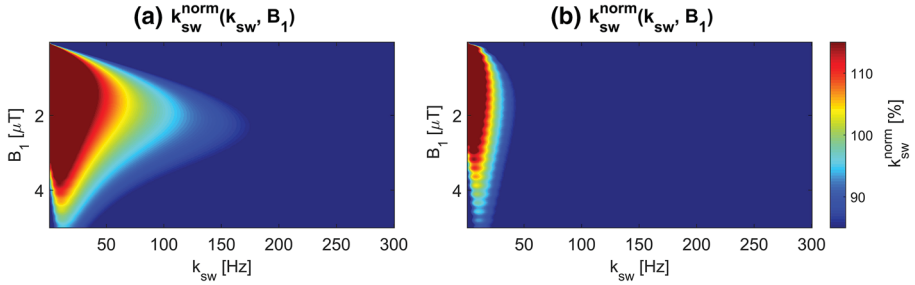

Fig. 1 Normalized exchange rate k_{sw}^{norm} maps with a *color-coded* error range of 15% for the AREX method with (**a**) pulsed SL (**b**) trains of Gaussian-shaped pulses used for saturation. The k_{sw} values obtained from the quantitative CEST analysis were normalized to the theoretical values from the BM simulations

symmetry algorithm introduced by Kim et al. [29, 30]. The CEST data were normalized to the signal from the first acquisition at frequency offset −300 ppm. The offset map was used to correct the Z-spectrum on a pixel-basis. The inverse asymmetry MTR_{Rex} maps were generated at 1.9 ppm. Next, the AREX maps was calculated using average T_1 times, which were obtained as an average of the four tubes of each phantom. Finally, the relaxation-compensated Ω-plot analysis was then applied to the AREX signal. The form factors for the Gaussian-shaped pulses employed in this work were $c_1 = 0.5672$ and $c_2 = 0.6171$. In the case of spin-lock pulses, the form factors were $c_1 = c_2 = 1$. It was also assumed that $R_{2s} = 66.67$ Hz [31].

The measured data in the studied ROIs were tested for normal distribution using the Kolmogorov–Smirnov Test (KS Test) with $\alpha = 0.05$. Since the results deviated significantly from the normal distribution, the non-parametric Wilcoxon–Mann–Whitney test with a level of significance (p value) $\alpha = 0.05$ was used.

Results

Simulations

The Bloch–McConnell simulations over a wide range of B_1, f and k_{sw} values revealed significant differences in accuracy and feasibility between the examined CEST quantification methods and between two considered saturation pulse shapes. To demonstrate the general applicability of the methods, we calculated a normalized exchange rate k_{sw}^{norm} map and a normalized labile proton ratio f^{norm} map (only for the Ω-plot method) with a color-coded error range of ±15%. Note that independently of the irradiation scheme and quantification method, the lower exchange rates tend to be strongly overestimated in nearly the whole range of B_1 values. The AREX approach generates sufficiently accurate results in the k_{sw} range of 100 ± 50 Hz when applying the pulsed SL and B_1 between 1 and 3 μT (Fig. 1a), and in the k_{sw} range of about 30 ± 15 Hz using Gaussian-shaped RF pulses (Fig. 1b).

An advantage of the AREX-based Ω-plot method is the possibility of simultaneous determination of exchange rate and the labile proton ratio. Applying spin-lock pulses, both parameters can be estimated with very good accuracy over a wide range of k_{sw}, although the accuracy decreases at larger k_{sw} rates. This decreased accuracy at faster k_{sw} is amplified as the saturation power increases (Fig. 2a, c). This method can produce accurate estimates of fractional concentration for k_{sw} smaller than about 400 Hz at lower RF power (Fig. 2c, d). The results of the Ω-plot method for the Gaussian-shaped pulses show its decreased range of applicability in comparison to results obtained with the pulsed SL. The accuracy of the estimation of k_{sw} is strongly overestimated for slower k_{sw} rates (<100 Hz), but also significantly underestimated for faster k_{sw} rates. These accuracies are also nearly independent of the saturation power (Fig. 2e) and labile proton ratio (Fig. 2f).

In vitro MR experiments

To validate the simulations, we performed phantom MR measurements (Table 1). First, we determined the exchange rates as a function of pH (phantom 1 and phantom 2, Table 1) (Fig. 3b). For the graphic presentation, we normalized the results to the reference k_{sw} values obtained from the Eq. (12) (Table 1). At lower pH the k_{sw} rates are substantially overestimated. This is consistent with simulation findings. Interestingly, the AREX metric shows smaller error intervals than the Ω-plot method, regardless of pH value. Due to its small error and a good agreement with the corresponding reference value, the AREX method when using pulsed SL could be applicable for exchange rates between about 80–270 Hz (please see Table 1). It is worth noting, that the results of the Ω-plot method are in very good agreement with the reference values in the k_{sw} range

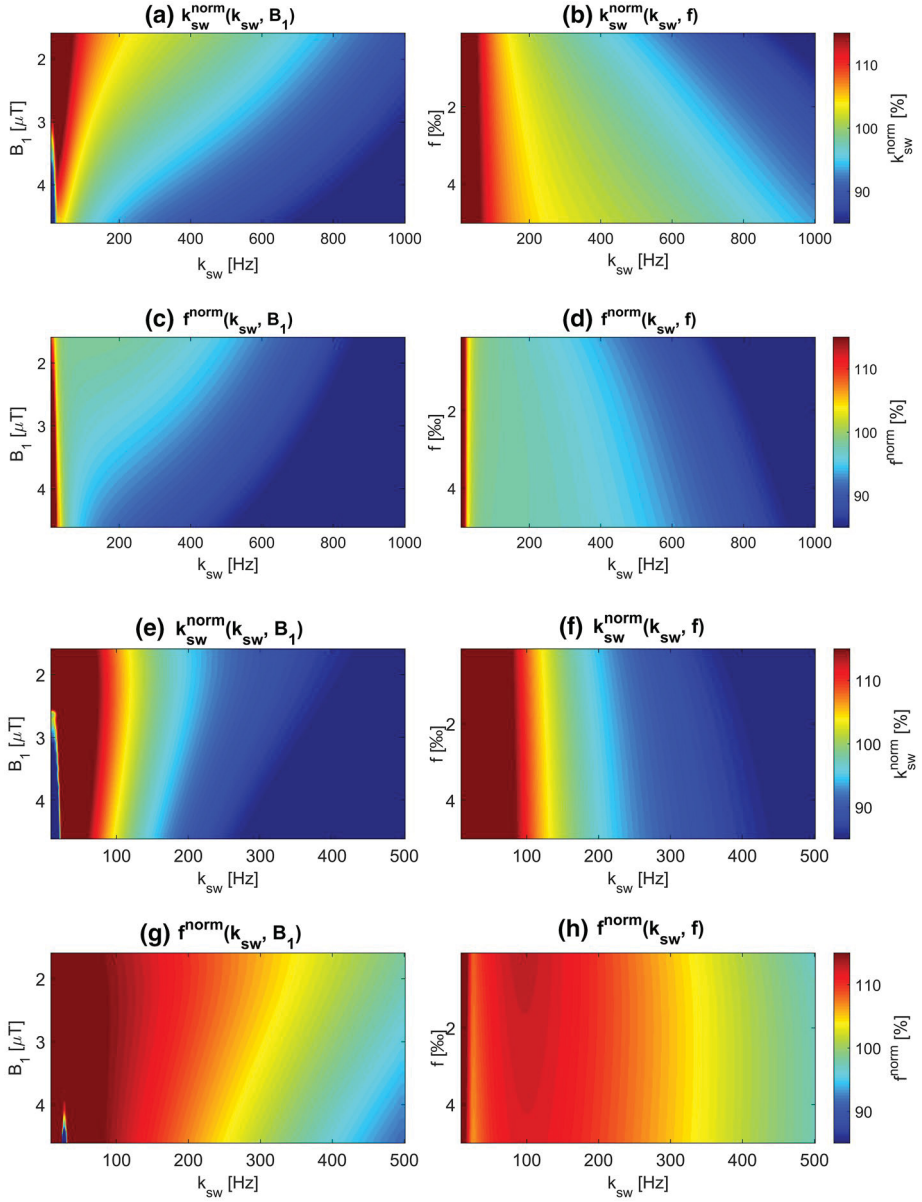

Fig. 2 Parameter maps with *color-coded* error range of 15% for the Ω-plot method with (**a**–**d**) pulsed SL and (**e**–**h**) trains of Gaussian-shaped pulses used for saturation. **a**, **d** The normalized exchange rate map k_{sw}^{norm} as a function of k_{sw} and B_1 **b**, **f** the normalized exchange rate map k_{sw}^{norm} as a function of k_{sw} and f, **c**, **g** the normalized labile proton ratio f^{norm} map as a function of k_{sw} and B_1, **d**, **h** the normalized labile proton ratio f^{norm} map as a function of k_{sw} and f. The k_{sw} and f values obtained from the quantitative CEST analysis were normalized to the theoretical values from the BM simulations

between 50 and 530 Hz if the spin-lock saturation preparation was applied. In the case of using Gaussian-shaped RF pulses, the Ω-plot method estimates the exchange rates between 170 and 530 Hz within the ±15% error range. Except for the AREX method and pulsed SL saturation scheme at pH 6.52 and 6.70 ($p = 0.925$), pH 6.52 and 6.83 ($p = 0.7031$), pH 6.70 and 6.83 ($p = 0.7631$), results of all other pairs were significantly different.

To further evaluate the Ω-plot methods when applying different pulsed pre-saturation schemes, we determined the labile proton ratios as a function of creatine molar concentration (phantom 3, Table 1) (Fig. 4). The number of labile protons per creatine molecule was assumed to be four [19, 28]. Our results verified the linear dependence of the labile proton ratio on creatine concentration. For both irradiation schemes, the results appear to be constantly overestimated, which is more substantial in the case of Gaussian-shaped RF pulse trains. All results were significantly different.

Next, we obtained the normalized exchange rate for different creatine concentrations (phantom 3, Table 1) at pH 7.0. In particular, the exchange rates estimated by means of the AREX method and pulsed SL, are in good agreement with the expected value. The variations of the results for the Ω-plot method also remain within the ±15% error range for creatine concentrations above 25 mM. In comparison to the

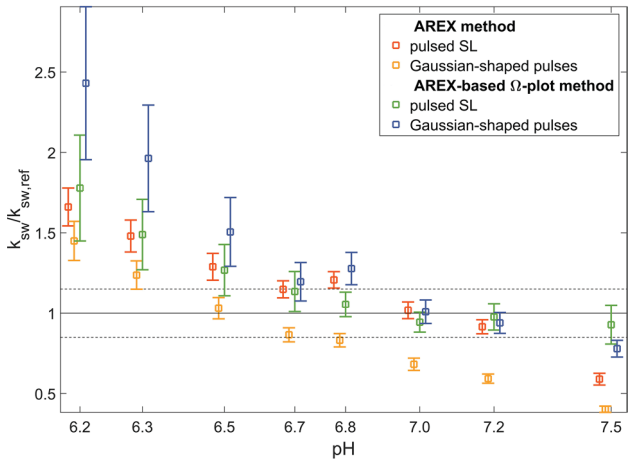

Fig. 3 Exchange rates k_{sw} estimates determined at varying pH values, normalized to the reference value $k_{sw,ref}$ obtained from the empirical relation given in Eq. (12) (Table 1). *Dashed lines* represent the 15% error tolerances

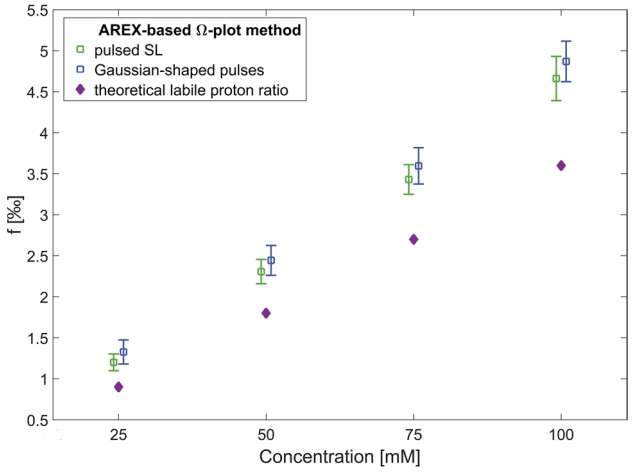

Fig. 4 Labile proton ratio f estimates determined at different creatine concentrations (25, 50, 75 and 100 mM) using the AREX-based Ω-plot method and two different RF saturation schemes—pulsed SL (*green square*) and Gaussian-shaped RF pulses (*blue square*). *Purple diamonds* represent theoretical labile proton ratio values

results obtained using the spin-lock saturation scheme, the k_{sw} rates determined with the AREX method when using Gaussian-shaped RF pulses are strongly underestimated. The deviation from the reference value is about 30% (Fig. 5).

Discussion

In the present study we compared two CEST quantification methods and two different saturation schemes based

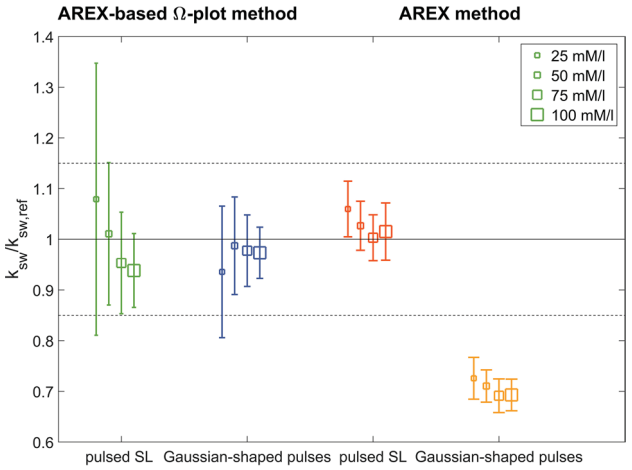

Fig. 5 Exchange rates k_{sw} estimates determined using Ω-plot analysis (*green* and *blue squares*) and the AREX method (*red* and *orange squares*) at different creatine concentrations (25, 50, 75, 100 mM) at pH 7, normalized to the reference value $k_{sw,ref}$ obtained from the empirical relation given in Eq. (12) (Table 1). *Dashed lines* represent the 15% error tolerances

on Gaussian-shaped RF pulse train and pulsed spin-lock preparation. Moreover, we performed our experiments at a clinical 3T MRI system.

The CEST methods evaluated in this study are based on several conditions. Our simulations revealed that all considered quantitative CEST methods tend to overestimate lower exchange rates. It is worth noting that the pulsed approach, used here, is based on the assumption that during the saturation pulse the water magnetization is "locked" in the direction of ω_{eff} and decays with the rate $R_{1\rho}$ and recovers during the interpulse delay t_d with the rate R_{1w} [22]. However, Roeloffs et al. showed that a biexponential decay of magnetization during the break should be taken into account. For exchange rates that are comparable with the inverse of the interpulse delay, this additional magnetization transfer may lead to a significant overestimation of the exchange rates. Our simulations confirmed that each saturation technique shows different accuracy in the exchange rate determination that is dependent on the exchange regime in which the analysis is performed. Using pulsed SL, the AREX method is applicable for higher exchange rates than in the case of Gaussian-shaped saturation pulses. For the SL technique, faster exchange between the water and metabolite pool boost signal dephasing that may be reduced with sufficient locking field ω_1. Therefore, the larger this dephasing effect is, the higher contrast enhancement may be obtained. This contrast was reported to decrease dramatically at higher and lower locking fields [23, 25]. Only around the maximum contrast, the signal-to-noise ratio is

sufficient for the MTR_{Rex} metric to reconstruct the ideal signal from the residual signal [19]. Thus, the accuracy of the AREX metric for pulsed SL is not a monotonic function of k_{sw}. It can increase or decrease with the k_{sw} depending on the RF saturation power. Also, the full-saturation limit $k_{sw} \ll \omega_1$ has to be taken into account [19].

Since the amplitude of the saturation is not constant for Gaussian-shaped pulses, the form factors should be considered, which compensate decreased saturation efficiency of the shaped pulses compared to the rectangular pulses [19]. The form factors defined for the Ω-plot method cannot be simply transferred to the AREX metric, which contributes to the poor results of the approach when using Gaussian-shaped pulses. In this study we used the numerical derived form factors for the Gaussian-shaped pulse, which improved the estimation of k_{sw} and f_c by the Ω-plot method compared with the results obtained with the analytical derived form factors (data not shown). The results of the simulations for the Ω-plot method using the pin-locking technique showed the great potential of this method. The increasing uncertainty in the determination of the exchange rate for small labile proton ratios is consistent with limitations of the method defined by Meissner et al. [20]. However, our simulations of the Ω-plot method at the 3T system presented a smaller area of validity compared to the results obtained by Meissner et al. at 7T in the case of using Gaussian-shaped pulses [20]. The specific frequency offset $\Delta\omega$ from water should be larger than the chemical exchange rate k_{sw} in order to better identify the CEST effect from creatine (large-shift limit) [3]. Since the frequency shift increases with the magnetic field strength, this assumption is better fulfilled for a higher magnetic field strength B_0 and smaller exchange rates.

The results of our in vitro studies clearly show that quantitative CEST imaging is possible at a clinical 3T scanner. The Ω-plot qCEST method provided particularly promising results if a train of spin-lock pulses was applied. Nevertheless, further investigations are needed to validate these results in vivo.

The overestimated exchange rate for the low pH tubes confirmed the trend that became apparent in the simulations. Smaller variations of the results at higher pH values are caused by the fact that the signal-to noise ratio (SNR) increases with increasing exchange rate. At high k_{sw} values, the exchange rates estimated using spin-lock pulses and Ω-plot method are in better agreement with the reference value than in the case of Gaussian-shaped RF pulses. It should be noted that the reference values used here are based on the formula introduced by Goerke et al. [28]. They assumed a constant estimation error of 10%. However, in the more recent work of the same research group, the actual error was reported to be greater [20]. To assess the determined quantitative parameters more accurately, it might be necessary to compare the results with other reference methods, such as the fitting of CEST data to the Bloch–McConnell equations in order to estimate the exchange rates [10]. However, these methods were mainly evaluated for continuous-wave (CW) RF irradiation. When using pulsed saturation schemes, the simulations become computationally more expensive. Thus, the reasonable computing time is a great advantage of analytical, quantitative CEST methods such as AREX, Ω-plot, QUEST, QUESP, QUESTP and QUESTRA [10–12, 19, 32]. The Water Exchange (WEX) spectroscopy might be also a useful reference method for exchange rate determination [28, 33].

The simulations and experimental results showed slightly different ranges of applicability of the methods for the determination of exchange rate and the labile proton ratio. This can be explained as a result of systematic effects. Firstly, the simulated spin-lock pulse had an ideal rectangular form, which is never the case in reality. Besides, the simulated preparation pulses were realized through a simple rotation of the magnetization. In practice, a flip angle of these RF pulses is spatially dependent on, for instance, tissue attenuation. Secondly, a slight change of the saturation field strength, caused by the B_1 field inhomogeneities, leads to the varying saturation efficiency between pixels. Also, the B_0 inhomogeneities may cause non-negligible errors in quantitative CEST imaging [31]. In general, the Gaussian-shaped pulse irradiation scheme is considered to be more robust against field inhomogeneities than the spin-lock pre-saturation technique [24]. Further elements of uncertainty in the comparison of the experimental and simulated results are the longitudinal relaxation time T_{1s} and transversal relaxation time T_{2s} of the solute pool, used for simulations. Because of very short T_{2s}, a short echo-time spectroscopy is required in order to determine these parameters experimentally. Due to this technical limitation, we used values reported in the literature [31]. The influence of the T_{1s} time is relatively small. However, for extremely low exchange rates, a longer T_{1s} leads to more accurate results [15]. Moreover, simulation results presented by Sun et al. revealed that a variation of the T_{2s} plays only a subordinate role, as long as it can be reasonably estimated [15].

The results obtained for phantom 3 showed a linear dependency of the fractional concentration and the creatine concentration in solutions. A similar trend was reported by other groups [7, 20]. The comparison of the calculated labile proton ratios for phantom 3 showed a

systematic and partially significant overestimation of the results. In the case of Gaussian-shaped saturation pulses, it is consistent with the simulation findings. For the pulsed SL saturation, however, a slightly underestimated result was expected. The surprisingly overestimated values of the fractional concentration could be explained as a result of the underestimation of the exchange rates.

In the present work we assessed the applicability of the methods using creatine solution. Quantitative CEST analysis of other endogenous CEST agents or even multi-pool CEST systems could be the next step. Since exchange rates increase with increasing temperature, the pulsed SL saturation technique could be of particular relevance for imaging of slow and intermediate-exchanging protons at 3T. Another factor, which should be taken into account, is the signal-to noise ratio (SNR) of the MRI data. The Rician noise, which introduces a bias into MRI experiments, may be crucial to the quantitative CEST analysis, especially for in vivo applications [34, 35]. The apparent semi-solid molecular magnetization transfer (MT) and nuclear overhauser (NOE) effects also have to be considered [36, 37].

As an alternative to the pulsed saturation scheme, a method based on a continuous RF saturation scheme using a parallel RF transmission technique has been developed, that allows the use of arbitrarily long RF saturation pulses via amplifier alternation within the SAR and RF duty-cycle limits [38, 39].

Although the first in vivo applications of AREX metrics and the Ω-plot method at 3T scanner have been already reported, further development and tissue-oriented optimization is still necessary. Zaiss et al. applied AREX of APT (amide proton transfer) to calculate the absolute pH map of a rat brain with a stroke lesion. One limitation of this method is that the labile proton ratio has to be known in order to determine k_{sw} and, thus, the pH map [19]. In contrast, the Ω-plot method allows simultaneous measurements of the exchange rate and the labile proton ratio. Therefore, Zhou et al. performed in vivo quantitative CEST imaging using the Ω-plot method in the intervertebral discs (IVDs) in a porcine model on a 3T clinical scanner. The exchange rates determined from the quantitative analysis were closely correlated with the pH value in the IVDs, which was measured using a needle-shaped tissue pH probe. The most important limitation of the study was the acquisition time (30–40 min for one IVD) [40]. The quantitative CEST analysis requires long saturation times to achieve the steady-state and multiple CEST experiments with varying B_1 in the case of using the Ω-plot method. Thus, the new fast imaging techniques such as compressed sensing or parallel imaging are necessary to accelerate CEST acquisitions [41]. In addition to brain and cartilage, it might be also possible to quantify the CEST effects from small metabolites and their by-products in other human tissues such as kidney, liver or muscles.

Conclusion

A quantitative CEST data evaluation approach, enabling the determination of the labile proton ratio f of exchanging protons and their exchange rate k_{sw} is an important step in improving the quality of the CEST imaging. Up to now, quantitative CEST imaging was mostly performed at a high field strength (7T) using continuous wave (CW) saturation pulses. Although higher magnetic field strengths are beneficial to the CEST phenomenon, the commonly used field strengths on clinical MR usually do not surpass 3T. Furthermore, due to scanner specifications and specific absorption rate guidelines, only pulse train pre-saturation should be considered for the CEST imaging in clinical routine. The Ω-plot method for pulsed SL saturation has proved to be particularly promising for imaging of intermediate-exchanging protons with exchange rates between 50 and 530 Hz. In summary, our studies showed that quantitative pulsed-CEST MRI is capable of producing reasonable results at clinically available MR systems and remains promising for clinical translation.

Acknowledgements We thank M. Zaiss (German Cancer Research Center, Heidelberg, Germany) for providing CEST MRI pulse sequence used in this study.

Author contributions Stabinska: Protocol/project development, data management, data analysis. Cronenberg: Protocol/project development, data collection, data analysis. Wittsack: Protocol/project development. Lanzman: Protocol/project development. Müller-Lutz: Protocol/project development.

Compliance with ethical standards

Conflict of interest The authors declare that they have no conflict of interest.

Ethical approval This article does not contain any studies with human participants or animals performed by any of the authors.

Funding This study was supported by a Grant from the Forschungskommission of the Faculty of Medicine, Heinrich-Heine-University, Düsseldorf (Grant No: 13/2015).

Appendix 1

See Figs. 6 and 7 and Table 2.

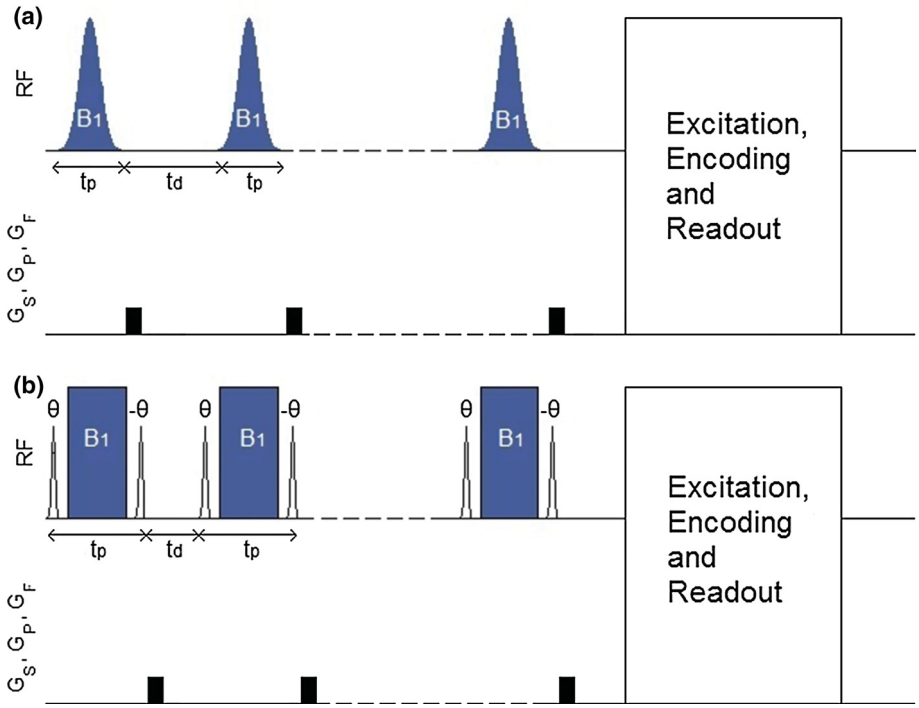

Fig. 6 A simplified schematic CEST pulse sequence diagram with a series of **a** Gaussian-shaped RF saturation pulses and **b** off-resonant spin-lock saturation pulses. Each saturation block consists of n pulses of average amplitude B_1 and duration t_p interleaved by delays t_d. Between the saturation pulses spoiling gradients in all three gradient dimensions are applied. After RF saturation a 2-D single-shot gradient echo sequence (GRE) was used for CEST image data acquisition. Diagram was created based on [22, 28]

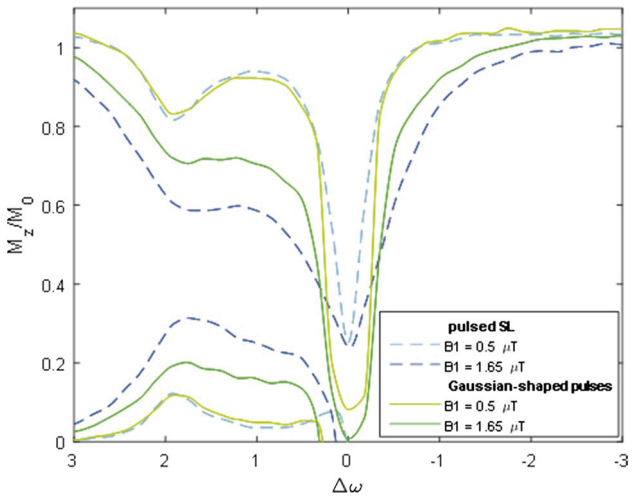

Fig. 7 Z-spectrum and AREX curves obtained with $B_1 = 0.5$ μT and $B_1 = 1.65$ μT using pulsed SL (*dashed blue lines*) and Gaussian-shaped saturation pulses (*solid green lines*). For the pulsed SL saturation, AREX yields higher contrast at higher B_1 compared to saturation with trains of Gaussian-shaped RF pulses

Table 2 Numerical simulation parameters

Quantitative CEST method	Saturation scheme	k_{sw}	B_1 variation (f = const)	f variation (B_1 = const)
AREX	Gaussian-shaped pulses Spin-lock pulses	1–300 Hz in steps of 1 Hz	0.1–5.0 μT in steps of 0.05 μT ($f = 2‰$)	–
AREX-based Ω-plot	Gaussian-shaped pulses Spin-lock pulses	10–500 Hz in steps of 10 Hz 10–1000 in steps of 10 Hz	Six datasets with linearly distributed RF amplitudes B_1 between 0.2 μT and a maximum B_1 value, which ranged between 1.6 and 4.6 μT in steps of 0.1 μT ($f = 2‰$)	0.05–5‰ in steps of 0.05‰ ($B_1 = 0.25$, 0.5, 1.0, 1.25, 1.65, 2.1 μT)

References

1. Ward KM, Aletras AH, Balaban RS (2000) A new class of contrast agents for MRI based on proton chemical exchange dependent saturation transfer (CEST). J Magn Reson 143:79–87
2. van Zijl PC, Yadav NN (2011) Chemical exchange saturation transfer (CEST): what is in a name and what isn't? Magn Reson Med 65(4):927–948
3. Vinogradov E, Sherry AD, Lenkinski RE (2013) CEST: from basic principles to applications, challenges and opportunities. J Magn Reson 229:155–172
4. Zhang S, Malloy CR, Sherry AD (2005) MRI thermometry based on PARACEST agents. J Am Chem Soc 127:17572–17573
5. Müller-Lutz A, Khalil N, Schmitt B, Jellus V, Pentang G, Oeltzschner G, Antoch G, Lanzman RS, Wittsack HJ (2014) Pilot study of Iopamidol-based quantitative pH imaging on a clinical 3T MR scanner. Magn Reson Mater Phy 27(6):477–485
6. Longo DL, Sun PZ, Consolino L, Michelotti FC, Uggeri F, Aime S (2014) A general MRI-CEST ratiometric approach for pH imaging: demonstration of in vivo pH mapping with Iobitridol. J Am Chem Soc 136(41):14333–14336
7. Wu R, Xiao G, Zhou IY, Ran C, Sun PZ (2015) Quantitative chemical exchange saturation transfer (qCEST) MRI–omega plot analysis of RF-spillover-corrected inverse CEST ratio asymmetry for simultaneous determination of labile proton ratio and exchange rate. NMR Biomed 28(3):376–383
8. Kim J, Wu Y, Guo Y, Zheng H, Sun PZ (2014) A review of optimization and quantification techniques for chemical exchange saturation transfer MRI toward sensitive in vivo imaging. Contrast Media Mol Imaging 10(3):163–178
9. Woessner DE, Zhang S, Merritt ME, Sherry AD (2005) Numerical solution of the Bloch equations provides insights into the optimum design of PARACEST agents for MRI. Magn Reson Med 53:790–799
10. McMahon MT, Gilad AA, Zhou J, Sun PZ, Bulte JW, van Zijl PC (2006) Quantifying exchange rates in chemical exchange saturation transfer agents using the saturation time and saturation power dependencies of the magnetization transfer effect on the magnetic resonance imaging signal (QUEST and QUESP): pH calibration for poly-L-lysine and a starburst dendrimer. Magn Reson Med 55(4):836–847
11. Dixon WT, Ren J, Lubag AJ, Ratnakar J, Vinogradov E, Hancu I, Lenkinski RE, Sherry AD (2010) A concentration-independent method to measure exchange rates in PARACEST agents. Magn Reson Med 63(3):625–632
12. Sun PZ (2012) Simplified quantification of labile proton concentration weighted chemical exchange rate (kws) with RF saturation time dependent ratiometric analysis (QUESTRA): normalization of relaxation and RF irradiation spillover effects for improved quantitative chemical exchange saturation transfer (CEST) MRI. Magn Reson Med 67(4):936–942
13. Sun PZ (2010) Simultaneous determination of labile proton concentration and exchange rate utilizing optimal RF power: radio frequency power (RFP) dependence of chemical exchange saturation transfer (CEST) MRI. J Magn Reson 202(2):155–161
14. Wu R, Liu CM, Liu PK, Sun PZ (2012) Improved measurement of labile proton concentration-weighted chemical exchange rate (kws) with experimental factor-compensated and T1-normalized quantitative chemical exchange saturation transfer (CEST) MRI. Contrast Media Mol Imaging 7(4):384–389
15. Sun PZ, Wang Y, Dai Z, Xiao G, Wu R (2014) Quantitative chemical exchange saturation transfer (qCEST) MRI–RF

spillover effect-corrected omega plot for simultaneous determination of labile proton fraction ratio and exchange rate. Contrast Media Mol Imaging 9(4):268–275
16. Sun PZ, Wang E, Cheung JS, Zhang X, Benner T, Sorensen AG (2011) Simulation and optimization of pulsed radio frequency (RF) irradiation scheme for chemical exchange saturation transfer (CEST) MRI—demonstration of pH-weighted pulsed-amide proton CEST MRI in an animal model of acute cerebral ischemia. Magn Reson Med 66(4):1042–1048
17. Schmitt B, Zaiss M, Zhou J, Bachert P (2011) Optimization of pulse train pre-saturation for CEST imaging in clinical scanners. Magn Reson Med 65:1620–1629
18. Sun PZ, Brenner T, Kumar A, Sorensen AG (2008) Investigation of optimizing and translating pH-sensitive pulsed-chemical exchange saturation transfer (CEST) imaging to a 3T clinical scanner. Magn Reson Med 60:834–841
19. Zaiss M, Xu J, Goerke S, Khan IS, Singer RJ, Gore JC, Gochberg DF, Bachert P (2014) Inverse Z-spectrum analysis for spillover-, MT-, and T1- corrected steady-state pulsed CEST-MRI–application to pH-weighted MRI of acute stroke. NMR Biomed 27(3):240–252
20. Meissner JE, Goerke S, Rerich E, Klika KD, Radbruch A, Ladd ME, Bachert P, Zaiss M (2015) Quantitative pulsed CEST-MRI using Ω-plots. NMR Biomed 28:1196–1208
21. Zaiss M, Bachert P (2013) Exchange-dependent relaxation in the rotating frame for slow and intermediate exchange–modeling off-resonant spin-lock and chemical exchange saturation transfer. NMR Biomed 26(5):507–518
22. Roeloffs V, Meyer C, Bachert P, Zaiss M (2014) Towards quantification of pulsed spinlock and CEST at clinical MR scanners: an analytical interleaved saturation-relaxation (ISAR) approach. NMR Biomed 28:40–53
23. Jin T, Aution J, Obata T, Kim SG (2011) Spin-locking versus chemical exchange saturation transfer MRI for investigating chemical exchange process between water and labile metabolite protons. Magn Reson Med 65:1448–1460
24. Jin T, Kim SG (2014) Advantages of chemical exchange-sensitive spin-lock (CESL) over chemical exchange saturation transfer (CEST) for hydroxyl- and amine-water proton exchange rates. NMR Biomed 27(11):1313–1324
25. Cobb JG, Li K, Xie J, Gochberg DF, Gore JC (2014) Exchange-mediated contrast in CEST and spin-lock imaging. Magn Reson Imaging 32(1):28–40
26. Yuan J, Zhou J, Ahuja AT, Wang YX (2013) MR chemical exchange imaging with spin-lock technique (CESL): a theoretical analysis of Z-spectrum using a two-pool $R_{1\rho}$ relaxation model beyond the fast-exchange limit. Phys Med Biol 57(24):8185–8200
27. Murase K, Tanki N (2011) Numerical solutions to the time-dependent Bloch equations revisited. Magn Reson Imaging 29(1):126–131
28. Goerke S, Zaiss M, Bachert P (2014) Characterization of creatine guanidinium proton exchange by water-exchange (WEX) spectroscopy for absolute-pH CEST imaging in vitro. NMR Biomed 27(5):507–518
29. Kim M, Gillen J, Landmann BA, Zhou J, van Zijl PC (2009) Water saturation shift referencing (WASSR) for chemical exchange saturation transfer experiments. Magn Reson Med 61(6):1441–1450
30. Müller-Lutz A, Matuschke F, Schleich C, Wickrath F, Boos J, Schmitt B, Wittsack HJ (2016) Improvement of water saturation shift referencing by sequence and analysis optimization to enhance chemical exchange saturation transfer imaging. Magn Reson Imaging 34(6):771–778
31. Sun PZ, Farrar CT, Sorensen AG (2007) Correction for artifacts induced by B0 and B1 field inhomogeneities in pH-sensitive chemical exchange saturation transfer (CEST) imaging. Magn Reson Med 58(6):1207–1215
32. Randtke EA, Chen LQ, Corrales LR, Pagel MD (2014) The Hanes-Woolf linear QUESP method improves the measurements of fast chemical exchange rates with CEST MRI. Magn Reson Med 71(4):1603–1612
33. Zhou J, Wilson DA, Sun PZ, Klaus JA, van Zijl PC (2004) Quantitative description of proton exchange processes between water and endogenous and exogenous agents for WEX, CEST and APT experiments. Magn Reson Med 51(5):945–952
34. Sun PZ, Wang E, Cheung JS (2012) Imaging acute ischemic tissue acidosis with pH-sensitive endogenous amide proton transfer (APT) MRI–correction of tissue relaxation and concomitant RF irradiation effects toward mapping quantitative cerebral tissue pH. Neuroimage 60(1):1–6
35. Gudbjartsson H, Patz S (1995) The Rician distribution of noisy MRI data. Magn Reson Med 34(6):910–914
36. Henkelman RM, Stanisz GJ, Graham SJ (2001) Magnetization transfer in MRI: a review. NMR Biomed 14:57–64
37. Jones CK, Huang A, Xu J, Edden RA, Schär M, Hua J, Oskolkov N, Zacà D, Zhou J, McMahon MT, Pillai JJ, van Zijl PC (2013) Nuclear overhauser enhancement (NOE) imaging in the human brain at 7T. Neuroimage 77:114–124
38. Keupp J, Togao O, Zhou J, Suzuki Y, Yoshiura T (2012) Optimization of saturation pulse length in parallel transmission based amide proton transfer MRI for oncology applications. Proc Int Soc Magn Reson Med 20:4258
39. Togao O, Hiwatashi A, Keupp J, Yamashita K, Kikuchi K, Yoshiura T, Yoneyama M, Kruiskamp MJ, Sagiyama K, Takahashi M, Honda H (2016) Amide proton transfer imaging of diffuse gliomas: effect of saturation pulse length in parallel transmission-based technique. PLoS One 11(5):e0155925
40. Zhou Z, Bez M, Tawackoli W, Giaconi J, Sheyn D, de Mel S, Maya MM, Pressman BD, Gazit Z, Pelled G, Gazit D, Li D (2016) Quantitative chemical exchange saturation transfer MRI of intervertebral disc in a porcine model. Magn Reson Med 76(6):1677–1683
41. Heo HY, Zhang Y, Leen DH, Jiang S, Zhao X, Zhou J (2016) Accelerating chemical exchange saturation transfer (CEST) MRI by combining compressed sensing and sensitivity encoding techniques. Magn Reson Med 77:779–786

Received: 25 September 2018 | Revised: 6 March 2019 | Accepted: 28 March 2019

DOI: 10.1002/mrm.27778

FULL PAPER

Magnetic Resonance in Medicine

Proton exchange in aqueous urea solutions measured by water-exchange (WEX) NMR spectroscopy and chemical exchange saturation transfer (CEST) imaging in vitro

Julia Stabinska[1] | Philipp Neudecker[2,3] | Alexandra Ljimani[1] | Hans-Jörg Wittsack[1] | Rotem Shlomo Lanzman[1] | Anja Müller-Lutz[1]

[1]Department of Diagnostic and Interventional Radiology, Medical Faculty, Heinrich Heine University Düsseldorf, Dusseldorf, Germany

[2]Institute of Physical Biology, Heinrich Heine University Düsseldorf, Dusseldorf, Germany

[3]Institute of Complex Systems: Structural Biochemistry (ICS-6), Forschungszentrum Jülich, Julich, Germany

Correspondence
Julia Stabinska, Department of Diagnostic and Interventional Radiology, Medical Faculty, Heinrich Heine University Düsseldorf, Moorenstr. 5, 40225 Düsseldorf, Germany.
E-mail: Julia.Stabinska@med.uni-duesseldorf.de

Purpose: To characterize the proton exchange in aqueous urea solutions using a modified version of the WEX II filter at high magnetic field, and to assess the feasibility of performing quantitative urea CEST MRI on a 3T clinical MR system.

Methods: In order to study the dependence of the exchange-rate constant k_{sw} of urea as a function of pH and T, the WEX-spectra were acquired at 600 MHz from urea solutions in a pH range from 6.4 to 8.0 and a temperature range from $T = 22°C$ to 37°C. The CEST experiments were performed on a 3T MRI scanner by applying a train of 50 Gaussian-shaped pulses, each 100-millisecond long with a spacing of 100 milliseconds, for saturation. Exchange rates of urea were calculated using the (extended) AREX metric.

Results: The results showed that proton exchange in aqueous urea solutions is acid and base catalyzed with the rate constants: $k_a = (9.95 \pm 1.1) \times 10^6$ l/(mol·s) and $k_b = (6.21 \pm 0.21) \times 10^6$ l/(mol·s), respectively. Since the urea protons undergo a slow exchange with water protons, the CEST effect of urea can be observed efficiently at 3T. However, in neutral solutions the exchange rate of urea is minimal and cannot be estimated using the quantitative CEST approach.

Conclusions: By means of the WEX-spectroscopy, the kinetic parameters of the proton exchange in urea solutions have been determined. It was also possible to estimate the exchange rates of urea in a broad range of pH values using the CEST method at a clinical scanner.

KEYWORDS
CEST, exchange rate, proton exchange, urea, urCEST, WEX

1 | INTRODUCTION

Urea is the major end-product of protein catabolism and serves an important role in the maintenance of pH homeostasis in mammals.[1,2] It is formed in the liver from ammonia, and later transported in the blood to the kidneys for excretion in the urine.[3,4] Diseases that compromise the function of the kidney are often associated with reduced urea elimination and consequently its increased concentration in blood, as measured by the blood urea nitrogen (BUN) test.[5] To assess

the structural changes in kidneys, well-established imaging techniques such as ultrasound (US), computed tomography (CT), and magnetic resonance tomography (MRI) are performed. Nevertheless, they usually do not provide adequate functional information.[6]

Chemical exchange saturation transfer (CEST) is a novel mechanism of MRI contrast that may overcome this limitation, since it has been shown to be sensitive to the concentrations of the endogenous metabolites and microenviromental properties such as pH and temperature.[7-10] Urea is a potentially attractive CEST agent for in vivo use. Although the normal blood urea level is relatively low (5-10 mM), the urea concentration in the urine may be 20-100 times higher than in the blood in humans, as reported in Ref. [[11]] Urea is an amide with two $-NH_2$ groups joined by a carbonyl ($C = O$) functional group.[12] Already in 1998, Guivel-Sharen et al. identified urea as a major contributor to the kidney/urine chemical exchange at ca. 1 ppm (with water proton frequency defined as 0 ppm).[13] Two years later, Dagher et al. were able to produce a urea distribution map in vivo at 1.5 T using CEST MRI.[14] Apart from an ISMRM abstract in 2015,[15] no further studies on urea-weighted CEST (urCEST) at a clinical MRI system have been published.

Knowledge about the chemical shift, exchange rate, and relaxation properties of urea leads to better understanding of the saturation transfer effects in the human kidney in vivo. Because many kidney diseases alter pH and urea gradients in kidney, an implementation of pH-sensitive CEST imaging might be of great interest particularly in the clinical context.[7,16] In this study, we characterize the proton exchange properties of urea with water using water exchange spectroscopy (WEX II)[17] at ultrahigh magnetic field, and evaluate the feasibility of performing quantitative urea CEST analysis at 3T. In particular, we determine the chemical exchange rates k_{sw} between urea amide protons s and water w as a function of pH, concentration, and temperature by means of WEX spectroscopy and CEST experiments.

Moreover, in order to examine the specificity of the urea-weighted CEST imaging in kidney, we study the CEST effect of other important kidney metabolites, eg, creatinine, ammonia, hippuric acid, and citric acid at different pH values.[18,19] Eventually, we investigate the contribution of the urCEST to the total CEST effect in urine.

2 | METHODS

2.1 | Preparation of the aqueous urea solutions

For WEX experiments, six aqueous model solutions containing 250 mM urea (≥99.5% cryst. urea, Carl Roth, Karlsruhe, Germany), 50 mM sodium/potassium phosphate buffer (≥99% disodium hydrogen phosphate, and ≥99.5% potassium dihydrogen phosphate, Carl Roth, Karlsruhe, Germany) and 5% (v/v) deuterium oxide (D_2O, 99.8 atom % D, Carl Roth, Karlsruhe, Germany) for the field-frequency lock were prepared at different pH = (6.39, 6.56, 6.96, 7.38, 7.72, 7.97) and measured at temperature $T = 37.0°C$. The samples with pH = 6.56 and pH = 7.97 were additionally measured at varied temperatures T = (22.0°C, 27.0°C, 32.0°C, 37.0°C).

For CEST studies, sixteen 50 ml aqueous solutions with 250 mM urea concentration were mixed with 50 mM Na/K phosphate buffer at pH = (5.66, 5.72, 5.93, 6.12, 6.20, 6.37, 6.54, 6.86, 7.00, 7.20, 7.37, 7.65, 7.80, 8.02, 8.20, 8.41). In addition, four samples containing different urea concentration c_s = (10 mM, 25 mM, 50 mM, 100 mM) at pH 7.60 were prepared.

The other studied metabolites were: creatinine, ammonia, hippuric acid, citric acid, taurine, creatine, histidine, glucose, glutamine, myo-inositol, alanine, lysine, allantoin, threonine, lactate, sorbitol, glutamic acid, choline, and glycogen. The concentration of most compounds was 100 mM, and the remainder determined by their solubility in the sample buffer. Each phantom consisted of four tubes containing model solution dissolved in 50 mM Na/K phosphate buffer at pH = (6.2, 6.6, 7.0, 7.4). Additionally, individual and mixed aqueous solutions of 180 mM urea, 15 mM creatinine, and 1 mM creatine, corresponding to the normal concentrations of these metabolites in urine, were prepared. In addition, an urine sample was collected from a healthy volunteer. The pH value of the model mixture and the urine sample were: 5.97 and 5.90 at $T = 37°C$, respectively.

The temperature of the model solutions during the measurements was kept constant $T = (37 \pm 1)°C$ by using an MR-compatible cooling box.

2.2 | WEX experiments

The WEX spectra were acquired on a Bruker Avance III HD 600-MHz NMR spectrometer (Bruker, Ettlingen, Germany) equipped with a cryogenically cooled quadruple resonance probe with z-axis pulsed field gradient capabilities. The sample temperature was calibrated using methanol-d_4.[20] The exchange of water protons with urea was monitored with the pulse sequence shown in Figure 1 using 33 different mixing times (T_m) ranging from 20 milliseconds to 2000 milliseconds. For each mixing time, 32 transients were recorded with a recycle delay of 4.7 seconds. The resulting spectra were processed using NMRPipe and NMRDraw[21] and the ^{1}H resonance of urea was integrated.

2.3 | CEST experiments

All CEST experiments were performed on the 3T whole body MR clinical scanners (Magnetom Trio and Magnetom Prisma, Siemens Healthineers, Erlangen, Germany). Z-spectra were obtained using presaturated gradient-echo imaging with

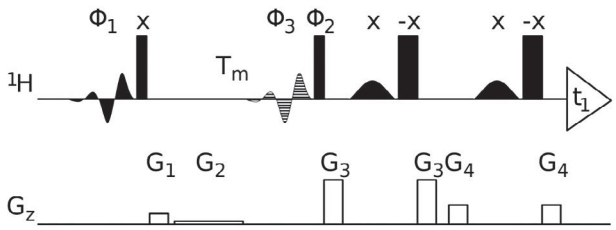

FIGURE 1 WEX II pulse sequence with excitation sculpting and water flip-back. Narrow and wide bars are hard rectangular 90° and 180° pulses, respectively, applied at maximum permissible amplifier power with the phase indicated above each pulse. Water-selective 90° pulses have an E-BURP-1 shape[39] and a duration of 12.0 milliseconds (at 600 MHz). Water-selective 180° pulses have a shape corresponding to the central lobe of a sinc function and a duration of 4.0 milliseconds. The basic phase cycle of the WEX II sequence is ϕ_1: $x, -x, x, -x$; ϕ_2: $x, x, -x, -x$; ϕ_3: $x, -x, -x, x$; receiver: $x, -x, -x, x$ and is expanded by EXORCYCLE phase cycling of the 180° pulses in the excitation sculpting sequence. The pulsed field gradients are G_1: 10 G/cm, 1.0 milliseconds; G_2: 1 G/cm; G_3: 43 G/cm, 0.5 milliseconds; G_4: 19 G/cm, 0.5 milliseconds

the following parameters: $FOV = 130 \times 130\,\text{mm}^2$, matrix size: 128×128, slice thickness = 5.0 mm, repetition time $T_R = 7.7$ milliseconds and echo time $T_E = 3.61$ milliseconds. In the urCEST experiments, presaturation was achieved using 50 Gaussian-shaped pulses with low RF saturation power of $B_1 = 1.0\,\mu$T, pulse duration $t_{pd} = 100$ milliseconds and interpulse delay $t_{ipd} = 100$ milliseconds (duty cycle $DC = 50\%$, total saturation time $T_{sat} = 9.9$seconds). Forty-three saturated images at evenly distributed frequency offsets between ± 4 ppm and an unsaturated image at 300 ppm were acquired. To determine B_0 maps using the water saturation shift referencing method (WASSR),[22] a single Gaussian-shaped pulse with RF saturation power of $B_1 = 0.1\,\mu$T and pulse duration $t_{pd} = 56$ milliseconds was applied. The WASSR z-spectra were obtained at 42 offsets between −1 ppm and 1 ppm. Additionally, T1-weighted images were measured by a turbo inversion recovery sequence. Altogether, 12 contrasts at different inversion delays (TI) ranging from 25 milliseconds to 5 seconds were fitted to calculate T_1 maps. The same measurement protocol was applied to acquire the CEST signals in the phantom including mixed solution of urea, creatinine, and creatine as well as in the urine sample.

Further phantom experiments were performed using 20 Gaussian-shaped pulses with three different RF amplitudes, $B_1 = (0.8, 1.2, 1.6)\,\mu$T and pulse duration $t_{pd} = t_{ipd} = 100$ milliseconds. Z-spectra were acquired at 45 frequency offsets between −6 and 6 ppm.

2.4 | Data analysis

Post-processing was performed using in-house written programs in MATLAB (Mathworks, Natick, Massachusetts). The T_1 maps were obtained by pixel-by-pixel least-squares fitting of the signal equation $I = I_0 \cdot [1 - 2 \cdot \exp(-TI/T_1)]$, where I is the signal intensity and TI is the inversion time. The exchange rates of urea were calculated as described in the following sections.

2.5 | Determination of k_a and k_b for urea by WEX

As in standard amides, proton exchange in urea solutions is acid and base catalyzed and therefore strongly pH dependent[23,24]:

$$k_{sw} = k_b \cdot 10^{pH - pK_w} + k_a \cdot 10^{-pH} + k_0 \tag{1}$$

where k_b, k_a and k_0 (in l/(mol·s)) are rate constants for the base-, acid- and water-catalyzed protolysis, respectively. The rate of the spontaneous reaction (k_0) is very slow compared to acid and base catalyses, and thus assumed to be negligible.[24] The pK_w refers to the negative decadic logarithm of the ionization constant, which is temperature dependent according to the solution of the van't Hoff equation[25,26]:

$$pK_w(T) = pK_w(T_0) - \left(\frac{\Delta H_R^0}{R \cdot \ln(10)}\right)\left(\frac{1}{T_0} - \frac{1}{T}\right) \tag{2}$$

$pK_w(T_0)$ here refers to the logarithm of the water-ion product at temperature $T_0 = 25$°C, $\Delta H_R^0 = 55.84$ kJ/mol is the standard reaction enthalpy for the self-dissociation of water and $R = 8.314$ J/(mol K) is the gas constant.[25,26] Thus, we assumed $pK_w = 13.617$ at $T = 37$°C. The urea signal intensity $S_s(T_m)$ as a function of the mixing time T_m is given by[26]:

$$S_s(T_m) = \underbrace{\frac{k_{ws} M_{zw}(0)}{k_{sw} + R_{1s} - R_{1w}}}_{C} \left[e^{-R_{1w} \cdot (T_m - T_{WFB})} - e^{-(k_{sw} + R_{1s}) \cdot (T_m - T_{WFB})}\right] \tag{3}$$

where R_{1w}, R_{1s} are the longitudinal relaxation rates of the water and solute pool, respectively; k_{sw} is the chemical exchange rate between solute s and water pool w and k_{ws} is the back-exchange rate; $M_{zw}(0)$ is the z magnetization of the water protons at the beginning of the mixing period. The $k_{sw} + R_{1s}$ values were obtained from a fit of Equation 3 to the measured urea signal integrals $S_s(T_m - T_{WFB})$ at any given pH and temperature in MATLAB, where TWFB is a variable fitting parameter introduced to account for the effects of the water flip-back pulse at the end of the mixing period (see below). Eventually, the k_b and k_a rates at given temperature were estimated by bi-exponential fit of the measured $k_{sw} + R_{1s}$ values with the following equation:

$$k_{sw} + R_{1s} = k_b \cdot 10^{pH - pK_w} + 10^{-pH} + R_{1s} \tag{4}$$

Furthermore, the activation energies $E_{A,b}$ and $E_{A,a}$ of, respectively, base- and acid-catalyzed reactions were calculated by fitting the measured $k_{sw} + R_{1s}$ values at pH 7.97 and pH 6.56 as a function of temperature. It was assumed that at pH 7.97, the proton exchange with water is dominantly base catalyzed, hence[27]:

$$k_{sw} + R_{1s} = k_b(310.15\,\mathrm{K}) \cdot \left[\frac{\mathrm{mol}}{l}\right] \cdot 10^{pH-14+\frac{\Delta H_R^0}{R\cdot\ln(10)}\left(\frac{1}{298.15\,\mathrm{K}}-\frac{1}{T}\right)+\frac{E_{A,b}}{R\cdot\ln(10)}\left(\frac{1}{310.15\mathrm{K}}-\frac{1}{T}\right)} + R_{1s} \quad (5)$$

Similarly, at pH 6.56, the exchange process between water and amide protons of urea is mainly acid catalyzed, and thus[27]:

$$k_{sw} + R_{1s} = k_a(310.15\,\mathrm{K}) \cdot \left[\frac{\mathrm{mol}}{l}\right] \cdot 10^{-pH+\frac{E_{A,a}}{R\cdot\ln(10)}\left(\frac{1}{310.15\mathrm{K}}-\frac{1}{T}\right)} + R_{1s} \quad (6)$$

where $k_b(310.15\,\mathrm{K})$ and $k_a(310.15\,\mathrm{K})$ are the obtained rate constants at $T = 310.15$ K. The R_{1s} was assumed to be independent of temperature.[27]

2.6 | Determination of k_{sw} for urea by CEST

Recently, several theoretical approaches of quantifying proton exchange rates from data obtained in CEST experiments were proposed,[28-33] especially a novel magnetization transfer (MT) ratio called MTR_{Rex}, which eliminates spillover effect and semi-solid macromolecular magnetization transfer, was introduced by Zaiss et al.[34]:

$$MTR_{Rex} = \frac{1}{Z_{lab}} - \frac{1}{Z_{ref}} = \frac{R_{ex}\cdot DC}{R_{1w}} \quad (7)$$

where $Z_{lab} = Z(+\Delta\omega)$ is the label scan around the resonance of the CEST pool s, $Z_{ref} = Z(-\Delta\omega)$, the reference scan at the opposite frequency with respect to water, R_{ex} refers to the exchange-dependent relaxation in the rotating frame and R_{1w}, is the relaxation rate of the water pool w. Duty cycle, $DC = t_{pd}/(t_{ipd} + t_{pd})$, is determined by the pulse duration t_{pd} and the inter-pulse delay t_{ipd}. The MTR_{Rex} metric can be extended to an apparent exchange-dependent relaxation metric, $-AREX$:

$$AREX = MTR_{Rex}\cdot R_{1w} \quad (8)$$

More recently, Roeloffs et al. demonstrated that in the case of exchange rates that are small with respect to the inter-pulse delay, modeling magnetization transfer during the pauses between the RF pulses might be crucial.[35] In their theoretical model, they assume bi-exponential dynamics of the magnetization in the water pool during the inter-pulse delay (ISAR2), instead of a mono-exponential recovery with rate R_{1w} (ISAR1), as had been previously presumed.[36] As a result, the MTR_{rex} metric has to be extended by an additional term[35]:

$$MTR_{Rex} = \frac{1}{Z_{lab}} - \frac{1}{Z_{ref}} = \frac{R_{ex}\cdot DC}{R_{1w}}\cdot\left(1+\frac{1-R_{1w}t_{ipd}}{t_{pd}k_{sw}}\right) \quad (9)$$

In the large shift limit (LS) (i) $\delta\omega_s \to \infty$ and in the full saturation limit (FS) (ii) $\omega_1 \gg R_{2s} + k_{sw}$, when applying RF pulse at the CEST pool s resonance, $R_{ex} = f_s \cdot k_{sw}$ and hence[34]:

$$k_{sw} = \frac{MTR_{Rex}\cdot R_{1w}}{DC\cdot f_s} \quad (10)$$

where k_{sw} describes the exchange rate of urea, f_s the proton fraction (see below), R_{2s} the transverse relaxation rate of the CEST pool s, ω_1 the RF irradiation amplitude and $\delta\omega_s$ corresponds to the frequency offset of pool s. The proton fraction is given by[34]:

$$f_s = \frac{n_s}{n_w}\cdot\frac{c_s}{c_w} \quad (11)$$

c_i and n_i are the concentration and number of exchangeable protons per molecule of pool i ($i = s$ or w). It is assumed that $c_w = 55$ M and $n_w = 2$.

3 | RESULTS

3.1 | Implementation of the WEX II pulse sequence

For the measurement of water exchange rates we used a phase-cycled difference experiment based on water-selective inversion using the WEX II filter sequence with a 1D ^{1}H readout as described by Mori et al.[17] Because the broad ^{1}H resonance of urea (5.45 ⋯ 6.05 ppm) is separated from the ^1H_2O resonance (between 4.66 ppm and 4.80 ppm in the temperature range studied here) by only 0.65 ppm (390 Hz at 600 MHz) (Figure 2), such an experiment requires not only highly frequency-selective water inversion but also a 1D ^{1}H readout with excellent water suppression with water flip-back, a uniform excitation profile with an extremely narrow transition region near the ^1H_2O resonance, and an exceptionally flat baseline. To this end, the 3-9-19-WATERGATE water suppression scheme used in the original WEX II sequence [17] was replaced by an excitation sculpting[37] readout with water flip-back[38] (Figure 1). Water-selective excitation and water flip-back was achieved by 12.0 millisecond self-refocusing E-BURP-1[39] 90° pulses, water-selective refocusing by 4.0 milliseconds 180° pulses with a shape corresponding to the central lobe of a sinc(x) = sin(x)/x function. Simulations based on the Bloch equations and control experiments were used to establish that these pulses are sufficiently frequency selective that their effect on the ^{1}H resonance of urea is negligible. In brief, the initial combination of water selective and hard 90° pulses in Figure 1 selectively aligns the water magnetization along either the negative (−z) or the positive (+z) longitudinal axis in successive transients. Solute magnetization is rotated into the transverse plane and dephased by the crushing gradient G_1. The differential transfer of the (negative or positive) longitudinal magnetization of water protons

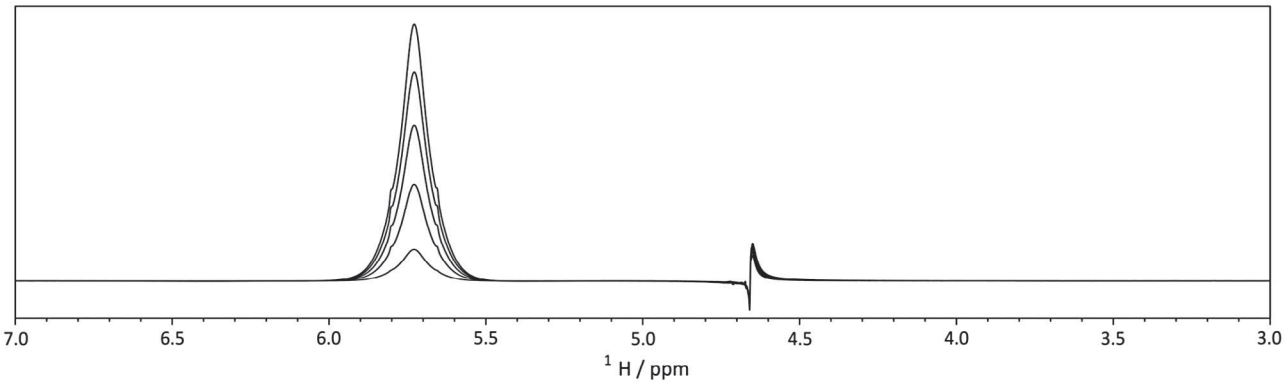

FIGURE 2 Overlay of the 1D ^{1}H WEX II spectra recorded using the pulse sequence shown in Figure 1 at pH 6.96 and 37.0°C with T_m = 20.0 milliseconds, 40.0 milliseconds, 60.0 milliseconds, 80.0 milliseconds, and 100.0 milliseconds (from bottom to top). Due to scalar relaxation of the second kind caused by the fast quadrupolar relaxation of the most abundant nitrogen isotope ^{14}N the urea ^{1}H resonance is very broad[61]; the ^{15}N satellites cause a doublet separated by the scalar coupling $^{1}J_{NH}$ which is visible as shoulders on the main ^{1}H resonance of urea. Excitation sculpting with water flip-back results in highly efficient suppression of the residual $^{1}H_2O$ resonance at approximately 4.66 ppm with a very flat baseline. Magnetization transfer to the urea resonance due to water exchange is approximately linear with the effective mixing time in the initial slope regime, but due to the effects of the water flip-back pulse in Figure 1 the effective mixing time ($T_{m-T_{WFB}}$) is systematically shorter than T_m, which is reflected in the disproportionally weak intensity of the urea resonance for T_m = 20.0 milliseconds

to other metabolites during the mixing time, T_m, in successive scans is obtained by phase cycling the pulses of the WEX II filter together with the receiver.[17] A weak gradient (G_2) is applied during the mixing time to prevent radiation damping.[17] Any longitudinal magnetization transferred to the solute is then detected with a 1D ^{1}H pulse sequence with excitation sculpting[37] preceded by a water flip-back pulse[38] to achieve excellent water suppression and a very flat spectral baseline (Figure 2). While this sequence preserves most of the salient features of the original WEX II sequence,[17] we prefer to apply the long (12.0 milliseconds) water flip-back pulse at the end of T_m before the hard 90° readout pulse in order to keep the excitation sculpting gradient double echo short enough to limit transverse relaxation and any homonuclear scalar coupling evolution. As a result of the complex trajectory of the water magnetization during this water flip-back pulse, the effective mixing time is somewhat shorter than T_m and no longer known a priori, but has to be corrected a posteriori by a variable parameter during data analysis. An important technical consideration—especially on modern high-field instruments with highly sensitive cryoprobes—is the effect of radiation damping, which opposes water-selective pulses that rotate the magnetization away from the positive longitudinal axis ("flip-down") but reinforces water-selective pulses that rotate the magnetization toward the positive longitudinal axis ("flip-up"). As a result, flip-down and flip-up water-selective pulses are significantly different and have to be calibrated independently.[40] The water-selective WEX II excitation pulse in Figure 1 has to be calibrated as a flip-down pulse because it rotates the magnetization from the positive (+z) longitudinal axis into the transverse plane. By contrast, the water flip-back pulse at the end of T_m (hatched in Figure 1) rotates the magnetization from either −z or +z into the transverse plane and therefore alternates between a flip-up and flip-down pulse, respectively, in successive transients. If only flip-down pulses are used for the sake of convenience, water flip-back will be incomplete and it is important to choose a recycle delay long enough for longitudinal relaxation of $^{1}H_2O$ between successive transients. As an alternative to the 1D ^{1}H readout presented in Figure 1, it is also straightforward to take advantage of the much sharper linewidth of the $^{15}NH_2$ groups of urea at natural abundance by combining the WEX II filter with a [^{1}H, ^{15}N] HSQC readout sequence with gradient coherence selection and water flip-back[41] if the signal-to-noise ratio is not limiting.

3.2 | Determination of the exchange rate constants k_a and k_b and the activation energies $E_{A,a}$ and $E_{A,b}$ of urea by WEX

The chemical shift of the urea amide protons in the WEX spectra is δ = 5.73 ppm at pH 6.96 and T = 37.0°C. The experimentally determined signal intensities of urea are in an excellent agreement with the fitted function $S_s(T_m)$ (Equation 3) (Figure 3) proven by mean fit quality of R^2 = 1.0.[42] Similarly, the $k_{sw} + R_{1s}$ values obtained from six measured samples at different pH match well the fitted function $k_{sw}(pH) + R_{1s}$ (Equation 4) (Table 1, Figure 4). With a fit quality of R^2 = 0.996, the estimated acid- and base- catalyzed exchange rate constants of urea at 37.0°C (310.15 K) are $k_a = (9.95 \pm 1.11) \times 10^6$ l/(mol·s) and $k_b = (6.21 \pm 0.21) \times 10^6$ l/(mol·s), respectively. The assumption of bi-exponential dependence of the urea exchange rate on pH is thus clearly verified. It is worth noting that the acid-catalyzed rate constant is much faster than the base-catalyzed rate constant. Using the calculated k_a and k_b values, it is possible to extrapolate the k_{sw} for any pH value (Table 2).

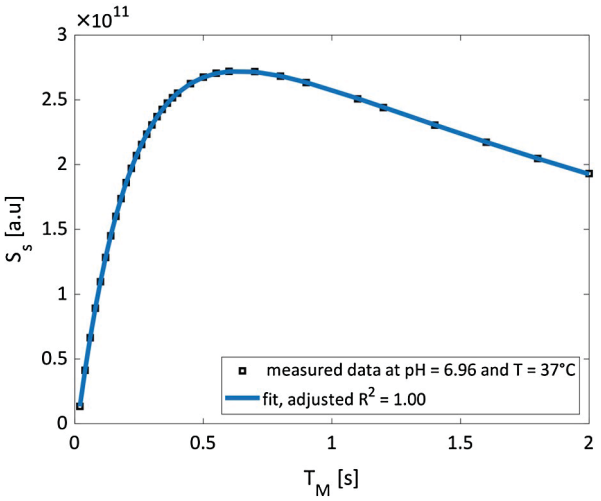

FIGURE 3 Integrated signal intensities S_s of the urea peaks (squares) at pH = 6.96 and T = 37.0°C as a function of mixing time T_m, and the fit function $S_s(T_{m-T_{WFB}})$ (Equation 3) (solid blue line). The quality of the fit was R^2 = 1.00

TABLE 1 $k_{sw} + R_{1s}$ [1/s] and R_{1w} [1/s] values in urea aqueous solutions (c_s = 250 mM) measured by WEX at different pH and temperatures. The standard errors are approximately 0.04% and R^2 = 1.0

pH	T [°C]	R_{1w} [1/s]	$k_{sw} + R_{1s}$ ([1/s])
6.39	37.0	0.29	6.22
6.56	22.0	0.39	2.92
6.56	27.0	0.35	3.56
6.56	32.0	0.33	4.31
6.56	37.0	0.31	5.26
6.96	37.0	0.30	4.63
7.38	37.0	0.30	5.82
7.72	37.0	0.30	9.63
7.97	22.0	0.38	3.78
7.97	27.0	0.35	6.14
7.97	32.0	0.32	9.93
7.97	37.0	0.30	16.19

The activation energies for base- and acid-catalyzed proton exchange in urea solution are $E_{A,b}$ = 43.52 ± 9.56 kJ/mol (quality of the fit: R^2 = 0.995) and $E_{A,a}$ = 79.13 ± 15.87 kJ/mol (quality of the fit: R^2 = 0.975). The Arrhenius plot (ln(k_{sw}) against 1/T) gives, as expected, a straight line (Figure 4).

3.3 | Determination of the exchange rates k_{sw} of urea by CEST

The CEST peak from urea is located at ca. 1 ppm with respect to the water resonance, which is arbitrarily set at 0 ppm. After correction of the MTR_{Rex} data for effects of T_1 relaxation (by multiplying with the R_{1w} maps), we obtained the apparent exchange-related relaxation metric (AREX) (Equation 8). The bi-exponential dependence of the AREX values on pH confirms that the proton exchange in aqueous urea solutions is acid and base catalyzed (Figure 5). By varying the urea concentration c_s at fixed pH = 8.04 and T = (37 ± 1)°C, we could also demonstrate that the (corrected) AREX is linearly proportional to the urea concentration (R^2 = 0.991) (Figure 5).

Using Equation 11 and the $k_{sw,ref}$ values determined by extrapolation of Equation 4 with the rate constants k_a and k_b measured by means of WEX spectroscopy, we were able to calculate the proton fraction f_s and thus the number of

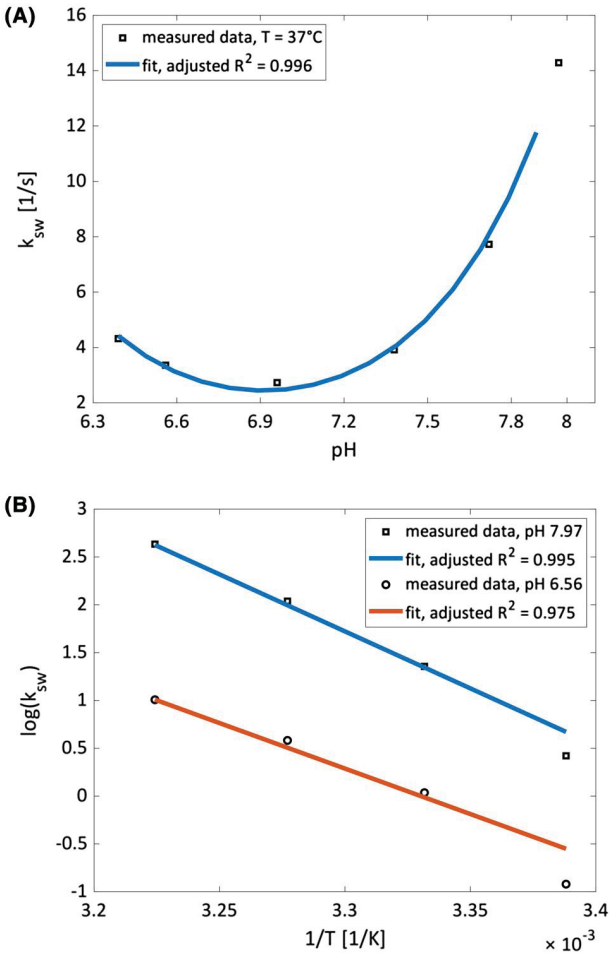

FIGURE 4 Determined k_{sw} (squares) values of urea as a function of (A) pH and (B) temperature. A, Temperature T = 37.0°C and urea concentration c_{urea} = 250 mM were fixed. Data were fitted using Equation 4 (solid blue line) yielding the following parameters: k_b = (6.21 ± 0.21) × 10^6 l/mol ·s, k_a = (9.95 ± 1.11) × 10^6 l/mol ·s and R_{1s} = (1.90 ± 0.31) s^{-1} (R^2 = 0.996). B, Arrhenius plot from data measured at fixed urea concentration c_{urea} = 250 mM at pH 7.97 (square) and pH 6.56 (circle). Data were fitted using Equation 5 (solid blue line) and 6 (solid yellow line) yielding the following values of activation energies: $E_{A,b}$ = 43.52 ± 9.56 kJ/mol (R^2 = 0.995) and $E_{A,a}$ = 79.13 ± 15.87 kJ/mol (R^2 = 0.975)

TABLE 2 Exchange rate k_{sw} [1/s] values in urea model solutions (c_s = 250 mM) obtained from CEST at different pH and $k_{sw,ref}$ estimated from WEX by extrapolation of Equation [5]

pH	T [°C]	k_{sw} [1/s]	$k_{sw,ref}$ [1/s]
5.66	37 ± 1	21.10 ± 2.80	21.84
5.72	37 ± 1	19.92 ± 2.20	19.04
5.93	37 ± 1	14.38 ± 2.33	11.82
6.12	37 ± 1	7.87 ± 2.25	7.75
6.20	37 ± 1	3.88 ± 1.88	6.51
7.37	37 ± 1	1.04 ± 2.10	4.60
7.65	37 ± 1	5.66 ± 2.41	6.92
7.80	37 ± 1	8.07 ± 1.85	9.61
8.02	37 ± 1	15.68 ± 2.31	15.80
8.20	37 ± 1	23.26 ± 3.14	23.83
8.41	37 ± 1	34.11 ± 3.81	38.58

labile protons in urea n_s (Equation 11). Using the AREX maps of eight model solutions at pH = (5.66, 5.72, 5.92, 6.12, 7.8, 8.02, 8.20, 8.41), we obtained $n_s = 4.10 \pm 0.21$. This result suggests that urea possesses four labile protons. Finally, employing the Equation 10 with $f_s = 4$, the exchange rate k_{sw} maps of urea can be calculated (Figure 5). The k_{sw} derived experimentally from CEST data agree well with the reference values $k_{sw,ref}$, at pH values below 6.2 and above 7.4 at 37°C (Figure 5, Table 2). In the neutral solutions the exchange rate of urea is minimal and could not be accurately estimated from the CEST data. In general, it is possible to determine the pH maps by solving the Equation 1 with the k_{sw} values calculated from the CEST data. However, in the case of bi-exponential function we obtain two real solutions and without additional information, we cannot univocally decide which of the two possible pH values is "correct".

3.4 | Assessment of pH dependence of the CEST effect of other kidney metabolites

In order to identify major kidney metabolites, which possess exchangeable protons and may generate an experimentally measurable CEST effect under physiological condition, results from animal[18] and human studies[43] on kidney tissues as well as the Urine Metabolome Database[19] were analyzed.

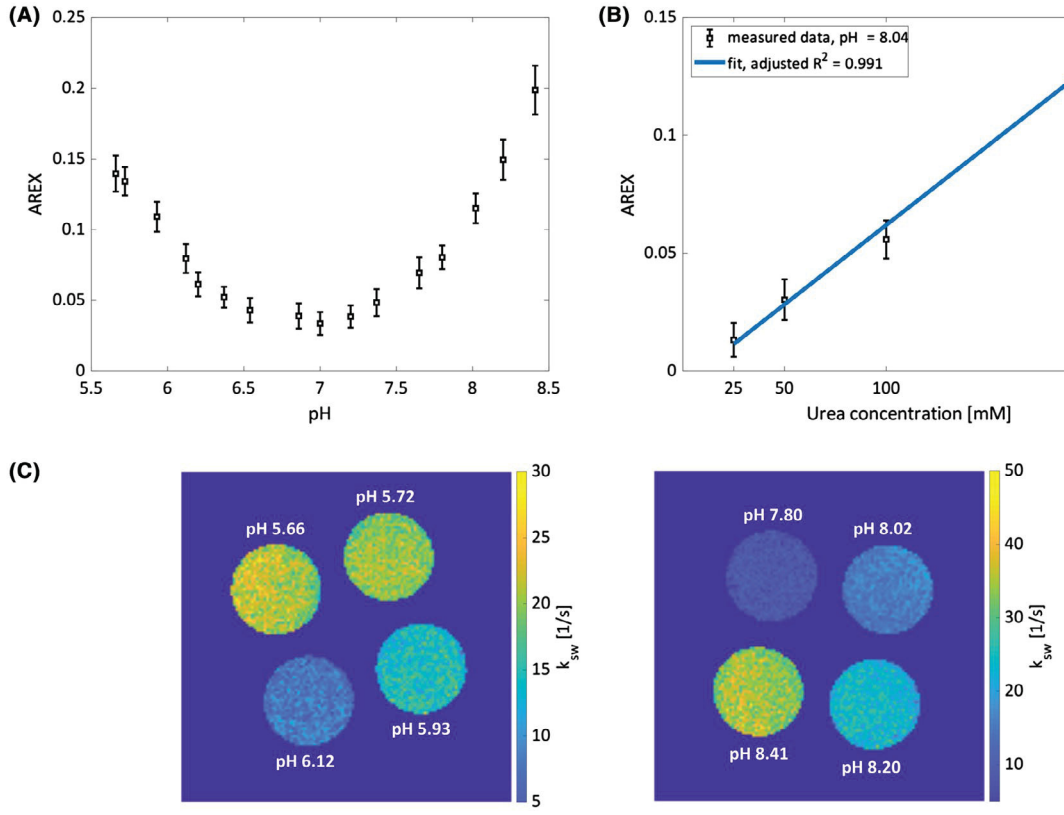

FIGURE 5 Apparent exchange-dependent relaxation (AREX) as a function of (A) pH and (B) urea concentration c_{urea} and (C) two exemplary exchange rates k_{sw} maps. A, Temperature T = (37 ± 1)°C and urea concentration c_{urea} = 250 mM were fixed. The AREX values were obtained from Equations 8 and 9. B, Temperature T = (37 ± 1)°C and pH_{fixed} = 8.04 were fixed. Data were fitted (solid blue line) using Equations 8-11. The fit quality was: R^2 = 0.991. C, The k_{sw} maps for two sets of the urea model solutions: #1 (pH 5.66, c_s = 250 mM), #2 (pH 5.72, c_s = 250 mM), #3 (pH 5.93, c_s = 250 mM), #4 (pH 6.12, c_s = 250 mM), #5 (pH 7.80, c_s = 250 mM), #6 (pH 8.02, c_s = 250 mM), #7 (pH 8.20, c_s = 250 mM), #8 (pH 8.41, c_s = 250 mM) obtained from the quantitative CEST experiments at T = 37°C

TABLE 3 An overview of important kidney metabolites and their CEST properties

Compound	Functional group	δ_s [ppm][a]	k_{sw} [1/s][b]	c_s in urine[c],[19]
Sugars	Hydroxyl protons (−OH)			
Glucose	−OH	1.2, 2.2, 2.8[62]	∼2000[63,64]	37.5 (12.5-58.4)
Sorbitol	−OH	1.0[7]	n/a	9.9 (2.5-18.7)
Glycogen	−OH	1.2, 2.2, 3.0[65]	∼600[65]	n/a
Myo-inositol	−OH	∼0.8, ∼0.9, ∼1.1[66]	600[66]	22.4 (7.9-36.1)
Amino acids	Amino protons ($-NH_2$)			
Creatinine	$-NH_2$	∼1.3	n/a	14743±9797[d]
Creatine	Guanidinium protons	1.9	∼490[e],[55]	46 (3-448)
Histidine	$-NH_2$, −NH	n/a	n/a, 1700[f],[67]	43 (17-90)
Glutamine	$-NH_2$	2.9	n/a	37.3 (19.1-77.9)
Alanine	$-NH_2$	3.0[7]	∼3030[g],[68]	21.8 (7.1-43.1)
Lysine	$-NH_2$	3.0[7]	4000[f],[67]	17.2 (3.7-51.3)
Threonine	$-NH_2$, −OH	n/a, n/a	n/a, 700[f],[67]	13.3 (6.4-25.2)
Glutamate	$-NH_2$	∼3.0	∼2000[i],[65]	8.5 (3.3-18.4)
Miscellaneous				
Urea	$-NH_2$	1.0	∼1	12285 (174-49097)
Ammonia	NH_3	2.4[13]	n/a	1900.0 ± 350.0
Hippuric acid	−OH, −NH	n/a, n/a	n/a, n/a	229 (19-622)
Citric acid	−OH	0.6-0.8[69]	>2000[69]	203 (49-600)
Taurine	$-NH_2$	∼3.0[65]	300[h],[65]	81 (13-251)
Allantoin	$-NH_2$, −NH	∼1.0, ∼3.0	n/a, n/a	15.4 (4.9-29.3)
Lactate	−OH	0.4[70]	350[i],[70]	11.6 (3.5-29.3)
Choline	−OH	∼1.0[65]	∼400[65]	3.5 (1.4–6.1)

[a] δ_s in ppm is relative to the resonant frequency of water. [b]Measured at pH 7.4 and at $T = 25°C$ unless otherwise noted. [c]Concentrations of all compounds are given in [μM/mM creatinine] unless otherwise noted. [d] μM [e]Measured at pH 7.51. [f]Measured at pH 7.0 and $T = 36°C$. [g]Measured at pH 7.0 and $T = 22°C$. [h]Measured at pH 5.6. [i]Measured at pH 7.0.

Only molecules found in relatively high abundance in kidney tissue and urine were investigated. Finally, a comprehensive list of the potential CEST-active metabolites was created (Table 3). The z-spectra and magnetization transfer ratio asymmetry (MTR_{asym}) curves were measured at various pH values. While all of the systematically tested metabolites possess exchangeable protons, not all of them generate large CEST contrast at 3T in the measured pH range of 6.2-7.4 and temperature $T = 37°C$ (z-spectra and MTR_{asym} curves not shown). Creatinine, creatine, glutamine, alanine, allantoin, and glutamate showed the highest CEST effect under physiological conditions (Figure 6).

3.5 | Investigation of the specificity of urea-weighted CEST imaging

To examine the specificity of urCEST, aqueous solutions containing three most abundant urine metabolites that show measurable CEST effect, namely urea, creatinine, and creatine, were prepared at pH 5.97 and measured at $T = 37°C$ (Figure 7). The concentrations of the individual compounds were: 180, 15, and 1 mM for urea, creatinine and creatine, respectively, corresponding to the normal concentrations of these metabolites in urine (Table 3). The determined exchange rate of urea was: $k_{sw} = 9.25 \pm 1.79$, indicating good agreement with the reference k_{sw} value ($k_{sw} = 10.80 \pm 1.13$). Moreover, the calculated z-spectrum and the MTR_{asym} curve of the mixed phantom were similar to those obtained in the urine sample at pH 5.90. Both CEST spectra reveal a dominant peak at ca. 1 ppm, which can be assigned to the exchanging amide protons of urea.

4 | DISCUSSION

4.1 | Proton exchange in aqueous urea solutions

In our study, we were able to determine experimentally the urea exchange rate constants with high accuracy. The previously reported rate constants of urea are: $k_a = (7.0 \pm 2.0) \times 10^6$

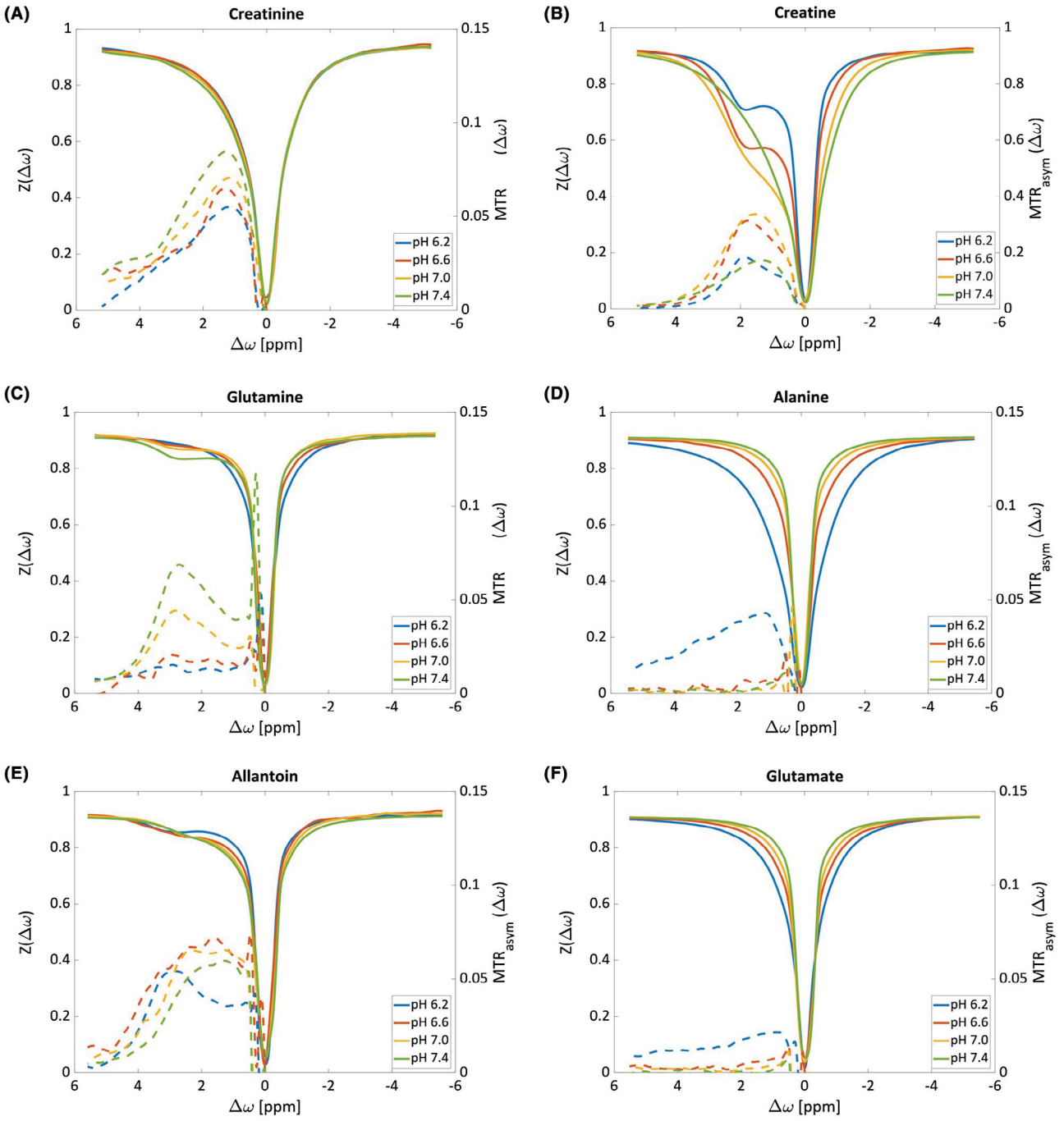

FIGURE 6 Experimentally obtained z-spectra (solid lines) and MTR_{asym} curves (dashed lines) of different kidney metabolites at $T = 37°C$. The metabolites are: (A) creatinine (100 mM), (B) creatine (100 mM), (C) glutamine (100 mM), (D) alanine (100 mM), (E) allantoin (35 mM), (F) glutamate (50 mM)

l/(mol·s), $k_b = (4.8 \pm 1.6) \times 10^6$ l/(mol·s) at $T = 22°C$ (29), and $k_a = (9.0 \pm 1.0) \times 10^6$ l/(mol·s), $k_b = (2.4 \pm 1.0) \times 10^6$ l/(mol·s) at $T = 35°C$ [24,44] and have been measured by use of line shapes of urea and water in ^{1}H NMR. For amides, this method is not exact because of line broadening associated with ^{14}N quadrupole relaxation of the amide nitrogen.[45] As an alternative, line shapes for the proton-coupled ^{15}N NMR spectra were calculated for investigating the NH-exchange rates of urea, yielding the following results: $k_a = (18.0 \pm 12.0) \times 10^6$ l/(mol·s), $k_b = (4.4 \pm 1.0) \times 10^6$ l/(mol·s) at $T = 32°C$.45 It seems that the WEX II method provides smaller standard errors than the linewidth-based methods and thus improves the accuracy and precision of predictions. Although all previous estimated k_a and k_b values are in good agreement, direct comparison of the results is difficult due to differences in the experimental conditions, such as the buffer concentration

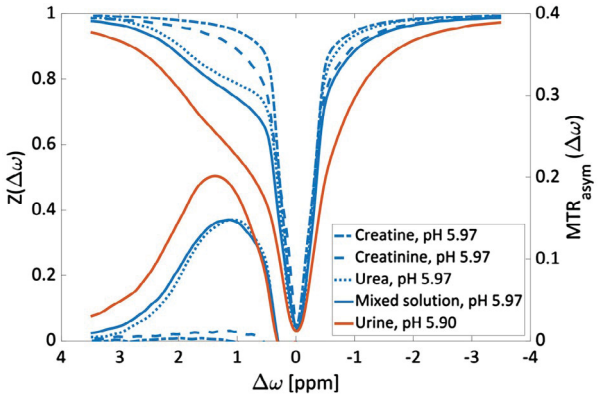

FIGURE 7 Z-spectra and MTR_{asym} curves for the individual solutions of 180 mM urea (blue dotted line), 15 mM creatinine (blue dashed line), 1 mM creatine (blue dash-dot line), their mixture (blue solid line) at pH 5.97 and for the urine sample (red solid line) at pH 5.90. The temperature of the model solutions during the measurements was kept constant at $T = (37 \pm 1)$°C

and temperature. Since the pH in urea solutions tends to drift slowly because of CO_2 absorption and decomposition of urea into ammonium and cyanate ions,[24,46] we dissolved urea in 50 mM Na/K-phosphate buffer. The pH value did not change over a period of several hours.

The acid-catalyzed rate constant of urea is large compared to rate constants for acid-catalyzed protolysis of most amides.[23,44] High k_a rate constant suggests higher probability of H_3O^+ with nitrogen than with oxygen, resulting in observable proton transfer.[44] Thus, the large value of k_a for urea solution implies protonation on urea nitrogen rather than oxygen.[44]

The comparison of the estimated activation energies $E_{A,a} \approx (19 \pm 4)$ kcal/mol and $E_{A,b} \approx (10 \pm 2)$ kcal/mol with the apparent heat of activation for amide hydrogen exchange of about 17 kcal/mol, reported by Englander et al shows good agreement.[47] Recently, Bodet et al. estimated the effective activation energy of amide proton exchange $E_{b,eff} = (54.12 \pm 9.15)$ kJ/mol $\approx (13 \pm 2)$ kcal/mol in carnosine solutions buffered with (1/15) M PBS buffer.[27] The same study also showed that the buffer has a strong influence on the amide hydrogen exchange rate and its dependence on pH and temperature. This finding should be taken into consideration when analyzing our results.

4.2 | WEX and CEST methods

Several methods have been proposed for estimation exchange rates, which is possible due to their dependence on the saturation power and time.[29,31-33,48-50] The water exchange (WEX) filter sequence has already been used for measuring exchange rates of slowly exchanging species.[17,27,37] Therefore, we decided to apply this method to amide exchange in aqueous urea solutions. In contrast to the original WEX II sequence, we used excitation sculpting instead of WATERGATE technique for water suppression. Because of the large width of the urea peak and its nearness to the water resonant frequency, we expect that the WATERGATE water suppression may negatively impact the urea signal due to the lack of sufficient selectivity.[51] One of the challenges with the spectroscopy (MRS)-based methods, such as the WEX approach, is the low sensitivity, which makes it difficult to detect low abundance metabolites in vivo. Furthermore, the WEX experiments are not suitable for measuring faster rates since the signal of the exchangeable peak is reduced owing to exchange with suppressed water proton.[28,52] The WEX spectroscopy has been already used to measure exchange rates of creatine guanidinium protons and amide protons of carnosine on a 3T clinical MRI system.[26,27] However, this method is not applicable to urea samples at low magnetic field.

The exchange rates of urea derived from CEST experiments are in good agreement with those obtained by WEX experiments. However, it was not possible to determine the k_{sw} values of urea in the physiologically relevant pH range. Derivation of the exchange-dependent relaxation rate R_{ex} used here is based on the assumption that the influence of the R_{1s} is negligible against k_{sw} for exchanging system.[53,54] This requirement is not fulfilled for exchange rates that are in the order of the longitudinal relaxation rate R_{1s}. Moreover, in the neutral solutions the CEST effect was minimal and thus the signal to noise ratio was insufficient for a proper quantification.

In order to determine the quantitative CEST parameters of urea, we have applied the extended steady-state method AREX, introduced by Roelloffs et al.[34,35] For extremely slow exchange rates of urea, modeling of bi-exponential decay during the break was important. The exchange rates obtained using the "standard" AREX approach, were significantly overestimated (approximately 40%). Since the CEST contrast depends on both concentration and k_{sw}, it is necessary to employ quantitative methods that allow separating these parameters. Previous study have shown that the CEST effect can be represented as a linear function of $1/B_1^2$ and that the exchange rate and proton fraction can be determined independently by linear regression (the so-called ω-plot).[31-33,48,49] However, this method seems to be not applicable at low exchange rates due to a high noise level and small B_1 dispersion.[26,55]

In our study, we have investigated a number of important kidney/urine metabolites with exchangeable protons that may produce a CEST effect in vivo. However, for most of them no CEST contrast in the examined pH range and at a buffer concentration of 50 mM was observed at 37°C. This is consistent with the fast exchange. Moreover, in the case of hydroxyl groups of, eg, myo-inositol, glucose, and glycogen the resonance peaks were possibly within the linewidth of the water resonance. Therefore, it is unlikely that any of these metabolites contribute to the total CEST effect at ca. 1 ppm in kidney

at clinical field. Besides urea, several other compounds show a measurable CEST effect under physiological conditions at 3T. These might potentially overlap with the urea CEST signal in the urine/kidney in vivo. The absolute urea quantification might be, therefore, considerably hampered. In our study, we were able to estimate the k_{sw} of urea from CEST experiments performed on a mixture model solution of urea, creatinine, and creatine. However, we have assumed that the urea concentration is much higher than the creatinine concentration (12:1), as had been previously measured in urine (Table 3).[19] The difference in MTR_{asym} between the urine and mixture peaks results most likely from slightly different pH values as well as different concentrations of individual metabolites in urine compared with the mixed solution. To the best of our knowledge, no study determined absolute concentrations of metabolites in human kidney in vivo. Further extensive research is necessary in order to assess the contribution of other kidney metabolites superimposed on the urCEST effect at different pH.

pH-sensitive chemical exchange saturation transfer (CEST) MRI is a promising new method for in vivo applications.[56-60] Exogenous CEST agent pH mapping have already been applied for kidney imaging. The measured pH in kidneys was shown to vary between 5.4 and 7.4 for healthy mice.[58] Since the exchange rate of urea is minimal at this pH range, it might be challenging to obtain the pH maps of kidneys using only the quantitative urea-weighted CEST method. On the other hand, pH could be measured independently using paraCEST (eg, Lanthanide-DOTA-tetraamide complexes,[56] Eu3+ based agents[56,57]) or diaCEST agents (eg, Iopamidol[58,59]) in order to derive urea concentration by combining Equations 1 and 10.[60]

5 | CONCLUSIONS

In our study, we present a successful application of the WEX spectroscopy for determining exchange rate constants of urea and evaluate the feasibility of the quantitative urea-weighted CEST imaging at a clinical MRI system. We show that similar to simple amides, proton exchange in aqueous urea solutions is acid and base catalyzed with the rate constants: $k_a = (9.95 \pm 1.1) \times 10^6$ l/(mol·s) and $k_b = (6.21 \pm 0.21) \times 10^6$ l/(mol·s), and activation energies: $E_{A,a} = 79.13 \pm 15.87$ kJ/mol and $E_{A,b} = 43.52 \pm 9.56$ kJ/mol, respectively. Although urea protons undergo a slow exchange with water protons, it was possible to estimate its exchange rate at pH values below 6.2 and above 7.4 at $T = (37 \pm 1)$°C using the quantitative CEST analysis. Moreover, several other kidney metabolites, which are expected to partially conceal the CEST effect of urea in vivo, were examined. Further investigations are needed to characterize the explicit dependence of the exchange rate constant of urea amide protons on different pH buffer systems.

ACKNOWLEDGMENTS

This study was supported by a Grant from the Forschungskommission of the Faculty of Medicine, Heinrich Heine University, Düsseldorf (Grant No: 13/2015). The authors acknowledge access to the Jülich-Düsseldorf Biomolecular NMR Center.

REFERENCES

1. Bennion BJ, Daggett V. The molecular basis for the chemical denaturation of proteins by urea. *Proc Nat Acad Sci USA* 2003;100:5142–5147.
2. Atkinson DE, Bourke E. The role of ureagenesis in pH homeostasis. *Trends Biochem Sci*. 1984;9:297–300.
3. Weiner ID, Mitch WE, Sands JM. Urea and ammonia metabolism and the control of renal nitrogen excretion. *Clin J Am Soc Nephrol*. 2015;10:1444–1458.
4. Champe PC, Harvey RA, Ferrier DR. *Lippincott's Illustrated Reviews: Biochemistry*. 5th ed. Philadelphia: Lippincott Williams & Wilkins; 2004.
5. Baum N, Dichoso CC, Carlton CE. Blood urea nitrogen and serum creatinine: physiology and interpretations. *Urology* 1975;5:583–588.
6. Herget-Rosenthal S. Imaging techniques in the management of chronic kidney disease: current developments and future perspectives. *Seminars Nephrol*. 2011;31:283–290.
7. Ward KM, Aletras AH, Balaban RS. A new class of contrast agents for MRI based on proton chemical exchange dependent saturation transfer (CEST). *J Magn Reson*. 2000;143:79–87.
8. van Zijl PCM, Yadav NN. Chemical exchange saturation transfer (CEST): what is in a name and what isn't? *Magn Reson Med*. 2011;65:927–948.
9. Heo H-Y, Zhang Y, Burton TM, et al. Improving the detection sensitivity of pH-weighted amide proton transfer MRI in acute stroke patients using extrapolated semisolid magnetization transfer reference signals. *Magn Reson Med*. 2017;78:871–880.
10. Zhang S, Malloy CR, Sherry AD. MRI thermometry based on PARACEST agents. *J Am Chem Soc*. 2005;127:17572–17573.
11. Yang B, Bankir L. Urea and urine concentrating ability: new insights from studies in mice. *Am J Phys-Renal Phys*. 2005;288: F881–F896.
12. Hastings J, de Matos P, Dekker A, et al. The ChEBI reference database and ontology for biologically relevant chemistry: enhancements for 2013. *Nucleic Acids Res*. 2013;41:D456–D463.
13. Guivel-Scharen V, Sinnwell T, Wolff SD, Balaban RS. Detection of proton chemical exchange between metabolites and water in biological tissues. *J Magn Reson*. 1998;133:36–45.
14. Dagher AP, Aletras A, Choyke P, Balaban RS. Imaging of urea using chemical exchange-dependent saturation transfer at 1.5T. *J Magn Reson Imaging* 2000;12:745–748.
15. Vinogradov E, Liu Z, Madhuranthakarn A, et al. Endogenous urea CEST (urCEST) for MRI monitoring of kidney function. In Proceedings of the 23th Annual Meeting of ISMRM, Toronto, Canada, 2015:3375.
16. Kim J, Wu Y, Guo Y, Zheng H, Sun PZ. A review of optimization and quantification techniques for chemical exchange saturation transfer MRI toward sensitive in vivo imaging. *Contrast Media Mol Imaging* 2015;10:163–178.

17. Mori S, Abeygunawardana C, van Zijl PCM, Berg JM. Water exchange filter with improved sensitivity (WEX II) to study solvent-exchangeable protons. Application to the consensus zinc finger Peptide CP-1. *J Magn Res Ser B*. 1996;110:96–101.
18. Serkova N, Fuller TF, Klawitter J, Freise CE, Niemann CU. ^{1}H-NMR-based metabolic signatures of mild and severe ischemia/reperfusion injury in rat kidney transplants. *Kidney Int*. 2005;67:1142–1151.
19. Bouatra S, Aziat F, Mandal R, et al. The human urine metabolome. *PLoS One* 2013;8:e73076.
20. Findeisen M, Brand T, Berger S. A ^{1}H-NMR thermometer suitable for cryoprobes. *Magn Reson Chem*. 2006;45:175–178.
21. Delaglio F, Grzesiek S, Vuister GW, Zhu G, Pfeifer J, Bax AD. NMRPipe: a multidimensional spectral processing system based on UNIX pipes. *J Biomol NMR* 1995;6:277–293.
22. Kim M, Gillen J, Landman BA, Zhou J, van Zijl PCM. Water saturation shift referencing (WASSR) for chemical exchange saturation transfer (CEST) experiments. *Magn Reson Med*. 2009;61:1441–1450.
23. Berger A, Loewenstein A, Meiboom S. Nuclear magnetic resonance study of the protolysis and ionization of N-Methylacetamide1. *J Am Chem Soc*. 1959;81:62–67.
24. Klotz IM, Hunston DL. Proton exchange in aqueous urea solutions. *J Phys Chem*. 1971;75:2123–2127.
25. Foote HW. Elements of physical chemistry. *Science* 1907;26:588–588.
26. Goerke S, Zaiss M, Bachert P. Characterization of creatine guanidinium proton exchange by water-exchange (WEX) spectroscopy for absolute-pH CEST imaging in vitro. *NMR Biomed*. 2014;27:507–518.
27. Bodet O, Goerke S, Behl NGR, Roeloffs V, Zaiss M, Bachert P. Amide proton transfer of carnosine in aqueous solution studied in vitro by WEX and CEST experiments. *NMR Biomed*. 2015;28:1097–1103.
28. McMahon MT, Gilad AA, Zhou J, Sun PZ, Bulte JWM, van Zijl PCM. Quantifying exchange rates in chemical exchange saturation transfer agents using the saturation time and saturation power dependencies of the magnetization transfer effect on the magnetic resonance imaging signal (QUEST and QUESP): Ph calibration for poly-L-lysine and a starburst dendrimer. *Magn Reson Med*. 2006;55:836–847.
29. Dixon WT, Ren J, Lubag AJM, et al. A concentration-independent method to measure exchange rates in PARACEST agents. *Magn Reson Med*. 2010;63:625–632.
30. Sun PZ. Simplified quantification of labile proton concentration-weighted chemical exchange rate (kws) with RF saturation time dependent ratiometric analysis (QUESTRA): normalization of relaxation and RF irradiation spillover effects for improved quantitative chemical exchange saturation transfer (CEST) MRI. *Magn Reson Med*. 2011;67:936–942.
31. Sun PZ. Simultaneous determination of labile proton concentration and exchange rate utilizing optimal RF power: Radio frequency power (RFP) dependence of chemical exchange saturation transfer (CEST) MRI. *J Magn Reson*. 2010;202:155–161.
32. Wu R, Xiao G, Zhou IY, Ran C, Sun PZ. Quantitative chemical exchange saturation transfer (qCEST) MRI—omega plot analysis of RF-spillover-corrected inverse CEST ratio asymmetry for simultaneous determination of labile proton ratio and exchange rate. *NMR Biomed*. 2015;28:376–383.
33. Meissner J-E, Goerke S, Rerich E, et al. Quantitative pulsed CEST-MRI using Ω-plots. *NMR Biomed*. 2015;28:1196–1208.
34. Zaiss M, Xu J, Goerke S, et al. Inverse Z-spectrum analysis for spillover-, MT-, and T_1-corrected steady-state pulsed CEST-MRI—application to pH-weighted MRI of acute stroke. *NMR Biomed*. 2014;27:240–252.
35. Roeloffs V, Meyer C, Bachert P, Zaiss M. Towards quantification of pulsed spinlock and CEST at clinical MR scanners: an analytical interleaved saturation—relaxation (ISAR) approach. *NMR Biomed*. 2014;28:40–53.
36. Santyr GE, Fairbanks EJ, Kelcz F, Sorenson JA. Off-resonance spin locking for MR imaging. *Magn Reson Med*. 1994; 32:43–51.
37. Hwang TL, Shaka AJ. Water suppression that works. Excitation sculpting using arbitrary wave-forms and pulsed-field gradients. *J Magn Reson Ser A*. 1995;112:275–279.
38. Grzesiek S, Bax A. The importance of not saturating water in protein NMR. Application to sensitivity enhancement and NOE measurements. *J Am Chem Soc*. 1993;115:12593–12594.
39. Geen H, Freeman R. Band-selective radiofrequency pulses. *J Magn Reson (1969)* 1991;93:93–141.
40. Cavanagh J, Fairbrother WJ, Palmer AG, IIIRance M, Skelton NJ. *Protein NMR Spectroscopy*. 2nd ed. Burlington: Elsevier Academic Press; 1996.
41. Zhang O, Kay LE, Olivier JP, Forman-Kay JD. Backbone ^{1}H and ^{15}N resonance assignments of the N-terminal SH3 domain of drk in folded and unfolded states using enhanced-sensitivity pulsed field gradient NMR techniques. *J Biomol NMR* 1994;4:845–858.
42. Seber GAF, Wild CJ. *Nonlinear Regression*; New York: John Wiley and Sons; 1989.
43. Bassi R, Niewczas MA, Biancone L, et al. Metabolomic profiling in individuals with a failing kidney allograft. *PloS One* 2017;12:e0169077-e0169077.
44. Vold RL, Daniel ES, Chan SO. Magnetic resonance measurements of proton exchange in aqueous urea. *J Am Chem Soc*. 1970;92:6771–6776.
45. Yavari I, Roberts JD. Nitrogen-15 nuclear magnetic resonance spectroscopy. NH proton exchange reactions of urea and substituted ureas. *Organ Magn Reson*. 1980;13:68–71.
46. Dortch RD, Horch RA, Does MD. Development, simulation, and validation of NMR relaxation-based exchange measurements. *J Chem Phys*. 2009;131:164502.
47. Englander SW, Downer NW, Teitelbaum H. Hydrogen exchange. *Annual Rev Biochem*. 1972;41:903–924.
48. Wu R, Liu C-M, Liu PK, Sun PZ. Improved measurement of labile proton concentration-weighted chemical exchange rate (kws) with experimental factor-compensated and T_1-normalized quantitative chemical exchange saturation transfer (CEST) MRI. *Contrast Media Mol Imaging* 2012;7:384–389.
49. Sun PZ, Wang Y, Dai Z, Xiao G, Wu R. Quantitative chemical exchange saturation transfer (qCEST) MRI—RF spillover effect-corrected omega plot for simultaneous determination of labile proton fraction ratio and exchange rate. *Contrast Media Mol Imaging* 2014;9:268–275.
50. Bottomley PA, Griffiths JR. *Handbook of Magnetic Resonance Spectroscopy in vivo: MRS Theory, Practice and Applications*. Chichester, UK: Wiley; 2016.
51. Liu L, Mo H, Wei S, Raftery D. Quantitative analysis of urea in human urine and serum by ^{1}H nuclear magnetic resonance. *Analyst* 2012;137:595–600.

52. Valérie CP, Allen MJ. *Contrast Agents for MRI: Experimental Methods (New Developments in NMR)*. 1st ed. Cambridge: Royal Society of Chemistry; 2017.
53. Zaiss M, Bachert P. Exchange-dependent relaxation in the rotating frame for slow and intermediate exchange—modeling off-resonant spin-lock and chemical exchange saturation transfer. *NMR Biomed*. 2012;26:507–518.
54. Zaiss M, Bachert P. Chemical exchange saturation transfer (CEST) and MR *Z*-spectroscopy in vivo: a review of theoretical approaches and methods. *Phys Med Biol*. 2013;58:R221–R269.
55. Stabinska J, Cronenberg T, Wittsack H-J, Lanzman RS, Müller-Lutz A. Quantitative pulsed CEST-MRI at a clinical 3T MRI system. *Magn Reson Mater Phys Biol Med*. 2017;30:505–516.
56. Pavuluri K, McMahon MT. pH Imaging using chemical exchange saturation transfer (CEST) MRI. *Israel J Chem*. 2017;57:862–879.
57. Wu Y, Zhang S, Soesbe TC, et al. pH imaging of mouse kidneys in vivo using a frequency-dependent paraCEST agent. *Magn Reson Med*. 2015;75:2432–2441.
58. Longo DL, Dastrù W, Digilio G, et al. Iopamidol as a responsive MRI-chemical exchange saturation transfer contrast agent for pH mapping of kidneys: in vivo studies in mice at 7 T. *Magn Reson Med*. 2010;65:202–211.
59. Longo DL, Sun PZ, et al. A general MRI-CEST ratiometric approach for pH imaging: demonstration of in vivo pH mapping with iobitridol. *J Am Chem Soc*. 2014;136:14333–14336.
60. Sun PZ, Longo DL, Hu W, Xiao G, Wu R. Quantification of iopamidol multi-site chemical exchange properties for ratiometric chemical exchange saturation transfer (CEST) imaging of pH. *Phys Med Biol*. 2014;59:4493–4504.
61. Finer EG, Franks F, Tait MJ. Nuclear magnetic resonance studies of aqueous urea solutions. *J Am Chem Soc*. 1972;94:4424–4429.
62. Chan KWY, McMahon MT, Kato Y, et al. Natural D-glucose as a biodegradable MRI contrast agent for detecting cancer. *Magn Reson Med*. 2012;68:1764–1773.
63. Hills BP. Multinuclear NMR studies of water in solutions of simple carbohydrates. *Mol Phys*. 1991;72:1099–1121.
64. Wiebenga-Sanford BP, DiVerdi J, Rithner CD, Levinger NE. Nanoconfinement's dramatic impact on proton exchange between glucose and water. *J Phys Chem Lett*. 2016;7:4597–4601.
65. Lee J-S, Xia D, Jerschow A, Regatte RR. In vitro study of endogenous CEST agents at 3T and 7T. *Contrast Media Mol Imaging* 2015;11:4–14.
66. Haris M, Cai K, Singh A, Hariharan H, Reddy R. In vivo mapping of brain myo-inositol. *NeuroImage* 2011;54:2079–2085.
67. Liepinsh E, Otting G. Proton exchange rates from amino acid side chains—implications for image contrast. *Magn Reson Med*. 1996;35:30–42.
68. Wermter FC, Bock C, Dreher W. Investigating GluCEST and its specificity for pH mapping at low temperatures. *NMR Biomed*. 2015;28:1507–1517.
69. Basharat M, deSouza NM, Parkes HG, Payne GS. Determining the chemical exchange saturation transfer (CEST) behavior of citrate and spermine under in vivo conditions. *Magn Reson Med*. 2016;76:742–746.
70. DeBrosse C, Nanga RPR, Bagga P, et al. Lactate chemical exchange saturation transfer (LATEST) imaging in vivo a biomarker for LDH activity. *Sci Rep*. 2016;6:19517.

How to cite this article: Stabinska J, Neudecker P, Ljimani A, Wittsack H-J, Lanzman H-RS, Müller-Lutz A. Proton exchange in aqueous urea solutions measured by water-exchange (WEX) NMR spectroscopy and chemical exchange saturation transfer (CEST) imaging in vitro. *Magn Reson Med*. 2019;82:935–947. https://doi.org/10.1002/mrm.27778